Structural Stabilization of

α-Helical Antifreeze Protein Variants

Using the Trp-cage Protein

Dissertation
zur Erlangung des Doktorgrades
der Mathematisch-Naturwissenschaftlichen Fakultät
der Christian-Albrechts-Universität zu Kiel

vorgelegt von

Joana Gronow

Kiel, 2019

Erster Gutachter: Prof. Dr. Frank D. Sönnichsen

Zweiter Gutachter: Prof. Dr. Ulrich Lüning

Tag der mündlichen Prüfung: 28.01.2020

Preface

Die vorliegende Arbeit wurde unter Anleitung von

Prof. Dr. Frank D. Sönnichsen

in der Zeit von Oktober 2013 bis Mai 2019

am Otto Diels-Institut für Organische Chemie

der Christian-Albrechts-Universität zu Kiel angefertigt.

Eigenständigkeitserklärung

Hiermit erkläre ich, Joana Gronow, die vorliegende Dissertation selbstständig und ausschließlich unter Zuhilfenahme der angegebenen Quellen und Hilfsmittel angefertigt zu haben. Inhalt und Form der Arbeit habe ich, abgesehen von Beratung durch meinen Betreuer, Prof. Dr. Frank D. Sönnichsen, eigenständig erarbeitet und verfasst. Bei der Entstehung der Arbeit wurden die Regeln guter wissenschaftlicher Praxis der Deutschen Forschungsgemeinschaft eingehalten. Weder die gesamte Arbeit noch Teile hiervon wurden an anderer Stelle im Rahmen eines Prüfungsverfahrens eingereicht. Diese Dissertation ist mein erster Promotionsversuch.

Teile von Projekten mit Kooperationspartnern wurden in Peer-Review-Zeitschriften publiziert. Diese wurden aufgrund der unterschiedlichen Thematik nicht mit in die Arbeit aufgenommen.

(1) Müller, A.; Kobarg, H.; Chandrasekaran, V.; Gronow, J.; Sönnichsen, F. D.; Lindhorst, T. K. Synthesis of Bifunctional Azobenzene Glycoconjugates for Cysteine-Based Photosensitive Cross-Linking with Bioactive Peptides. *Chem. Eur. J.* **2015**, *21*, 13723-13731.

Kiel, 05.11.2019 Joana Gronow

Danksagung

Ich weiß noch genau, wie ich das erste Mal zu Frank Sönnichsen ins Büro gegangen bin und mit ihm über mein F3-Praktikum gesprochen habe. Damals war Hauke Kobarg in deinem Arbeitskreis und er hat mich in den Peptid-Synthesizer eingewiesen. Ungefähr zeitgleich mit mir fing dann auch Matthias Lipfert an und Kannika Thonghkhao kam für zwei Jahre aus Thailand. Den internationalen Austausch hast du weiter gefördert, Frank, indem zu mit uns zur IBP gefahren bist. Das produktive Miteinander in unserer kleinen Gruppe wurde auch immer durch den Arbeitskreis Staubitz und Lüning, mit denen wir einen regen Austausch führten, beeinflusst. Mit der Zeit änderten sich die Mitglieder des Arbeitskreises und Katrin Bamberg und Nils Preußke kamen hinzu. Dabei ließ das Interesse für die spannenden, etwas außergewöhnlichen Forschungsthemen bei mir nie nach. Danke, Frank, dass du mir ermöglicht hast, Antigefrierproteinen zu erforschen. Danke auch an das Landesgraduiertenstipendium für die finanzielle Förderung.

Im Rahmen meiner Arbeit konnte ich auch Studierende in meine Forschung einarbeiten. Es hat mir viel Spaß gemacht, mit Christian und Mike zu arbeiten.

Besonders finde ich auch die Kooperation, die mit dem Arbeitskreis Axel Scheidig entstanden ist. Vielen Dank für das schöne Zusammenarbeiten an Brigitte, Chrissy, Kubi, Felix, …

Und selbstverständlich möchte ich mich bei Gitta, Marion und Holger bedanken. Ihr kümmert euch nicht nur großartig um die NMRs. Vielen Dank für die kleinen Gespräche, Ideen und Termine am 600er.

‚The largest fish […] yielded half a cubic centimeter of blood,

the medium-sized fish was eaten by a dog,

and the little one […] yielded a tiny drop of eye chamber fluid.‘

Scholander, P. F.; van Dam, L.; Kanwisher, J. W.; Hammel, H. T; Gordon, M. S. Supercooling and osmoregulation in arctic fish. *J. Cell. Comp. Physiol.* **1957**, *49*, 5-24.

Kurzzusammenfassung

Antigefrierproteine werden in vielen Spezies exprimiert, die in Temperaturen um und unter dem Gefrierpunkt leben. Die Proteine erniedrigen den Gefrierpunkt des Wassers und ermöglichen so ein Überleben in diesem Temperaturbereich. Eine der Spezies, die Antigefrierproteine exprimiert, sind Fische. Trotz der strukturellen Vielfalt der Sekundär- und Tertiärfaltungen ist das α-helikale Antigefrierprotein der Winderflunder (WflAFP) das wahrscheinlich am besten untersuchte. Die Antigefrieraktivität aller Antigefrierproteine wurde mit der Größe und Ebenheit einer Eis-bindenden Seite in Zusammenhang gebracht. Bei WflAFP befindet sie sich auf einer Seite der α-Helix. Die Bestimmung der notwendigen Größe der Eis-bindenden Seite wurde im Fall des WflAFP allerdings dadurch erschwert, dass mit einer Verkürzung der Sequenz auch ein Verlust der α-Helizität einhergeht. In dieser Studie wurde deshalb eine C-terminal Capping Unit, die Helizes stabilisiert und die Faltung induziert, verwendet – der Trp-cage. Als erstes wurde der Effekt der Modifikation auf die Antigefrieraktivität des WflAFP untersucht. Nachdem ein negativer Einfluss der C-terminalen Veränderung auf die Proteineigenschaften ausgeschlossen wurde, konnte die Abhängigkeit der Antigefrieraktivität von der Größe der Eis-bindenden Seite evaluiert werden. Die Verbindung beider Proteine erfolgte dafür nach zwei unterschiedlichen Konzepten: Das Fusions-Konzept basiert auf der getrennten Synthese von Antigefrierprotein-Segment und Trp-cage und der Kombination beider Teile in einem zweiten Schritt. Das Chimeren-Konzept basiert auf der Tatsache, dass sowohl in der Primärsequenz des Trp-cages als auch des Antigefrierprotein-Segments Aminosäuren austauschbar sind. Durch die Überlappung von zwei Proteinbereichen entsteht ein insgesamt kürzeres Protein.

Vier unterschiedlich lange Antigefrierproteinvarianten wurden mit dem Trp-cage stabilisiert. Drei der Eis-bindenden Trp-cage Chimeren wurden auch als GFP gelabelte Proteine hergestellt und mit UV/vis-, CD- und NMR-Spektroskopie sowie Massenspektrometrie charakterisiert. Die Antigefrieraktivität und die Form der Eiskristalle in Gegenwart der einzelnen Eis-bindenden Trp-cage Chimeren wurden mikroskopisch untersucht. Alle Proteine, die nach dem Chimeren-Konzept designt wurden, waren gefaltet, das Protein, das nach dem Fusion-Konzept designt wurde, dagegen hatte eine verringerte Faltungsstabilität. Dennoch wurden alle Proteine auf ihre Antigefrieraktivität hin untersucht. Die Proteine, die basierend auf WflAFP designt wurden, hatten eine vergleichbare Aktivität mit dem Wildtyp, für die anderen konnte keine Antigefrieraktivität gemessen werden. Zusammenfassend hat die C-terminale Modifikation die Antigefrieraktivität des WflAFP nicht beeinflusst. Allerdings ist eine α-helikale Faltung nicht die einzige Voraussetzung für Eis-Aktivität. Da die kürzeren Eis-bindenden Trp-cage Chimeren keine Antigefrieraktivität aufweisen, ist die Proteingröße, die notwendig ist für Aktivität, identisch mit der von dem Wildtyp des WflAFP.

Abstract

Antifreeze proteins are prevalent in many species that experience freezing or close to freezing temperatures. The proteins lower the freezing point of water, enabling the species to survive subzero temperatures. One of these species is fish, in which antifreeze proteins originally were discovered. While antifreeze proteins can be found in a wide variety of secondary and tertiary structures, the α-helical antifreeze protein from winter flounder (WflAFP) is probably the most extensively studied. The antifreeze activity of all antifreeze proteins has been correlated to size and flatness of the ice-binding surface which for WflAFP has been demonstrated to be on one side of the α-helix, comprising primarily regularly spaced alanine and threonine side chains. The analysis of the size necessary for activity, however, was complicated in the case of WflAFP as a shortening of the sequence also lead to a reduction in α-helicity. To overcome this difficulty, in this work a C-terminal stabilizing and α-helicity inducing capping unit, the Trp-cage, was employed. In a first step, the effect of the C-terminal modification on the wild-type antifreeze protein had to be studied to eliminate any interference of the modification on ice activity. In a second step, after eliminating any negative influence of the capping unit, the dependence of ice activity on the size of the ice-binding surface could be analyzed. The combination of both Trp-cage and antifreeze protein segment was pursued using two different approaches: The fusion approach was based on the synthesis of both the Trp-cage capping unit and an antifreeze protein segment separately and fusing them together in a second step. The chimera approach is based on the fact, that in the primary sequence of both Trp-cage and antifreeze protein some amino acids are interchangeable leading to an overlapping sequence and overall a shorter protein.

Four α-helical antifreeze protein variants of different lengths were stabilized using the Trp-cage. Of the four ice-binding Trp-cage chimera (IBTC), three were also obtained as GFP labeled variants. All IBTC were characterized using NMR-, CD-, and UV/vis-spectroscopy, mass spectrometry and their antifreeze activity or ice growth retardation as well as ice shaping abilities were determined. All ice-binding Trp-cage chimera designed based on the chimera approach were well folded. The IBTC designed based on the fusion approach, on the other hand, had a less pronounced fold according to ^{1}H NMR data. All folded IBTC also satisfied the criteria for α-helicity in a chemical shift deviation plot and the CD data also indicate α-helicity for all IBTC. The analysis of ice activity gave surprising results. The IBTC based on the wild-type antifreeze protein had comparable antifreeze activity to WflAFP. However, no antifreeze activity could be observed for the other IBTC. As a result, even though the C-terminal capping unit has no influence on the antifreeze activity of the IBTC, the induction and stabilization of α-helicity is not the only criteria necessary for activity. Rather, the size of the ice-binding surface has to match the one present in nature to generate antifreeze activity.

Content

1 Introduction and Objectives

1.1 Introduction

"'When arctic fishes swim about in ice water at -1.7° to -1.8°, why don't they freeze? Do they have twice as high an osmotic concentration as ordinary fishers, or what is the story?'" This question from Dr. R. H. Backus to M. S. Gordon does not only show good observation skills and scientific interest but marks the beginning of the research area termed nowadays antifreeze or ice binding proteins.[1] While Scholander and his colleagues set out to find out how teleost fishes can survive at water temperatures of -1.9 °C when the freezing point of their blood is around -0.7 °C at the coast of Labrador,[1] DeVries and Wohlschlag were the ones to identify a serum soluble glycoprotein which is responsible for 30% of the freezing-point depression in *Trematomus borchgrevinki*. Their data also showed a larger freezing-point depression than could be expected for the number of molecules. Consequently the freezing point depression caused by antifreeze proteins is a non-colligative property. The difference between melting and freezing point of water is called thermal hysteresis.[2]

With the first antifreeze (glyco)protein discovered, several fish in the northern and southern hemispheres were tested for antifreeze activity. The teleostei present a high structural diversity of antifreeze proteins in primary, secondary and tertiary structure: single alanine-rich α-helices, termed Type I,[3,4] C-type lectin-like Type II of which some are Ca^{2+}-dependent,[5–7] globular proteins containing short β-strands comprising a flattened surface Type III,[8,9] and the above mentioned antifreeze glycoproteins[2] (see Fig. **1**).

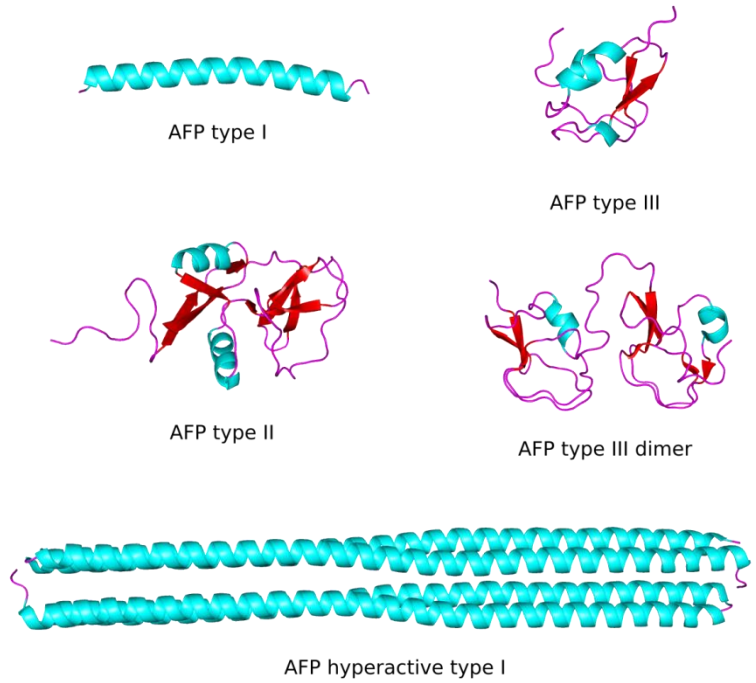

Fig. 1: Overview of the different types of antifreeze proteins found in fish. The secondary structure elements of the cartoon representation of AFP type I as well as the AFP hyperactive type I from winter flounder (PDB: 1WFA and 4KE2), AFP type II from sea ravens (PDB: 2AFP), AFP type III and the AFP type III dimer from eelpout (PDB: 1AME and 1C8A) are colored in cyan for α-helices, red for β-sheets, and magenta for loop structures.[3,5,10–12]

The high structural diversity of antifreeze proteins even between fish of the same taxonomic order – although both the sea raven and the sculpin belong to the family cottoidei, they express type II and type I antifreeze proteins, respectively – suggest that the evolution of antifreeze proteins is a recent event in geological time. The sea-level glaciation event in the southern hemisphere during the Eocene-Oligocene transition (~34 million years ago)[13] and in the northern hemisphere ~2.5 million years ago (Pliocene)[14] have been postulated by Scott *et al.* as driving force for the evolution of antifreeze proteins (see Fig. 2).[15–17]

Interestingly, the Arctic cod and Antarctic toothfish, two phylogentically distant fish, both produce antifreeze glycoproteins consisting of a similar repetitive tripeptide. However, the coding sequences of both genes are drastically different and the intron-exon organization of both genes is dissimilar hinting to separate genomic origins. *Chen et al.* concluded that both fish have evolved their antifreeze glycoproteins through convergent evolution.[17]

However, a comparison between other antifreeze proteins from smelt (*omeridae*) and herring (*clupeidea*) showed a high sequence similarity not only in the coding region but also in the

introns. The additional facts that the smelt antifreeze protein sequence is found just once in the genome compared to a usual high copy number and that the differences between different smelt of the same genus is of the same order as to herring (different superorder) all point to a lateral gene transfer between both fish species as an additional way to acquire antifreeze properties (see Fig. **2**).[18–21]

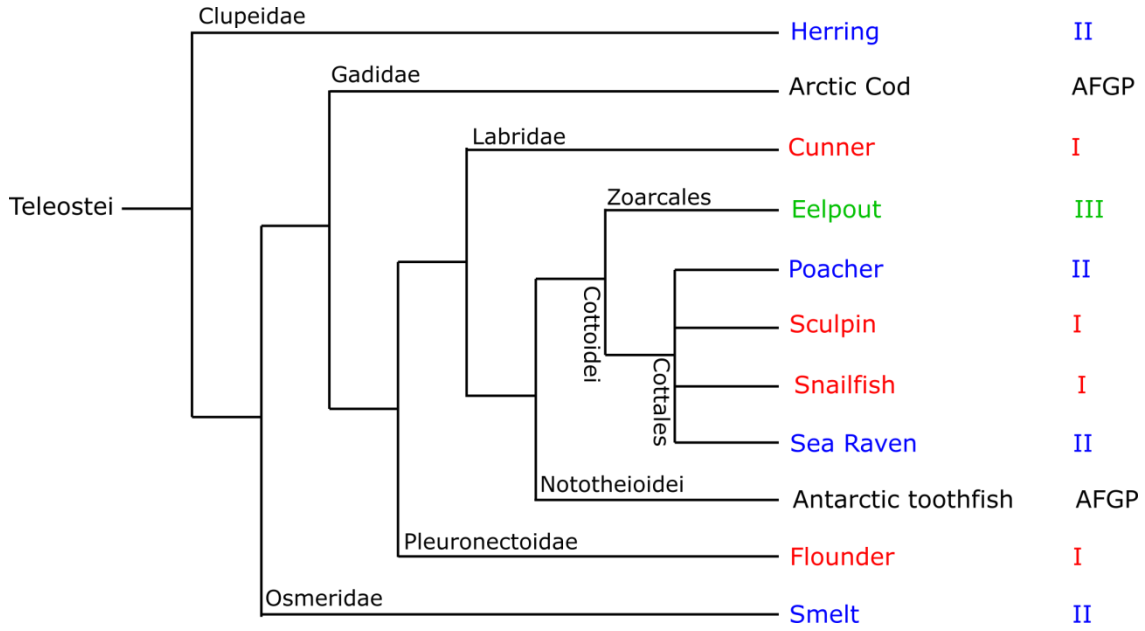

Fig. 2: Phylogenic relationship between AFP-producing fish according to Betancur-R *et al.*[16,17,22] Species names are colored by AFP type. The scientific names are as follows: herring (*Clupea harengus*)[6], arctic cod (*Boreogadus saida*)[17],cunner (*Tautogolabrus adspersus*)[23], eelpout (*Zoarces americanus*, *Lycodichtys dearborni*, *Zoarces viviparus*, *Zoarces elongates*)[9,10,24,25], poacher (*Brachyosis rostratus*)[7], sculpin (*Myoxocephalus scorpius*, *Myoxocephalus aenaeus*, *Myoxocephalus octodecemspinosus*, *Myoxocephalus scorpioides*)[4,26–28], snailfish (*Liparis atlanicus*, *Liparis gibbus*)[29], sea raven (*Hemitripterus americanus*)[5], Antarctic toothfish (*Dissostichus mawsoni*)[17], flounder (*Pseudopleuronectes americanus*, *Limanda ferruginea*, *Pleuronectes quadritaberulatus*)[3,30], smelt (*Omerus mordax*)[18].

Even though the antifreeze proteins from fish are probably the most extensively studied, antifreeze proteins have also been discovered in bacteria, plants, fungi, and arthropods[31–34], adding to the structural diversity of antifreeze proteins. The antifreeze proteins form *Lolium perenne* or *Tenebrio molitor* as well as *Marinomonas primoryensis* for example are all β-helices (see Fig. **3**). While some antifreeze proteins show an antifreeze activity[3], others inhibit ice recrystallization[32], have an ice structuring effect[35], or act as ice adhesives[31,36].

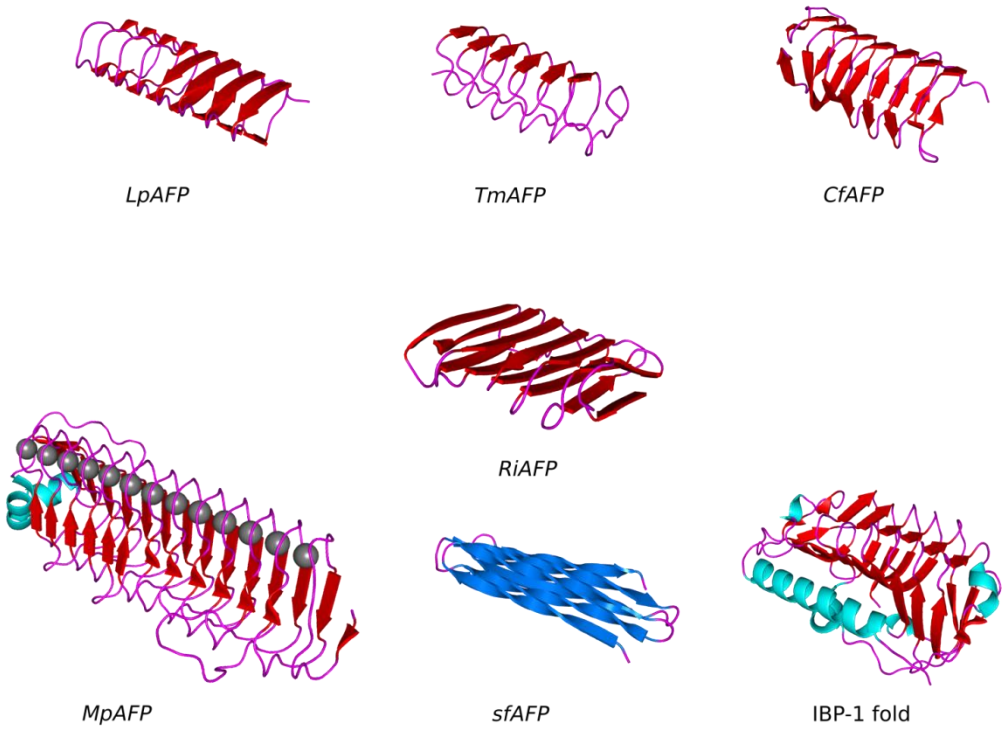

Fig. 3: Overview over the structural diversity of antifreeze proteins without the fish AFP with the ice active side on top. The cartoon representation of LpAFP from *Lolium perenne (PDB: 3ULT), TmAFP from Tenebrio* molitor (PDB: 1EZG), MpAFP from *Marinomonas primoryensis* (PDB: 3P4G), sfAFP from snow flea (PDB: 2PNE), IBP-1 fold from snow mold fungus (PDB: 3VN3), CfAFP from *Chorisoneura fumiferana* (spruce budworm) (PDB: 1M8N), and RiAFP from *Rhagium inquisitor* (PDB:4DT5) are colored according to their secondary structure: cyan for α-helices, red for β-sheets, magenta for loop structures, marine for polyglycine II helices, and grey spheres for calcium ions.[31–34,37–39]

The high structural diversity of antifreeze proteins raises the question of their structure-function relationship. Raymond and DeVries proposed an adsorption inhibition mechanism by which antifreeze proteins bind irreversibly to the surface of ice crystals. After the irreversible binding of antifreeze proteins to the ice, a further addition of water molecules to the ice is only possible in the gaps between the proteins resulting in a curvature of the ice surface. A further growth on a curved front is energetically less favorable and the growth retarded, which is called Kelvin or Gibbs-Thompson effect (see Fig. **4**).[40,41]

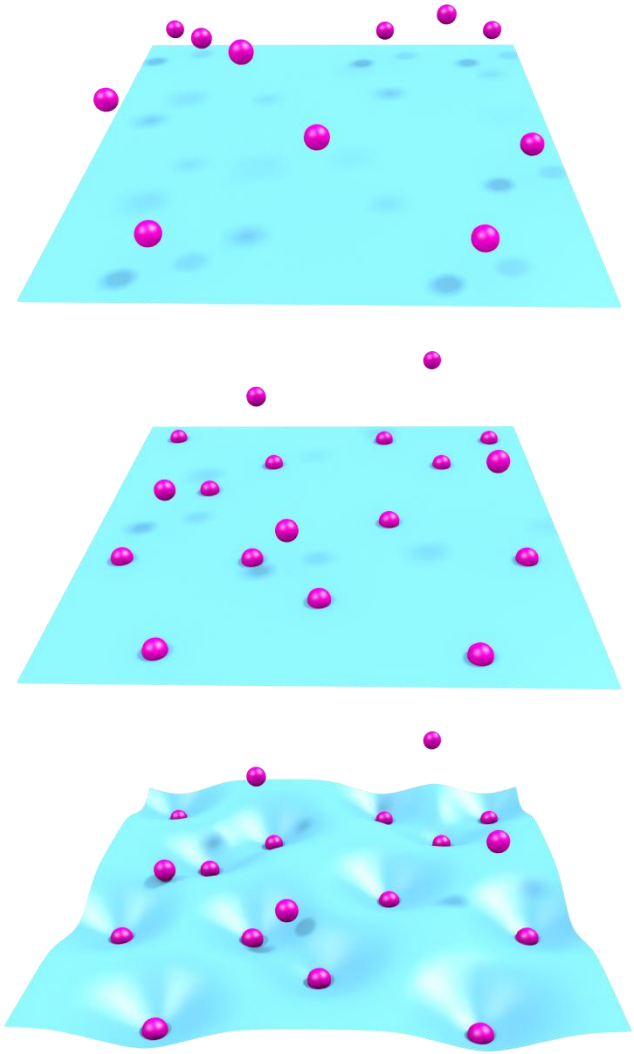

Fig. 4: Schematic view of the binding of antifreeze proteins (purple spheres) to an ice following the mattress-button model. The antifreeze proteins are in solution until an ice crystal starts to form (top view). The antifreeze proteins bind to the surface of the ice crystal (middle) so that a further growth of the ice crystal is only possible in the free space between the proteins leading to an unfavorable curved front (bottom view).

The irreversible binding of antifreeze proteins to ice was subject to discussion until Pertaya *et al.* studied the attachment of an antifreeze protein type III fused with green fluorescent protein (GFP) to ice using fluorescence recovery after photobleaching (FRAP). They let the fused protein accumulate on the surface of an ice crystal and then bleached the proteins bound to the whole or part of the ice crystal until the fluorescence was reduced to low levels. Observation for up to 20 h showed no recovery of the fluorescence indicating a quasi-permanent attachment.[42] Using a

microfluidic device Celik *et al.* later showed that the antifreeze proteins bound to the ice surface are sufficient to stabilize an ice crystal by first letting the antifreeze proteins bind to the ice crystal and then exchanging the surrounding solution to buffer. The ice crystal retained its size and shape in the cooled buffer solution.[43]

Under normal pressure the only stable form of ice at <0 °C is hexagonal ice, I_h (see Fig. 5).[44] Ice crystal growth in absence of any impurities takes place along each prism face, in Bravais-Miller indices $\{10\bar{1}0\}$ (see Fig. **5**, blue plane).[45] With the growth along the *a*-axes being swifter than along the *c*-axis, flat discs are formed.

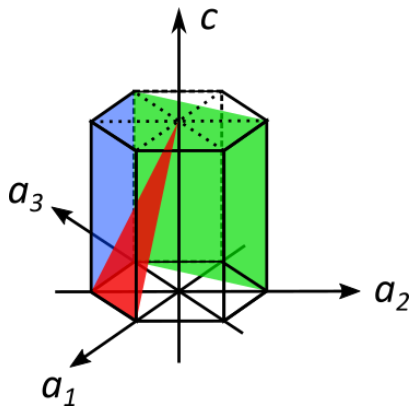

Fig. 5: Illustration of the different ice crystal surfaces to which an antifreeze protein can bind. The basal plane {0001} is perpendicular to the *c*-axis, the prism plane $\{\mathbf{10\bar{1}0}\}$ is shown in blue, the secondary prism plane $\{\mathbf{11\bar{2}0}\}$ in green, and the pyramidal plane $\{\mathbf{20\bar{2}1}\}$ in red.

However, in the presence of antifreeze proteins Raymond and DeVries observed long ice needles whose axes where aligned with the ice *c*-axis.[40] The formation of needles aligned with the *c*-axis indicates a reversal in growth speed along the *a*- and *c*-axes, with a faster ice crystal growth along the *c*-axis. By binding to a specific plane of ice crystals, like the primary or secondary prism plane (Fig. **5**, blue and green plane respectively) or the pyramidal plane (red), antifreeze proteins block the growth at this plane and cause a change in the observable ice crystal structure. Most fish antifreeze proteins bind to only one ice crystal plane. The winter flounder antifreeze protein for instance binds to the pyramidal plane.[46] As the pyramidal plane is symmetric within the hexagonal crystal lattice, the growth along *a*- and *c*-axis is hindered, giving hexagonal bipyramidal ice crystals. However, as the antifreeze proteins do not bind to the basal plane, upon supercooling the ice crystal bursts at the tips. On the other hand, other antifreeze proteins can bind to several ice crystal planes. By interacting with the basal and primary prism plane for

example, the ice crystal growth is inhibited in both *a*- and *c*-axis direction and the 'hyperactive' antifreeze proteins have a thermal hysteresis activity of several degree Celsius. [39,47,51]

The determination of the crystallographic planes on which antifreeze proteins bind can be done using either ice hemisphere etching or a variation of it, the fluorescence-based ice plane affinity (FIPA). For ice hemisphere etching a single orientated ice crystal is grown in a dilute solution of antifreeze protein and then allowed to evaporate at -10 to -15 °C for several hours. An etching pattern appears showing the incorporation of antifreeze proteins into ice and indicating the specific adsorption plane (see Fig. 6).[48] FIPA analysis is based on ice etching but the antifreeze protein is fluorescently labeled. It can either be a fluorescent protein fused to the antifreeze protein or a covalently bound fluorescent dye. The experimental set up is the same but in contrast to the ice etching method the binding of the antifreeze protein can be monitored during the growth of the ice hemisphere using an UV lamp and the determination of the adsorption plane doesn't necessitate the etching step (see Fig. **7**).[49,50]

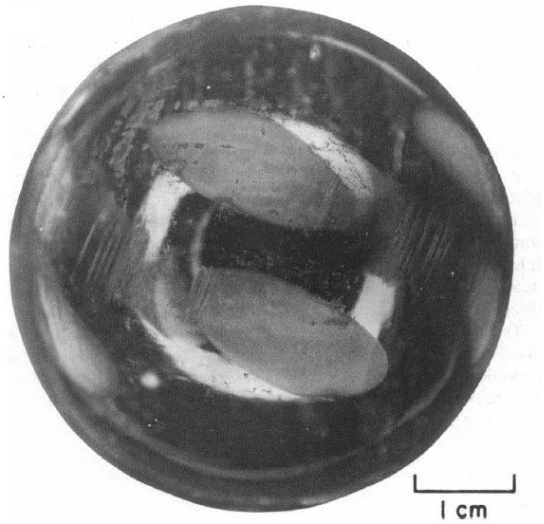

Fig. 6: Photographs of a single-crystal hemisphere grown from winter flounder AFP solution. Bottom view of a hemisphere grown with a prism plane oriented normal to the long axis of the cold finger, scraped and etched. The bright reflections are portions of the ring light reflected from the mirror-smooth, curved ice surface where no antifreeze was incorporated. Reprint with permission by Elsevier.[48]

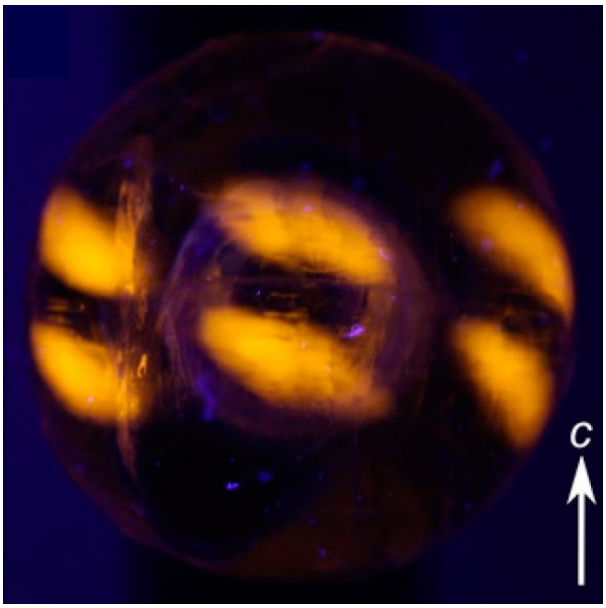

Fig. 7: Single ice-crystal hemisphere of tetramethylrhodamine-labeled type I AFP. The crystal was mounted with a primary prism plane oriented perpendicular to the ice finger. The diameter of the hemisphere is approx. 5 cm. Reprint with permission.[31]

The binding of antifreeze proteins to ice can be explained by a structural match between the antifreeze protein fold and the ice crystal lattice as well as a mixture of hydrogen bonding and hydrophobic interactions. Additionally, a proposed anchored clathrate model will be discussed.

With mutagenesis studies on several antifreeze proteins their active ice binding sites could be identified.[33,49,51,52] Common to all antifreeze proteins is that their ice binding site is flat and hydrophobic. Amino acid side chains which were determined to be important for binding are spaced evenly apart on the ice binding surface. The hydrophobic but also the hydrophilic functional groups are positioned in a good surface match to the ice crystal lattice. The sum of hydrophobic interactions and hydrogen bonds resulting through the steric match are both important for the irreversible binding to ice.[53] The surface complementarity will be further explored in the following chapter of the winter flounder antifreeze protein.

The anchored clathrate model is based on a crystal structure of MpAFP from the bacterium *Marinomonas primoryensis*. For the first time the ice binding sites of an antifreeze protein were not oriented towards each other in a protein crystal and hydration water on the ice binding site could be observed. The water on the ice-antifreeze protein interface was ordered by the amino acid side chains into an ‘anchored clathrate’ motif which is proposed to facilitate binding to ice.[31] This preordering of the water molecules before binding however could not be proven experimentally[54] and a recent molecular dynamics simulation shows that in solution the studied

antifreeze protein did not show anchored clathrate-like water.[55] The direct protein-ice interaction today still eludes our direct experimental possibilities and presents a challenging field of scientific research.

1.1 Winter Flounder Antifreeze Protein

The winter flounder antifreeze protein (WflAFP) from *Pseudopleuronectus americanus* is a 37 amino acid short peptide with an amidated C-terminus. The amino acid sequence consists of three 11-residue repeating segments, T-X_2-polar amino acid-X_7, with X predominantly alanine. Structurally, it folds to an α-helix, has a salt bridge between K18 and E22, and capping structures at the N- and C-termini, with the amidated C-terminal arginine forming a 3_{10} helix (see Tab. **1** and Fig. **8**).[56] Both N- and C-terminal caps form hydrogen bonds with the neighboring amino acids and neutralize the positive helix dipole moment at the N-terminus and the negative helix dipole moment at the C-terminus.[57] Its short sequence and simple secondary structure makes it probably the most extensively studied antifreeze protein.

Tab. 1: Primary sequence of WflAFP.*

	1	10	20	30
WflAFP	D TASDAAAAAAL	TAANAKAAAEL	TAANAAAAAAA	TAR-NH_2

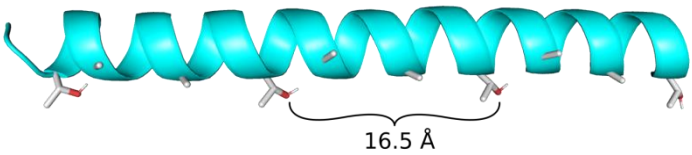

Fig. 8: Backbone representation of the secondary structure of WflAFP. Threonine and alanine side chains are shown as sticks in the following color code: carbon is grey, oxygen red and hydrogen white. (PDB: 1WFA)[3]

WflAFP binds to the pyramidal plane of ice and shapes ice crystals to hexagonal bipyramids with a *c*- to *a*-axes ratio of 3.3:1 (see Fig. 9).[59] Upon extreme supercooling, the ice crystal bursts at its tips, the only two points at which WflAFP cannot bind.

* The amino acid sequence of all proteins is presented in one letter code according to IUPAC.[58]

By mutating several amino acids, the evenly spaced threonines where determined as important for binding to ice. Based on the ice etching pattern of WflAFP along $\langle 01\bar{1}2 \rangle$, a match between the 16.7 Å repeat spacing of the ice and the spacing of the threonine residues of 16.5 Å was proposed (see Fig. 8).[48,60,61]

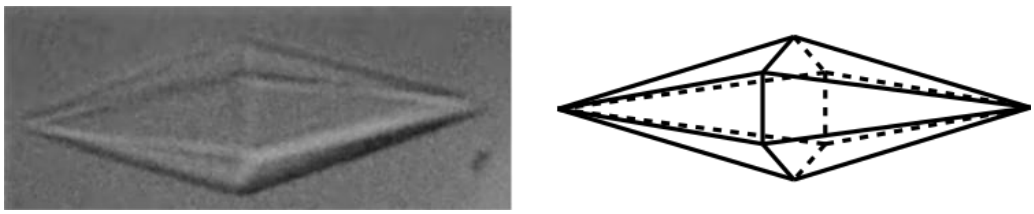

Fig. 9: Shape of an ice crystal in the presence of an antifreeze protein type I as observed under the microscope (left) and a schematic representation (right). By binding to the pyramidal plane the antifreeze protein hinders a growth along this face and shapes the ice crystal into a hexagonal bipyramid.

A postulated hydrogen bonding to ice lattice oxygen via the hydroxyl groups of the threonines was put into question by substituting the threonines with serines or valines. While both mutants maintain α-helicity, the serine-analogue showed no interaction with the ice surface in contrast to the valine-analogue which showed thermal hysteresis comparable to the wild type.[62–64] A combination of hydrogen bonds and hydrophobic interactions between antifreeze protein and ice seems to be the key for irreversible binding to ice.[53]

The influence of the protein fold on activity was studied by several groups. A decrease in helicity was always accompanied by a decrease in activity. Then again, restoring the helicity led to retrieval of some activity. For instance, Patel *et al.* analyzed the effect of the C-terminal amidation by comparing amidated and nonamidated WflAFP. A reduction of the thermal hysteresis activity of nonamidated WflAFP was attributed to an increased flexibility of the C-terminus.[65] Other groups observed a loss of helicity and antifreeze activity upon shortening of the wild-type WflAFP sequence.[46,56,59,66] On the other hand, by stabilizing a 15 amino acid short segment with an internal lactam bridge the helical content could be increased to 90% and the stabilized peptide showed ice shaping properties but could not prevent ice crystal growth.[59]

A stable α-helical fold is a prerequisite for WflAFP activity and its shortened variants. Upon further consideration that is not surprising as only a correct fold maintains the 16.5 Å distance

between the threonines which is important for the surface complementarity to the pyramidal plane of ice.

1.2 Trp-cage

The Trp-cage is a 20 amino acid short peptide designed by Neidigh *et al.* originating from a 39 amino acid long exendin-4 from the gila monster salvia, *Heloderma suspectum*.[67,68] By shortening the N-terminus and mutating several amino acids, a protein dubbed Tc5b with an unusually stable fold under physiological pH was created (see Tab. **2** and Fig. **10**).[67]

Tab. 2: Primary sequence of Exendin-4 and the Trp-cage Tc5b.

Exendin-4	HGEGTFTSD LSKQMEEEAV RLFIEWLKNG GPSSGAPPPS-NH_2
Tc5b	NLYIQWLKDG GPSSGRPPPS

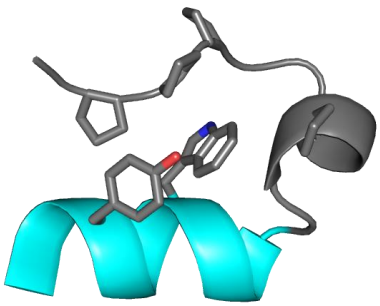

Fig. 10: Trp-cage Tc5b in cartoon representation. The side chains achieving the hydrophobic encapsulation of the tryptophan are shown in stick representation (Y3, W6, P12, P17, P18, P19). The α-helical N-terminus is colored cyan in the backbone, the cage loop backbone is grey as are the carbon atoms of the stick representation. Nitrogen is blue and oxygen red. (PDB: 1L2Y)[67]

Structurally, the Trp-cage is comprised of an N-terminal α-helix (residues 1-9), a 3_{10} helix from residue 11-14, and a polyproline II helix at the C-terminus (see Fig. **10**). The fold is stabilized by the hydrophobic burial of a tryptophan by several prolines, π-π interactions between Y3 and W6, and a 'hydrophobic staple' between Y3 and P19. Other interactions contributing to the fold stability are a π-CH interaction of the tryptophan side chain with an arginine side chain and a salt bridge between D9 and R16 (both not shown).[69,70]

The combination of all interactions results in an exceptionally well stabilized protein with a melting temperature of 42 °C at pH 7.[69] The complex and stable fold makes the Trp-cage an ideal model protein for experimental and computational studies.[71–74] While the folding pathway was postulated as a cooperative folding event, it is currently under discussion with some experimental evidence pointing to an intermediate for some Trp-cage variants with different melting temperatures for the helix and the cage, as supported by MD simulations.[70,71,75,76]

The group around N. H. Andersen increased the fold stability of the Trp-cage miniprotein further by exchanging amino acids and additionally determined amino acids critical for the fold. Replacing the eponymously tryptophan with other aromatic (unnatural) amino acids e.g. is detrimental, as is the mutation of P19 to alanine. The Y3 also is important because of its π-π interaction with W6 but can be exchanged to phenylalanine or leucine at the cost of decreasing fold stability.[69,77]

Additionally to fold stabilization via exchange of amino acids, a stabilizing effect through insertion of multiple alanines in the helical sequence was investigated by Lin *et al.*. An elongation of the N-terminus by up to six alanines showed an increase in Trp-cage fold stability, as observed by melting temperature determined through NMR melting curves, and a propagation of the α-helical fold.[75] This remarkable stability and propagation of the fold will be employed in this work and combined with the activity of antifreeze protein type I variants.

1.2 Fusion and Chimera Concept

In this thesis, the biological activity of antifreeze proteins and the structural stability of the Trp-cage are combined in newly designed proteins called **I**ce-**B**inding **T**rp-cage **C**himera (IBTC). The feasibility of the synergistic fusion of both proteins has already been proven by M. Lipfert and K. Bamberg (Master thesis) and is shown in Fig. 11 with the Trp-cage colored in grey and the antifreeze protein segment in red. The figure clearly visualizes the overlap of both sequences in the helical region.[78]

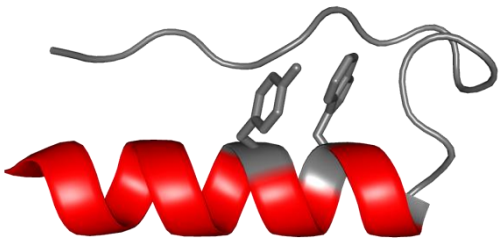

Fig. 11: A chimera protein consisting of the Trp-cage (grey) and a short antifreeze protein type I segment (red) in cartoon ribbon style. The Trp-cage side chains tyrosine and tryptophan are shown as sticks.

The fusion of two proteins is well known in literature[42,79] for e.g. fluorescent labeling or enhancement of protein expression. This approach usually uses a spacer of several amino acids between the proteins so as to allow the single proteins to behave independently from another and make sure that they are not affected in their fold or activity. The synergistic fusion approach in this work however aims to combine the properties of both single proteins in the designed protein, i.e. in this study the combination of the stable fold and solubility of the Trp-cage with the ice activity of the antifreeze protein. As the N-terminus of the Trp-cage is α-helical and as the fold of α-helices is known to be cooperative[80] by the formation of hydrogen bonds between the peptide amides i,i+4, propagating the α-helix, the Trp-cage functions as a helix nucleation point and stabilizing unit. This has been shown previously, by the elongation of the N-terminal sequence leading to stable folded α-helices.[75,78,81]

The combination of the Trp-cage with the α-helical antifreeze protein can be done following two different approaches: a chimera or a fusion approach (see Fig. 12).

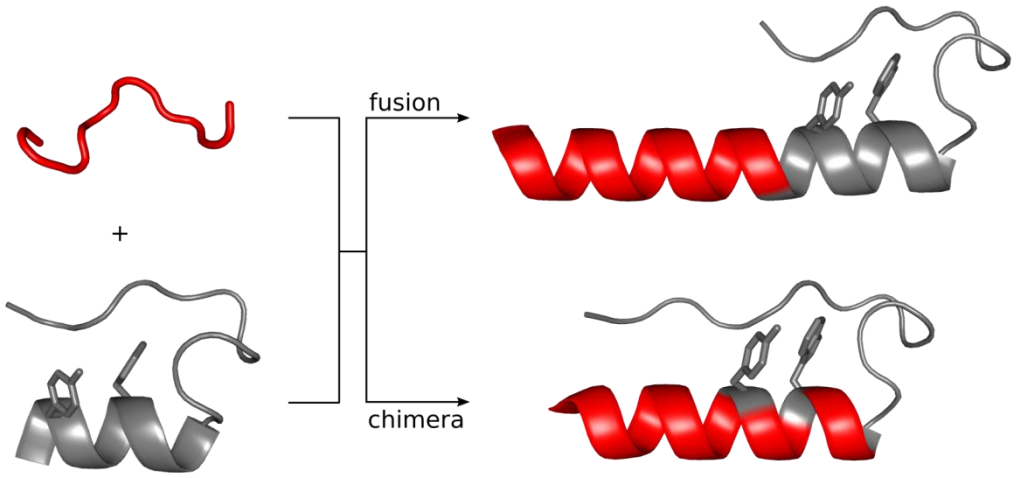

Fig. 12: Overview over the different combination strategies in cartoon style. The two small peptides can be directly fused to another or, by overlapping a short region of both, a shorter chimera protein is formed. In red the biological active protein is unfolded before the combination while the Trp-cage in grey is shown with the side chains from Y3 and W6 in stick representation.

In the fusion approach presented in Fig. 12, the grey Trp-cage sequence is elongated N-terminally with the sequence of the second partner colored in red. The Trp-cage retains its original amino acid composition and thus should not be influenced in its tertiary structure. The fusion partner also retains its original amino acid composition, but through fusion with the Trp-cage module an α-helical folding is induced. One advantage of this approach is that the amino acid composition of both fusion partners does not need to be modified. Furthermore, the orientation of the Trp-cage fold and the helix towards each other can be controlled by the addition of 1-4 spacer residues between the two. An additional advantage is the possibility to create building blocks consisting of (1) the Trp-cage and (2) the α-helical peptide separately and fusing them together in a later step.

In the chimera approach, the helical sequences of the grey Trp-cage and the red active peptide overlap, resulting in a reduction of overall protein length. However, the sequences of both proteins need to be evaluated carefully concerning the exchange of amino acids. The tryptophan in the helical sequence of the Trp-cage e.g. is necessary for its fold and a deletion would prove detrimental. An exchange of the tyrosine to phenylalanine, leucine or isoleucine is possible but results in a reduction of fold stability.[69] All other position can be either the original Trp-cage or the peptide sequence, depending on the characteristics of the peptide.

Proteins designed for either the fusion or chimera approach can be obtained by different methods. In this work, the Fluorenylmethyloxycarbonyl solid phase peptide synthesis (Fmoc-SPPS) and bacterial expression in *E. coli* were used. The fragment approach via SPPS enables a

gradual elongation by the addition of a previously synthesized fragment. Through the addition of several fragments it is possible to maintain a library of different proteins (see Fig. 13).

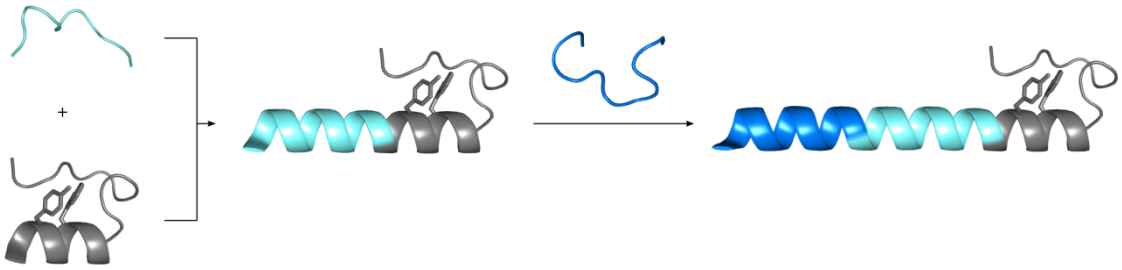

Fig. 13: The fusion approach visualized using the Trp-cage – antifreeze protein concept. The gradual addition of different fragment enables the synthesis of different proteins.

It also enables labeling with other protein, for example GFP.

In contrast to the chemical synthesis of proteins with SPPS, the expression of proteins enables the production of proteins larger than 50 amino acids. Usually, it is done in bacterial cells like *E. coli*, but among others yeast, human and cell free systems exist too. Depending on the host, not all post-translational modifications of the original protein necessarily can be performed. The expression of proteins which are toxic or the side specific incorporation of labeled and/or non-proteinogenic amino acids usually is done using cell free expression systems.[82] The labeling of a complete protein with ^{15}N or ^{13}C on the other hand can be done using cells and a minimal medium containing only the components needed for cellular growth. By supplying nitrogen and carbon only as isotopes, usually as $^{15}NH_4Cl$ or ^{13}C-glucose, all cellular components including the protein of interest incorporate these isotopes.[83]

One further advantage of the bacterial expression of proteins is the possibility of a fusion with the green fluorescent protein (GFP). For that spacer residues between the IBTC and GFP are employed to make sure that neither activity nor fold of the protein units are influenced by each other.

1.3 Previous Work

H. Kobarg was the first member of our group who synthesized the α-helical ice binding protein WflAFP (HPLC 6) from winter flounder (see Fig. **14**). However, synthesis by Fmoc-SPPS yielded low peptide amount of less than 20% (H. Kobarg, unpublished). The low yield can be traced back to a high alanine content of 62% of the peptide sequence as peptides containing a high proportion of alanine tend to form aggregates during Fmoc-SPPS.[84,85] H. Kobarg envisioned a postsynthetic modification of the WflAFP sequence and therefore mutated two residues to cysteines. This decreased the yield even further and, due to the formation of by-products with a similar retention time, complicated purification.

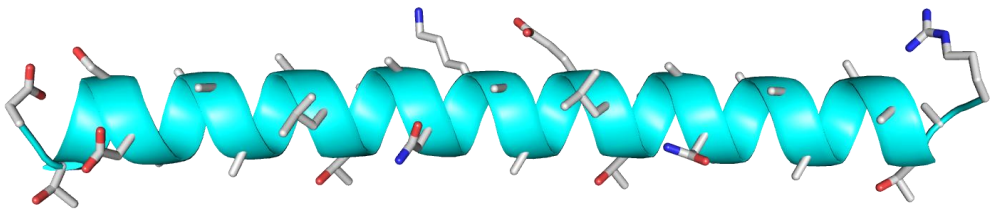

Fig. 14: The backbone of the winter flounder antifreeze protein is shown in cartoon style. The stick representation of all side chains visualizes the high alanine content of the protein with the carbon atoms in grey, oxygen in red, and nitrogen in blue. (PDB: 1WFA)[28]

To overcome low yields and to increase the solubility of the antifreeze protein, M. Lipfert pursued a new approach. He envisioned the transfer of helical fold stability to a short segment of the antifreeze protein type I. Therefore he fused an antifreeze protein segment with a helix stabilizing module, the Trp-cage.

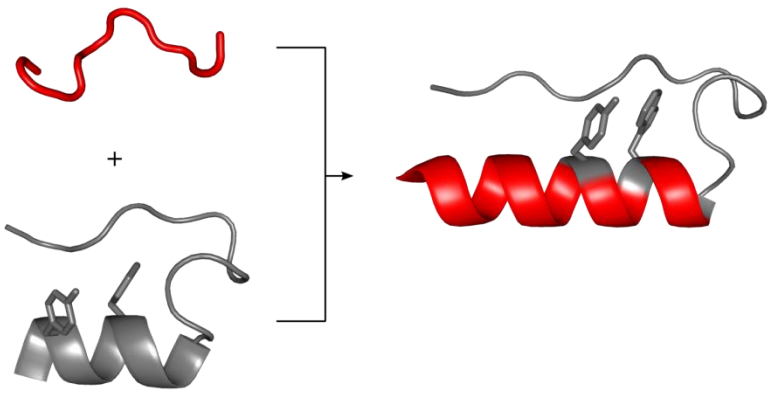

Fig. 15: Schematic representation of the chimera approach in cartoon style. The Trp-cage is grey, the short sequence in red is unfolded before the fusion.

An N-terminal extension of the Trp-cage sequence with amino acids of helical propensity had been studied previously by Lin *et al.* who found that an extension of the sequence with alanine is not only possible without affecting the stable Trp-cage fold but that the α-helical properties of the N-terminus are propagated and the α-helix elongated.[75] This was used by Liu *et al.* in a protein grafting approach to study the binding requirements between the critical residues of the E6-binding motif produced by the human papillomavirus with E6-associated protein. The circular dichroism spectra of the thus grafted proteins were similar to the original Trp-cage scaffold and exhibit characteristic minima at ~207 nm and ~224 nm indicating an α-helix and the nuclear magnetic resonance (NMR) data show the characteristic shifts of the Trp-cage (e.g. G11).[81] Both studies prove that the Trp-cage maintains its fold stability even if the N-terminal α-helix is elongated.

The concept pursued by M. Lipfert in his PhD thesis however represents a new approach. He envisioned to stabilize a short unfolded peptide sequence by a C-terminal capping unit. Importantly, the capping unit he employed was not one or two amino acids short but rather consisted of the Trp-cage sequence. Advantages of the Trp-cage are its high solubility and suitability for Fmoc-SPPS. The fusion of both Trp-cage and antifreeze protein segment was done without a spacer unit between the two fusion partners but in a chimera approach, coupling the structure of the α-helical antifreeze protein type I with the N-terminus of the Trp-cage (see Fig. **15**).[78] As part of the Trp-cage helix and antifreeze protein segment sequence overlap, M. Lipfert considered each residue in the overlapping helical regions of both single proteins carefully. The tryptophan of the Trp-cage as well as the tyrosine are important for folding and have to be preserved while the other positions can be changed to the antifreeze sequence. The advantage of

his approach is a reduction of the overall protein length when compared to a simple fusion of antifreeze protein and Trp-cage. It is however critical to evaluate the orientation of the active site of the antifreeze protein relative to the Trp-cage fold. Therefore four model proteins AFP-Tc-4 to AFP-Tc-7 were synthesized in which the relative orientation of the active side and Trp-cage are varied. While all chimera were folded some exhibited minor forms that were explained by negative interactions caused by the close proximity between N- and C-terminus. All proteins exhibited ice shaping activity with the most stable folded protein showing the strongest ice shaping. He concluded that the ice binding activity is dependent of the fold of the chimera rather than on the relative orientation of the active site compared to the Trp-cage tertiary fold.[78]

1.4 Motivation

The aim of this work is the expansion of knowledge about ice binding Trp-cage chimera proteins (IBTC) by design, synthesis and evaluation of several different IBTC chimeras. Amongst other things the effect of a C-terminal Trp-cage modification on the ice binding properties of WflAFP as well as the influence of a fluorescent labeling with green fluorescent protein on ice binding activity were of interest.

To study the influence of the Trp-cage C-terminal extension on a native antifreeze sequence, the complete length of the protein has to be obtained rather than a shortened version. An IBTC containing the complete WflAFP sequence as well as shortened variants were designed based on the original AFP-Tc-5 design synthesized by M. Lipfert.

Furthermore, the determination of the ice binding plane is of interest as the ice crystals observed by M. Lipfert suggest a preferred binding to the (secondary) prism plane of ice as compared to the pyramidal plane binding of the wild-type antifreeze protein. For fluorescent based ice-affinity assays, labeling the IBTC with a fluorescent marker GFP was envisioned. The corresponding proteins were obtained by bacterial expression in *E. coli* in cooperation with the group of Prof. A. Scheidig, Christiana-Albertina-University, Kiel.

Additionally, the evaluation of a different synthetic approach was pursued. The fusion approach enables a separation of the synthesis of the C-terminal Trp-cage segment and the N-terminal antifreeze protein segment into two independent synthesis followed by a fusion step. This method opens up the possibility of the sequential elongation by active antifreeze segments.

The experience gathered concerning the fusion approach, the determined influence of the C-terminal modification on antifreeze protein type I variants as well as the identified necessary protein length for antifreeze activity are presented in the following chapter.

2 Ice-Binding Trp-cage Chimera

2.1 The Fusion Approach

The Fluorenylmethyloxycarbonyl solid phase peptide synthesis (Fmoc-SPPS) is well established for the synthesis of short peptides. The synthesis of peptides containing more than 50 amino acids is possible, yet the yield and purity of the protein often decreases significantly. A solution to this problem is the synthesis of protein fragments and their ligation in a second step. Common procedures are e.g. the native chemical ligation or the (traceless) Staudinger ligation.[86–88] In this work a different method was used: the synthesis of peptide fragments and their combination in a second step (see Fig. **16**).[84] To achieve a specific reaction between the N- and C-termini of both fragments the reactive side chains of the amino acids have to be protected orthogonally. The synthesis of protected peptide fragments is explained in detail in the experimental section.

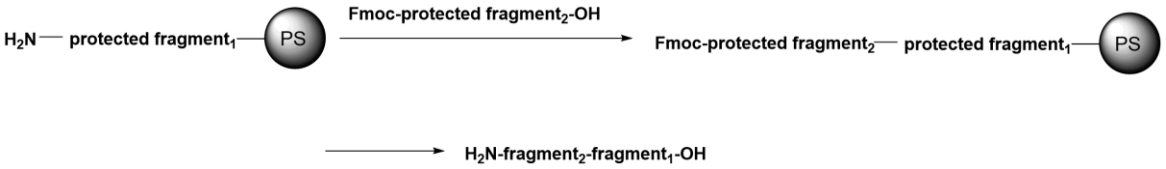

Fig. 16: The combination of two protein fragments yields a longer peptide. PS is short for polystyrene.

In the case of ice-binding Trp-cage chimera, the combination of two peptide fragments from two different proteins was envisioned. The aim was to combine the biological activity of an antifreeze protein fragment with the stable fold of the Trp-cage miniprotein (see Fig. 17).

The winter flounder antifreeze protein (HPLC 6) is an α-helical protein which lowers the freezing point of water. Its activity has been correlated with its fold stability. A decrease in activity of shortened variants has been explained by a decrease in helicity.[65,66] On the other hand, stabilizing the helical fold using a lactam bridge restored some activity to a short segment of the antifreeze protein.[59] The stabilization of α-helices with lactam bridges, hydrogen bond surrogate or cross-linkers however always requires a chemical modification of the peptide after synthesis.[59,89,90]

The Trp-cage has a stable fold under physiological pH but no intrinsic function. Its fold is driven by the hydrophobic encapsulation of a tryptophan side chain by the C-terminus and π-π interactions between the tryptophan and tyrosine side chains, both located in the N-terminal

α-helix of the Trp-cage.[67] An elongation of the N-terminal helix through the addition of amino acids showed that the helicity is propagated and that the Trp-cage can act as a nucleation point.[75,78,81] A fusion of both proteins therefore results in a folded protein with antifreeze activity as has been shown by M. Lipfert.[78]

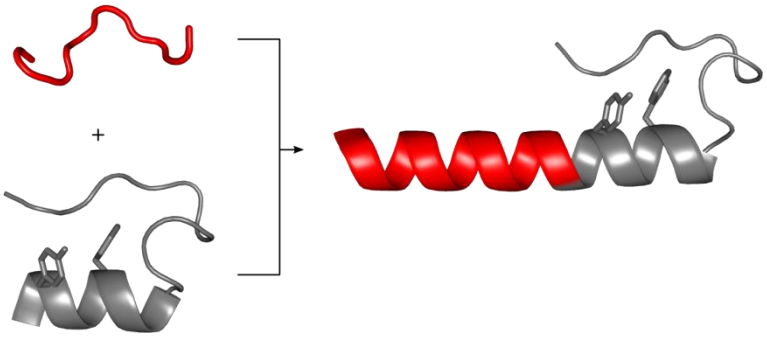

Fig. 17: Fusion approach as planned in this work. Structural and biological active elements of each single fragment can be transferred to the final protein.

The Trp-cage has been studied extensively towards the importance of almost every amino acid for fold stability leading to the characterization of >60 variants.[69] Based on the Trp-cage variant Tc10b[69], which is 99.5% folded at 280 K and pH 7, a further modification of the sequence has been conducted in our group by M. Lipfert, so as to chemically modify the Trp-cage after synthesis with an organic molecule.[78] The variant used by him, Tc10bKKA, but without acetylated N-terminus has been chosen as Trp-cage building block for this work (see Tab. 3).

Tab. 3: Primary sequence of Trp-cage variant Tc10b and Tc10bKKA. The differences between both sequences are marked in bold.

	1 6 11 16
Tc10b	DAYAQ WLKDG GPSSG RPPPS
Tc10bKKA	**Ac**-D**K**YAQ WL**A**DG GPSSG RPPP**K**

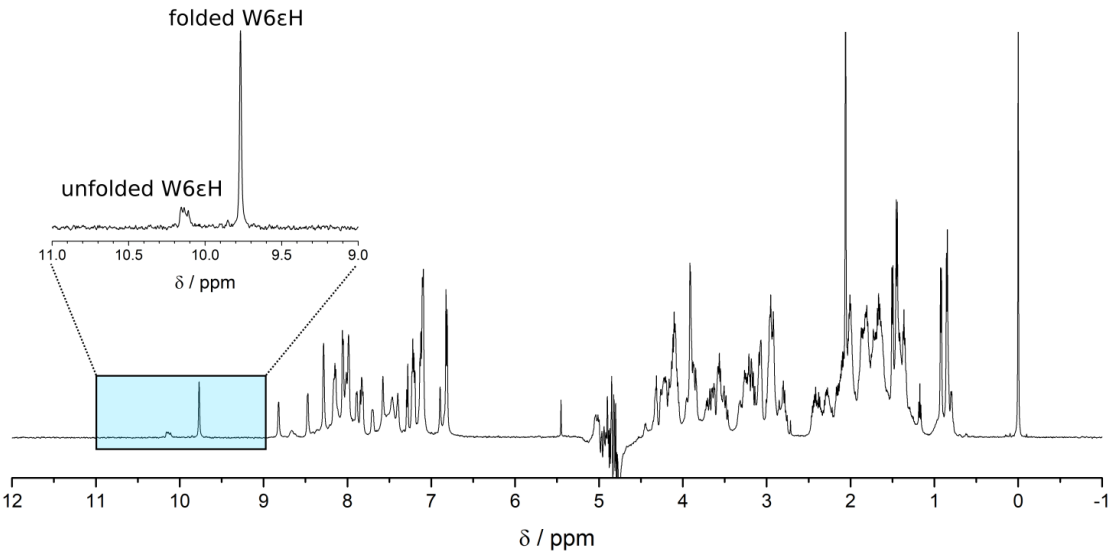

Fig. 18: ^{1}H NMR spectrum of Tc10bKKA in H_2O/D_2O, pH 3, at 300 K with enlargement of the indole proton region around 10 ppm.

The ^{1}H NMR spectrum of Tc10bKKA (Fig. 18) at pH 3 shows characteristics for a folded Trp-cage motif: chemical shift dispersion of aliphatic and aromatic resonances and the separated indole proton of the tryptophan side chain (W6Hε). While the good shift dispersion may not be visible for the untrained eye, the 2D NMR data enable an assignment of amino acids, with differences in the resonance of the same amino acid depending on structural differences. The indole proton (see the enlarged region of Fig. 18) at the chemical shift (δ) of δ = 9.77 ppm is significantly shifted from its random coil value of 10.22 ppm[91]. The upfield shift of W6Hε is caused by its hydrophobic encapsulation by, amongst other residues, prolines and is a strong indicator of Trp-cage fold. Neighboring to the sharp resonance of the indole proton, multiple small and broad resonances above 10 ppm are present. Similar additional signals have also been observed before by other groups.[70,74,76,78,92] Impurities can be discarded as a possible explanation for the additional signals because the purity of the sample has been proven with HPLC-ESI-MS (high performance liquid chromatography-electron spray ionization-mass spectrometry). Therefore, the signals must arise from the protein and represent different conformations. However, conformation exchange in proteins is usually fast. To give a separate signal during NMR acquisition, the conformational exchange transition has to be slow on NMR time scale. The only conformational exchange in proteins which is slow on the NMR time scale is the *trans/cis* isomerisation of the X-Pro bond (see Fig. 19).

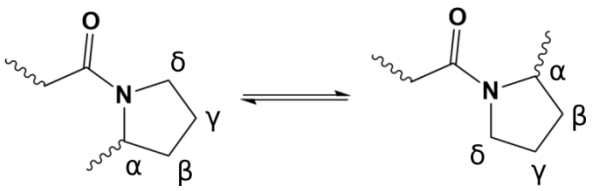

Fig. 19: Schematic representation of the X-Pro bond in *trans* (right) and *cis* (left).

The Trp-cage sequence contains four prolines, yielding a possibility of $2^4 = 16$ conformations. A probe to study the exchange between the all-*trans* folded form and the *cis* conformations of the Trp-cage spectroscopically with both transferred nuclear Overhauser effect (tr-NOE) and a standard ^{1}H, ^{1}H NOESY clearly showed that both forms interconvert.[78] Furthermore, the 2D coupling pattern of both W6Hε resonances are each characteristic for the indole proton of a tryptophan side chain. The additional signal clearly arises from a second form of the Trp-cage with one or more prolines in the *cis* conformation. The corresponding W6Hε ^{1}H resonances are influenced by the fold of the Trp-cage. If the Trp-cage is well folded then the indole side chain of the tryptophan is encaged by several prolines. Due to ring-current effects in the hydrophobic core of the Trp-cage, the NMR signal is shifted upfield. The additional signal however does not exhibit an upfield shift as compared to the *trans* conformation, so everything points to an either partially or completely unfolded Trp-cage sequence where the indole proton is not influenced by the hydrophobic core.

The integration of both signals in Fig. 18 gives a ratio of folded to unfolded of 75:25 which is in good agreement with the literature value of 69:31, as is the resonance of the tryptophan side chains indole proton at $\delta = 9.77$ ppm which is nearly identical to the literature value of $\delta = 9.75$ ppm.[78] The synthesis of the first building block thus was successful.

The second building block is a fragment of the WflAFP. Of the threefold repeat motif the WflAFP is made up of, each 11 amino acid long repetitive sequence qualifies as single building blocks (see **Tab. 4**). However, the first repeat motif was dismissed as it overlaps with the N-terminal capping sequence. The synthesis of both other protected fragments was pursued.

Tab. 4: Primary sequence of WflAFP and the derived possible fragments.

	1'	10'	20'	30'
WflAFP	DT	ASDAAAAAALT	AANAKAAAELT	AANAAAAAAAT AR-NH_2
Capping sequence	DT	ASD		
		Fragment 3	Fragment 1	Fragment 2
Name			1repeat	2repeat

The obtained protected fragment 1repeat-pg (pg stand for protection groups) was not soluble in either water or acetonitrile. Its low solubility in tetrahydrofuran however made purification with a gradient of tetrahydrofuran/acetonitrile using high performance liquid chromatography (HPLC) possible (data not shown). Tetrahydrofuran however is toxic, has a low boiling point, tends to form peroxides and is not compatible with all HPLC setups. Consequently, an alternative was sought. Although 1repeat-pg showed an increased solubility in dimethyl sulfoxide, purification with dimethyl sulfoxide as mobile phase during HPLC is not advisable as it damages the stationary phase. However, it is possible to dissolve the protein in dimethyl sulfoxide and inject the sample onto the column while using a water/acetonitrile gradient. To avoid the precipitation of the protected peptide fragment, the acetonitrile concentration has to be ≥50%. Pure 1repeat-pg was obtained with a low yield of 14%. However, the crude product was present in a high enough purity to perform the condensation of two protected fragments without the HPLC purification step.[84]

2repeat-pg has a low solubility in dimethyl sulfoxide, probably because of its high alanine content and a correlated propensity to form aggregates. While purification was possible, the yield was very low (4%) and the low solubility hampered the fusion of the protein fragment to the Trp-cage fragment as the reaction takes place in dimethyl sulfoxide.

The fusion of both protected peptide fragments is dependent on the solubility of both fragments in dimethyl sulfoxide. Due to the low solubility of 2repeat-pg a fusion with the Tc10bKKA fragment was not possible. The synthesis of a new IBTC consisting of 1repeat-pg and Tc10bKKA fragments however was performed successfully and is described in detail in the experimental section. After the N-terminal addition of 1repeat-pg to Tc10bKKA over a period of two days, first an threonine and then an aspartate residue were coupled at the N-terminus to complete an antifreeze motif of two threonines and the N-terminal capping unit, yielding (jg)IBTC-4 (see Tab. 5).[84] The analysis of its fold and antifreeze activity was pursued. The results will be discussed in chapter 2.3 and compared with the other IBTC.

Tab. 5: Primary sequence of (jg)IBTC-4, WflAFP, and Tc10bKKA.

WflAFP	DT ASDAAAAAALT AANAKAAAELT AANAAAAAAAT AR-NH_2
Tc10bKKA	Ac-DKYAQWLADGGPSSGRPPPK
(jg)IBTC-4	DT AANAKAAAELT DKYAQWLADGGPSSGRPPPK

2.2 The Chimera Approach

The chimera approach differs from the connection of two proteins with a spacer unit in between them. The protein resulting from the connection contains both functions of the single proteins in one large protein with both units acting independently. The chimera approach in contrast yields a protein which combines the functions of both proteins in a shorter protein and both functions are influenced by each other. For that the primary sequence of both proteins as well as their fold are evaluated and combined in an overlapping region. Creation of the chimera requires a careful assessment of amino acids and determination of which residues can be replaced by amino acids from the other sequence and which have to be retained (see Fig. 20).

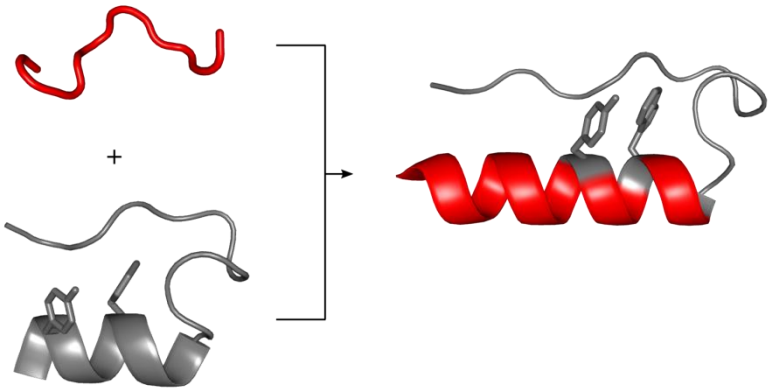

Fig. 20: The chimera approach based on the Trp-cage and a short protein segment. Both the tyrosine and tryptophan side chains are shown in stick representation and have to be retained for fold stability. All other amino acids in the α-helical region of the Trp-cage can be exchanged.

During his PhD thesis, M. Lipfert created chimera proteins between an antifreeze protein type I segment and a stabilizing module, the Trp-cage.[78] The synergistic combination of both proteins, where the properties of both proteins are combined – the stable fold of the Trp-cage and the ice activity of the antifreeze protein - gave four different proteins, AFP-Tc-4 to -7. They differ in the location of the ice active side of the antifreeze protein in relative orientation to the Trp-cage tertiary fold (see Fig. 21).[78]

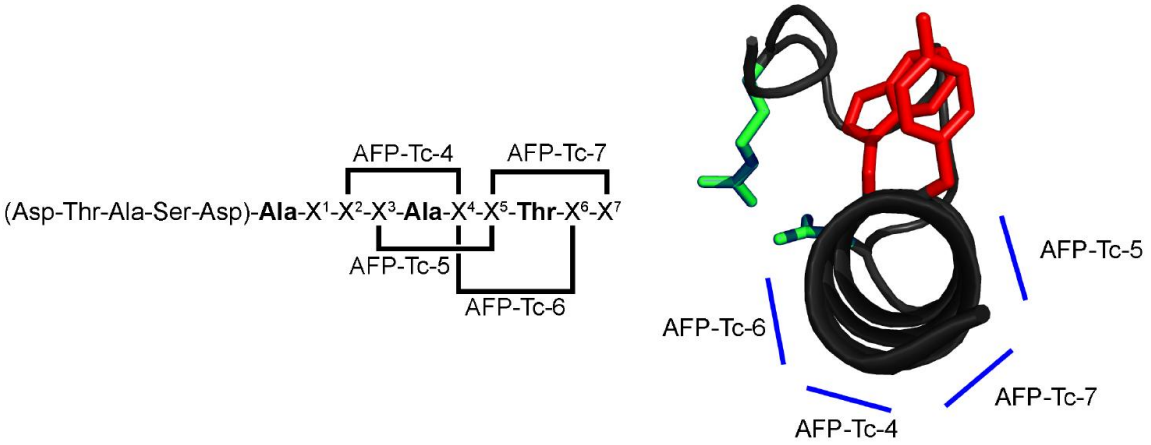

Fig. 21: Sequence pattern of the ice binding motif of AFP-Tc-4 to AFP-Tc-7 (left) and view along the helix (N to C) with marked orientations of the ice binding site (right). While the protein is represented in cartoon style, the tyrosine and tryptophan side chains are shown as red sticks and the aspartate and arginine side chains of the salt bridge as green sticks. (Reprinted with permission from M. Lipfert).[78]

While all four chimera showed ice shaping abilities, the activity seemed to be more dependent on the fold than the location of the ice binding site. Antifreeze activity was not observed.[78] Furthermore, the formation of hexagonal discs also gave rise to the question if the ice binding plane the chimera interacted with was changed to the prism plane as compared to the pyramidal plane to which the wild-type WflAFP binds.

Based on the chimera AFP-Tc-5, other variants were designed, synthesized and characterized in this study. (jg)IBTC-1 is similar to AFP-Tc-5 and only has two additional amino acids at the C-terminus. (jg)IBTC-2 contains two repeat motifs of the antifreeze protein motif and (jg)IBTC-3 three equating it with the wild-type WflAFP. The systematic increase in protein length enables a study of both the influence of antifreeze protein length on ice activity and of the C-terminal modification of the antifreeze protein on its activity.

Additionally, of all three IBTC the C-terminal GFP fusion proteins were designed for a later use in FIPA analysis. All six IBTC (see Tab. 6) were expressed in *E. coli* in the group of Prof. Axel Scheidig, Christiana-Albertina-University, Kiel. (Information can be found in the Experimental Section and the Appendix.)

Tab. 6: Primary sequences of all chimera constructs. The extension –GFP refers to a C-terminal fusion with green fluorescent protein and is visualized by the symbol •.

(jg)IBTC-1	DTASDAAAYAAWTADGGPSSGRPPPSGS
(jg)IBTC-2	DTASDAAAAAALTAANAAAYAAWTADGGPSSGRPPPSGS
(jg)IBTC-3	DTASDAAAAAALTAANAKAAAELTAANAAAYAAWTADGGPSSGRPPPSGS
(jg)IBTC-1-•	DTASDAAAYAAWTADGGPSSGRPPPSGS•
(jg)IBTC-2-•	DTASDAAAAAALTAANAAAYAAWTADGGPSSGRPPPSGS•
(jg)IBTC-3-•	DTASDAAAAAALTAANAKAAAELTAANAAAYAAWTADGGPSSGRPPPSGS•

WflAFP is stabilized by a capping unit at the N-terminus comprised of the amino acid sequence DTASD, however the expression of proteins always begins with a start codon coding for methionine. To nevertheless obtain the desired protein sequence, an N-terminal tag was employed – the small ubiquitin modifier (SUMO).[79] It can be cleaved side specific behind two glycines right before the desired protein sequence using the SUMO protease.[79,93] As both the SUMO tag and the SUMO protease contain a His-tag, a purification with affinity chromatography was possible.

Furthermore, the bacterial expression of proteins enables the design of large proteins which, due to their size, cannot be synthesized by SPPS. In this study, this applies to the GFP labeled IBTC.

2.3 Protein Fold and Ice Activity

The analysis of protein fold and biological activity especially of newly designed and obtained proteins is a standard procedure. The aim of this work was to design proteins which combine the properties of two single proteins in one.

The activity of antifreeze proteins is correlated to a flat ice binding side every antifreeze protein characterized to date possesses. For the α-helical winter flounder antifreeze protein (HPLC 6) it is one side of the α-helix containing alanine and threonine, with the threonines spaced 11 amino acids apart in a repetitive motif.[56] A Trp-cage C-terminal extension is supposed to stabilize the helical fold of antifreeze protein segments. A combination of both proteins (or segments of the antifreeze protein) thus should result in a stable folded protein with ice activity.

To analyze the protein fold, both NMR and CD spectroscopy were performed (see chapter 2.3.1ff and 2.3.4, respectively). The obtained NMR data enabled not only the calculation of the chemical shift deviation (CSD) and fraction folded values but in consequence the evaluation of the protein fold concerning α-helicy and Trp-cage stability. A stable Trp-cage fold is expected to correlate with a high percentage of α-helical fold in the N-terminal region of the IBTC. While the NMR data give local information about each residue, the CD data give a global overview over the secondary structure of the protein fold.

A stable α-helical fold is expected to result in ice activity which in turn is measured using thermal hysteresis measurements.

Four different IBTC as well as three C-terminal GFP fusion IBTC (see Tab. **7**) where characterized using the above mentioned methods.

Tab. 7: Primary sequences of all constructs and their predecessors. The extension –GFP refers to a C-terminal fusion with green fluorescent protein and is visualized in the primary sequence by the symbol •.

WflAFP	DTASDAAAAAALTAANAKAAAELTAANAAAAAAAATAR-NH_2
Tc10b	DAYAQWLKDGGPSSGRPPPA
Tc10bKKA	Ac-DKYAQWLADGGPSSGRPPPK
AFP-Tc-5	DTASDAAAYAAWTADGGPSSGRPPPS
(jg)IBTC-1	DTASDAAAYAAWTADGGPSSGRPPPSGS
(jg)IBTC-2	DTASDAAAAAALTAANAAAYAAWTADGGPSSGRPPPSGS
(jg)IBTC-3	DTASDAAAAAALTAANAKAAAELTAANAAAYAAWTADGGPSSGRPPPSGS
(jg)IBTC-4	DTAANAKAAAELTDKYAQWLADGGPSSGRPPPK
(jg)IBTC-1-GFP	DTASDAAAYAAWTADGGPSSGRPPPSGS•
(jg)IBTC-2-GFP	DTASDAAAAAALTAANAAAYAAWTADGGPSSGRPPPSGS•
(jg)IBTC-3-GFP	DTASDAAAAAALTAANAKAAAELTAANAAAYAAWTADGGPSSGRPPPSGS•

2.3.1 ^{1}H-NMR

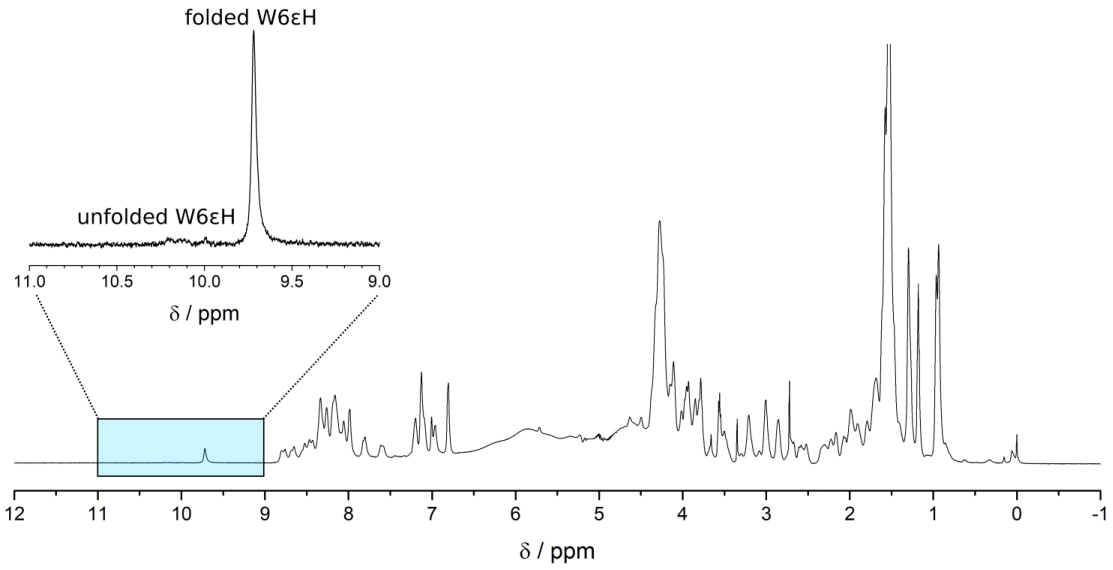

Fig. 22: ^{1}H NMR spectrum of (jg)IBTC-3 in 0.1 M NH_4HCO_3 buffer, pH 7.9, at 274 K with enlargement of the indole proton region around 10 ppm.

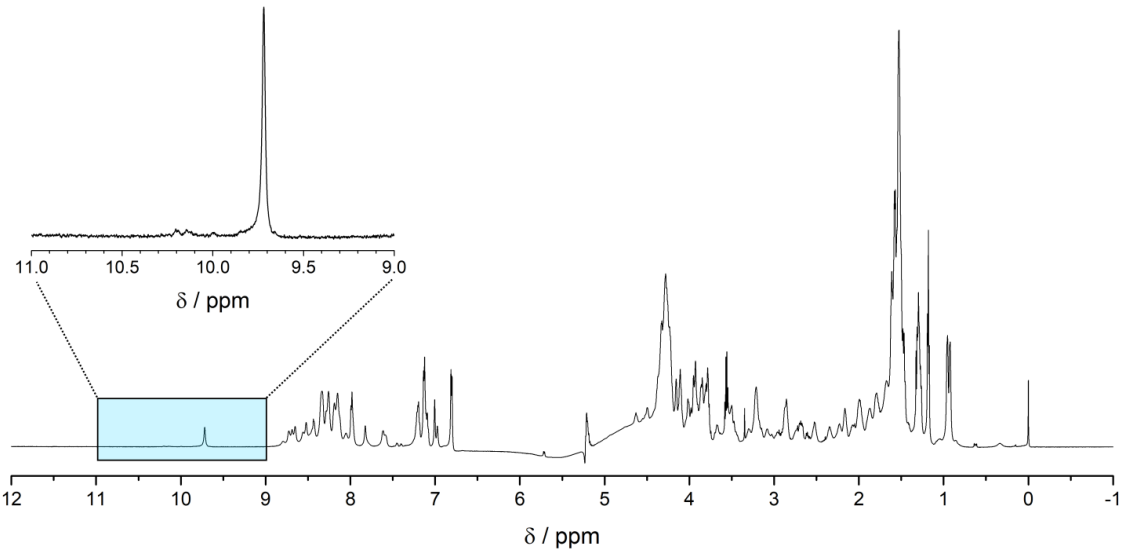

Fig. 23: ^{1}H NMR spectrum of (jg)IBTC-2 in 0.1 M NH_4HCO_3 buffer, pH 7.9, at 274 K with enlargement of the indole proton region around 10 ppm.

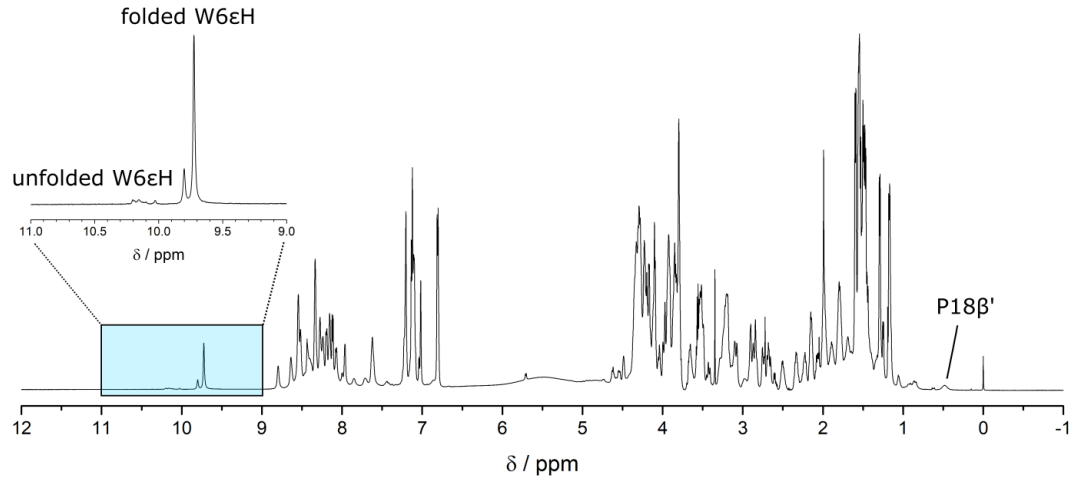

Fig. 24: ^{1}H NMR spectrum of (jg)IBTC-1 in 0.1 M NH_4HCO_3 buffer, pH 7.9, at 274 K with enlargement of the indole proton region around 10 ppm.

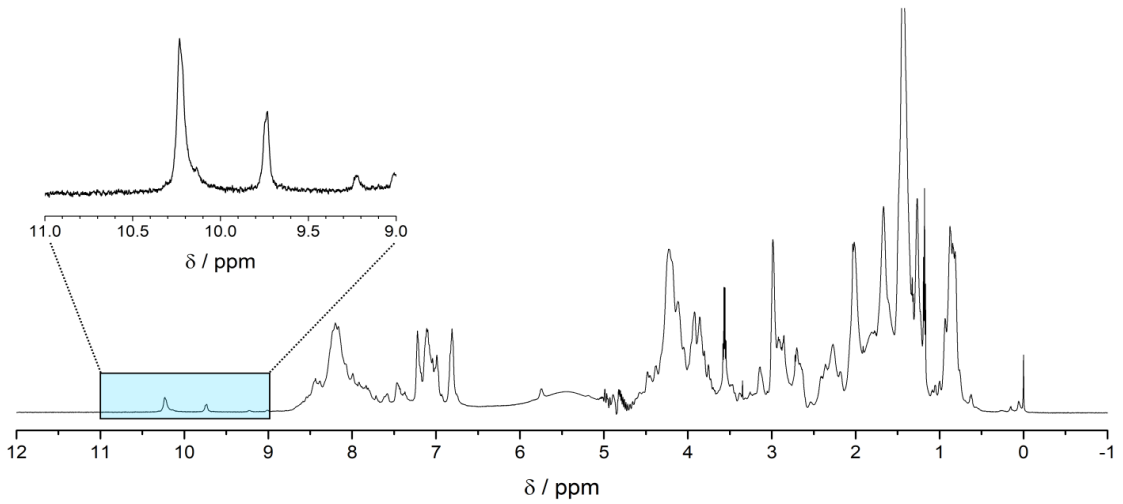

Fig. 25: ^{1}H NMR spectrum of (jg)IBTC-4 in 0.1 M NH_4HCO_3 buffer, pH 7.9, at 274 K with enlargement of the indole proton region around 10 ppm.

The ^{1}H NMR spectra of all IBTC in buffer at 274 K (Fig. 22-Fig. 25) all show characteristics of the Trp-cage fold. For three out of four IBTC the signal of β' of P18 is visible at around δ = 0.45 ppm. Additionally, qualitatively very similar sharp spectral resonances of the tryptophan side chain (W6Hε) at around δ = 9.7 ppm are visible in all four IBTC. The shift of this resonance supports that the Trp-cage segment is folded. However, further resonances can be observed above 10 ppm that we attribute to additional populations. The amount is <5% for (jg)IBTC-3 and (jg)IBTC-2 as determined by integration of the signals. The third construct, (jg)IBTC-1, has a signal ratio of 17:83 and, surprisingly, for (jg)IBTC-1 a third resonance is observed for the indole proton (Fig. 24). The similarity of its shift at δ = 9.80 ppm to that of the folded conformation indicates that this is also a folded conformation. Again, the separate resonance requires an underlying slow exchange process and therefore is *cis*/*trans* X-Pro isomerisation. A comparable observation has been made before for AFP-Tc-5. It has been explained by an unfavorable charge-charge interaction between the aspartate side chain of residue 5' and the C-terminal carboxyl group at neutral pH, leading to a *cis* configuration of either the X-P18 or X-P19 peptide bond and as a consequence to a different shielding of the tryptophan indole proton resulting in a different chemical shift.[78]

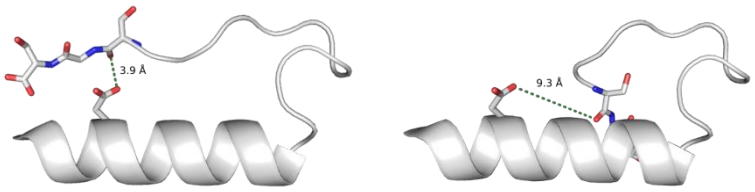

Fig. 26: (jg)IBTC-1 shown in cartoon representation with the side chains of D5, S2, and G21 shown as sticks. The nitrogens are colored blue, the oxygen atoms red. The left representation visualizes the short distance between the side chain oxygen of D5 and the oxygen atom of the S20-G21 amide bond in *trans* conformation of the X-P19 bond. A *cis* isomerization of the X-P19 bond leads to an increase in distance from 3.9 Å (*trans*, left) to 9.3 Å (*cis*, right).

Analysis of (jg)IBTC-1 shows a potentially unfavorable interaction between the carboxyl group of D5 and the oxygen of the amide bond between residues 20 and 21 (Fig. 26, left). Upon isomerization of the X-P18/19 bond the distance between both charges would increase as is shown in Fig. 26. The potential energy of the charge-charge interaction is inversely proportional to the distance, an isomerization thus would lead to a reduction of the repulsive effect between both negative charges and an increase in the relative stabilization of the *cis* isoform in comparison to the *trans* isoform.

This hypothesis is supported by the ^{1}H NMR spectrum at pH 3. As the carboxyl group of D5 is mostly protonated (pKa ~3.8[94]), there should be no repulsive interactions with the oxygen of the S20-G21 amide bond. Indeed, under these conditions there are no signals of minor forms of (jg)IBTC-1 visible (Fig. 27).

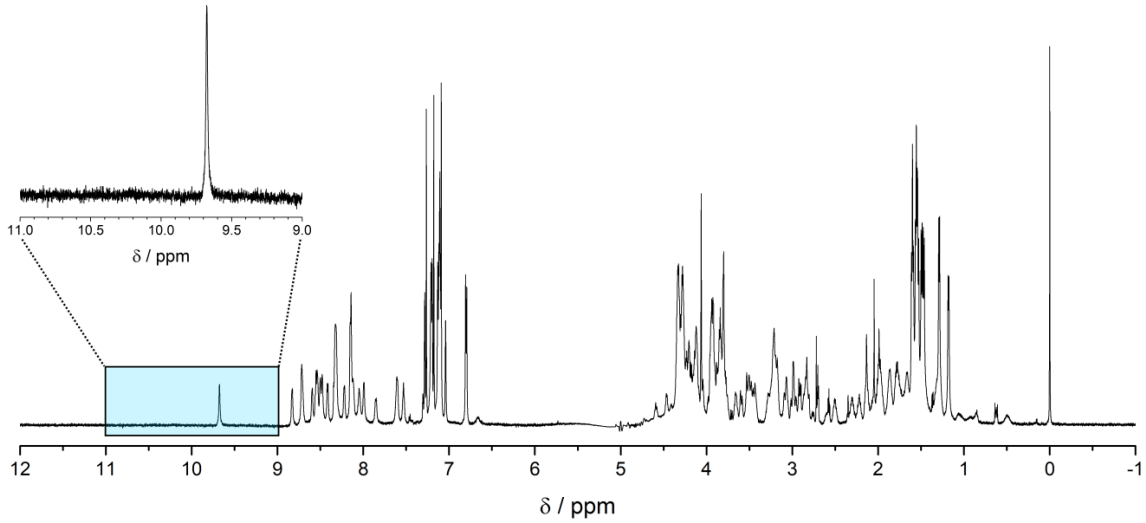

Fig. 27: ^{1}H NMR spectrum of (jg)IBTC-1 in H_2O/D_2O, pH 3, at 274 K with enlargement of the indole proton region around 10 ppm.

Returning to the analysis of the ratio of folded:unfolded conformation for (jg)IBTC-4, the signal for the unfolded fraction is very sharp and the ratio of 71:29 favors the unfolded form. The low ratio of folded fraction is surprising as the design is based on the most stable form Tc10b(KKA). The elongated protein had been expected to be as stably folded as the Trp-cage variant. As Tc10b as single protein is well folded, the destabilizing effect most likely originates in the helical extension or its interaction with the Trp-cage sequence. An unfavorable interaction of the C-terminus with side chains of amino acids in the helical sequence seems unlikely as none are apparent through analysis of the modeled secondary structure of (jg)IBTC-4. Additionally, there is no effect of different pH observable as the WH6ε signals of folded and unfolded form at pH 3 and 7.9 are nearly identical, as is the fold ratio. One notable difference is that the capping sequence of (jg)IBTC-4 varies from the other peptides (DTAAN/DTASD). However, the fact that aspartate still caps the N-terminus and the helical dipole moment should be most important.[95] Thus, the reason for the relative low fold stability remains unclear. A possible explanation for the decrease in fold stability needs to be studied further.

A comparison of the ^{1}H NMR spectra (jg)IBTC-1 to -4 (Fig. 28) shows an increase in fold stability from (jg)IBTC-1 to -2 as the second folded form vanishes. (jg)IBTC-2 and -3 seem to both possess the same stability of the Trp-cage fold at 0.1 M NH_4HCO_3 buffer, pH 7.9, and 274 K. (jg)IBTC-4 is

the least stable folded protein in this study as deduced by analysis of the WH6ε signals and spectral dispersity.

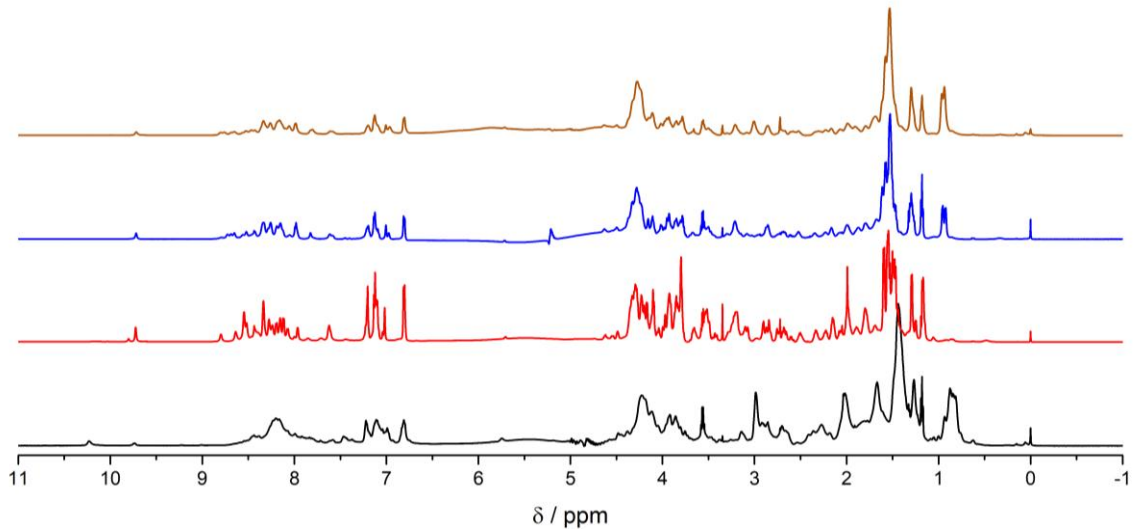

Fig. 28: ^{1}H NMR spectra of (jg)IBTC-4 (black), (jg)IBTC-1 (red), (jg)IBTC-2 (blue), and (jg)IBTC-3 (brown) in order of increasing fold stability at 274 K and 0.1 M NH_4HCO_3 buffer, pH 7.9.

2.3.1.1 (jg)IBTC-1-GFP, (jg)IBTC-2-GFP, (jg)IBTC-3-GFP

The three chimeras (jg)IBTC-1-GFP, (jg)IBTC-2-GFP, and (jg)IBTC-3-GFP were designed as fluorescently labeled variants of (jg)IBTC-1 to -3. The attachment of a green fluorescent protein (GFP) tag to the C-terminus of the protein was planned with two spacer residues between both proteins (Fig. 29). The as fusion protein designed IBTC-GFP could be obtained via bacterial expression in *E. coli*. ^{1}H NMR spectra of all three IBTC, (jg)IBTC-1-GFP, (jg)IBTC-2-GFP, and (jg)IBTC-3-GFP, were obtained. As GFP consists of 238 amino acids, the majority of NMR resonances stem from the GFP so that it may be difficult to observe Trp-cage resonances in the 1D NMR spectrum.

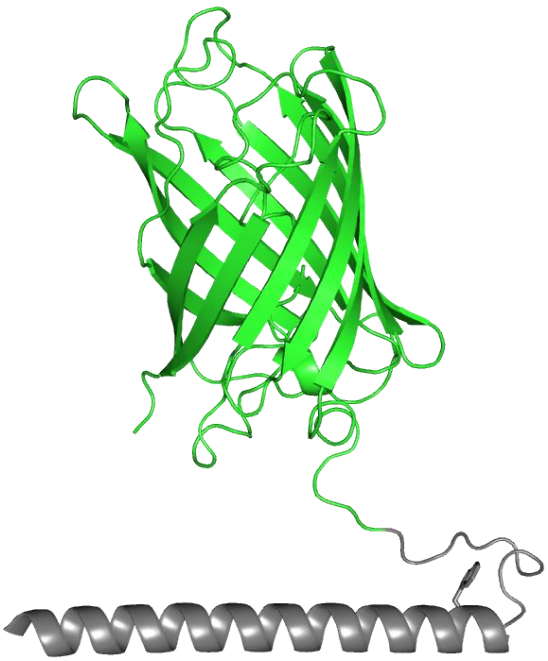

Fig. 29: The cartoon style representation of a structural model of (jg)IBTC-3-GFP. The chimera is colored grey, the GFP in green. The tryptophan side chain of the chimera is shown as stick representation. (PDB GFP: 2Y0G; Trp-cag: PDB: 1L2Y)[67,96]

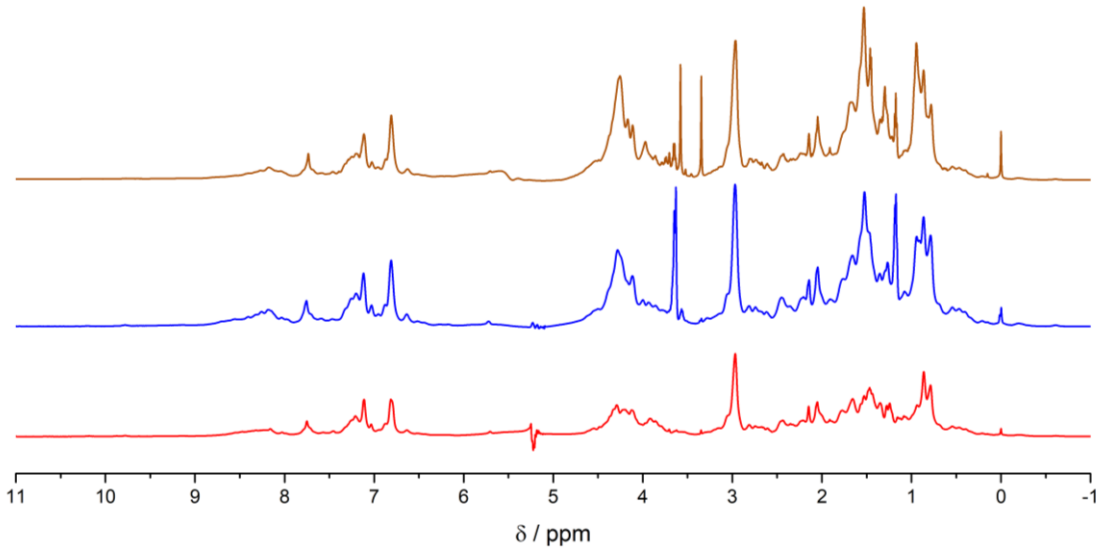

Fig. 30: ^{1}H NMR spectra of (jg)IBTC-1-GFP (red), (jg)IBTC-2-GFP (blue), and (jg)IBTC-3-GFP (brown) at 274 K and 0.1 M NH_4HCO_3 buffer, pH 7.9.

A comparison of the spectra (Fig. 30) shows the similarities and differences of all IBTC-GFP proteins. The intensity of all resonances in the aromatic regions of all spectra are similar, probably due to the presence of eleven tyrosines and twelve phenylalanines in the GFP

sequence. The prominent signals around δ = 3 ppm can be explained by six arginine and 20 lysine residues in the GFP sequence. Different is an increase of the signals at ~1.5 ppm, which can be attributed to a higher ratio of alanines origination form the increasing number of antifreeze repeat motifs in the following order (jg)IBTC-3-GFP > (jg)IBTC-2-GFP > (jg)IBTC-1-GFP.

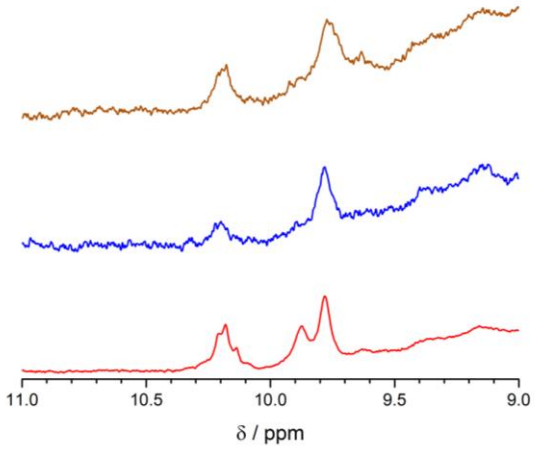

Fig. 31: Expansion of the indole proton region of the ^{1}H NMR spectra of (jg)IBTC-1-GFP (red), (jg)IBTC-2-GFP (blue), and (jg)IBTC-3-GFP (brown) at 274 K and 0.1 M NH_4HCO_3 buffer, pH 7.9.

Expanding the region between 9 – 11 ppm, the patterns appear similar to the corresponding chimera without GFP. A signal at δ = 9.78 ppm can be ascribed to a W6Hε resonance, indicating a Trp-cage fold. (jg)IBTC-1-GFP shows a second folded form just as (jg)IBTC-1. There is also a broad signal above 10 ppm in all spectra, which possibly originates from an unfolded Trp-cage.[97] This hypothesis however needs further support by 2D NMR data as Khan *et al.* recorded NMR data of the GFP at pH 7.2 and 310 K and assigned signals above 10 ppm to NH resonances of A37, W57Hε, G127 and R168. Consequently, an unambiguous assignment of the signals in the expansion of the indole region of our IBTC is not possible due to a possible signal overlap (Fig. 31).

2.3.2 Folded Fraction

Deducing secondary structure elements of proteins using NMR is possible in multiple ways. The simplest method was developed by Wishart *et al.* by determining reference random coil values for H, C and N of every amino acid.[98] Depending on secondary structure of the peptide or protein

the chemical shift is influenced by the fold. The difference between the observed (δ_{obs}) and reference (δ_{ref}) chemical shift is called chemical shift deviation (CSD) or secondary chemical shift

$$CSD = \delta_{obs} - \delta_{ref}$$

According to Wishart *et al.*, a Hα CSD <0.1 ppm for a cluster of at least four amino acids out of five (if not interrupted by a value >0.1 ppm) is an indication of an α-helical fold. A Hα CSD >0.1 ppm for a cluster of at least three amino acids of four (if not interrupted by a value <0.1 ppm) on the contrary indicates a β-strand.[99] As the proton shifts of Hα' of G11, Hβ' of P18 as well as Hδ and Hδ' of P19 in the Trp-cage show a strong influence by the ring current of the indole, Lin *et al.* calculated reference random coil values, which are 4.02, 2.29, 3.59 and 3.74 ppm, respectively.[75]

In the following figures, the secondary chemical shifts of the folded conformations are displayed to confirm and compare the secondary structures of all constructs with the exception of the GFP fused IBTC.

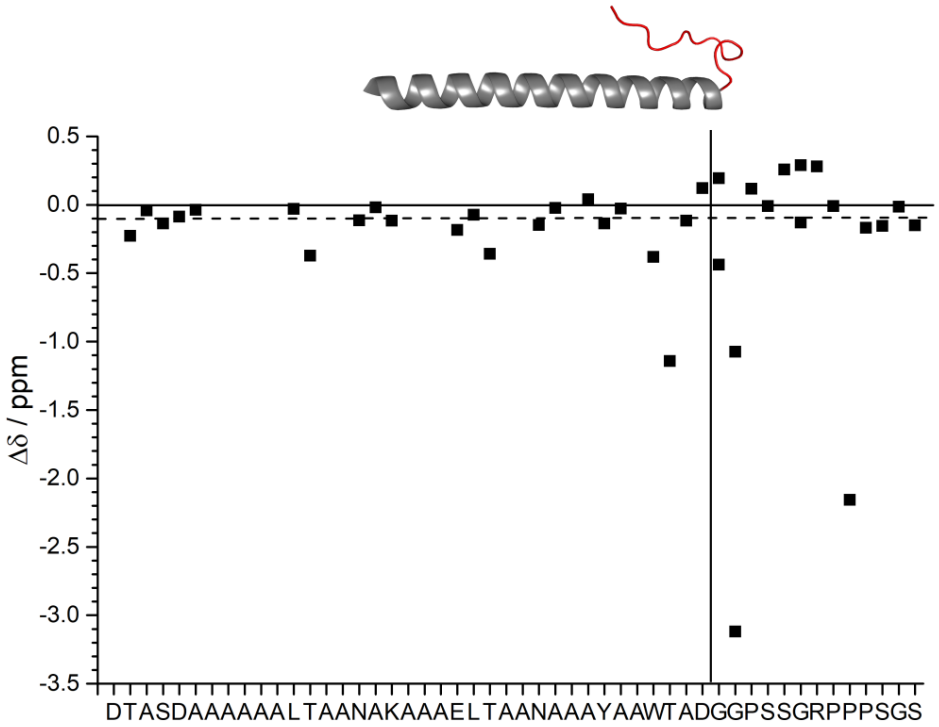

Fig. 32: Hα chemical shift deviation of (jg)IBTC-3 at 274 K and pH 3. The dashed line represents the helical cutoff value. The vertical solid line separates the different secondary structures: helix (left) and rigid loop (right).

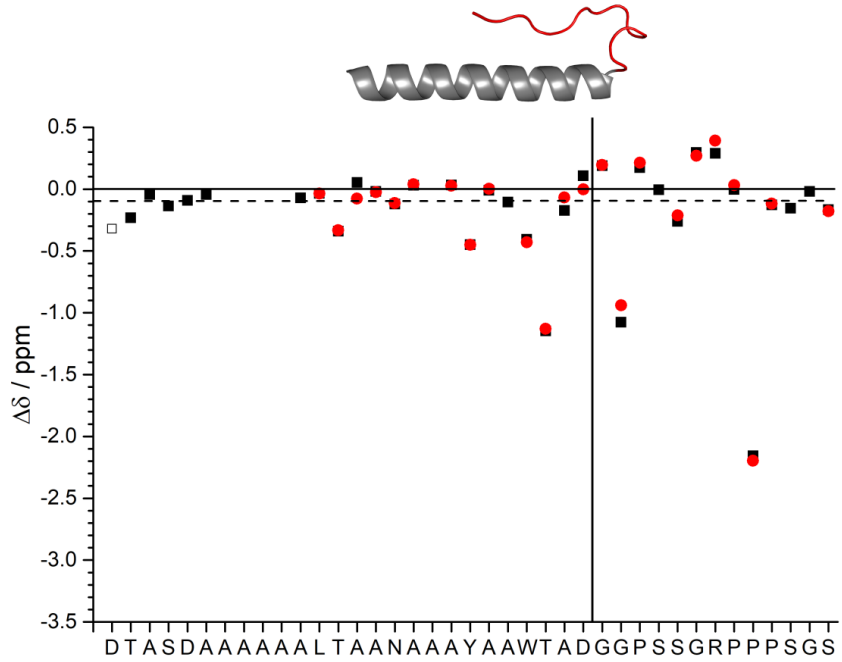

Fig. 33: Hα chemical shift deviation of (jg)IBTC-2 at 274 K and pH 3 (black squares) and pH 7.9 (red circles). The dashed line represents the helical cutoff value. The vertical solid line separates the different secondary structures: helix (left) and rigid loop (right).

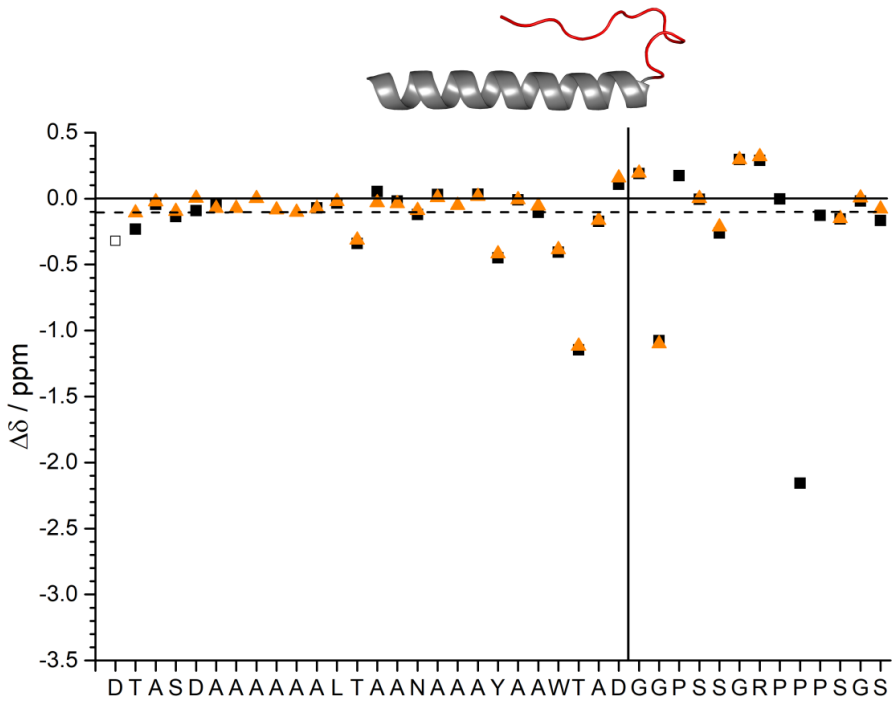

Fig. 34: Hα chemical shift deviation of (jg)IBTC-2 at pH 3 and 274 K (black squares) or 278 K (orange triangles). The dashed line represents the helical cutoff value. The vertical solid line separates the different secondary structures: helix (left) and rigid loop (right).

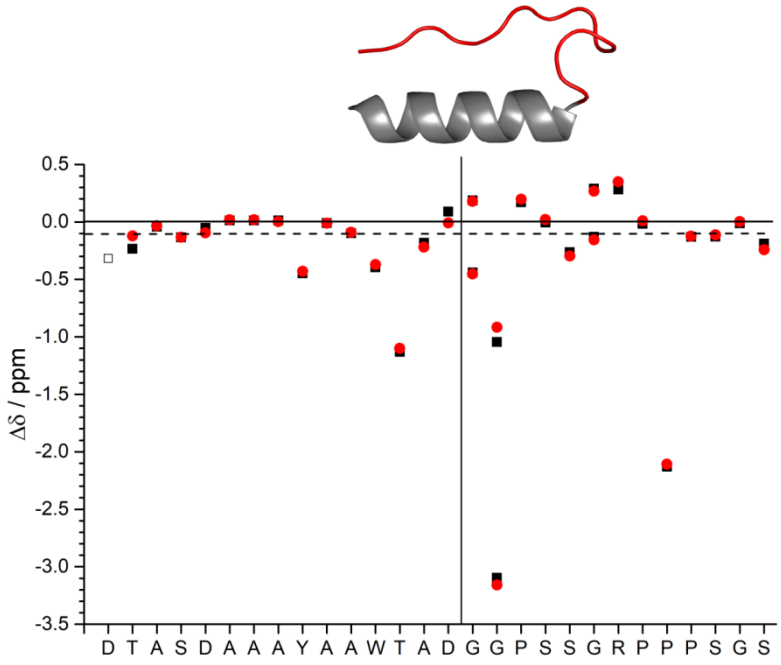

Fig. 35: Hα chemical shift deviation of (jg)IBTC-1 at 274 K and pH 3 (black squares) and pH 7.9 (red circles). The dashed line represents the helical cutoff value. The vertical solid line separates the different secondary structures: helix (left) and rigid loop (right).

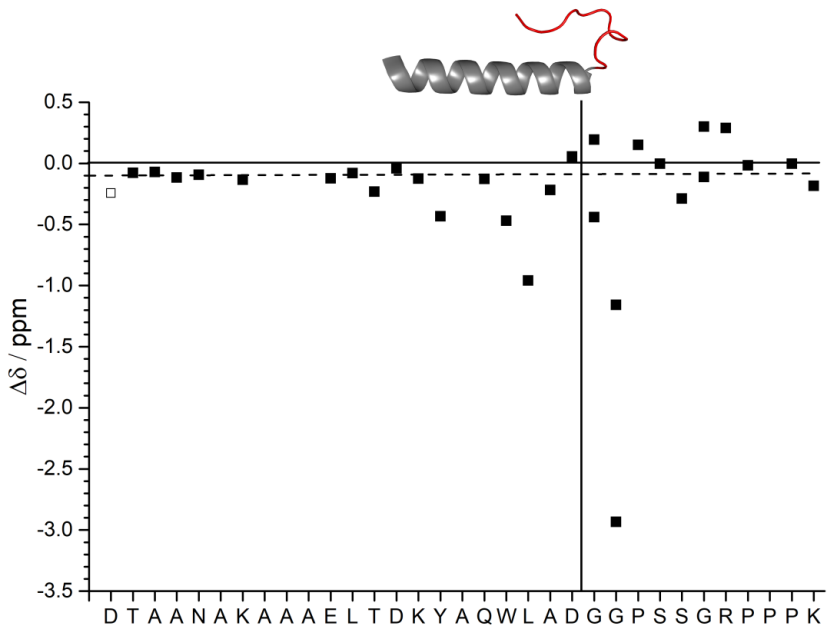

Fig. 36: Hα chemical shift deviation of the folded conformation of (jg)IBTC-4 at 274 K and pH 3. The dashed line represents the helical cutoff value. The vertical solid line separates the different secondary structures: helix (left) and rigid loop (right).

The IBTC structure and in consequence the Hα CSD plot of the IBTC (Fig. 32-Fig. **36**) can be divided into two parts - the helical region, comprised of the chimera helix and the helical extension, and the cage loop. The analysis of (jg)IBTC-3 and -2 was complicated by a relative high amount of alanine residues in the primary sequence which complicated the unambiguous assignment of all alanine Hα resonances of the helical extension due to signal overlap. By expressing a ^{15}N labeled (jg)IBTC-2, 3D NMR spectra were obtained which enabled the assignment of all amino acids except for the prolines (Fig. 34). A decrease in temperature also increased the unambiguous assignments of residues.

The CSD data for all IBTC in the region of the helical extension do not show any indication for secondary structure according to Wishart *et al.* as most of the values to not exceed the helical limit.[98] Neither do the CSD data for the chimera helix region for (jg)IBTC-1 to -3. However, the CSD of T7 in the chimera helix of (jg)IBTC-1 to -3 is strongly negative, possibly due to a neighboring effect to the ring-current effect of the preceding side chain W6. The negative chemical shift of residue 7 is characteristic for a folded Trp-cage. On the other hand, the chemical shift deviations of the chimera helix of (jg)IBTC-4 are negative and indicate a helical structure. However, it is important to remember that the Hα CSD is just for the folded part of (jg)IBTC-4, which represents approximately 29% according to ^{1}H NMR data.

The cage loop starting at residue 10 and separated in the figures by a vertical line exhibits no classical secondary structure, but many absolute CSD values are >0.1 ppm, with the deviations being positive and negative. The dispersion pattern of the CSD is typical for a Trp-cage loop, indicating structure and absence of conformational flexibility. The most characteristic CSD of the cage loop are the strong negative CSDs of G11α' and P18α. The upfield shift of both protons can be explained by their proximity, their position above the tryptophan side chain and their experience of the ring current effect. Consequently both protons are good indicators for an intact cage fold. According to the CSDs of G11α' (or G11α) and P18α all IBTC are folded in the cage loop region.

For (jg)IBTC-4 a comparison was also possible with the literature data for Tc10bKKA. The NMR data are in good agreement with the NMR data for the Trp-cage sequence.[78] A comparison of the helical region of (jg)IBTC-4 with the synthesized unprotected fragment 1repeat (AANAKAAAELT) shows an increased chemical shift deviation towards a helical fold (Fig. 37). The C-terminal Trp-cage fusion thus leads to an α-helical fold of the previously unfolded peptide.

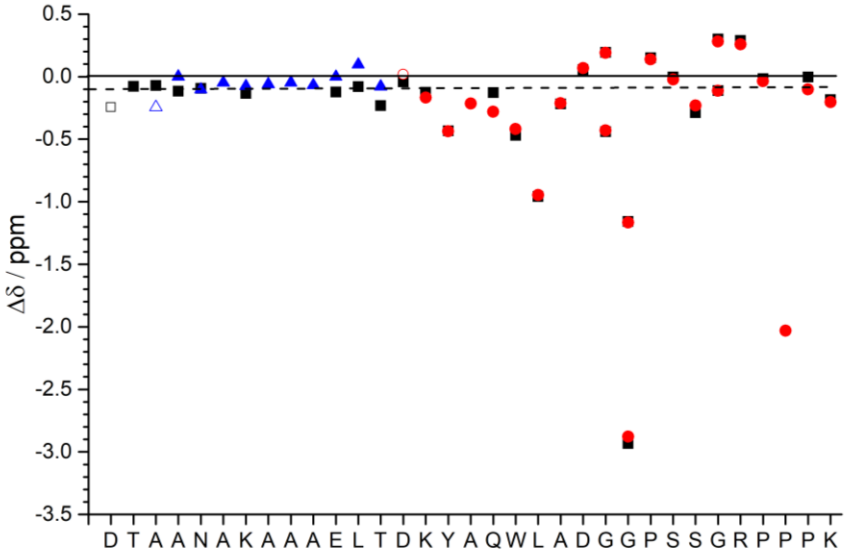

Fig. 37: Hα chemical shift deviation of the folded conformation of (jg)IBTC-4 (black squares) at 274 K and pH 3 and Tc10bKKA (red circles) and 1repeat (AANAKAAAELT) (blue triangles). The dashed line represents the helical cutoff value. [78]

To quantify the folding quality of the Trp-cage and the helical region, a conversion of the CSDs into folded-fraction estimates can be performed. The division into two parts enables not only the separate evaluation of the fold quality of helix and cage within one chimera but also a better comparison between the different IBTC. Based on calculations by Lin *et al.*, for the chimera helix the sum of Hα CSDs of residue 2 – 8 (if necessary without residue 2 or 5) was taken. For the cage loop the CSDs of X7α, G11α', P18β' as well as Hδ and Hδ' of P19 were added.[75] Both sums were compared with a reference, the Trp-cage variant Tc10b from Barua *et al.* which was shown to be 99.5% folded at 280 K and pH 3. The fraction-folded (χ_F) was calculated according to[69]

$$\chi_F = 0.995 \cdot \frac{CSD_{obs}}{CSD_{ref}}$$

Tab. 8: CSDs for selected protons representing the chimera helix or the cage loop of (jg)IBTC-3 at pH3 and 274 K and 298 K.

Cage Loop	T7α	G11α'	P18α	Pro18β'	P19δ	P19δ'		
	Δδ(ppm)						Σ(ppm)	χ_F (%)
274 K	-1.14	-3.01	-2.16	-1.85	-0.53	-0.90	-9.60	96
298 K	-0.86	-2.07	-1.55	-0.81	-0.35	-0.69	-6.34	63
Chimera Helix	Y3α	A4α	W6α	T7α	A8α			
	Δδ(ppm)						Σ(ppm)	χ_F (%)
274 K	-0.13	-0.03	-0.38	-1.14	-0.12		1.80	72
298 K	-0.14	-0.08	-0.32	-0.86	-0.12		1.52	61

Tab. 9: CSDs for selected protons representing the chimera helix or the cage loop of (jg)IBTC-2 at pH3 and pH 7.9 and 274 K, 278 K and 298 K.

Cage Loop	T7α	G11α'	P18α	Pro18β'	P19δ	P19δ'		
	Δδ(ppm)						Σ(ppm)	χ_F (%)
pH 7.9, 274 K	-1.13	-3.19	-2.20	-1.94	-0.50	-0.89	-9.85	98
pH 3, 274 K	-1.15	-3.03	-2.16	-1.85	-0.53	-0.90	-9.62	96
pH 3, 298 K	-0.87	-1.89	-1.48	-1.23	-0.36	-0.69	-6.53	65

Chimera Helix	A2α	Y3α	A4α	A5α	W6α	T7α	A8α		
	Δδ(ppm)							Σ(ppm)	χ_F (%)
pH 7.9, 274 K	0.03	-0.45	0.00		-0.43	-1.13	-0.07	-2.05	81
pH 3, 274 K	0.03	-0.45	-0.01	-0.11	-0.41	-1.15	-0.17	-2.26	76
pH 3, 278 K	0.02	-0.42	-0.01	-0.06	-0.39	-1.12	-0.17	-2.13	72
pH 3, 298 K		-0.25	-0.07		-0.30	-0.87	-0.09	-1.57	63

Tab. 10: CSDs for selected protons representing the chimera helix or the cage loop of (jg)IBTC-1 at pH3 and pH 7.9 and 274 K and 298 K.

Cage Loop	T7α	G11α'	P18α	Pro18β'	P19δ	P19δ'		
	Δδ(ppm)						Σ(ppm)	χ_F (%)
pH 7.9, 274 K	-1.10	-3.05	-2.11	-1.81	-0.48	-0.83	-9.38	94
pH 3, 274 K	-1.13	-2.99	-2.13	-1.79	-0.52	-0.88	-9.44	94
pH 3, 298 K	-0.79	-1.89	-1.35	-1.08	-0.30	-0.63	-6.03	60
Chimera Helix	A2α	Y3α	A4α	A5α	W6α	T7α	A8α	
	Δδ(ppm)						Σ(ppm)	χ_F (%)
pH 7.9, 274 K	0.00	-0.43	-0.01	-0.09	-0.37	-1.10	-0.22	-2.22	74
pH 3, 274 K	0.01	-0.45	-0.01	-0.10	-0.40	-1.13	-0.18	-2.25	76
pH 3, 298 K	-0.11	-0.32	-0.08	-0.05	-0.27	-0.79	-0.18	-1.80	61

Tab. 11: CSDs for selected protons representing the chimera helix or the cage loop of (jg)IBTC-4 at pH3 and 274 K and 298 K.

Cage Loop	L7α	G11α'	P18α	Pro18β'	P19δ	P19δ'		
	Δδ(ppm)						Σ(ppm)	χ_F (%)
pH 3, 274 K	-0.97	-2.82	-1.36	-1.38	0.22	-0.14	-6.45	64
pH 3, 298 K	-0.86	-2.18	-1.24		-0.41	0.75	-3.94	49
Chimera Helix	K2α	Y3α	Q5α	W6α	L7α	A8α		
	Δδ(ppm)						Σ(ppm)	χ_F (%)
pH 3, 274 K	-0.13	-0.43	-0.13	-0.47	-0.96	-0.22	-2.33	85
pH 3, 298 K	-0.10	-0.36	-0.23	-0.39	-0.85	-0.21	-2.14	77

For all IBTC a decrease of the sum of the CSDs (Σ(ppm)) for the cage loop and chimera helix upon an increase in temperature can be observed. This can be attributed to an increased amount of energy in the system and a correlated partial unfolding ('melting') of the protein fold.

For (jg)IBTC-4 the chimera helix always has a higher fraction-folded value than the cage loop. In some cases helix formation before cage formation could be observed as seems to be the case for this IBTC.[69,71]

Notably however, at 274 K there is a high difference in the fraction-folded values of the cage loop to the chimera helix for (jg)IBTC-3 to -1 of more than 15%. The cage loop has a higher fraction-folded value than the chimera helix, a result which is not consistent with neither previous

experimental data nor theoretical considerations. Both values in theory have to be similar or, if different, the fraction-folded value of the helix has to be higher than the fraction-folded value of the cage loop. This is because a folded N-terminal helix is a prerequisite for the cage formation so as to position the tryptophan and tyrosine side chains.[69,71] The helical folded-fraction therefore cannot be lower than the fraction-folded cage loop.

The unusual fraction-folded values of (jg)IBTC-1 to-3 thus prompted a further analysis of the data. A comparison of the Hα chemical shifts of the helical region of all IBTC to the wild-type WflAFP (HPLC 6) was performed. The WflAFP data recorded at pH 7 and 278 K showed a near perfect fit within an error of ±0.05 ppm to all IBTC.[78,100] Thus (jg)IBTC-1 to -3 must be 100% folded under these conditions. The discrepancy between fraction folded values and the comparison of the chemical shift with the WflAFP sequence has also been observed by M. Lipfert, who postulated that the fraction-folded calculation for the chimera helix underestimates its actual fold.[78]

Tab. 12: CSDs for selected protons representing the cage loop of at pH3 and 274 K. X represents either the amino acid T or L.

Cage Loop	X7α	G11α'	P18α	Pro18β'	P19δ	P19δ'		
	Δδ(ppm)						Σ(ppm)	χ_F (%)
(jg)IBTC-3	-1.14	-3.01	-2.16	-1.85	-0.53	-0.90	-9.60	96
(jg)IBTC-2	-1.15	-3.03	-2.16	-1.85	-0.53	-0.90	-9.62	96
(jg)IBTC-1	-1.13	-2.99	-2.13	-1.79	-0.52	-0.88	-9.44	94
(jg)IBTC-4	-0.97	-2.82	-1.36	-1.38	0.22	-0.14	-6.45	64

A direct comparison of the fraction folded values for the cage loop region gives nearly identical values for (jg)IBTC-1 to -3. (jg)IBTC-4 has a lower fraction folded value of 64% and thus is less stable folded than the first three proteins. The fraction folded values of 94%/96% indicate a stable folded cage loop. However, the chimera helix fraction folded values for (jg)IBTC-1 to -3 were lower than the cage loop values. As a folded chimera helix is a prerequisite for folding of the cage loop, the fraction folded values for the chimera helix cannot be a good representation of the helical region in ice binding Trp-cage chimeras. The NMR shifts of (jg)IBTC-1 to -3 are in good agreement with previously published data of the wild-type WflAFP.[100] As the wild-type antifreeze protein is 100% helical under the published conditions, so should the IBTCs. The Hα CSD consequently is not a suitable method to determine the helical content of these chimera and probably all alanine-rich proteins, so we took a look at the ^{13}C chemical shift deviation.[98]

2.3.3 ^{13}C Chemical Shift Deviation and the Helical Fold

The chemical shift of carbon is influenced by structural elements in the same way as are protons, and the CSD is consequently calculated according to

$$CSD(^{13}C\alpha) = \delta_{obs} - \delta_{ref}$$

However, the Cα CSD are in the opposite direction as compared to protons and exhibit a larger deviation (~10x). Thus, a value of >0.7 ppm is indicative of an α-helix and a CSD of <0.7 ppm a β-strand.[101]

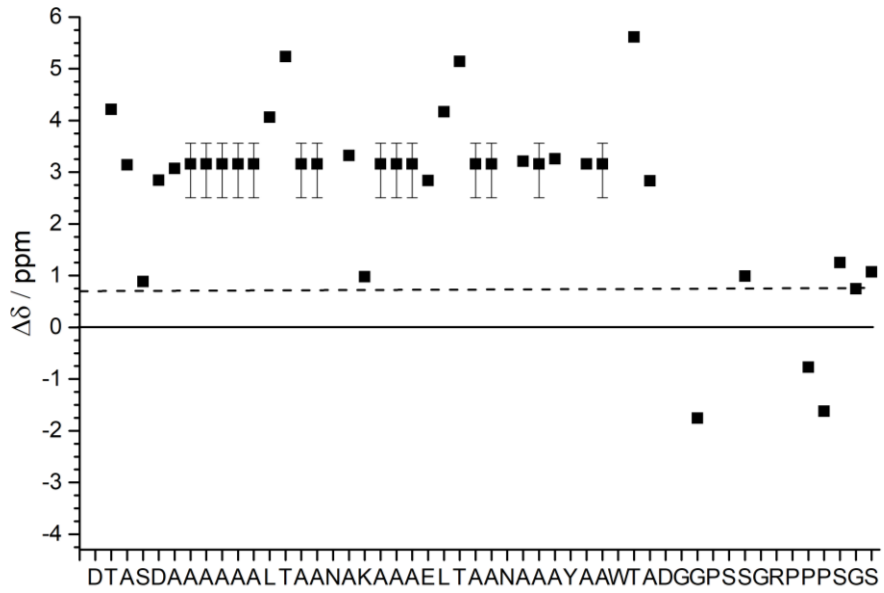

Fig. 38: Cα chemical shift deviation of (jg)IBTC-3 at 274 K and pH 3. The dashed line represents the helical cutoff value. Overlapping alanine Cα resonances where averaged according to signal intensity.

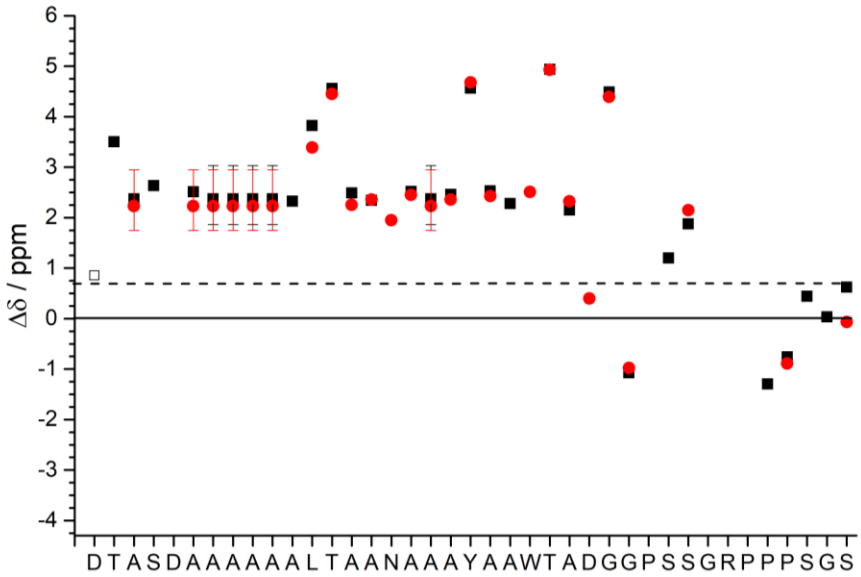

Fig. 39: Cα chemical shift deviation of (jg)IBTC-2 at 274 K and pH 3 (black squares) and pH 7.9 (red circles). The dashed line represents the helical cutoff value. Overlapping alanine Cα resonances where averaged according to signal intensity.

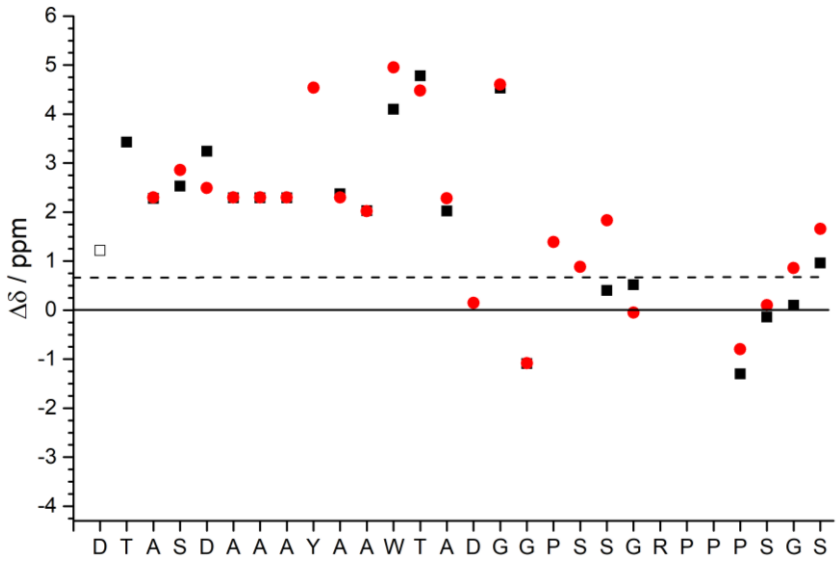

Fig. 40: Cα chemical shift deviation of (jg)IBTC-1 at 274 K and pH 3 (black squares) and pH 7.9 (red circles). The dashed line represents the helical cutoff value.

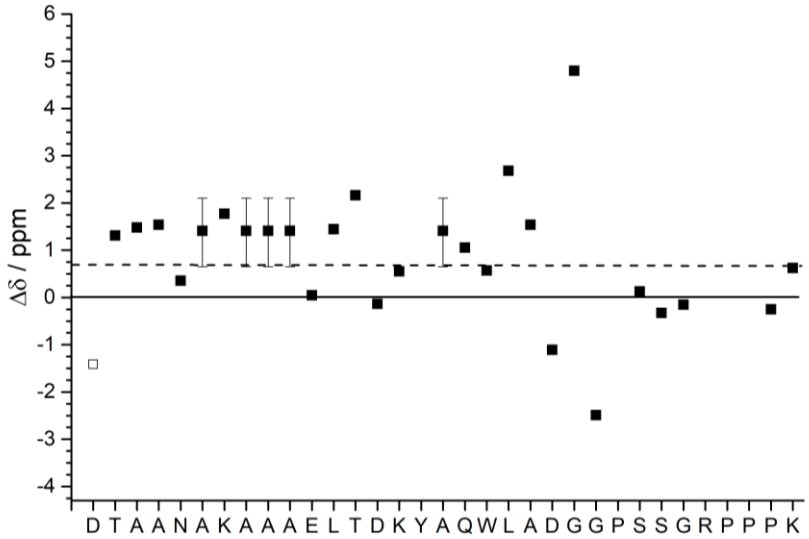

Fig. 41: Cα chemical shift deviation of the folded fraction of (jg)IBTC-4 at 274 K and pH 3. The dashed line represents the helical cutoff value. Overlapping alanine Cα resonances where averaged according to signal intensity.

An unambiguous assignment of all alanine resonances for (jg)IBTC-3, -2, and -4 was not possible due to resonance overlap and some of the chemical shift deviations of the alanines had to be averaged.

Importantly, a positive chemical shift deviation can be observed for the helical elongation and chimera helix for all IBTC, with all residues exceeding the helical limit indicating an α-helical secondary structure. The α-helical fold also includes the N-terminus, with no indication for N-terminal fraying which has previously been observed for AFP-Tc-5 at pH 3 with the Cα CSDs of the first threonine and the second aspartate being below the helical limit.

Remarkable are the large downfield shifts of leucine and threonine in the helix of (jg)IBTC-2 and -3. M. Lipfert hypothesized that the strong CSD of residue 7 is due to an effect of the tertiary Trp-cage structure.[78] However, as all threonines exhibit the strong CSD, the value of residue 7 cannot be explained by the fold alone. It rather seems to be an intrinsic property of the antifreeze protein.

The chemical shift deviations of (jg)IBTC-4 are in size lower than for the other chimera. While the values indicate a helical secondary structure it is noteworthy that the usually strong chemical shift deviations of tryptophan and residue 7 are not as pronounced.

To quantify the helical fold and enable a comparison between different chimeras, M. Lipfert established the parameter 'average helical fold' ($\overline{\Delta\delta}$) by summing up the CSDs and dividing the sum by the number of amino acids *n*.[78]

$$\overline{\Delta\delta} = \frac{\Sigma_n(CSD)}{n}$$

Due to the stark difference in protein length, neither a reference against the samples from M. Lipfert nor with each other was not performed for the average helical fold. However, a separation of the helix in helical extension and chimera helix is possible. The chimera helix always contains the same amount of amino acids and a comparison of proteins of different lengths is possible.

Tab. 13: Average chemical deviations ($\overline{\Delta\delta}$, determined by 13Cα shifts) for all IBTC at 274 K and pH 3 for the complete helix, the chimera helix and the helical extension. The values in brackets include the averaged alanine Cα shifts.

	Helix	Chimera Helix	Helical extension
	$\overline{\Delta\delta}$ (ppm)	$\overline{\Delta\delta}$ (ppm)	$\overline{\Delta\delta}$ (ppm)
(jg)IBTC-3	3.41 (3.30)	3.72 (3.53)	3.32 (3.24)
(jg)IBTC-2	3.06 (2.93)	3.35 (3.19)	2.91 (2.75)
(jg)IBTC-1	2.80	2.84	2.75
(jg)IBTC-4	1.17 (1.23)	1.04 (1.09)	1.26 (1.31)

By comparing the $\overline{\Delta\delta}$ of all four ice binding Trp-cage proteins, a clear order of helical fold stability can be deducted: (jg)IBTC-3 ≈ (jg)IBTC-2 > (jg)IBTC-1 > (jg)IBTC-4. Principally, upon elongation of the helix, a further stabilization can be observed. The high alanine content might be favorable for the helical fold [75], as is an additional salt bridge in (jg)IBTC-3. (jg)IBTC-4 is an exception as it is longer than (jg)IBTC-1 but exhibits the lowest helical fold values. Even though the helical fold appears to be propagated the overall fold stability is not as high as with the other chimera proteins as is apparent from the ^{1}H NMR spectra.

2.3.4 Circular Dichroism Spectroscopy

The evaluation of the secondary structure elements of a protein is not restricted to NMR spectroscopy. Circular dichroism (CD) spectroscopy is based on the UV absorption of the peptide bonds amide. As a protein is a chiral molecule it absorbs left- and right-polarized light differently. The difference spectrum shows the predominant fold of the protein, averaged over all residues. The global fold is characteristic for α-helices, β-strands, and random coil global structures. A α-helical fold has two minima at λ = 222 nm and λ = 208 nm as well as a maximum at λ = 196 nm. A n-π* transition is responsible for the first minimum at about λ = 222 nm, at about λ = 208 nm a π-π* transition of perpendicular polarized light is visible. The maximum at approximately λ = 190 nm is a π-π* transition by parallel polarized light.[102,103]

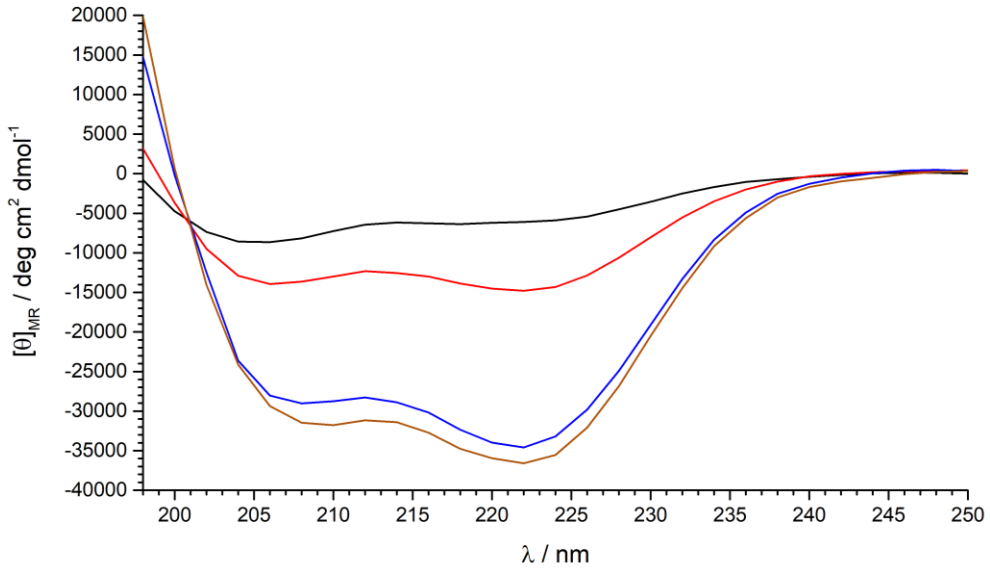

Fig. 42: : CD spectra of (jg)IBTC-4 (black), (jg)IBTC-1 (red), (jg)IBTC-2 (blue), and (jg)IBTC-3 (brown) in order of increasing fold stability at 274 K and 0.1 M NH_4HCO_3 buffer, pH 7.9.

The CD spectra of all four IBTC exhibit helical structure characteristics - the minima at λ ≈ 222 nm and λ ≈ 208 nm as well as a maximum to lower wavelength for (jg)IBTC-2 and (jg)IBTC-3. By comparing the signal intensity of the spectra and comparing the minima at λ = 222 nm, a trend about the α-helical fold is deductable: (jg)IBTC-3 ≥ (jg)IBTC-2 > (jg)IBTC-1 > (jg)IBTC-4. This trend is in agreement with the one previously determined using the helical fold $\overline{\Delta\delta}$ and the fraction folded values of the helical region.

To quantify the helical content the mean residue ellipticity $[\Theta]_{obs}$ at λ = 222 nm is taken and divided by a reference

$$Helical\ content = 100 \cdot \frac{[\Theta]_{obs}}{[\Theta]_{ref}}$$

The reference value for each IBTC is a 100% α-helical protein which can be estimated using the equation (based on empirical observations)[104]

$$[\Theta]_{222} = \left(1 - \frac{1}{n}\right) \cdot (-44.000 + 250 \cdot T)$$

with *n* is the number of residues and *T* the temperature in °C.

Tab. 14: Helical content as determined by CD spectroscopy for (jg)IBTC-1 to -4 at 274 K and pH 7.9. Values for pH 3 can be found in the Appendix.

	(jg)IBTC-3	(jg)IBTC-2	(jg)IBTC-1	(jg)IBTC-4
$[\Theta]_{obs}$ (deg cm^2 dmol^{-1})	-36070	-34195	-14871	-5977
$[\Theta]_{ref}$ (deg cm^2 dmol^{-1})	-42875	-42628	-42188	-42424
Helical content (%)	84	80	35	14

For (jg)IBTC-3, a 50 amino acids long peptide, by assuming a 100% stable helix, a helical content of 84% implies that 42 residues contribute to the helix. That exceeds the expected amount of 37 residues by 5. The same applies to (jg)IBTC-2 with 31 residues calculated to contribute to the helical fold as to the expected 26. However, the difference can be explained by further contributions possibly by the 3_{10} helix in the loop region. An overestimation of the helicity due to the contribution of the tryptophan side chain towards the signal at λ = 222 nm also is possible and has been observed for Tc5b before but would apply to all IBTC chimeras.[67,77,105] In both proteins the fraction folded of the cage loop indicates a nearly 100% fold. Thus, according to NMR and CD spectroscopy, both proteins exhibit a stable fold at 274 K in 0.1 M NH_4HCO_3 buffer, pH 7.9.

Both $[\Theta]_{obs}$ (-14871 deg cm^2 dmol^{-1}) and helical content (35%) of (jg)IBTC-1 are lower than the literature values of AFP-Tc-5. The C-terminal elongation by two amino acids however increases the size of the peptide without being expected to contribute to the helical fold. Calculating the residues in helical conformation gives 10 residues, which is comparable to AFP-Tc-5. As

15 residues were expected, the helix seems to be just 66% stable. This is in good agreement with the literature.[78]

The helical content of (jg)IBTC-4 is the lowest in comparison with the other chimeras. The calculated amount of residues in helical conformation is 5 residues, expected are 22. Taking into account that according to the ^{1}H NMR spectrum 71% of the cage loop are unfolded and correcting for it, 11 residues of the folded fraction are in helical conformation. The helix appears to be 50% stable folded.

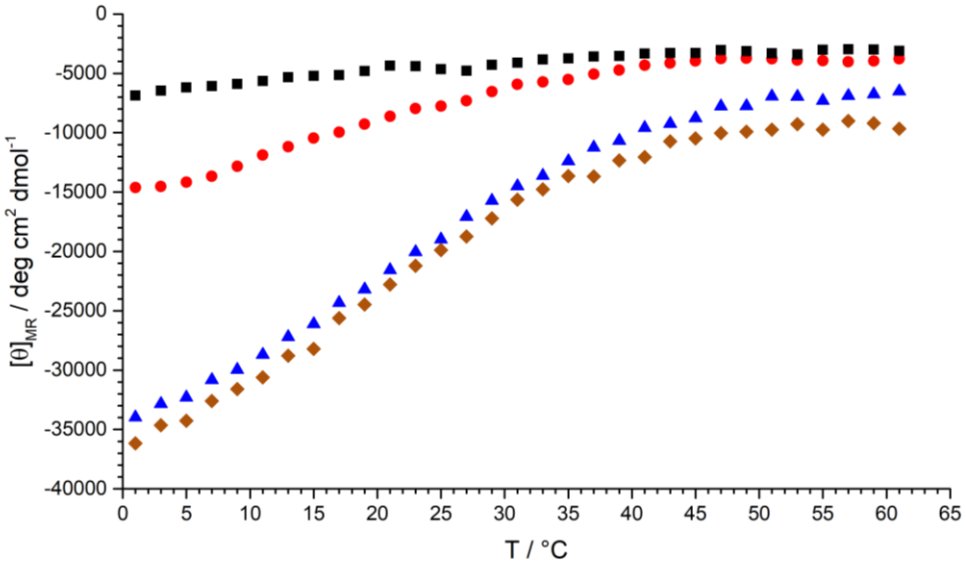

Fig. 43: CD spectra of the thermal denaturation upon heating of (jg)IBTC-4 (black), (jg)IBTC-1 (red), (jg)IBTC-2 (blue), and (jg)IBTC-3 (brown) in 0.1 M NH_4HCO_3 buffer, pH 7.9.

Thermal denaturation curves were recorded by observing $[\Theta]_{222}$ while raising the temperature from 274 K to 334 K. The unfolding of the IBTC was fully reversible for all four chimeras as heating and cooling curves overlap (see Appendix). The melting Temperature (T_m) for (jg)IBTC-4 was estimated to be 283 K and for (jg)IBTC-3 285 K. For (jg)IBTC-2 and -3 an unconstrained Boltzmann fit gave 292.8±1 K and 291.8±1 K, respectively.

The thermal melting point for WfIAFP has been previously determined to be 294±1 K. [59,62] Both chimeras (jg)IBTC-2 and -3 exhibit consequently a fold stability in good agreement with the fold stability of the wild-type antifreeze protein.

All measured data support a grouping upon fold stability according to

(jg)IBTC-3 ≈ (jg)IBTC-2 > (jg)IBTC-1 > (jg)IBTC-4.

The CD spectra for (jg)IBTC-1-GFP to (jg)IBTC-3-GFP are not shown as the spectra are superimposed by the large β-barrel structure of the green fluorescent protein.

2.3.5 Ice Activity Assay

A unique feature of antifreeze proteins is their property to lower the freezing point of water non-colligatively. Though the mechanism by which antifreeze proteins interact with ice still needs to be determined definitely, all data point to an absorption inhibition mechanism. The antifreeze proteins are postulated to bind to the surface of a small ice crystal and inhibit the further growth of the ice crystal at the bound ice plane via the Gibbs-Thompson or Kelvin-Effect. [40,41] Depending on the plane of ice the antifreeze protein binds to, the ice crystal develops into a characteristic shape. The native winter flounder antifreeze protein (HPLC 6) e.g. binds to the pyramidal plane, shaping the ice crystal into a hexagonal bipyramid (see Fig. 9). In buffer, no ice shaping can be observed (Fig. **44**).

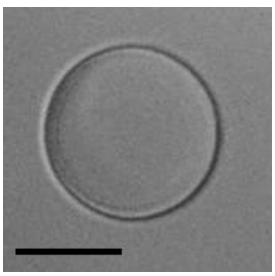

Fig. 44: Shape of an ice crystal in 0.1 M NH_4HCO_3, pH 7.9, upon slight supercooling.

As the goal of this work was to create chimeras that combine the stable fold of the Trp-cage and the ice activity of the antifreeze protein, the ice activity of all protein chimeras was tested using a Nanoliter Osmometer. A Nanoliter Osmometer enables a precise temperature regulation of a sample on a specific sample holder through a Peltier element. The temperature can be tuned as finely as in steps of 1 mOs, with 1000 mOs corresponding to 1.6 °C. During this period, the sample is observed under the microscope.

Fully active antifreeze proteins shape ice crystals into specific forms in the thermal hysteresis gap as mentioned above. By constantly reducing the temperature, these metastable ice crystals finally burst upon reaching a threshold temperature. The burst point temperature minus the melting point temperature gives the TH value. However, not all IBTC studied in this work exhibited ice growth inhibition. Especially the shorter IBTC only exhibited ice growth retardation. As this has been observed in our group before for other IBTC, K. Bamberg established a method which enables an analysis of the ice growth retardation of the less effective IBTC. (Details can be found in chapter 4.3.17.)

2.3.5.1 (jg)IBTC-3

Based on the native winter flounder sequence, (jg)IBTC-3 consists of the three 11 residue long repeat motifs and is elongated at its C-terminus with a cage loop sequence from the Trp-cage. As the IBTC which resembles the wild-type antifreeze protein the most, it is the best chimera in this study to evaluate the influence of the C-terminal capping sequence on the activity of the antifreeze protein.

Three different concentration of (jg)IBTC-3 were tested for ice activity and all three shaped the ice crystal into a hexagonal bipyramid and exhibited a freezing point depression.

Tab. 15: Thermal hysteresis and *c*- to *a*-axes ratio of (jg)IBTC-3.

Concentration (mg/mL)	Thermal hysteresis (°C)	*c*-:*a*-axes ratio
1	0.3	2.8:1
10	0.6	2.8:1
80	0.8	3.1:1

(jg)IBTC-3 shows an increase in TH upon increase of the protein concentration. This effect has also been observed for the native WflAFP.[46] However, the increase in thermal hysteresis is limited to the occupation of all 'binding sites' of the ice by antifreeze protein. Upon reaching the saturation concentration a further increase does not lead to an increase in TH. A concentration-thermal hysteresis curve has the shape of a saturation curve. Thus it is not surprising, that the exceptionally TH measured for the high concentration of (jg)IBTC-3 at 80 mg/mL is in accordance with the TH value measured at 23 mg/mL for the WflAFP. The other concentrations fit well with the literature data too.[46] As a result, the antifreeze activity of the chimera protein does not seem

to be affected by the C-terminal cage loop capping structure although further analysis at different concentrations are necessary for a definite statement.

However, the ice crystal morphology varies from the native WflAFP. The hexagonal bipyramid is slightly twisted, like a hexagonal trapezohedral (Fig. 45). This has been observed before for shortened WflAFP sequences as well as hydrophobic analogues, and other fish AFP.[25,50,66,106–108] Analysis of the ice binding plane for the type III antifreeze protein showed a binding to the pyramidal plane like the winter flounder antifreeze protein. However, Kuiper *et al.* designed an α-helical antifreeze protein which shapes ice crystals into hexagonal trapezohedrals and has been shown to bind to a different plane of ice by ice etching.[109] A determination of the ice binding plane of (jg)IBTC-3 consequently remains of interest.

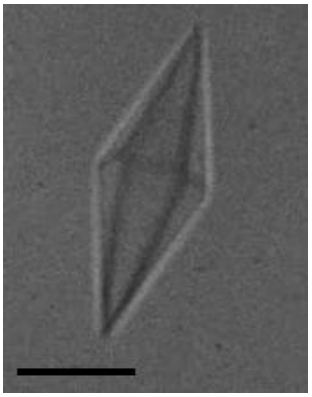

Fig. 45: Ice crystals in the presence of (jg)IBTC-3 in 0.1 M NH_4HCO_3, pH 7.9. The slightly twisted hexagonal bipyramidal shape (the upper pyramid is rotated against the lower pyramid) is shown in the side view. The black scale is 10 µm.

2.3.5.2 (jg)IBTC-2

Varying from (jg)IBTC-3 by the deletion of one 11 residue repeat motif of the winter flounder antifreeze protein sequence, (jg)IBTC-2 still shapes ice crystals into a twisted hexagonal bipyramid over time (Fig. 46). Yet, the ice crystal growth is not stopped, only retarded. The ice growth retardation is 0.049 °C at a concentration of 80 mg/mL.

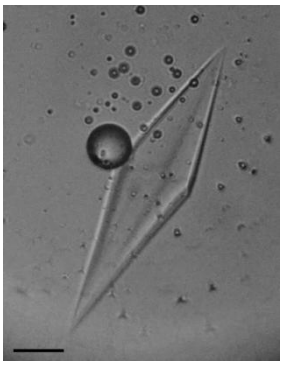

Fig. 46: The shape of a ice crystal in the presence of 80 mg/mL (jg)IBTC-2 in 0.1 M NH_4HCO_3, pH 7.9. The hexagonal bipyramidal shape is slightly twisted. The black scale is 10 µm long. The *c*- to *a*-axis ratio is 3.0:1.

As the shorter (jg)IBTC-2 is not able to halt the ice crystal growth even though the N-terminal helical sequence is 100% helical according to the NMR and CD data, the three repeat motifs of the native winter flounder antifreeze protein (HPLC6) with the four threonines seems to be the minimal sequence length required to achieve thermal hysteresis activity.

2.3.5.3 (jg)IBTC-1

Being the shortest IBTC chimera and containing just one repeat motif of the winter flounder, (jg)IBTC-1 shapes ice crystals into flat hexagonal (Fig. 47). The ice growth is slowed by 0.039 °C at a concentration of 80 mg/mL.

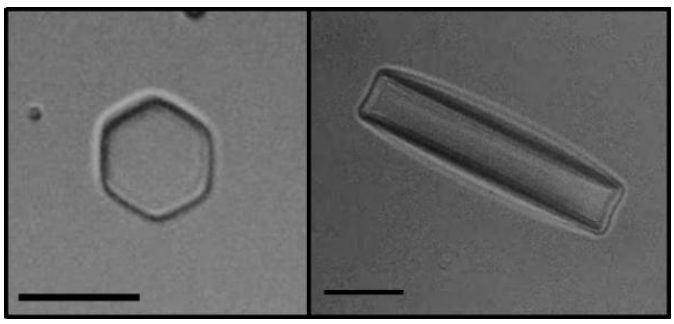

Fig. 47: Ice crystals during the growth in the presence of 80 mg/mL (jg)IBTC-1 in 0.1 M NH_4HCO_3, pH 7.9. Left the top view shows the view perpendicular to the basal plane, while on the right the side view of the crystal is shown. The black scale in each picture is 10 µm long.

The shaping of the ice crystal into a hexagonal disc is due to a higher growth rate along the a-axis than the c-axis of the crystal. As can be seen in the side view of Fig. 47, no tilt is observable indicating no binding of the IBTC to the pyramidal plane.

The result is in contrast to the findings of Kun *et al.*, who found thermal hysteresis activity for a short segment of following composition: DTASDAAAAAAL.[110] In contrast to (jg)IBTC-1 the sequence is shorter, lacks the α-helix stabilizing C-terminal Trp-cage, and also contains only one threonine, which is postulated to be important for ice binding. As the published CD spectra of DTASDAAAAAAL are similar to (jg)IBTC-1 and the ice crystal morphology pictures taken by Zhang *et al.* also show a hexagonal disc[111], the stark difference in the thermal hysteresis measurements cannot be explained to date.

2.3.5.4 (jg)IBTC-4

Containing one repeat motif of the winter flounder antifreeze protein like (jg)IBTC-1, (jg)IBTC-4 was synthesized by fusing two peptides (see Tab. **7**).

Tab. 16: Primary sequence of (jg)IBTC-4, WflAFP, and 1repeat.

1repeat	AANAKAAAELT
Tc10bKKA	Ac-DKYAQWLADGGPSSGRPPPK
(jg)IBTC-4	DT AANAKAAAELT DKYAQWLADGGPSSGRPPPK

As a reference for (jg)IBTC-4, 1repeat – a 11 residue long repeat motif of the winter flounder sequence – was also tested. NMR and CD data both show that 1repeat has no secondary structure in 0.1 M NH_4HCO_3 buffer (see chapter 5.3). Also no ice activity could be observed for 1repeat. (jg)IBTC-4 on the other hand shapes ice crystals into hexagonal discs and retards the ice growth by 0.040 °C at a concentration of 80 mg/mL (Fig. 48).

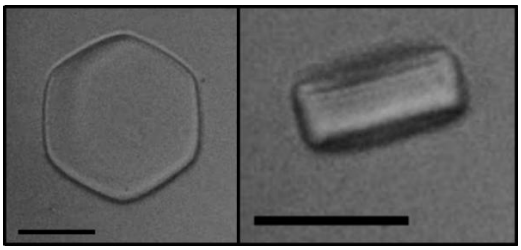

Fig. 48: Ice crystals during the growth in the presence of 80 mg/mL (jg)IBTC-4 in 0.1 M NH_4HCO_3, pH 7.9. Left the top view shows the view perpendicular to the basal plane, while on the right the side view of the crystal is shown. The black scale in each picture is 10 µm long.

Even though (jg)IBTC-4 appears to be a only 30% folded protein according to NMR and the crystal edges are not as sharp as (jg)IBTC-1, the ice growth retardation of (jg)IBTC-4 and -1 is comparable. A possible explanation is the high concentration of both samples of 80 mg/mL. In the case of (jg)IBTC-4, 70% unfolded sample would still amount to 24 mg/mL of folded protein. As ice activity is correlated to concentration and the correlation follows the shape of a saturation curve, the plateau of the saturation curve of (jg)IBTC-4 could be reached at 24 mg/mL. 30% folded protein at 80 mg/mL thus would be enough for ice growth retardation activity. Another possible explanation is an effect of the ice on the structure of the protein by inducing the α-helical fold.

2.3.5.5 (jg)IBTC-3-GFP

Containing a C-terminal GFP, the remainder of (jg)IBTC-3-GFP is made up of the same sequence as (jg)IBTC-3 and would be expected to have a comparable ice activity.

Tab. 17: Thermal hysteresis and *c*- to *a*-axes ratio of (jg)IBTC-3-GFP. *Ice growth retardation

Concentration (mg/mL)	Thermal hysteresis (°C)	*c*-:*a*-axes ratio
0.81	0.029*	Not determined
15	0.4	2.8:1
80	0.9	3.0:1

The threshold concentration needed for thermal hysteresis activity of WflAFP was determined to be 0.06 M.[112] As the concentration of 0.81 mg/mL equals 0.03 M, the ice growth retardation is in accordance with literature. The thermal hysteresis activity of the other two concentrations

however is higher than both (jg)IBTC-3 and the wild type WflAFP. An increase in thermal hysteresis activity upon fusing antifreeze proteins with a second (larger) protein has been reported before. The enhanced thermal hysteresis activity has been proposed to be due to an increased coverage of the ice surface or a steric hindrance of the ice crystal to overgrow the larger molecule.[113,114] The shape of the ice crystal as shown in Fig. 49 is the same as that of the untagged (jg)IBTC-3: a twisted hexagonal bipyramid with the upper pyramid rotated against the lower pyramid (see Fig. 49).

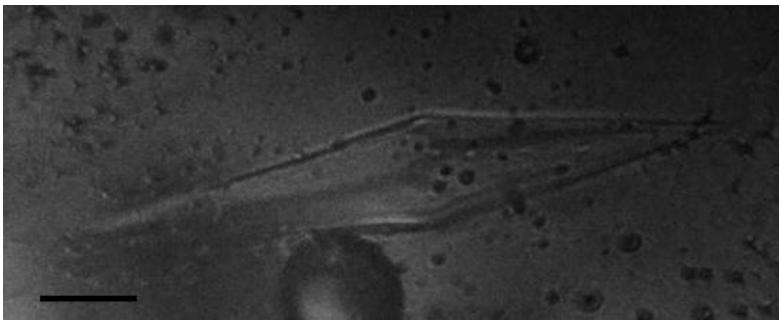

Fig. 49: The ice crystal shape in the presence of 80 mg/mL (jg)IBTC-3-GFP in 0.1 M NH_4HCO_3, pH 7.9. The slightly twisted hexagonal bipyramidal is best visualized shortly before the burst. The black scale is 10 µm long. The dark gray spheres are air bubbles.

Having produced an active WflAFP-IBTC-GFP fusion variant discards the concerns of Pertaya *et al.*, who pondered a negative influence of the bulky GFP on binding of the antifreeze moiety to the ice surface.[42] The structural model of (jg)IBTC-3-GFP visualizes the size ratio of the ice binding site (IBS) to the GFP barrel (see Fig. 29). In comparison to the GFP, the length of the IBS is even greater than the barrel structure.

2.3.5.6 (jg)IBTC-2-GFP

A C-terminal GFP fusion protein of (jg)IBTC-2, (jg)IBTC-2-GFP behaves differently from the other two GFP fusion proteins as it does not exhibit any enhanced ice activity. Contrary, it only shapes ice crystals into hexagonal discs at any measured concentration up to 80 mg/mL. An increase in protein concentration leads to a more pronounced hexagonal shape (see Fig. 50).

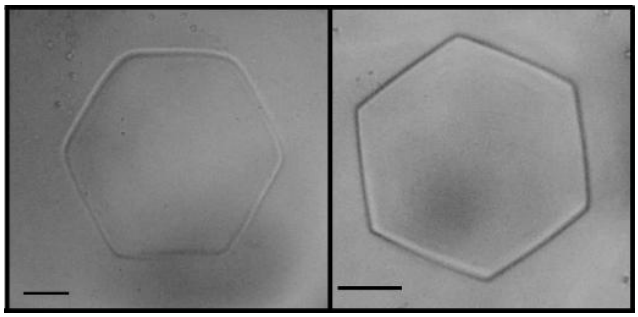

Fig. 50: Ice crystals during the growth in the presence of 4.23 mg/mL (left) and 80 mg/mL (right) (jg)IBTC-2-GFP in 0.1 M NH_4HCO_3, pH 7.9. The view is perpendicular to the basal plane. The black scale in each picture is 10 µm long.

The fact that (jg)IBTC-2-GFP does not exhibit any ice growth retardation is an exception in contrast to all other IBTC proteins and cannot be explained to date as samples from different batches and concentrations were tested. All samples were pure according to HPLC and contained only the protein of interest according to ESI-MS.

2.3.5.7 (jg)IBTC-1-GFP

Being a GFP tagged (jg)IBTC-1, (jg)IBTC-1-GFP has a similar ice growth retardation at a lower concentration than (jg)IBTC-1 (0.046 °C at 10 mg/mL vs. 0.039 °C at 80 mg/mL). The enhanced ice activity is in accordance with literature and (jg)IBTC-3-GFP.[113,114] The ice crystal is shaped into a hexagonal disc whose edges are well pronounced. In some cases a slight growth into part of a hexagonal bipyramid could be observed (see Fig. 51).

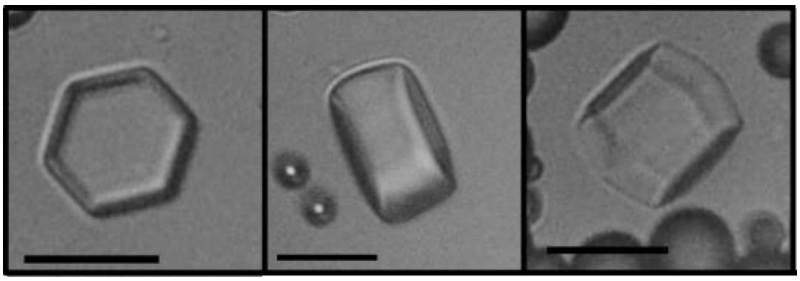

Fig. 51: Ice crystals during the growth in the presence of 10 mg/mL (jg)IBTC-1-GFP in 0.1 M NH_4HCO_3, pH 7.9. Left the top view shows the view perpendicular to the basal plane, while the middle and the right show the side view of the crystal. The black scale in each picture is 10 µm.

In summary, (jg)IBTC-3 and (jg)IBTC-3-GFP are the only two chimeras in this study which effectively suppress the freezing point of water. Of both, (jg)IBTC-3-GFP has the higher activity and represents to our knowledge the first GFP fusion protein with a type I antifreeze protein. Additionally to the two chimeras, (jg)IBTC-2 also shapes the ice crystals into hexagonal trapezohedrals and some capped and twisted hexagonal bipyramids could be observed in some rare cases. The other chimeras shape ice crystals into hexagonal discs. Ordering the IBTC according to activity gives following order:

(jg)IBTC-3-GFP > (jg)IBTC-3 > (jg)IBTC-2 ≈ (jg)IBTC-1-GFP ≈ (jg)IBTC-4 ≈ (jg)IBTC-1 > (jg)IBTC-2-GFP

The results are not in agreement with our expectations. Our hypothesis was that (jg)IBTC-3 would be the most active IBTC, followed by (jg)IBTC-2, then (jg)IBTC-1 and (jg)IBTC-4 in accordance with a decrease in antifreeze protein length and not considering the GFP labeled IBTC. However, the IBTC 1, 2, and 4 all exhibit a similar ice growth inhibition, especially if one takes the error margins into consideration. As the N-terminal helix of (jg)IBTC-2 is 100% folded under the conditions of the experimental setup, the only remaining explanation is that a stable fold is not the only necessary prerequisite for an active antifreeze protein, but that a critical size or in this case protein length is also vital.[46,115] A study by Warren *et al.* of synthetic α-helical antifreeze homologues containing two to six repeats showed activity for all except the shortest variant.[116] Additionally, previous studies have mostly correlated a loss of antifreeze activity with a loss in α-helicity.[65,66] This study however utilized a C-terminal stabilizing module and a loss of antifreeze activity consequently cannot be explained by a loss of secondary structure. The critical helix length for ice growth inhibition of WflAFP and its analogs thus consists of three repeat motifs.

3 Summary and Outlook

3.1 Summary

In this work, the synthesis and characterization of different ice binding Trp-cage chimera was pursued. Mainly two questions were of interest. First, if the C-terminal stabilizing Trp-cage unit has any effect on the biological activity of the antifreeze protein part. Second, the required antifreeze protein length necessary to achieve antifreeze activity. The proteins were obtained via SPPS or bacterial expression in *E. coli* and characterized amongst other methods with NMR- and CD-spectroscopy. Furthermore, their ice activity was measured using a Nanoliter Osmometer.

To answer the question if the C-terminal stabilizing Trp-cage unit has any effect on the biological activity of the antifreeze protein, an IBTC based on the full length wild-type antifreeze protein *WflAFP* and the Trp-cage was studied ((jg)IBTC-3). NMR- and CD-spectroscopy both showed the antifreeze part to be 100% helical folded without any N-terminal fraying. The ice activity analysis gave a comparable activity to the wild-type *WflAFP*, indicating no effect of the C-terminal capping unit on ice activity. However, the ice crystal formed during the thermal hysteresis gap differed slightly from the wild-type crystal. A twisted hexagonal bipyramid with the upper pyramid rotated against the lower one was observed.

The second question concerned the protein size. Therefore, the fold and ice activity of several IBTC variants each comprised of a different number of ice binding repeats was studied. Three analogs were compared. (jg)IBTC-3 is the largest of all characterized proteins concerning the antifreeze part and resembles the wild-type antifreeze protein. The other IBTC, (jg)IBTC-2, was one ice binding repeat shorter. (jg)IBTC-1 and (jg)IBTC-4 were each two ice binding repeats shorter. While (jg)IBTC-2 and -1 were well folded, especially in the helical region, (jg)IBTC-4 was only ~30% folded in buffer at 274 K according to NMR data. However, all three IBTC exhibited no antifreeze activity. Only ice growth retardation and ice shaping were observed. As the ice growth retardation ability of all is comparable, it was concluded that the minimal protein length necessary for antifreeze activity is three ice binding repeat motifs and therefore equal to the wild-type *WflAFP*.

Additionally to the above mentioned IBTC, some were chosen and labeled C-terminally with GFP. The advantage of adding a fluorescent tag to the proteins is that it enables a microscopic analysis. The labeled IBTC were (jg)IBTC-3-GFP, (jg)IBTC-2-GFP, and (jg)IBTC-1-GFP. They were characterized with particular emphasis of the ice activity studies. IBTC (jg)IBTC-3-GFP and

(jg)IBTC-1-GFP behaved as expected and had a greater activity than the IBTC without GFP. (jg)IBTC-2-GFP, however, behaved unexpectedly as no ice growth retardation could be recorded only ice shaping. The origin of this observation remains unclear and requires further analysis.

3.2 Determination of the Ice Binding Plane

The ice crystals formed in the presence of (jg)IBTC-2, (jg)IBTC-3, and (jg)IBTC-3-GFP are all twisted hexagonal bipyramids, better described as hexagonal trapezohedrals. In contrast, the WflAFP forms ice crystals into hexagonal bipyramids. Even though the shaping of ice crystals into hexagonal trapezohedrals has been observed before for variants of the WflAFP and a different type III antifreeze protein who all bound to the pyramidal plane of ice [25,50,66,106,107], a designed α-helical antifreeze protein, which produces a hexagonal trapezohedral ice crystal, shows a different ice etching pattern than WflAFP [109]. The source of this unusual shape could therefore be a difference in the ice binding plane.

The determination of the ice binding plane can be performed with an ice hemisphere etching experiment [48] or alternatively FIPA[50] (see Introduction). For FIPA analysis the binding of fluorescently labeled antifreeze proteins to a single ice crystal hemisphere is observed. Depending on the preferential binding to a specific ice plane a characteristic pattern is formed. While the tryptophan of the Trp-cage sequence as an intrinsic fluorescence, it can be quenched by electron transfer from the indole ring to neighboring side chains of asparagines or the amide backbone and fluorescence yields as low as 0.01 have been reported.[117] The covalent attachment of a fluorescent dye or tag like green fluorescent protein (GFP) are alternatives. Three of the proteins studied in this work are GFP-fusion proteins and thus candidates for FIPA analysis.

3.3 Photo-switchable Ice-Binding Trp-cage Chimeras

A control of the ice activity by changing the structure of the WflAFP has been of interest in our group for some time. Therefore the incorporation of a molecular switch was envisioned. The switchable molecule has to be stable in at least two different forms like conformation or constitutional isomers.[118] Both states need to be convertible into each other, preferably by an external stimulus like, in this case, light. Molecules which fulfill these requirements are amongst others azobenzenes[119], diazocines[120], and spiropyranes[121] (see Fig. 52).

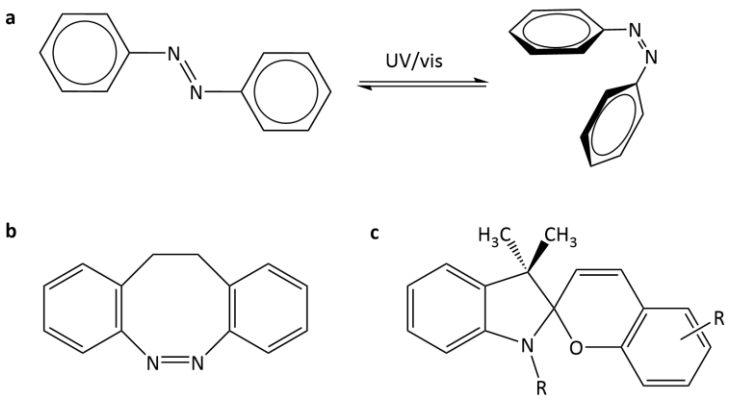

Fig. 52: Azobenzene (a), diazocine (b), and spiropyrane (c) as possible photoswitchable molecules. For the azobenzene the two different conformational states are shown: left *trans*, on the right *cis*.

The incorporation of the molecular switch into the cage loop is of special interest as by influencing the conformation of the photochromic molecule an unfolding of the cage loop and the hydrophobic encapsulated tryptophan side chain followed by an unfolding of the chimera helix and helical extension is envisioned (see Fig. **53**).

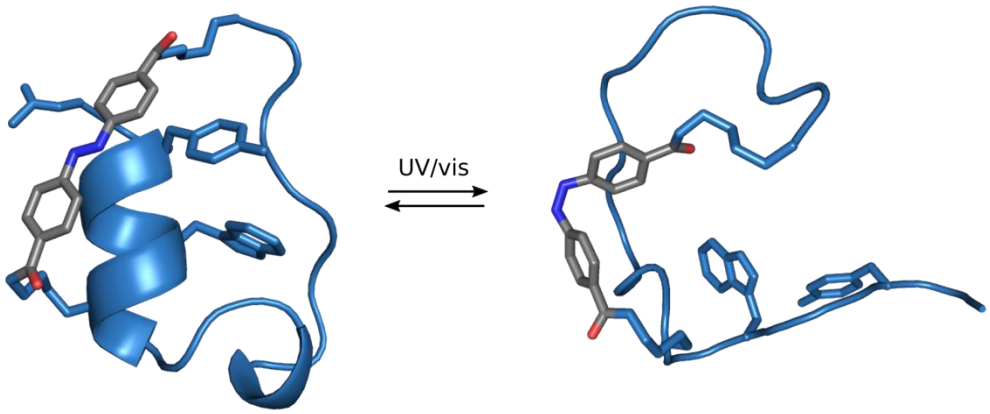

Fig. 53: Envisioned induced structural change of the folding of Trp-cage module through the conformational change of a photochromic molecule. The Trp-cage and selected side chains are colored light blue. The azobenzene is colored according to atoms: carbon is grey, oxygen red, and nitrogen blue. (PDBs were prepared by N. Preußke based on PDB: 1L2Y)[67]

The attachment of an azobenzene between two residues of a Trp-cage has been achieved in our group successfully.[78] The transfer of this concept to IBTC and a subsequent switching of the Trp-cage as well as the correlated antifreeze protein segment is currently under investigation by K. Bamberg.

The advantages of the bacterial expression of IBTC, especially GFP labeled variants, combined with a switching of antifreeze activity could facilitate the way to finally elucidate the interaction between antifreeze protein and ice crystal surface. Currently the linking reaction is performed between an activated N-hydroxysuccinimide (NHS) ester and a primary amine, mostly from the amino acid lysine even though shorter unnatural amino acids with a primary amine work, too. (N. Preußke, master thesis) However, for IBTC obtained via bacterial expression the cross-linking reaction is problematic. Not only is the N-terminus an additional primary amine which can interact with the molecular switch and form a hard to separate by-product. In the case of GFP labeled IBTC, the molecular switch can also react with any of the lysines of the GFP. Several ways to solve the problems are possible. The most promising is a different cross-linking reaction. The reaction between the thiol of cystein and iodoacetamide as reactive group of the photoswitch has been performed before in our group by H. Kobarg (unpublished work). However, the results were unsatisfactory. Another possible cross-linking reaction is between an alkyne and an azide (see Fig. 54). For this click-chemistry, unnatural amino acids have to be introduced into the sequence.[122] The incorporation of unnatural amino acids by SPPS follows the standard protocol and for the incorporation of unnatural amino acids during protein expression there are also solutions. One is the cell free expression of proteins.[123]

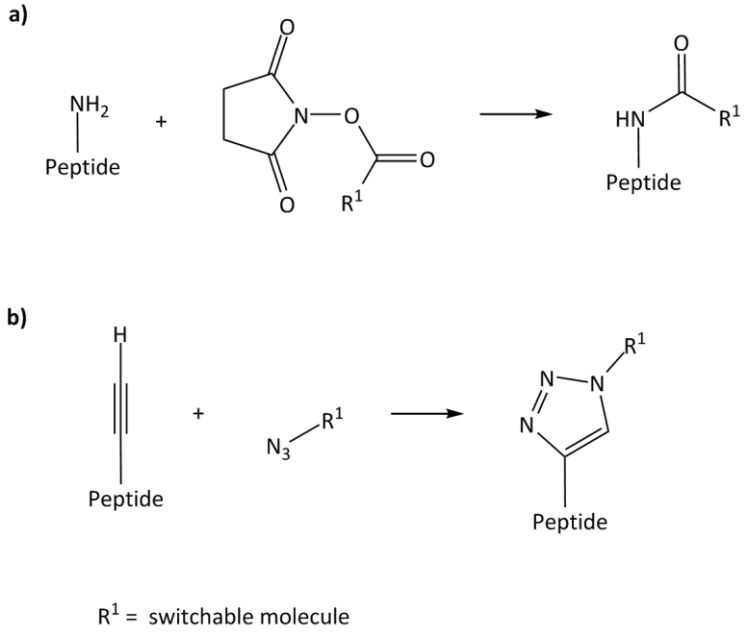

Fig. 54: Comparison of the cross-linking of a) a primary amine with an N-hydroxysuccinimed ester with b) the click-chemistry between an alkyne and an azide.[122,124]

3.4 Transfer of the Chimera Concept

The concept of the synergistic fusion of two proteins is transferable to other proteins as well. Both the α-helical stabilizing module and the α-helical biological active protein can be exchanged. As α-helical stabilizing peptide module the zinc finger motif [81,125], (avain) pancreatic polypeptide (aPP)[126–128], protein Z[129], or a subdomain of the villin headpiece (HP-35)[130] can be employed (see Fig. 55).

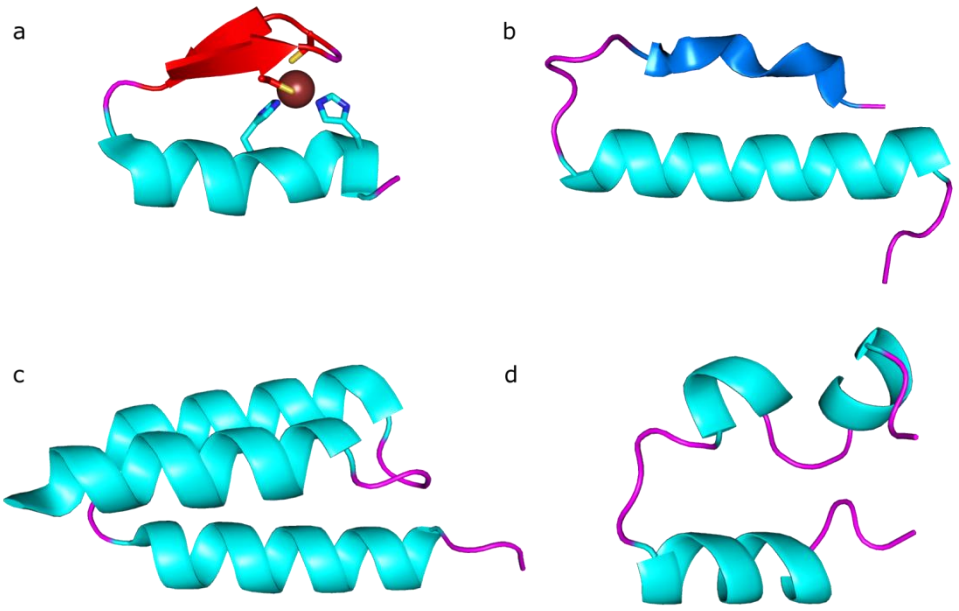

Fig. 55: Structures of zinc finger (a, PDB: 1ZNF)[125], aPP (b, PDB: 1PPT)[126], protein Z (c, PDB: 1LP1)[129], and the subdomain of the villin headpiece (d, PDB: 1VII)[130]. The secondary structure is colored in cyan for α-helices, magenta for loop structures, red for β-sheets, and marine for polyproline II helices. In a the zinc ion is shown in brown and the side chains for complexation shown. The nitrogens are colored blue and the sulfur atoms yellow.

The zinc finger is 25 residues long and consists of an N-terminal antiparallel β-sheet followed by a C-terminal α-helix. Two cysteine side chains in the β-sheet and two histidine side chains in the α-helical region coordinate a zinc ion, which stabilizes the fold.[125] aPP on the other hand consists of an N-terminal polyproline II helix followed by a C-terminal α-helical region. The fold is stabilized by hydrophobic interactions between the polyproline II helix and the α-helical region.[126] For a combination with an α-helical protein an elongation at the C-terminus of both the zinc finger and aPP is possible.

Protein Z is derived from the staphylococcal protein A and is made up of a three helix bundle.[129] The three helices of the thermostable subdomain of the villin headpiece are shorter than the one from protein Z.[130] While HP-35 is 35 amino acids long, protein Z is made up of 58 residues. An elongation at both N- and C-terminus are possible.

The most promising candidates for the transfer of the concept are both zinc finger and aPP. While aPP has several similarities to the Trp-cage, the zinc finger on the other hand coordinates a metal ion between four amino acid side chains. As the protonation/deprotonation of both amino acid side chains is pH dependent, so is the coordination of the zinc ion. Consequently, this stabilizing motif can be switched between folded and unfolded conformation by pH. As the zinc finger motif has to be added N-terminally and the Trp-cage, on the other hand, on the C-terminus, a combination of both stabilizing units with one α-helical sequence is possible. If the Trp-cage additionally is modified with a photoswitch, the structure and biological activity of the whole protein could be influenced by two factors – pH and light.

4 Experimental Section

4.1 Solid Phase Peptide Synthesis

The peptides synthesized for the fusion approach were prepared using Fmoc-based solid phase peptide synthesis (SPPS) on the semi-automated peptide synthesizer *Initiator*$^{+}$ *SP Wave* by Biotage. Solid phase peptide synthesis was developed by Merrifield in 1963[131] and describes the synthesis of a peptide from C- to N-terminus on a resin using protected amino acids. The amino group of the backbone is protected with a base labile Fmoc, the functional groups of the side chains by acid labile protecting groups. The orthogonal protecting strategy enables the specific and systematical synthesis of proteins. Here a general overview over the methods used to obtain either fully deprotected or protected peptides and to condense fragments is given. Details concerning the synthesis of each peptide (like the amount of protected amino acid in g) can be found in the Appendix.

4.1.1 Preparation of the Resin

The solid phase on which the peptide synthesis is carried out is a polystyrene-based resin. Different surface functionalizations are used to obtain different target proteins. Each resin has a special loading capacity of the functional group, i.e. the distribution of functionalizations per bead. The loading capacity value is supplied by the manufacturer. For this work the Wang resin, enabling the synthesis of fully deprotected peptides, as well as the 2-chlorotrityl chloride resin for protected peptide fragments were used. [84]

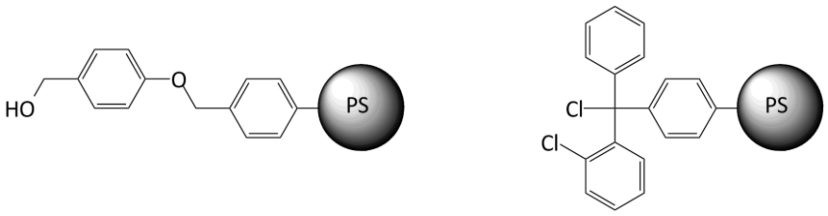

Fig. 56: Used resins for solid phase peptide synthesis. Wang resin (left) and 2-chlorotrityl chloride resin (right). PS stands for polystyrene.

Each resin was swollen in dichloromethane for 1 h prior to use, enhancing the volume and thus the surface accessibility.

4.1.2 Synthesis of Fully Deprotected Peptides

Before the coupling of the first amino acid the resin was washed with dimethylformamide (DMF). The Fmoc-protected amino acid (5 eq), 1-[Bis(dimethylamino)methylene]-1H-1,2,3-triazolo-[4,5-b]pyridinium 3-oxid hexafluorophosphate (HATU, 4.9 eq) and *N,N*-diisopropylethylamine (DIPEA, 10 eq) were dissolved in dimethylformamide and added to the swollen Wang resin. The microwave-assisted coupling of each amino acid was performed at 75 °C for 5 min and with 600 rpm followed by a washing cycle with dimethylformamide.[84]

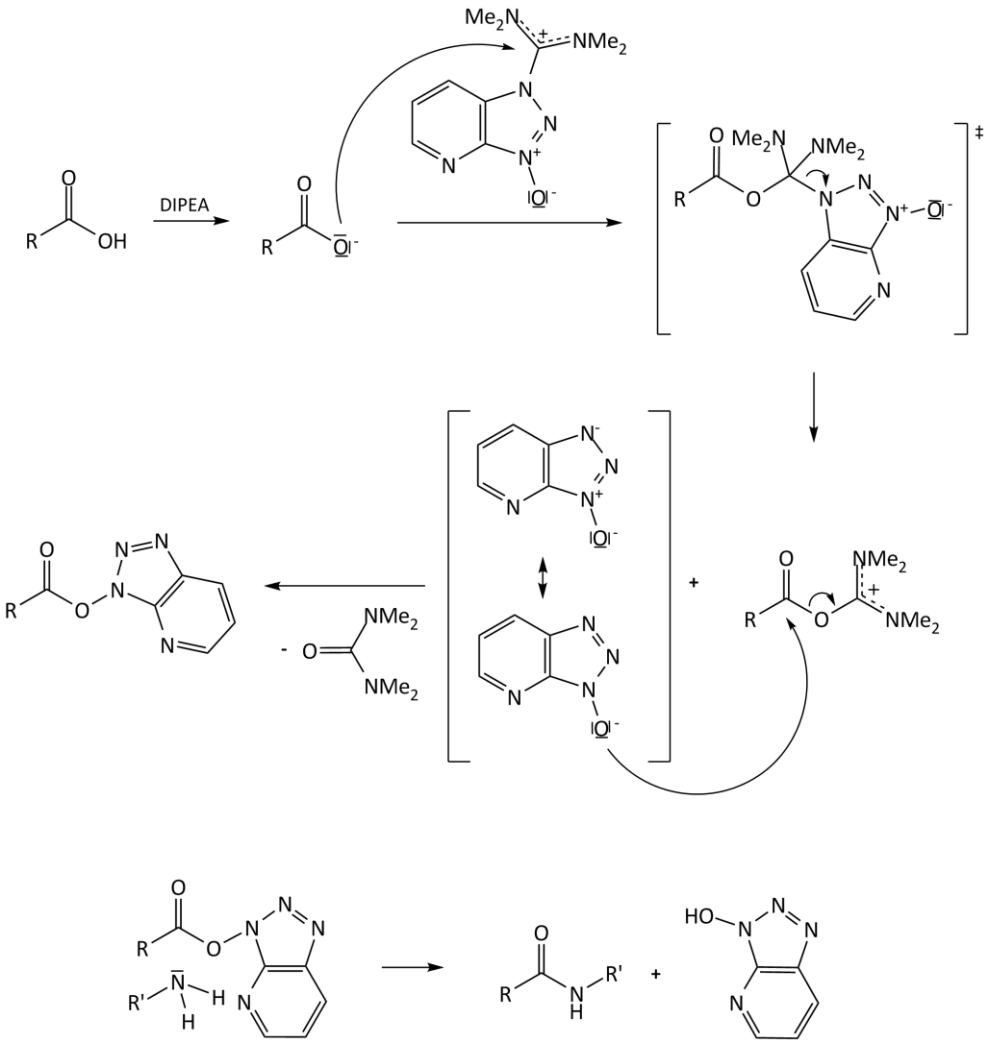

Fig. 57: Schematic representation of the peptide coupling with HATU and DIPEA.

The base DIPEA deprotonates the Fmoc-protected amino acid. The carboxylate anion reacts with HATU via an unstable intermediate to form the 1-hydroxy-7-azabenotriazole anion and *O*-acyl(tetramethyl)isouronium cation. The anion attacks the cation and, after release of

N,N,N',N'-tetramethylurea, the activated ester is formed. The addition of a nucleophile like an amine results in acylation, in this case the amide peptide bond. (see Fig. **57**)

An additional coupling step was performed for difficult couplings and unpolar amino acids, especially alanine, to ease purification and increase the overall yield. In case of a high alanine content a capping step with acetic anhydride, pyridine and dimethylformamide (v/v 1/1/2) was inserted before the deprotection step to quench unreacted sides using the same reaction conditions as for the coupling of amino acids.

The *N*-terminal Fmoc protecting group was removed with 25% piperidine in dimethylformamide at 75 °C for 30 sec and at 600 rpm followed by a second deprotection step lasting 3 min. For difficult deprotection steps an extended deprotection was performed, consisting of three parts each at 75 °C. While the first deprotection step lasts 30 sec, the second and third both take 4 min to completion. Before the coupling of the next amino acid a washing cycle with dimethylformamide was performed.

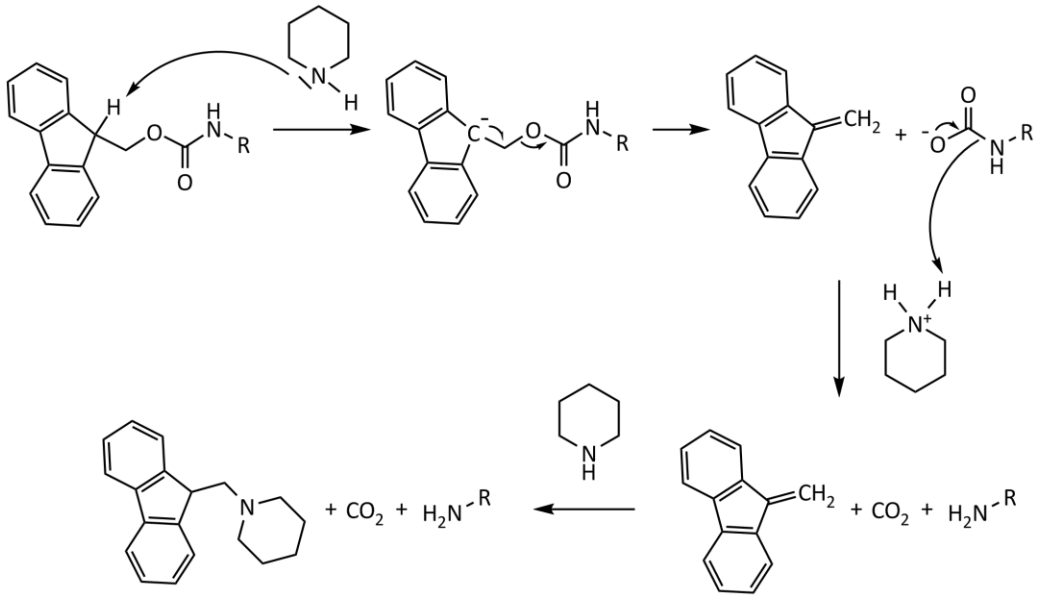

Fig. 58: Deprotection mechanism for the removal of Fmoc with the base piperidine.

The acidic fluorenyl proton of the Fmoc is removed by the base piperidine leading to a β-elimination finally resulting in 9-methylenen-fluorene, carbon dioxide and the free amine. 9-Methylene-fluorene can react further with piperidine. (Fig. 58)[132]

The cleavage from the resin and the deprotection of the peptide ensued after the coupling and deprotection of the last amino acid. An acidic solution of 2,2,2-trifluoroacetic acid and the

scavengers water and triisopropylsilane (v/v/v 95/2.5/2.5) was added to the dried resin at a ratio of 1 mL/100 mg. The mixture was incubated for 2-3 h at room temperature, filtrated and the resin washed twice with 2,2,2-trifluoroacetic acid. The combined filtrate was treated with cold diethyl ether to precipitate the peptide. The crude peptide was washed with diethyl ether, dissolved in water and lyophilized. The purification of the peptides was done using high-performance liquid chromatography.

4.1.3 Synthesis of Protected Peptides

The synthesis of protected peptide fragments varies from the one of the fully deprotected peptide in the following points: (1) instead of the Wang resin the 2-chlorotrityl chloride resin is used, (2) the coupling of the first amino acid, (3) the missing deprotection step of the last amino acid, and (4) the cleavage conditions.[84]

The coupling of the first amino acid was a double coupling step. A solution consisting of the Fmoc-protected first amino acid (2 eq) and *N*,*N*-diisopropylethylamine (5 eq) in dichloromethane was added to the swollen 2-chlorotrityl chloride resin and incubated at room temperature for 30 min. The second coupling step had a concentration of 5 eq amino acid and 10 eq *N*,*N*-diisopropylethylamine. After incubating for 1 h at room temperature the resin was washed with dichloromethane. The capping of unreacted functional groups on the resin was done twice at room temperature for 10 min and 600 rpm with 15 v/v% methanol and 5 v/v% *N*,*N*-diisopropylethylamine in dichloromethane.

The N-terminal Fmoc protecting group was removed with 25% piperidine in dimethylformamide at 75 °C for 30 s and at 600 rpm followed by a second deprotection step lasting 3 min. Before the coupling of the next amino acid a washing cycle with dimethylformamide was performed.

For the coupling of the following amino acids the Fmoc-protected amino acid (5 eq), HATU (4.9 eq) and *N,N*-diisopropylethylamine (10 eq) were dissolved in dimethylformamide. The microwave-assisted coupling of each amino acid was performed at 75 °C for 5 min and at 600 rpm followed by a washing cycle with dimethylformamide.

After the coupling of the last amino acid, the resin washed with methanol, dichloromethane and dried, leaving out the deprotection step.

For the cleavage of protected peptides a cleavage solution of 20% (v/v) 2,2,2-trifluoroethanol in dichloromethane was added to the resin. After incubating for 45 min the mixture was filtrated

and the resin washed with dichloromethane. The combined filtrate was treated with cold diethyl ether to precipitate the peptide. The peptide was solved in water and lyophilized.

Usually the protected peptide fragment can be used without further purification but a purification using high-performance liquid chromatography is possible (see 4.1.5 and Appendix).

4.1.4 Condensation of peptide fragments

The C-terminal fragment was synthesized like a fully deprotected peptide (see 4.1.2) utilizing Wang resin but omitting the cleavage step. The N-terminal protected peptide fragment (2 eq, about half the weight of the resin), Benzotriazol-1-ol (2 eq), and *N*,*N'*-diisopropylcarbodiimide (2 eq) were dissolved in dimethyl sulfoxide added to the resin bound fragment and incubated for 48 h at room temperature. Subsequently the resin was washed with dimethylformamide and capped with acetic anhydride, pyridine and dimethylformamide (v/v/v 1/1/2) at 75 °C for 5 min and at 600 rpm. The N-terminal Fmoc protecting group was removed with 25% (v/v) piperidine in dimethylformamide at 75 °C for 30 s and 600 rpm followed by a second deprotection step lasting 3 min. [58,84]

Additional N-terminal amino acids could be coupled using the procedure in chapter 4.1.2.

The cleavage from the resin and the deprotection of the peptide ensued after the coupling and deprotection of the last amino acid. An acidic solution of 2,2,2-trifluoroacetic acid and the scavengers water and triisopropylsilane (v/v/v 95/2.5/2.5) was added to the dried resin at a ratio of 1 mL/100 mg. The mixture was incubated for 2-3 h at room temperature, filtrated and the resin washed twice with 2,2,2-trifluoroacetic acid. The combined filtrate was treated with cold diethyl ether to precipitate the peptide. The crude peptide was washed with diethyl ether, dissolved in water and lyophilized. The purification of the peptides was done using high-performance liquid chromatography.

4.1.4 The DG Motif in SPPS

Aspartimide formation is a well known side reaction during Fmoc SPPS, in which the nitrogen of the amide bond of the previous amino acid reacts with the β-carboxy side chain of the aspartate to form a five-membered ring. Most commonly the reaction takes place between aspartate and glycine and can be either base or acid catalyzed.[84,133–135]

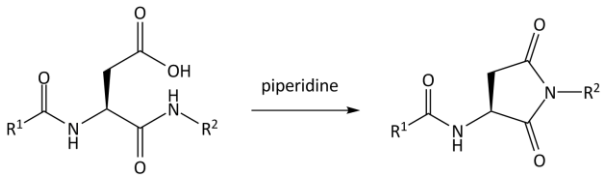

Fig. 59: The aspartimide formation between the aspartate side chain and the amide nitrogen of the previous amino acid.

The resulting aspartimide is prone to racemization via base catalysis. Ring opening in the presence of piperidine gives a mixture of α-, β-aspartyl peptides and α-, β-piperidides.

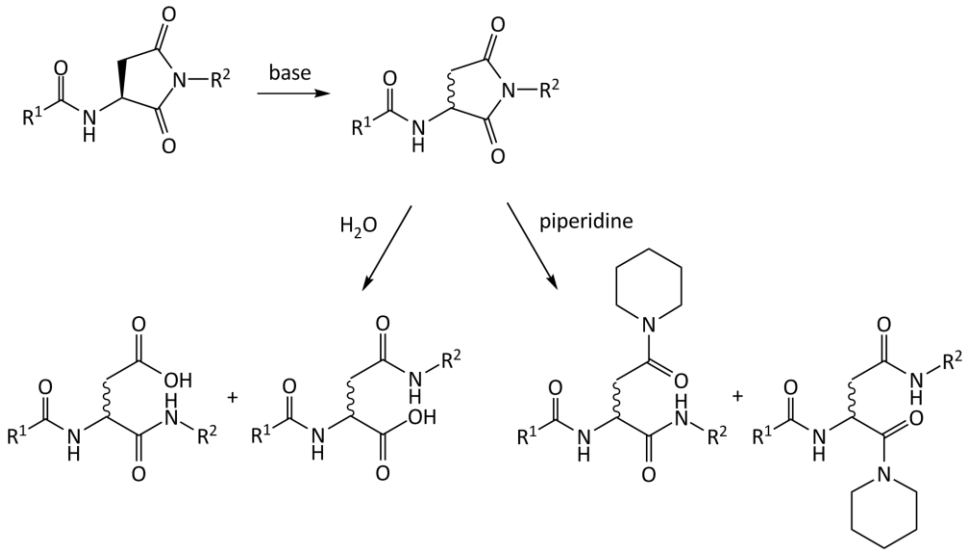

Fig. 60: By-product formation after ring-opening of an aspartimide by hydrolysis or with piperidine.

To prevent aspartimide formation a backbone protected amino acid was used previous to aspartate. For synthetic reasons a dipeptide Fmoc-Asp(O*t*Bu)-(Dmb)Gly-OH was employed.[84,136,137]

4.1.5 HPLC

The high-performance liquid chromatography consists of a mobile and a stationary phase. While the liquid solvent passes over the solid stationary phase each component of the sample interacts with the adsorbent material resulting in different retention times (t_R). A pumping device can generate a gradient between different solvents.

For the purification of the above mentioned peptides a stationary phase of poly(styrene-divinylbenzene) (PLRP-S) and a mobile phase of H_2O and acetonitrile was chosen. Both were acidified with 0.1% (v/v) 2,2,2-trifluoroacetic acid or formic acid.

For the purification of fully deprotected peptides first an analytical column was employed (for the solvent gradient see Tab. 18). During the linear gradient from 2.5 to 12.5 min the target protein elutes. Unpolar species are washed down with a gradient of 95% acetonitrile. Before the storage of the column it is reequilibrated with 95% H_2O and 5% acetonitrile.

Tab. 18: Solvent gradient of the analytical run.

time/ min	**H_2O, 0.1% TFA / %**	**acetonitrile, 0.1% TFA/ %**	**flow rate / mL/min**
0	95	5	1.000
2.5	95	5	1.000
12.5	40	60	1.000
13.5	5	95	1.000
16	5	95	1.000
17	95	5	1.000
18.5	95	5	1.000

Based on the retention time during the analytical run the method for the semi-preparative run can be determined: Subtracting the injection time (2.5 min) from t_R and determining the corresponding H_2O and acetonitrile concentrations gave the values for the starting point. For the end point 3.5% were added to the acetonitrile concentration (see Tab. **19**). During this time fractions corresponding to 0.25 – 1 min were collected.[138]

Tab. 19: Solvent gradient of the semi-preparative run.

time/ min	H_2O, 0.1% TFA / %	acetonitrile, 0.1% TFA/ %	flow rate / mL/min
0	95	5	6.000
5	95	5	6.000
35	Starting point		6.000
70	End point		6.000
80	5	95	6.000
90	5	95	6.000
95	95	5	6.000
105	95	5	6.000

The collected fractions were tested for purity using HPLC-ESI-MS, either with the analytical run (see Tab. **18**) or a longer, 60 min run.

Tab. 20: Solvent gradient of the longer analytical run.

time/ min	H_2O, 0.1% TFA / %	acetonitrile, 0.1% TFA/ %	flow rate / mL/min
0	95	5	1.000
2.5	95	5	1.000
45	40	60	1.000
50	5	95	1.000
53	5	95	1.000
58	95	5	1.000
60	95	5	1.000

Pure fractions were combined and lyophilized.

The purification of protected peptides had an acetonitrile concentration of at least 50% to prevent peptide precipitation. As the gradients vary depending on the fragments, details can be found in the Appendix (see Tab**. 27** and Tab**. 32**).[84]

4.2 Bacterial Expression in *E. coli*

The cloning and bacterial expression of proteins was done in cooperation with the group of Prof. Dr. Axel Scheidig. Additional bacterial expression was just carried out in cases where protein was depleted.

Furthermore a protocol for the bacterial expression of labeled proteins in minimal medium was adapted from the European Molecular Biology Laboratory, Heidelberg. A general overview over the protocols for bacterial expression will be given in the following chapters.

4.2.1 Protein Expression

Protein expression was induced by adding isopropyl β-D-1-thiogalacto-pyranoside (IPTG) to the cells in the culture medium after they reached an optical density at 600 nm (OD_{600}) of 0.6-0.8. The plasmids used for cloning all contain the *lac operon* and *lacI* next to the origin of replication, multiple cloning site, selection marker and other genes. The *lac operon* encodes for the transport of lactose into the cell and its metabolism. In the absence of lactose *LacI* inhibits the *lac operon* as a repressor. When lactose becomes available it is converted into allolactose which in turn inhibits the *LacI* repressor resulting in the transcription of the genes on the *lac operon*. IPTG is a structural analogue of allolactose which can inhibit the repressor but cannot be metabolized. Furthermore, the T7 RNA Polymerase, which is chromosomally encoded in the *lacUV5 operon*, can be regulated by the *LacI repressor* and is induced with IPTG.

After induction and incubation, the cells were harvested, disrupted and the proteins purified using affinity chromatography. As the proteins were expressed containing an N-terminal *Small ubiquitin modifier* (SUMO) tag, the targeted cleavage of the SUMO tag at the correct position before the starting aspartate of the IBTC was performed using SUMO protease (see chapter 4.2.2.1) and again purified by affinity chromatography. If necessary an additional purification step with high performance liquid chromatography was performed (see chapter 4.1.5).

4.2.1.1 SUMO Protease

The bacterial expression of the SUMO protease was done according to literature.[93]

4 L of Luria-Bertani (LB) medium (50 µg/mL kanamycin) were equally distributed in two 5 L Erlenmeyer flasks with baffles and a suspension of cells added to an OD_{600} of ~0.1. After

incubation of the cell culture at 37 °C and 80 rpm to an OD_{600} of 0.6, IPTG was added to a final concentration of 0.2 mM. The cells were incubated for another 3 h at 30 °C and then harvested. After washing them twice with PBS buffer (10 mM Na_2HPO_4, 1.8 mM KH_2PO_4, pH 7.4, 150 mM NaCl), the harvested cells were frozen in liquid nitrogen and stored at -80 °C.

4.2.1.2 SUMO fusion proteins

To 2 L of LB medium (50 µg/mL kanamycin) in a 5 L Erlenmeyer flasks with baffles, a suspension of cells was added to an OD_{600} of ~0.1. After incubation of the cell culture at 37 °C and 80 rpm to an OD_{600} of 0.6, IPTG was added to a final concentration of 1 mM to induce protein expression. The cells were incubated over night at 25 °C and then harvested. After washing them twice with PBS buffer (10 mM Na_2HPO_4, 1.8 mM KH_2PO_4, pH 7.4, 150 mM NaCl), the harvested cells were frozen in liquid nitrogen and stored at -80 °C. [139]

4.2.1.3 Minimal Medium

For the expression of ^{15}N labeled proteins the protocol was performed using minimal medium instead of LB medium. The composition of the minimal medium was derived from the European Molecular Biology Laboratory (EMBL). The ingredients are listed in Tab. 21.

Tab. 21: Composition of minimal medium.

Medium A (1 L)	10x M9 medium (1 L)	100x trace element solution (1 L)
100 mL 10x M9 medium	60 g Na_2HPO_4	5 g EDTA
10 mL 100x trace element solution	30 g KH_2PO_4	0.83 g $FeCl_3$ x 6 H_2O
20 mL 10% (w/v) glucose	5 g NaCl	84 mg $ZnCl_2$
1 mL 1 M $MgSO_4$	5 g $^{15}NH_4Cl$	13 mg $CuCl_2$ x 2 H_2O
0.3 mL 1 M $CaCl_2$		10 mg $CoCl_2$ x 6 H_2O
1 mL 1 mg/mL biotin		10 mg H_3BO_3
1 mL 1 mg/mL thiamine		1.6 mg $MnCl_2$ x 6 H_2O
Appropriate antibiotic		

4.2.1.4 Cell Disruption

The cell pellets were defrosted and resuspended in buffer (see Tab. 22) at a 1:10 (w/v) ratio. The physical cell disruption was done using an Avestin EmulsiFlex C3 at 1000 – 1500 bar and 4 °C. After centrifugation at 10 °C and 75600 rpm for 45 min the supernatant was taken and purified using affinity chromatography as specified in chapter 4.2.2.1.

Tab. 22: Composition of the resupension buffers.

Sumo protease	SUMO fusion proteins
50 mM HEPES, pH 7.4	300 mM NaCl
100 mM NaCl	50 mM NaH_2PO_4, pH 4.5
1 mM PMSF	1 mM PMSF
0.2 µg/mL DNAse	0.2 µg/mL DNAse

4.2.2 Biochemical Methods

4.2.2.1 Affinity Chromatography

The purification of the proteins from the supernatant of the physical cell disruption was done using Ni^{2+}-nitrilotriacetic acid agarose chromatography. The SUMO protease as well as the SUMO fusion proteins contain a His-tag, the later at the N-terminus. Proteins with His-tag bind on the column while impurities are washed off. The elution buffer contains a high concentration of imidazole which is a structural analog to the histidine side chain and competitively interacts with the nickel ions of the stationary phase.

Before the purification of the proteins with a fast protein liquid chromatography (FPLC) at 8 °C and a 5 mL HisTrap HP column the column was equilibrated with buffer until the base line absorption at 280 nm was constant. The sample was loaded on the column and, after a washing step with equilibration buffer, non-specifically bound impurities were removed with 5% of elution buffer. By applying a gradient of 5 - 100% elution buffer the sample was eluted and collected in fractions of 2 mL.

The fractions of SUMO protease were tested for purity via SDS-PAGE (see chapter 4.2.2.3). Pure fractions were combined, their concentration determined using a nanophotometer and frozen in liquid nitrogen in 200 – 500 µL aliquots. The storage was at -80 °C.

The pure fractions of SUMO fusion protein were combined and concentrated using Amicon Ultra-15 Centrifugal Filters 10.000 nominal molecular weight limit (NMWL)/3.000 NMWL and rebuffered to 50 mM Tris, pH 8, 20 mM NaCl, 5 mM DTT with a 5 mL HiTrap Desalting column. The concentration was determined using a nanophotometer. For the proteolytic cleavage of the SUMO tag, SUMO protease was added at a ratio of 1:100 and incubated for 1 h at 37 °C and 600 rpm. The purification via affinity chromatography yields the protein as eluent at the beginning as it no longer binds to the column. The fractions were combined and their concentration determined using a nanophotometer.

Tab. 23: Equilibration and elution buffers of the different proteins.

SUMO protease		**SUMO fusion proteins**	
Equilibration buffer	Elution buffer	Equilibration buffer	Elution buffer
50 mM HEPES, pH 7.4	50 mM HEPES, pH 7.4	50 mM NaH_2PO_4, pH 4.5	50 mM NaH_2PO_4, pH 4.5
100 mM NaCl	100 mM NaCl	300 mM NaCl	300 mM NaCl
	500 mM imidazole		500 mM imidazole

4.2.2.2 High performance liquid chromatography (HPLC)

All proteins with a molecular weight below 5 kDA cannot be concentrated by centrifugation with the above mentioned centrifugal filters or analyzed with SDS-PAGE. Thus the proteins were tested for purity using HPLC and ESI-MS. If necessary an additional purification step with high performance liquid chromatography was performed.

4.2.2.3 SDS-PAGE

The sodium dodecyl sulfate-polyacrylamide gel electrophoresis (SDS-PAGE) allows the separation of proteins by size. Consequently, the presence and purity of a sample can be tested. For the analysis 12% SDS-PAGE were prepared (see Tab. 24).

Tab. 24: Layout of materials for 12% SDS-PAGE gels.

Materials	12% separation gel	5% stacking gel
ddH_2O	1.65 mL	690 µL
1.5 M Tris-HCl, pH 8.8, 0.4% SDS	1.3 mL	-
1 M Tris-HCl, pH 6.8, 0.4% SDS	-	20 µL
10% APS	100 µL	2 µL
TEMED	4 µL	170 µL
Rotiphorese-Gel 30 (37,5:1)	2 mL	130 µL

The samples were prepared by mixing 6 µL of sample with 2 µL of 4x Laemmli buffer (40% glycerol, 240 mM Tris-HCl, pH 6.8, 8% SDS, 0.04% bromophenol blue, 5% β-mercaptoethanol) and heating to 95 °C for 5 min. The gel was loaded with 5 µL sample each and the gel electrophoresis performed at 250 V for 25 min in SDS running buffer (25 mM Tris, 0.2 M glycine, 0.1% SDS).

For the visualization the SDS was removed from the gel by heating in water and incubating 15 min at room temperature. The staining was done over night with colloidal Coomassie CBB G-250 (0.02% CBB G-250, 5% aluminium sulfate octahydrate, 10% of 96% Ethanol, 2% of 85% phosphoric acid).[36]

4.2.2.4 Regeneration of the column

After each purification the 5 mL HisTrap HP column was regenerated by first washing the column with bidestilled water (ddH_2O) then applying stripping and binding buffer, separated by a second washing step, adding Ni^{2+} as a chloride salt and storing the column in 20% ethanol (see Tab. **25**).

Tab. 25: Regeneration of the HisTrap HP column.

buffer	**volume**
ddH_2O	3 CV
Stripping Buffer (20 mM NaH_2PO_4, 0.5 M NaCl, 50 mM EDTA, pH 7.4)	5 CV
ddH_2O	3 CV
Binding Buffer (20 mM Tris-HCl, 0.5 M NaCl, 20 mM imidazole, pH 7.4)	5 CV
ddH_2O	3 CV
0.1 M $NiCl_2$	0.5 CV
ddH_2O	3 CV
Ethanol (20%)	3 CV

4.3 Other used Methods, Materials and Instruments

4.3.1 Chemicals and Materials

All chemicals were purchased from abcr, Acros Organics, Alfa Aesar, AppliChem, BCD Chemie, Biesterfeld, Cambridge Isotope Laboratories, Carbolution Chemicals, ChemPep, Deutero, Eurisotop, Grüssing, Honeywell, Iris, Merck, Nippon Genetics, Novabiochem, Roth, Serva, Sigma-Aldrich, TCI, Ted Pella Inc., VWR. Solvents for peptide synthesis were purified by distillation before use, except for *N,N*-dimethylformamide which was ordered low in water. Solvents for HPLC were purchased as HPLC grade solvents.

Consumables were purchased from Hassa, Merck Millipore, neolab, Roth, Sarstedt.

4.3.2 Peptide Synthesis

Fmoc-based solid phase peptide synthesis was performed on a microwave-assisted, semi-automated peptide synthesizer *Initiator*$^{+}$ *SP Wave* by Biotage version 4.1.1.

4.3.3 Lyophilizer

Lyophilization of the samples was done with a lyophilizer Alpha 2-4 by Martin Christ and a RZ6 vacuum pump by Vacuubrand and a typical vacuum of 0.1 mbar.

4.3.4 HPLC

The high performance liquid chromatography was performed with a LaChrom Elite by VWR-Hitachi with a L2400 UV-detector. Analysis and purification was achieved by reversed phase column with a stationary phase of poly(styrene-divinylbenzene) (PLRP-S) with a particle size of 8 µm and a pore diameter of 30 nm by Agilent Technologies. The dimensions for the analytical column are 150 mm x 4.6 mm and for the semi-preparative 325 mm x 30 mm. For detection of the molecules, an UV detector at λ = 220 nm was used. An automated fraction collector Foxy® R1 by Teledyne Isco and an autosampler 717-Plus by Waters are connected to the HPLC.

The program used to operate the HPLC and fraction auto-collector is EZChrom SI version 3.3.2 SP2.

4.3.5 Mass Analysis

The molecular mass of the synthesized proteins was determined by either an electron spray ionization mass spectrometer (ESI MS) connected to the HPLC, Expression-L CMS by Advion with a hexapol as separator, manually by matrix-assisted laser desorption ionization (MALDI) with a time of flight (ToF) mass separator, Biflex III by Bruker, or a hybrid quadrupole-orbitrap mass spectrometer, Q Exactive Plus 2.8 by Thermo Scientific.

As matrix for MALDI-ToF, (*E*)-2-cyano-3-(4-hydroxyphenyl)prop-2-enoate was employed.

The program for operation of the directly to the HPLC connected ESI-MS is Advion Mass Express version 2.0.50.9 and Advion Data Express version 2.0.45.4 for analysis of the spectra. The MALDI-ToF is operated by Bruker Daltonics flexControl version 3.0 and the Q Exactive Plus by tune version 2.8 and with licenses Enhanced Resolution Unlimited and Protein Mode Unlimited.

4.3.6 Bacterial expression

For bacterial expression the bacterial strain *E. coli BL21 Gold (DE3)* with the following genotype B, F^-, *ompT, hsdS*($r_B^- m_B^-$), *dcm*$^+$, Tet^r, *gal* λ(DE3), *endA,* Hte from Agilent Technologies was used.

Plasmids from the group of Prof. Dr. Axel Scheidig (based on pETM11-SUMO3GFP by Huseyin Besir, EMBL) were used. pET28a-SENP2 (catalytic domain) was a gift from Guy Salvesen (Addgene plasmid # 16357 ; http://n2t.net/addgene:16357 ; RRID:Addgene_16357).[93]

4.3.7 Incubator

The incubation of cell culture medium was carried out using a Multitron by Infors Hat. For the incubation during the proteolytic cleavage a Thermomixer comfort by Eppendorf was used.

4.3.8 Centrifuges

For cell harvesting or after cell disruption a Heraeus Multifuge 3SR+ centrifuge by Thermo Fisher Scientific or an Avanti J-26 XP by Beckman Coulter were used. During SPPS, protein precipitation was facilitated by an EBA 20 by Hettich.

4.3.9 Cell disruption

The cells were physically disrupted using an EmulsiFlex-C3 from Avestin.

4.3.10 ÄKTA

The purification and desalting of proteins from the bacterial expression was done using an ÄKTA-FPLC by GE Healthcare. It was operated by the program Unicorn 5.31.

The columns, HisTrap HP 5 mL and HiTrap Desalting 5 mL, were also from GE Healthcare.

4.3.11 SDS-PAGE

Sodium dodecyl sulfate-polyacrylamide gel electrophoresis was performed with a Mini-PROTEAN Tetra System equipped with a voltage unit Power Pac 300 both by Bio-Rad. Documentation of the gels was done on a light plate FastGene White Light Plate by Nippon Genetics using a Penta Mix-1 digital camera by Ricoh Imaging.

4.3.12 pH Measurements

The determination of the pH of samples and for buffer preparation was performed with either a pH 526 by WTW for buffers or a pH meter 320 by Corning for protein samples. If necessary, a calibration step was performed before the pH measurements.

4.3.13 Protein Concentration Determination

The concentration of protein samples with an extinction coefficient of ε_{280} >10000 $M^{-1}cm^{-1}$ was done with a nanophotometer P300 by Implen. All other protein concentrations were determined using UV/vis spectroscopy.

4.3.14 UV/vis Spectroscopy

UV/vis spectra were recorded on a Lambda 14 two channel spectrometer by PerkinElmer. It is equipped with a thermostat E100 by Lauda and operated by UV WinLab, 2.80.03. All measurements were performed in quartz cuvettes with a path length of 10 mm by Hellma Analytics at 25 °C ±0.1 °C. Measurements were performed under the same conditions and with the same stock solution as the CD measurements.

The extinction coefficients for all proteins can be found in Tab**. 26**.

4.3.15 CD Spectroscopy

CD spectra were recorded on a Jasco J-720 spectropolarimeter. The temperature was controlled with a thermostat WKL 26 by Haake and a PTC-423S Peltier element by Jasco. All measurements were performed in quartz cuvettes with a path length of 1 mm by Hellma Analytics. The lower limit of the spectra was tested manually as the voltage should not exceed 700 V as the data becomes unreliable. Spectra were recorded with protein samples of ~0.1 mg/mL concentration, with a data pitch of 2 nm and a scanning speed of 5 nm/min. Accumulation of three repeats and subtraction of the background signal gave the final spectrum. The instrument was operated with the program Spectra Manager for Windows 95/NT version 1.53.00.

The resulting signal is converted to mean residue ellipticity $[\Theta]_{MR}$,

$$[\Theta]_{MR} = \frac{100 \cdot \Theta}{c \cdot l \cdot n}$$

with *Θ* the measured CD signal, *c* the concentration in mol/L, *l* the path length of the cuvette and *n* the number of residues.

Calculations were performed with the program OriginPro 2016, version b9.3.206. Curves were smoothed using the method *Salvitzky-Golay* with 5 points of window and a polynomial order of 2.

Thermal denaturation curves were recorded starting at 1 °C to 61 °C with a temperature slope of 1 °C/min and a data pitch of 2 °C followed by a reverse temperature scan. The melting point was either estimated visually or calculated with the above mentioned program employing an unconstrained fitting using a sigmoidal Boltzmann function and a Levenberg-Marquardt iteration algorithm.

The signal at 222 nm is usually taken to quantify the helical content, using the following formula:

$$Helical\ content = 100 \cdot \frac{[\Theta]_{obs}}{[\Theta]_{ref}}$$

with $[\Theta]_{ref}$ at 222 nm for a 100% folded helix calculated by

$$[\Theta]_{222} = \left(1 - \frac{1}{n}\right) \cdot (-44.000 + 250 \cdot T)$$

Where *n* is the number of residues and *T* the temperature in °C.[104]

4.3.16 NMR Spectroscopy

The NMR spectra were recorded on Fourier transform-NMR (FT-NMR) spectrometers Avance III 600 with a frequency of 600.1 MHz for ^{1}H-, 150.9 MHz for ^{13}C-, and 60.81 MHz for ^{15}N-nuclei and equipped with a triple resonance cryo probe head, as well as a DRX500 spectrometer with a frequency of 500.1 MHz for ^{1}H-, and 125.8 MHz for ^{13}C-nuclei by Bruker. Both spectrometers have a variable temperature unit. As internal standard 4,4-dimethyl-4-silapentane-1-sulfonic acid (DSS) was used for aqueous samples, tetramethylsilane (TMS) with organic solvents. ^{13}C and ^{15}N were referenced indirectly using the IUPAC recommendations for the frequency ratio to ^{1}H. [140] For locking of the aqueous samples 10% D_2O was added. [141]

Chemical shifts are given in ppm. Signal assignment was done based on one-dimensional ^{1}H NMR and two- or three-dimensional NMR spectroscopy, namely ^{1}H,^{1}H-corelated spectroscopy (COSY), ^{1}H,^{1}H-total correlation spectroscopy (TOCSY), ^{1}H,^{1}H-nuclear Overhauser enhancement spectroscopy (NOESY), ^{1}H,^{13}C-heteronuclear single quantum coherence (HSQC), ^{1}H,^{15}N-HSQC,

^{1}H,^{1}H-TOCSY-^{1}H,^{15}N-HSQC and ^{1}H,^{1}H-NOESY-^{1}H,^{15}N-HSQC. Water suppression in the ^{1}H and ^{1}H,^{1}H-correlation spectra was done using an excitation sculpting with gradient pulses (esgp), ^{1}H,^{13}C-HSQC had a presaturation of water and ^{1}H,^{15}N-HSQC a flip-back pulse for water.[142]

The spectra were processed using TopSpin by Bruker. Peak assignments were performed with NMRView version 9.2.0-b11 following the guide of Wüthrich.[143]

4.3.16.1 Chemical Shift Deviation

Calculation of the chemical shift deviation (CSD) was performed using random coils values derived from Wishart and Sykes.[98] The CSD is the difference between the observed (δ_{obs}) and referential random coil (δ_{ref}) chemical shift

$$CSD = \delta_{obs} - \delta_{ref}$$

The CSD is dependent of the secondary structure of the protein. While a Hα CSD <0.1 ppm for a cluster of at least four amino acids of five (if not interrupted by a value >0.1 ppm) is an indication of an α-helical fold, a Hα CSD >0.1 ppm for a cluster of at least three amino acids of four (if not interrupted by a value <0.1 ppm) is on the contrary indicates a β-strand. For Cα CSD a value of >0.7 ppm indicates an α-helix and a CSD of <0.7 ppm a β-strand under the above mentioned conditions.[99]

The proton shifts of Hα' of G11, Hβ' of P18 as well as Hδ and Hδ' of P19 in the Trp-cage are sequence corrected random coil values from Lin *et al*., which are 4.02, 2.29, 3.59 and 3.74 ppm, respectively.[75,144]

4.3.17 Ice Activity Measurements

Thermal hysteresis and ice growth retardation measurements were performed using a nanoliter osmometer by Clifton equipped with a Peltier element cooling station which is cooled to 10 °C with glycol as thermal fluid by a Ministat 230 by Huber. The cooling station is mounted on an Eclipse NI microscope with a D7000 camera by Nikon. Pictures were recorded with a 50x magnification with the Camera Control Pro 2 version 2.23.0 software by Nikon.

The sample holder's bores have a diameter of 200 µm. Before loading the sample, the bores were filled with high viscosity immersion oil (type B). Utilizing a glass capillary connected to a Hamilton syringe, a nanoliter sized drop was placed in the middle of the bore without touching the

surrounding metal. The sample was flash frozen to -40 °C. Careful heating gave just one single ice crystal. For thermal hysteresis measurements the temperature was decreased constantly at 30 or 40 mOs/min until the ice crystal burst at the tips.

For samples which do not show a burst point, ice growth retardation was determined by first decreasing the temperature and then measuring the correlating growth rate *v* (µm/s) of the ice crystal over time. For every sample at least 10 different temperatures were evaluated. A plot of the crystal growth rate against the temperature shows the ice growth retardation for the first several low decreases in temperature and then a rapid rise in crystal growth. By plotting two linear regressions through the correlating data points and determining their intersection the ice growth retardation was determined. It is important to mention that the observable ice crystals show a hexagonal shape thus enabling a measurement from opposing edge-to-edge or tip-to-tip. As the antifreeze protein binds to the edge a correction of values derived from tip-to-tip measurements by cos(30°) is necessary (see Fig. 61).[46,112], (K. Bamberg, Masters thesis)

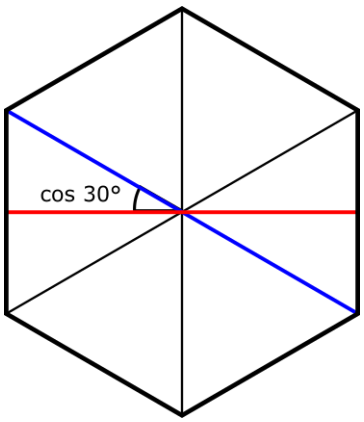

Fig. 61: Schematic representation of the top view of a hexagonal ice crystal. To evaluate its size a measurement from tip-to-tip (blue) or edge-to-edge (red) is possible.

The measurements were done with Adobe Photoshop CS6 version 13.0 and the plotting and calculations with OriginPro 2016 version b9.3.206.

As internal reference for the size of the ice crystal, the diameter of the bore was used. A freezing point depression of 1000 mOs corresponds to 1.86 °C.[22]

4.3.18 Molecular Modelling

All structures presented in this work were prepared starting from the first structure of the NMR ensembles of Tc10b by Barua *et al.* (PDB entry: 2JOF).[69] They were prepared and extended using Schrödingers Maestro version 11.4.011[145] while energy minimizations were performed with Schrödingers MacroModel.[146] As a potential *Optimized Potentials For Liquid Simulations* (OPLS3) with the solvent water was chosen.[147–150] The charges were set as in the force field and an extended cutoff for the non-bonded interactions. The energy minimization followed the Polak-Ribiere conjugate gradient (PRCG) method with a maximum of 2500 iterations and a gradient convergence.[151]

Pictures of proteins and protein models were rendered by PyMol Molecular Graphics System version 2.1.1.[152]

4.3.19 Calculation of Absorption Coefficient and Molecular Weight

Calculation of the molecular weight and absorption coefficient ε_{280} was done with ExPASY's ProtParam by the Swiss Institute of Bioinformatics.[153]

Tab. 26: Absorption coefficients and molecular weight of some peptides.

	MW/Da	**ε_{280}/ $M^{-1}cm^{-1}$**
(jg)IBTC-1	2620.68	6990
(jg)IBTC-1-GFP	29412.96	28880
(jg)IBTC-2	3517.68	6990
(jg)IBTC-2-GFP	30309.96	28880
(jg)-IBTC-3	4529.81	6990
(jg)IBTC-3-GFP	31322.09	28880
(jg)IBTC-4	3355.68	6990
(jg)SUMO-IBTC-1	14968.52	11460
(jg)SUMO-IBTC-1-GFP	41847.87	33350
(jg)SUMO-IBTC-2	15865.52	11460
(jg)SUMO-IBTC-2-GFP	42744.87	33350
(jg)SUMO-IBTC-3	16877.65	11460
(jg)SUMO-IBTC-3-GFP	43757.00	33350
1repeat	1029.55	28200*/9763^{+}
SUMO protease	31111.52	41160
Tc10bKKA	2127.35	6990

* ε_{205} [154]/$^{+}$ ε_{214} [155]

5 Appendix

In this chapter, the synthesis, purification (HPLC- and ÄKTA-profiles), mass spectra (MALDI or ESI), UV/vis, CD and NMR spectra as well as ice activity data of all substances are presented. Spectra presented above are recurring with new numbering to enable a quick and focused overview over all experimental data. Additionally, the proton, carbon and nitrogen chemical shifts of all peptides as well as the corresponding CSD plots, and Fraction Folded values are listed.

5.1 Tc10bKKA as fragment on Wang resin

Sequence [78]	DKYAQWLADGGPSSGRPPPK
Molecular weight	2127.32 g/mol
Absorption coefficient	ε_{280}= 6990 $M^{-1}cm^{-1}$
Peptide amount	0.4 g / 0.188 mmol
Resin type	Wang
Resin loading capacity	0.85 mmol/g
Resin amount	220 mg
Capping	acetic anhydride, pyridine, dimethylformamide (1/1/2)

	Double Coupling	Single Coupling	
HATU (4.9 eq, g)	0.700	0.350	
DIPEA (10 eq, mL)	0.655	0.328	
Amino acids (5 eq, g)			
K		0.440	
Capping			
P		0.317	
P		0.317	
P		0.317	
R		0.610	Extended deprotection
G	0.559		
S		0.360	
S		0.360	
P		0.317	
G	0.559		Extended deprotection
DG		0.582	
A		0.293	
L	1.329		
W		0.495	
Q		0.574	
A	0.585		
Y		0.432	
K	0.881		
D		0.387	

Yield 611.4 mg dry resin with Tc10bKKA fragment

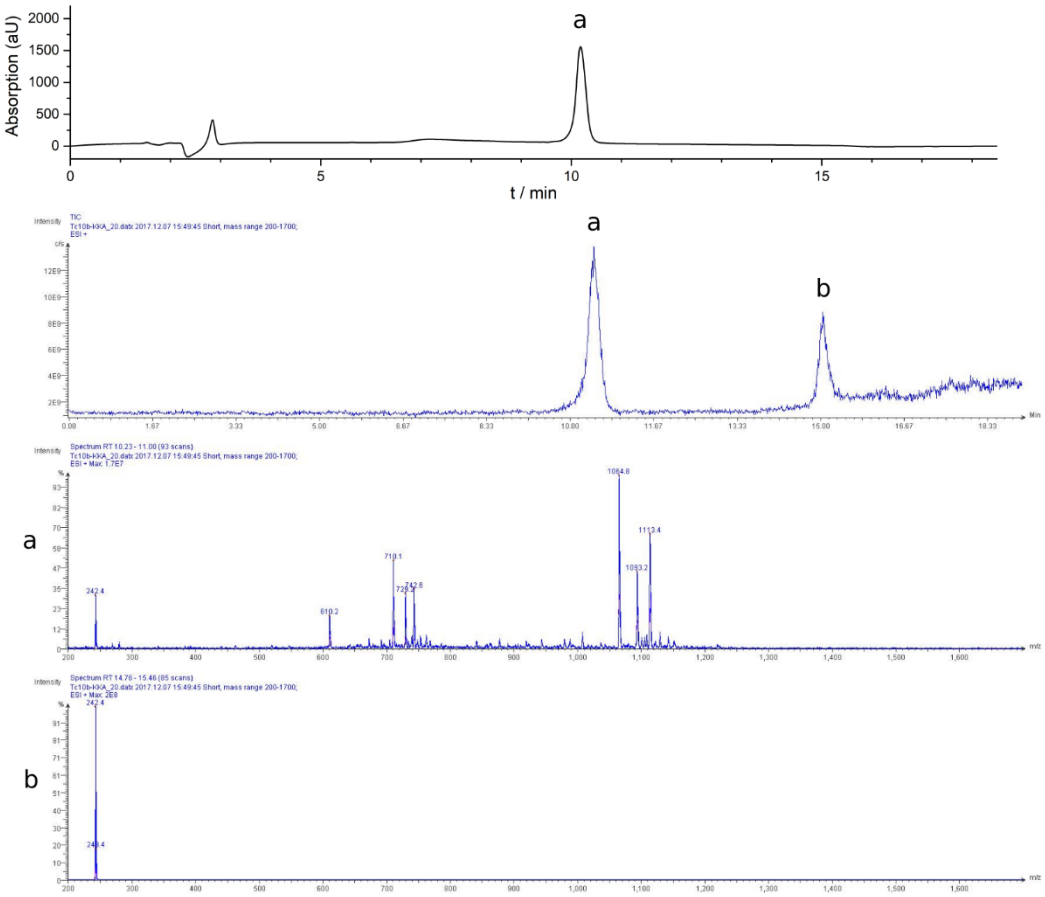

Fig. 62: HPLC profile of the analytical run (top), ion chromatogram (2nd panel from top) and MS spectra of all signals of purified Tc10bKKA. *m/z*: $[M+2H]^{2+}$ calcd 1065, found 1064.8; $[M+3H]^{3+}$ calcd 710.1, found 710.1. t_R is 10.1 min.

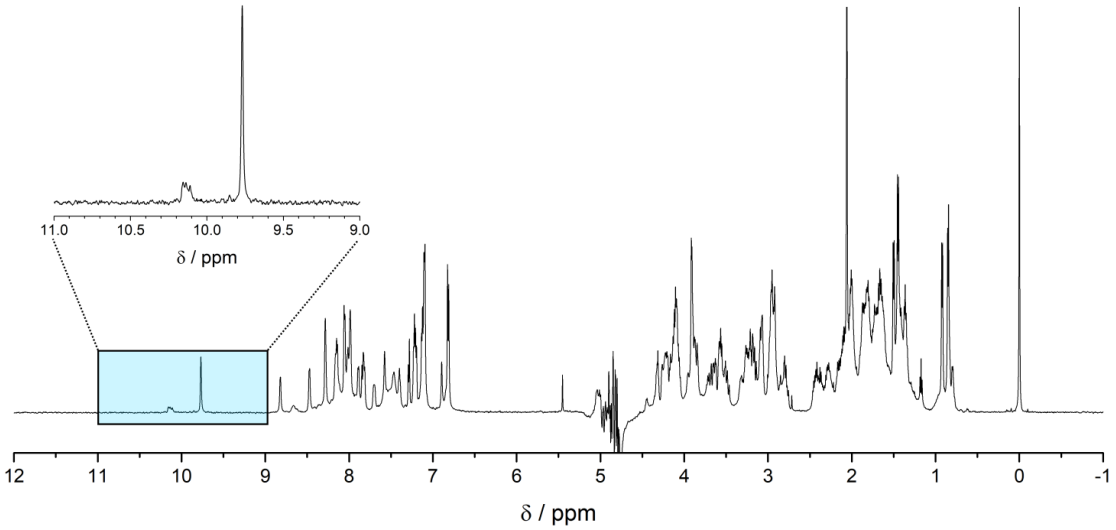

Fig. 63: ^{1}H NMR spectrum of Tc10bKKA in H_2O/D_2O, pH 3, at 300 K with enlargement of the indole proton region around 10 ppm.

5.2 2repeat-pg

Sequence	Fmoc-AAN(Trt)AAAAAAAT(*t*Bu)-OH
Molecular weight	1393.61 g/mol
Peptide amount	0.38 g / 0.273 mmol
Resin type	2-Chlorotrityl chloride
Resin loading capacity	0.71 mmol/g
Resin amount	396 mg
Capping	acetic anhydride, pyridine, dimethylformamide (1/1/2)

		Single Coupling	
HATU (4.9 eq, g)		0.508	
DIPEA (10 eq, mL)		0.475	
Amino acids (5 eq, g)			
	T (2 eq, g)	0.216	See 4.1, no deprotection
	T	0.540	See 4.1, Capping
	A	0.423	Capping
	A	0.423	Capping
	A	0.423	Capping
	A	0.423	Capping
	A	0.423	Capping
	A	0.423	Capping
	A	0.423	Capping
	N	0.811	
	A	0.423	Capping
	A	0.423	No deprotection, capping

Yield 11.4 mg (4%)

Tab. 27: Solvent gradient of the semi-preparative run of 2repeat-pg. Fractions were collected from 65 – 85 min.

time/ min	**H_2O, 0.1% TFA / %**	**acetonitrile, 0.1% TFA/ %**	**flow rate / mL/min**
0	50	50	6.000
5	50	50	6.000
90	37	63	6.000
100	5	95	6.000
110	5	95	6.000
115	50	50	6.000
130	50	50	6.000

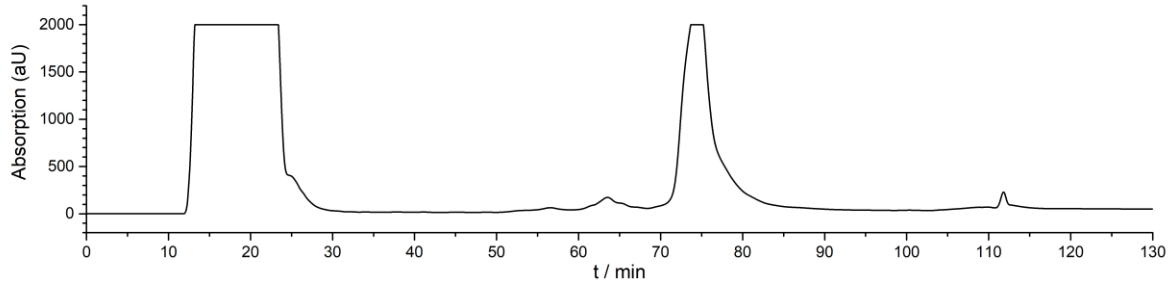

Fig. 64: HPLC profile of the semi-preparative run of 2repeat-pg. t_R is 75 min.

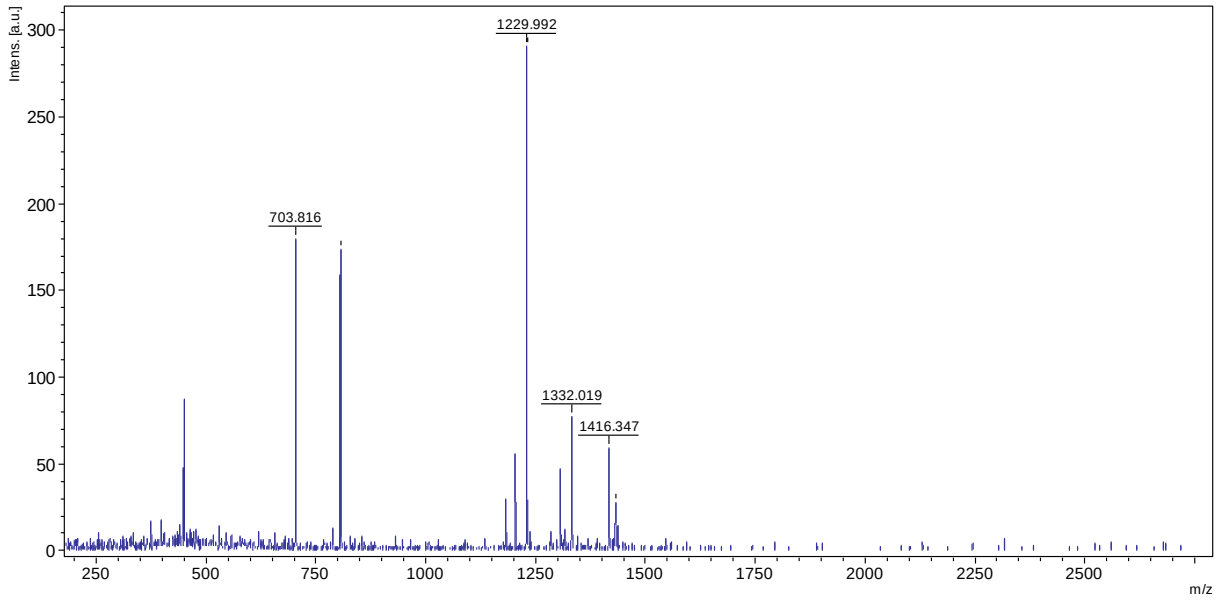

Fig. 65: Ion chromatogram of purified 2repeat-pg. *m/z*: $[M+Na]^+$ calcd 1417, found 1416.3.

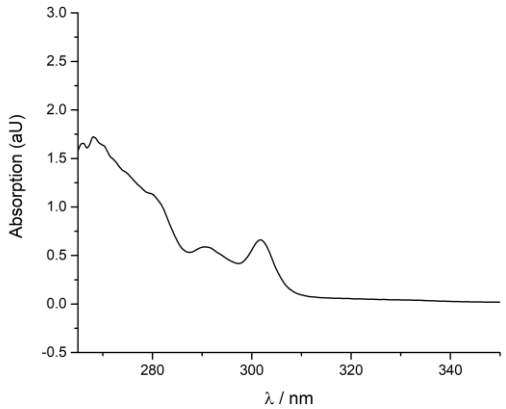

Fig. 66: UV/vis spectrum of 2repeat-pg in dimethyl sulfoxide-d_6 at 298 K. The spectrum was measured to 600 nm, displayed only to 350 nm.

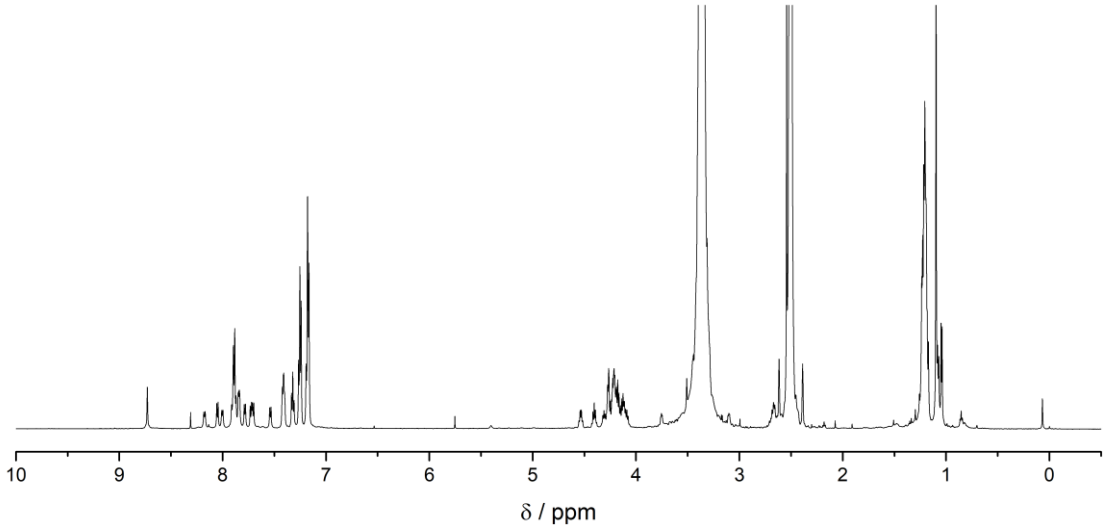

Fig. 67: ^{1}H NMR spectrum of 2repeat-pg in dimethyl sulfoxide-d_6 at 298 K.

Tab. 28: ^{1}H-chemical shifts of 2repeat-pg in dimethyl sulfoxide-d_6 at 298 K.

Residue		Chemical shift δ (ppm)				
		NH	α	β	γ	
1	Ala	7.538	4.087	1.192		
2	Ala	8.003	4.310	1.219		
3	Asn	8.176	4.533	2.672		δ 7.539, 7.074
4	Ala	7.891	4.165	1.205		
5	Ala	7.907	4.138	1.076		
6	Ala	7.842	4.223	1.176		
7	Ala	7.907	4.138	1.076		
8	Ala	7.842	4.223	1.176		
9	Ala	7.875	4.259	1.215		
10	Ala	8.051	4.404	1.212		
11	Thr	7.413	4.218	4.118	1.212	

Tab. 29: ^{1}H-chemical shifts of the protecting groups of 2repeat-pg in dimethyl sulfoxide-d_6 at 298 K.

Residue		Chemical shift δ (ppm)
1	Fmoc-Ala	7.887 (d) (2H, *H*-1), 7.717 (q) (2 H, *H*-4), 7.410 (m) (2 H, *H*-2), 7.322 (t) (2 H, *H*-3)
3	Asn(Trt)	7.251 (t) (6 Ar-H), 7.178 (t) (9 Ar-H)
11	Thr(*t*Bu)	1.096 (s) (9 H)

Tab. 30: ^{15}N and ^{13}C-chemical shifts of 2repeat-pg in dimethyl sulfoxide-d_6 at 298 K. Shifts marked with an asterix are averaged.

Residue		Chemical shift δ (ppm)				
		^{15}N		Cα	Cβ	
1	Ala			50.33	18.34	
2	Ala	119.16		48.49	18.85	
3	Asn	115.60	δ91.47	50.27	38.58	
4	Ala	118.42*		48.74	18.85	
5	Ala	118.42*		48.85	17.73	
6	Ala	118.42*		48.49	18.34	
7	Ala	118.42*		48.85	17.73	
8	Ala	118.42*		48.49	18.34	
9	Ala	118.42*		48.30	18.85	
10	Ala	119.27		48.23	18.85	
11	Thr	107.64		57.77	67.48	γ 18.85

Tab. 31: ^{15}N and ^{13}C-chemical shifts of the protecting groups of 2repeat-pg in dimethyl sulfoxide-d_6 at 298 K.

Residue		Chemical shift δ (ppm)
1	Fmoc-Ala	120.48 (*C*-1), 125.74 (*C*-4), 128.11 (*C*-2), 127.53 (*C*-3)
3	Asn(Trt)	128.92, 127.86, 126.80
11	Thr(*t*Bu)	28.63

5.3 1repeat-pg

Sequence	Fmoc-AAN(Trt)AK(Boc)AAAE(O*t*Bu)LT(*t*Bu)-OH
Molecular weight	1707.05 g/mol
Peptide amount	0.47 g / 0.275 mmol
Resin type	2-Chlorotrityl chloride
Resin loading capacity	0.71 mmol/g
Resin amount	396 mg
Capping	acetic anhydride, pyridine, dimethylformamide (1/1/2)

		Single Coupling	
HATU (4.9 eq, g)		0.513	
DIPEA (10 eq, mL)		0.479	
Amino acids (5 eq, g)			
	T (2 eq, g)	0.219	See 4.1, no deprotection
	T	0.547	See 4.1, Capping
	L	0.487	
	E	0.586	
	A	0.429	Capping
	A	0.429	Capping
	A	0.429	Capping
	K	0.645	
	A	0.429	Capping
	N	0.821	
	A	0.429	Capping
	A	0.429	No deprotection, capping

Yield 38 mg (14%)

Tab. 32: Solvent gradient of the semi-preparative run of 1repeat-pg. Fractions were collected from 135-170 min.

time/ min	**H_2O, 0.1% TFA / %**	**acetonitrile, 0.1% TFA/ %**	**flow rate / mL/min**
0	50	50	6.000
5	50	50	6.000
140	30	70	6.000
150	5	95	6.000
170	5	95	6.000
180	50	50	6.000
200	50	50	6.000

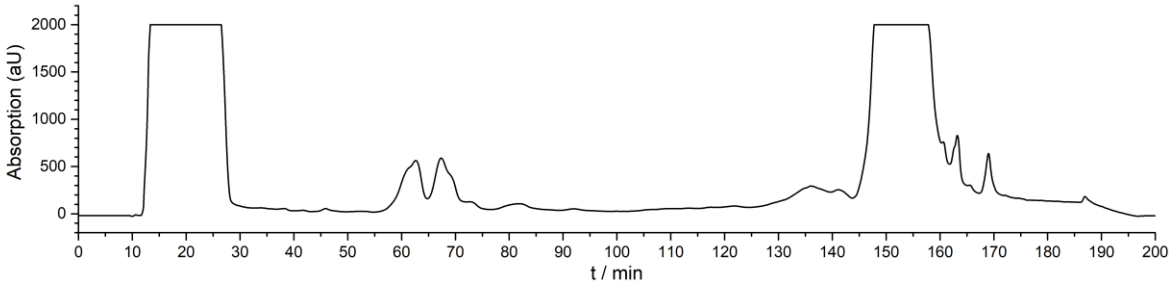

Fig. 68: HPLC profile of the semi-preparative run of 1repeat-pg. t_R is 157 min.

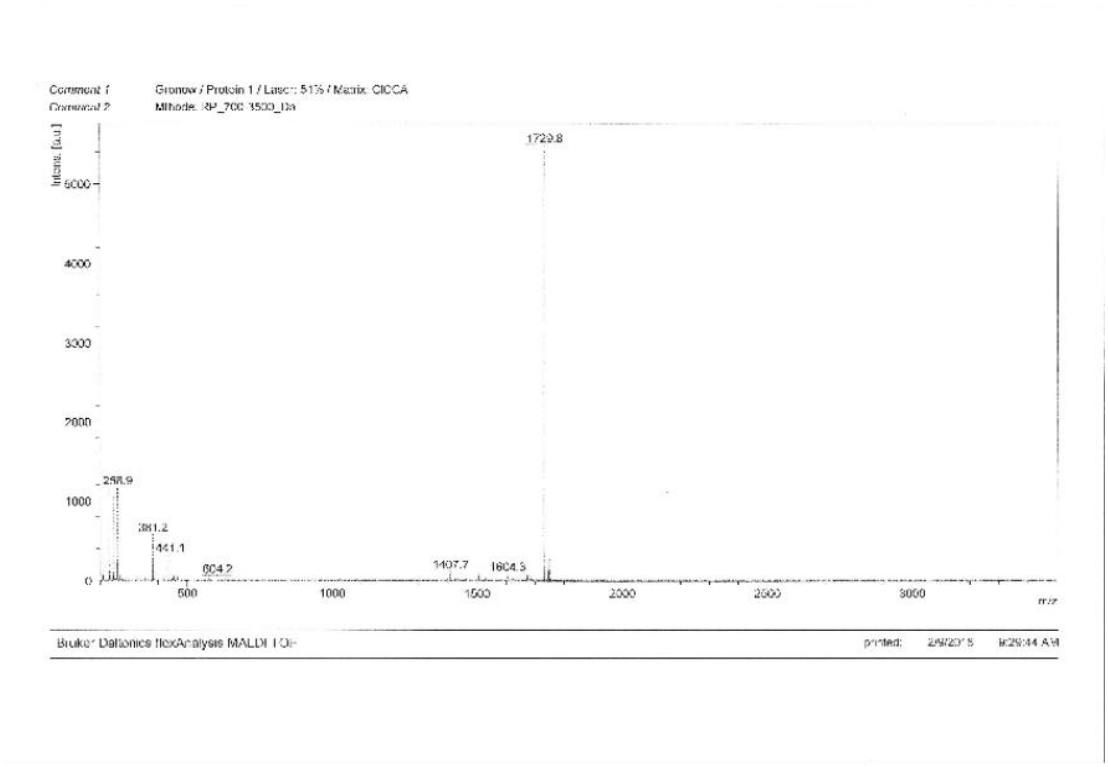

Fig. 69: Ion chromatogram of purified 1repeat-pg. *m/z*: $[M+Na]^+$ calcd 1730, found 1729.8.

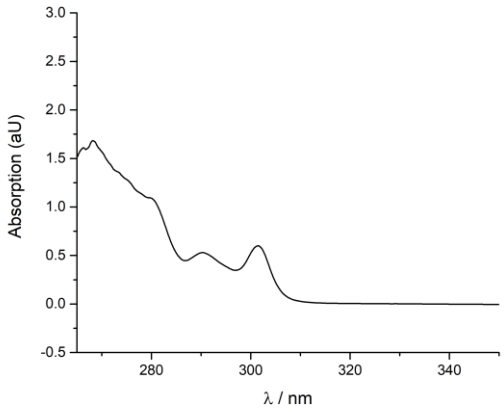

Fig. 70: UV/vis spectrum of 1repeat-pg in dimethyl sulfoxide-d_6 at 298 K. The spectrum was measured to 600 nm, displayed only to 350 nm.

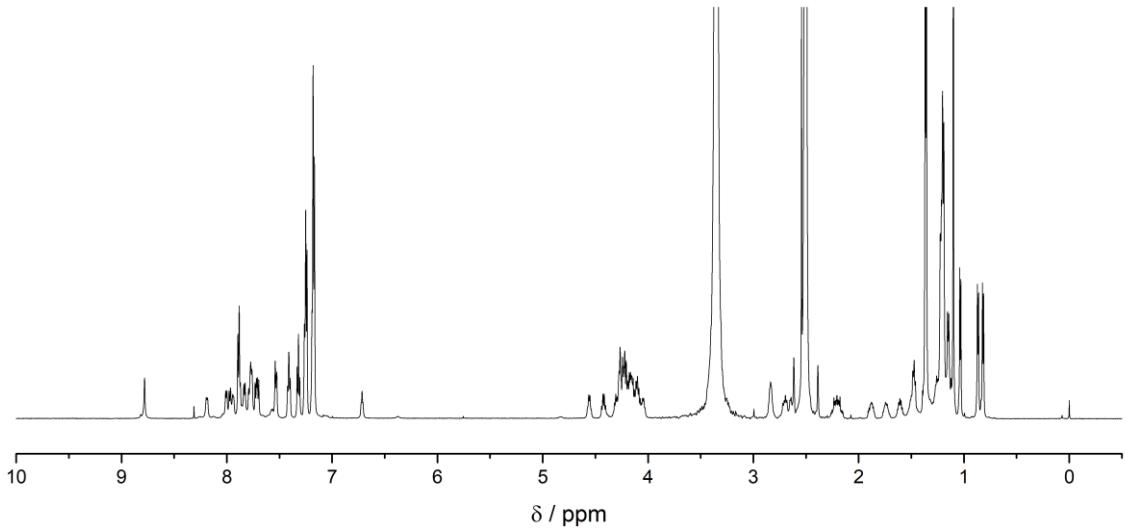

Fig. 71: ^{1}H NMR spectrum of 1repeat-pg in dimethyl sulfoxide-d_6 at 298 K.

Tab. 33: ^{1}H-chemical shifts of 1repeat-pg in dimethyl sulfoxide-d_6 at 298 K.

Residue		Chemical shift *δ* (ppm)				
		NH	α	β	γ	
1	Ala	7.517	4.226	1.194		
2	Ala	7.995	4.300	1.214		
3	Asn	8.172	4.555	2.698, 2.638		δ 7.518, 7.016
4	Ala	7.945	4.146	1.219		
5	Lys	7.748	4.036	1.502, 1.322	1.510	δ 1.189 ε 6.694
6	Ala	7.864	4.166	1.195		
7	Ala	7.754	4.129	1.146		
8	Ala	7.815	4.210	1.199		
9	Glu	7.768	4.260	1.887, 1.752	2.225, 2.225	
10	Leu	7.952	4.407	1.598, 1.598	1.472	δ 0.086
11	Thr	7.516	4.227	4.090	1.034	

Tab. 34: ^{1}H-chemical shifts of the protecting groups of 1repeat-pg in dimethyl sulfoxide-d_6 at 298 K.

Residue		Chemical shift *δ* (ppm)
1	Fmoc-Ala	7.889-7.854 (d) (2H, *H*-1), 7.709 (q) (2 H, *H*-4), 7.407 (t) (2 H, *H*-2), 7.316 (t) (2 H, *H*-3)
3	Asn(Trt)	7.247 (t) (6 Ar-H), 7.150 (t) (9 Ar-H)
5	Lys(Boc)	1.103 (s) (9 H)
9, 11	Glu(O*t*Bu), Thr(*t*Bu)	1.367 (s) (9 H), 1.357 (s) (9 H)

Tab. 35: ^{15}N and ^{13}C-chemical shifts of 1repeat-pg in dimethyl sulfoxide-d_6 at 298 K.

Residue		Chemical shift *δ* (ppm)				
		N		Cα	Cβ	
1	Ala	91.41		51.4	21.14	
2	Ala	118.64		51.32		
3	Asn	115.76	δ 33.21	53.19		
4	Ala	120.59		70.23		
5	Lys	115.77	ε 85.66	56.28		
6	Ala	118.50		51.81		
7	Ala	119.70		53.28		
8	Ala	118.57		49.94	20.89	
9	Glu	114.56		54.66		
10	Leu	118.88		54.01	27.42	γ 43.42 δ 26.49, 24.77
11	Thr	109.70		60.55		γ 23.48

Tab. 36: ^{15}N and ^{13}C-chemical shifts of the protecting groups of 1repeat-pg in dimethyl sulfoxide-d_6 at 298 K.

Residue		Chemical shift δ (ppm)
1	Fmoc-Ala	123.34 (*C*-1), 128.53 (*C*-4), 130.94 (*C*-2), 130.16 (*C*-3)
3	Asn(Trt)	130.76, 131.81, 129.68
5	Lys(Boc)	31.66
9, 11	Glu(O*t*Bu), Thr(*t*Bu)	31.11, 31.66

5.3 1repeat

Sequence	AANAKAAAELT
Molecular weight	1029.55 g/mol
Absorption coefficient	ε_{205}=28200 $M^{-1}cm^{-1}$
	ε_{214}=9763 $M^{-1}cm^{-1}$
Peptide amount	0.12 g / 0.117 mmol
Resin type	Wang
Resin loading capacity	0.86 mmol/g
Resin amount	139 mg
Capping	acetic anhydride, pyridine, dimethylformamide (1/1/2)

	Single Coupling		
HATU (4.9 eq, g)		0.217	
DIPEA (10 eq, mL)		0.203	
Amino acids (5 eq, g)			
	T	0.232	Capping
	L	0.412	
	E	0.248	
	A	0.181	Capping
	A	0.181	Capping
	A	0.181	Capping
	K	0.273	
	A	0.181	Capping
	N	0.348	
	A	0.181	Capping
	A	0.181	Capping

Yield 8 mg (7%)

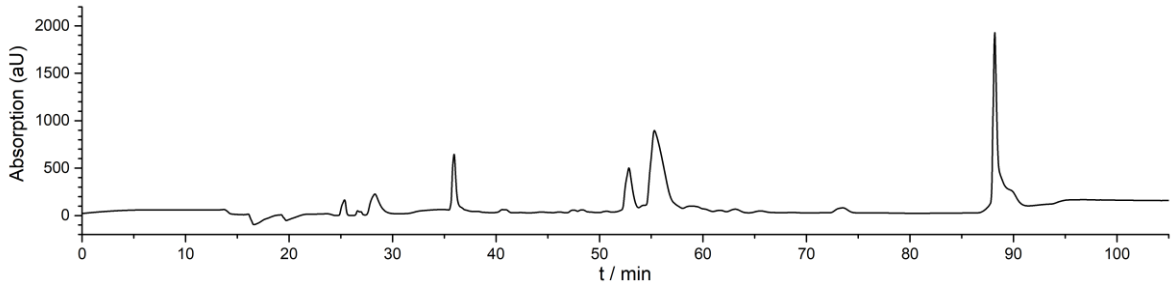

Fig. 72: HPLC profile of the semi-preparative run of 1repeat. t_R is 57 min.

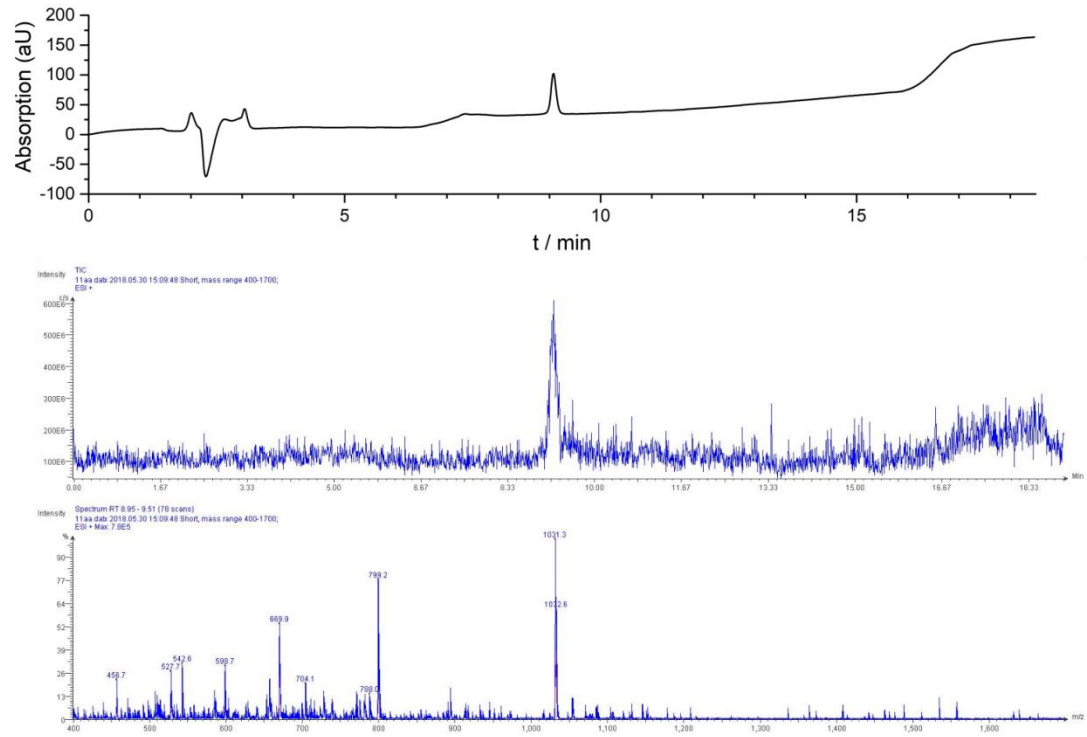

Fig. 73: HPLC profile of the analytical run (top), ion chromatogram (2nd panel from top) and MS spectra of all signals of purified 1repeat. *m/z*: $[M+H]^+$ calcd 1031, found 1031.3. t_R is 9.1 min

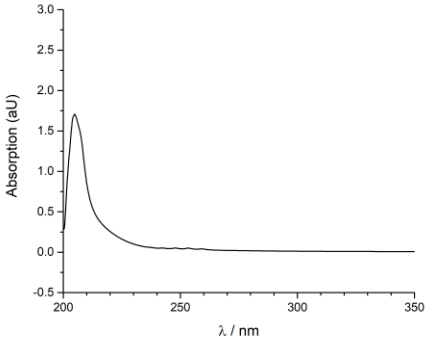

Fig. 74: UV/vis spectrum of 1repeat at 298 K in 0.1 M NH_4HCO_3 buffer, pH 7.9. The spectrum was measured to 600 nm, displayed only to 350 nm.

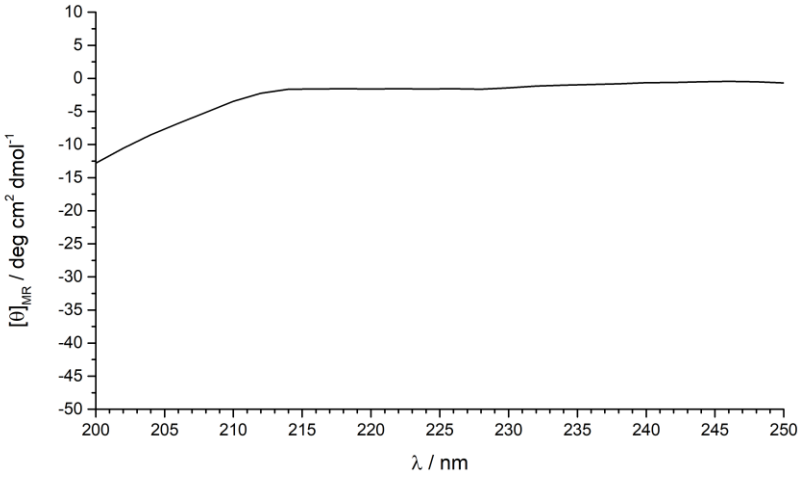

Fig. 75: CD spectrum of 1repeat at 274 K in 0.1 M NH_4HCO_3 buffer, pH 7.9. The scale is different from the other CD spectra.

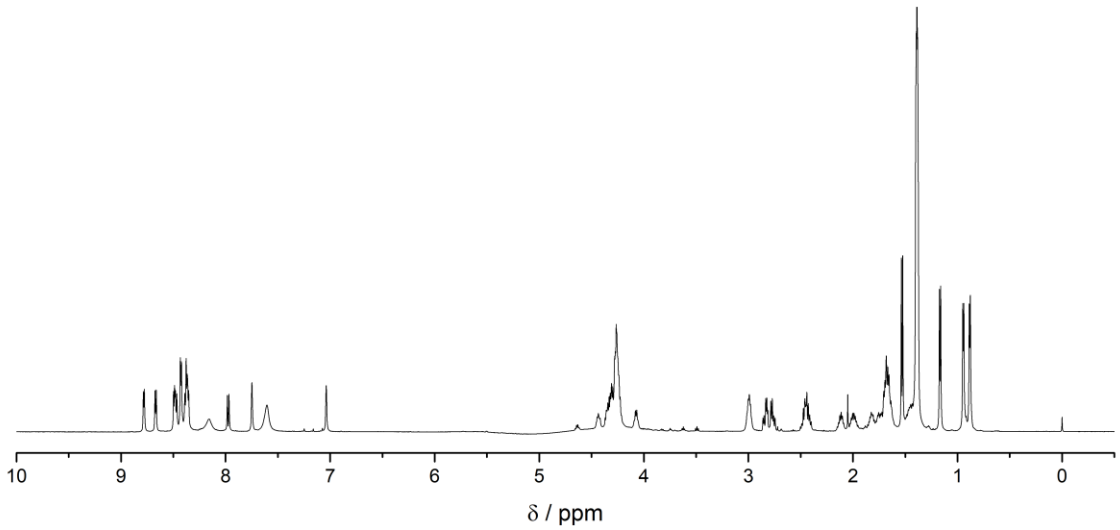

Fig. 76: ^{1}H NMR spectrum of 1repeat in H_2O/D_2O, pH 3, at 278 K.

Tab. 37: ^{1}H-chemical shifts of 1repeat in H_2O/D_2O, pH 3, at 278 K.

Residue		Chemical shift *δ* (ppm)				
		NH	α	β	γ	
1	Ala	exch.	4.076			
2	Ala	8.782	4.321	1.381		
3	Asn	8.669	4.637	2.838, 2.780		δ 7.748, 7.037
4	Ala	8.493	4.273	1.391		
5	Lys	8.428	4.245	1.825, 1.750	1.463	δ 1.682 ε 2.997 ζ 7.609
6	Ala	8.373	4.259	1.390		
7	Ala	8.366	4.273	1.301		
8	Ala	8.379	4.252	1.3980		
9	Glu	8.382	4.350	2.212, 1.987	2.456	
10	Leu	8.473	4.437	1.708, 1.656	1.396	δ 0.949, 0.887
11	Thr	7.979	4.272	4.272	1.168	

Tab. 38: ^{15}N and ^{13}C-chemical shifts of 1repeat in H_2O/D_2O, pH 3, at 278 K.

Residue		Chemical shift δ (ppm)				
		N		Cα	Cβ	
1	Ala			51.74		
2	Ala	123.57		52.57	19.12	
3	Asn	118.83	δ 113.34	n.d.	38.48	
4	Ala	125.29		52.58	19.12	
5	Lys	121.04		56.21	32.85	γ 24.75 δ 29.22
6	Ala	123.93		52.57	19.12	
7	Ala	123.24		52.58	19.12	
8	Ala	125.89		52.57	19.12	
9	Glu	119.71		55.53	29.16	γ 33.18
10	Leu	124.18		n.d.	42.36	δ24.94, 23.21
11	Thr	117.20		61.79	70.92	γ 21.76

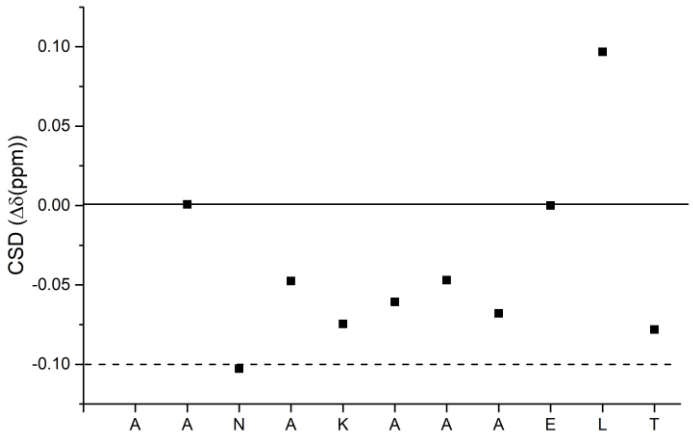

Fig. 77: Hα CSD plot of 1repeat at pH 3 and 278 K. The dashed line at y=-0.1 ppm represents the helical limit. The scale is different from the other CSD plots.

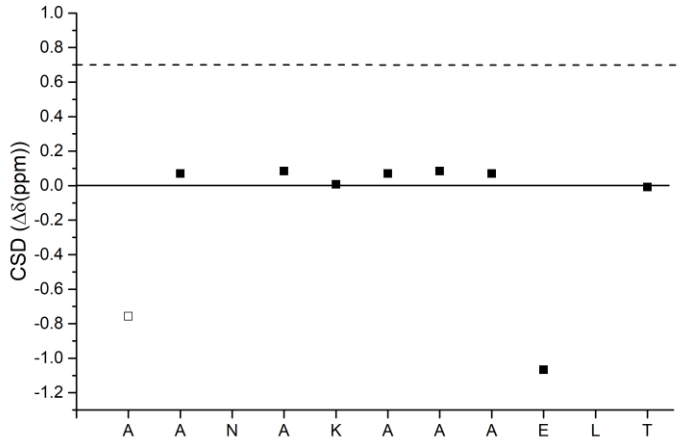

Fig. 78: Cα CSD plot of 1repeat at pH 3 and 278 K. The dashed line at y=0.7 ppm represents the helical limit. The scale is different from the other CSD plots.

Antifreeze activity (10 mg/mL, 0.1 M NH_4HCO_3, pH 7.9):

- No thermal hysteresis
- No ice shaping

5.4 (jg)IBTC-4

Sequence	DTAANAKAAAELTDKYAQWLADGGPSSGRPPPK
Molecular weight	3355.68 g/mol
Absorption coefficient	ε_{280}= 6990 $M^{-1}cm^{-1}$
Peptide amount	0.079 g / 0.023 mmol
Resin type	with Tc10bKKA preloaded Wang resin
Resin amount	171 mg
Capping	acetic anhydride, pyridine, dimethylformamide (1/1/2)

	Single Coupling	
HOBT (2 eq, g)	0.009	
DIC (2 eq, mL)	0.010	
HATU (4.9 eq, g)	0.043	
DIPEA (10 eq, mL)	0.040	
Peptide fragment (2 eq, g)	0.080	Capping
Amino acids (5 eq, g)		
	T	Capping
	D	Capping

Yield 8.7 mg (11%)

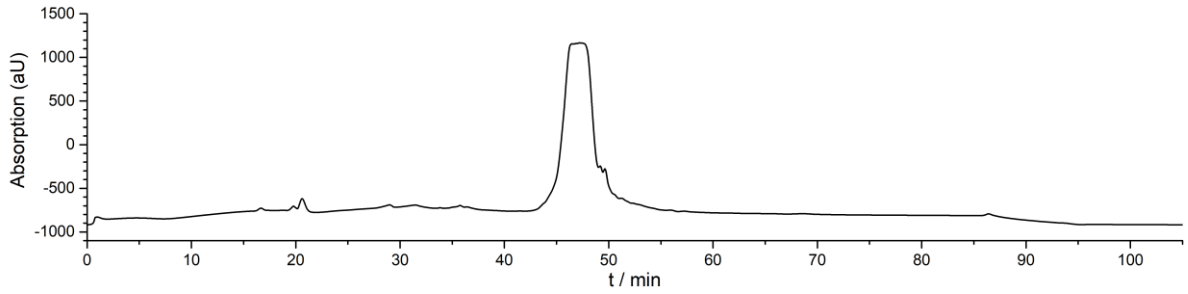

Fig. 79: HPLC profile of the semi-preparative run of (jg)IBTC-4. t_R is 46 min.

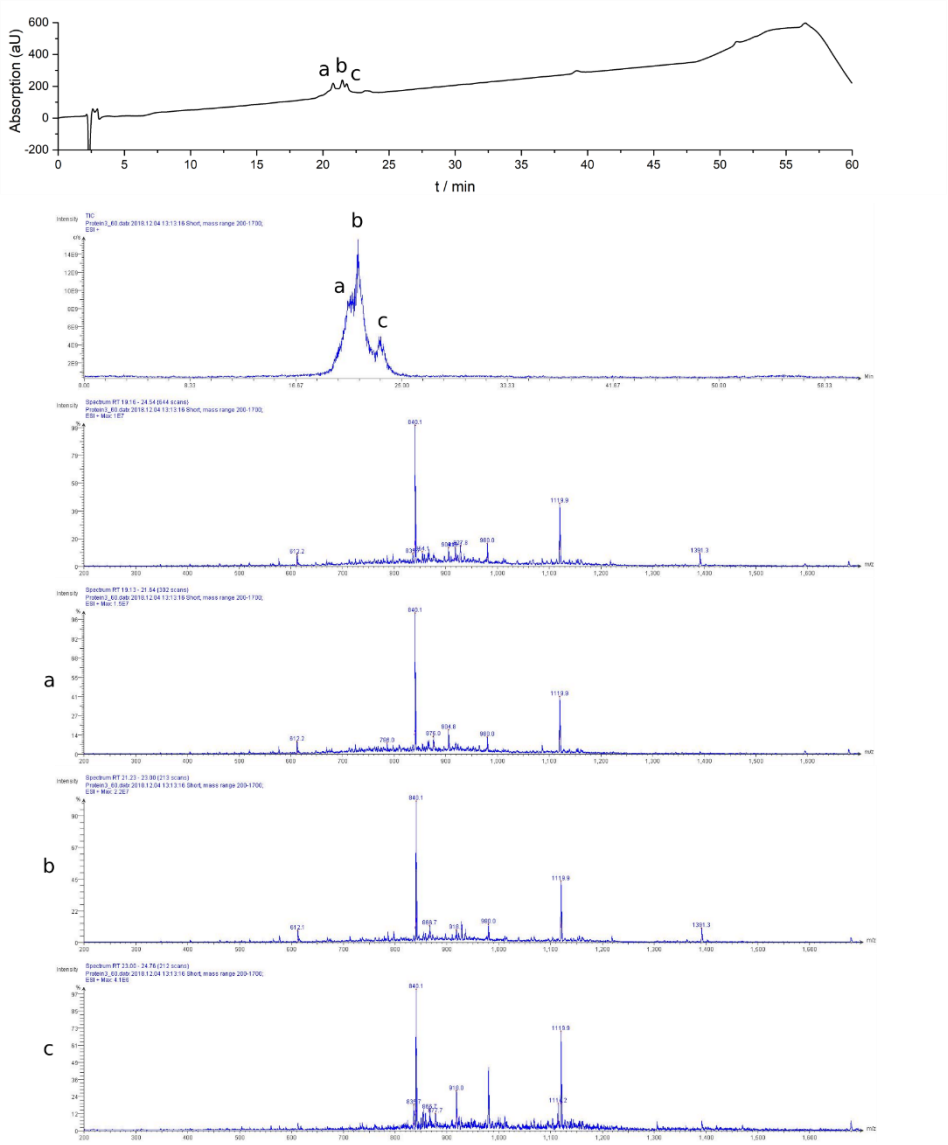

Fig. 80: HPLC profile of a 60 min analytical run (top), ion chromatogram (2nd panel from top) and MS spectra of all signals of purified (jg)IBTC-4. *m/z*: $[M+3H]^{3+}$ calcd 1119.6, found 1119.9; $[M+4H]^{4+}$ calcd 839.9, found 840.1. t_R is 21.8 min.

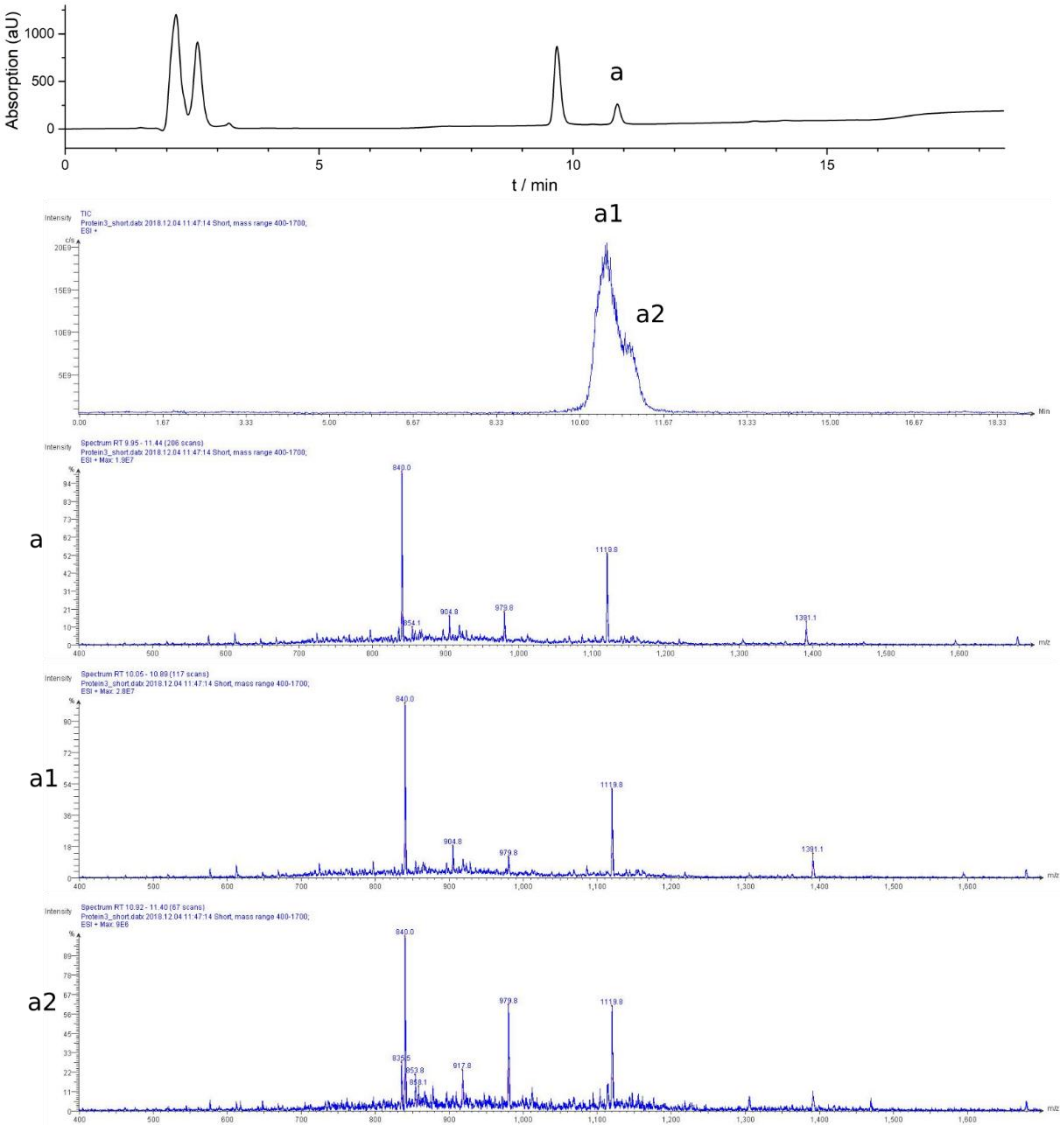

Fig. 81: HPLC profile of the analytical run (top), ion chromatogram (2nd panel from top) and MS spectra of all signals of purified (jg)IBTC-4. *m/z*: $[M+3H]^{3+}$ calcd 1119.6, found 1119.8; $[M+4H]^{4+}$ calcd 839.9, found 840.0. t_R is 10.9 min.

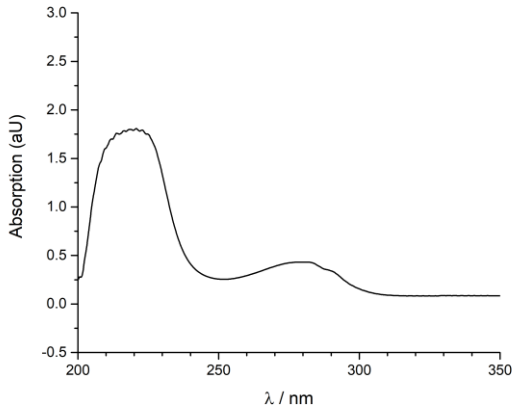

Fig. 82: UV/vis spectrum of (jg)IBTC-4 at 298 K in 0.1 M NH_4HCO_3 buffer, pH 7.9. The spectrum was measured to 600 nm, displayed only to 350 nm.

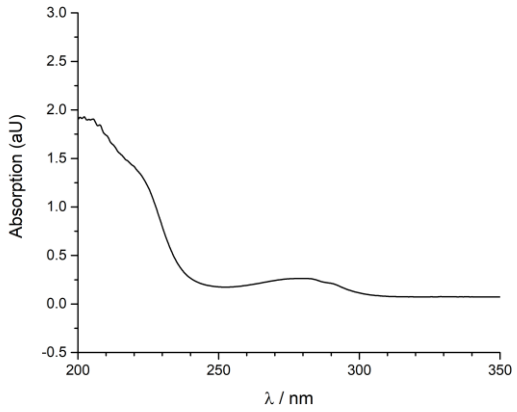

Fig. 83: UV/vis spectrum of (jg)IBTC-4 at 298 K in water at pH 3. The spectrum was measured to 600 nm, displayed only to 350 nm.

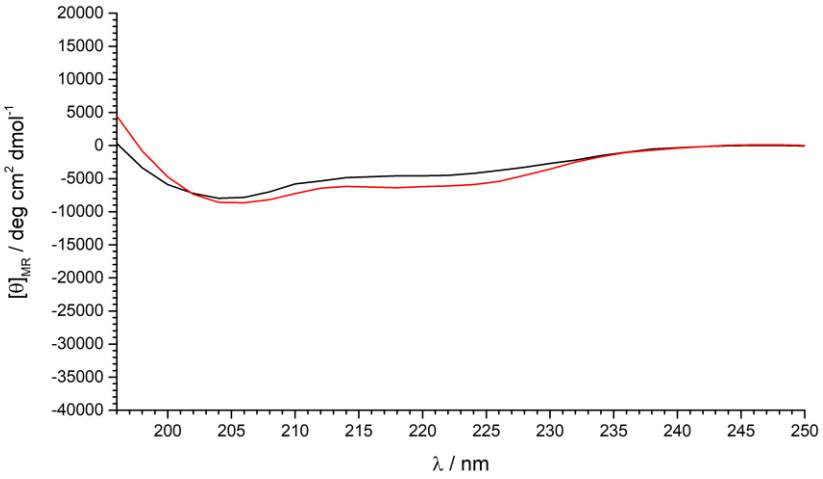

Fig. 84: CD spectra of (jg)IBTC-4 in 0.1 M NH_4HCO_3 buffer, pH 7.9, at 298 K (black) and 274 K (red).

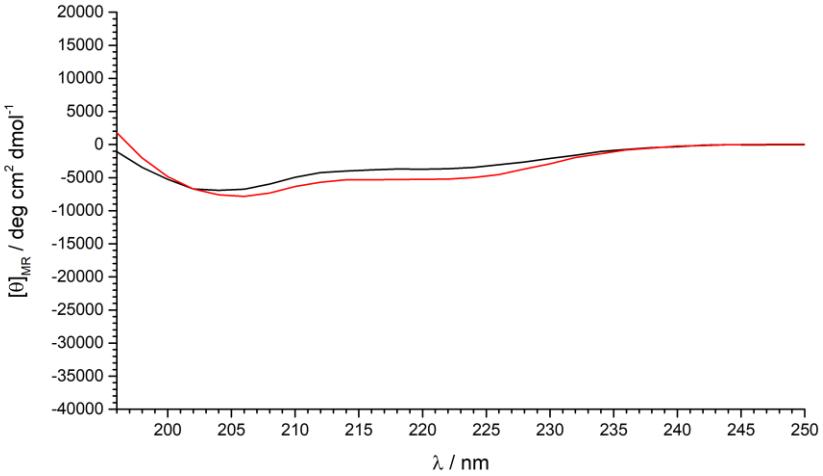

Fig. 85: CD spectra of (jg)IBTC-4 in water, pH 3, at 298 K (black) and 274 K (red).

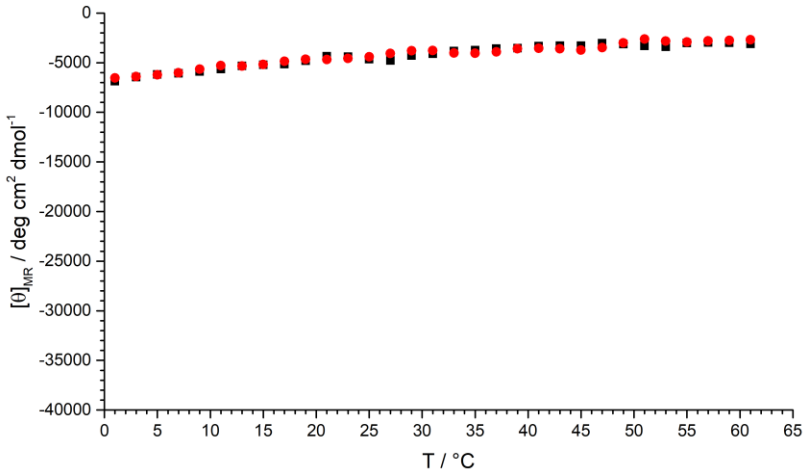

Fig. 86: CD thermal denaturation scans of (jg)IBTC-4 in 0.1 M NH_4HCO_3 buffer, pH 7.9. The black squares show the heating curve, the red circles the cooling curve. The estimated T_m is 10 °C, while the sample shows a complete unfolding above 40 °C.

Tab. 39: Helical content of (jg)IBTC-4 at 1 °C and 0.1 M NH_4HCO_3 buffer, pH 7.9, or water, pH 3.

	0.1 M NH_4HCO_3, pH 7.9	pH 3
$[\Theta]_{obs}$ (deg cm^2 dmol^{-1})	-5.977	-5.144
$[\Theta]_{ref}$ (deg cm^2 dmol^{-1})	-42.424	-42.424
Helical content (%)	14	12

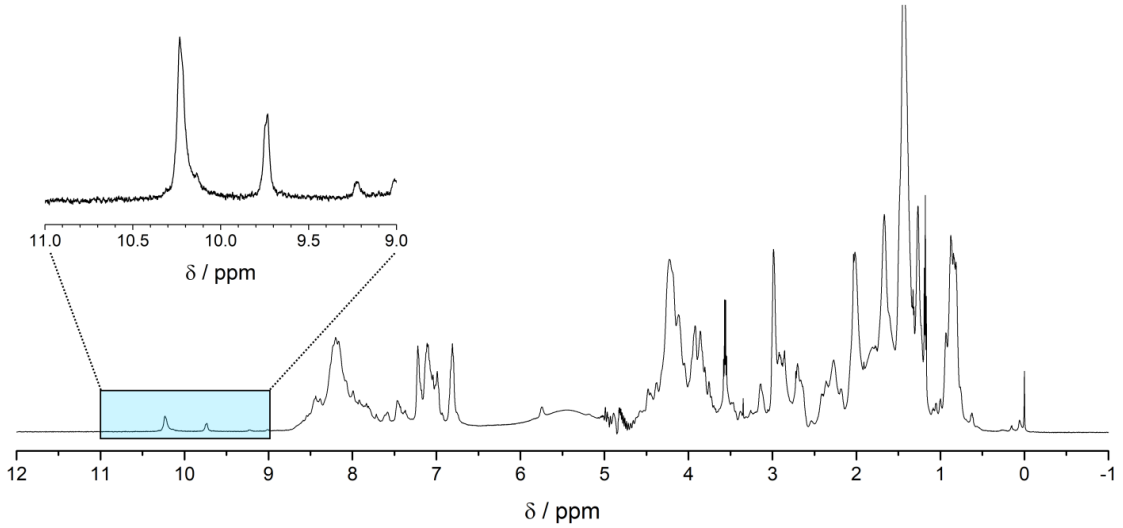

Fig. 87: ^{1}H NMR spectrum of (jg)IBTC-4 in 0.1 M NH_4HCO_3 buffer, pH 7.9, at 274 K with enlargement of the indole proton region around 10 ppm.

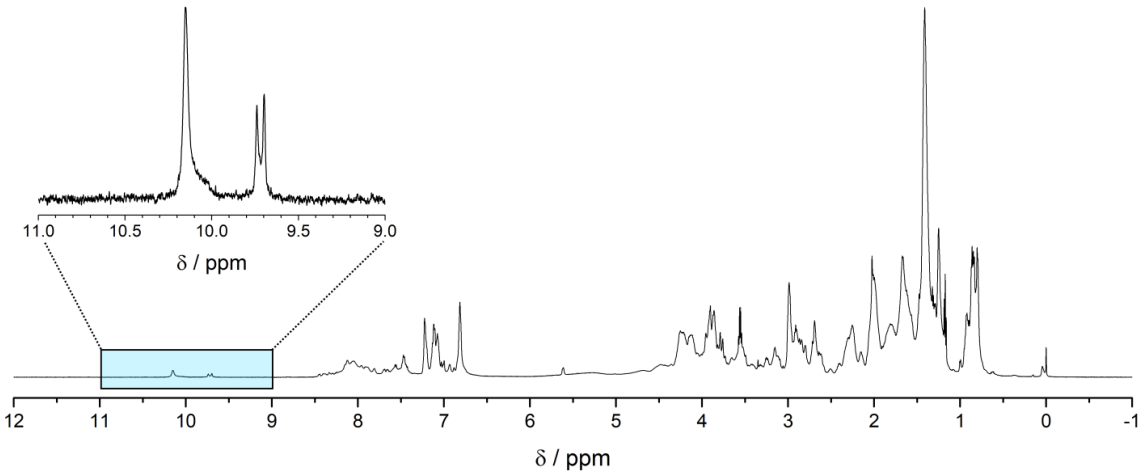

Fig. 88: ^{1}H NMR spectrum of (jg)IBTC-4 in 0.1 M NH_4HCO_3 buffer, pH 7.9, at 298 K with enlargement of the indole proton region around 10 ppm.

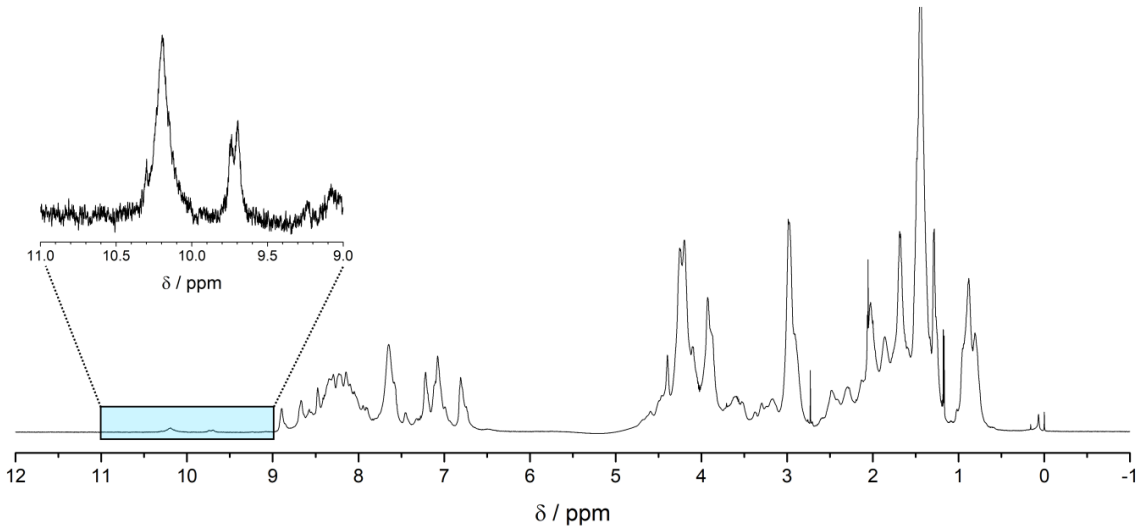

Fig. 89: ^{1}H NMR spectrum of (jg)IBTC-4 in H_2O/D_2O, pH 3, at 274 K with enlargement of the indole proton region around 10 ppm.

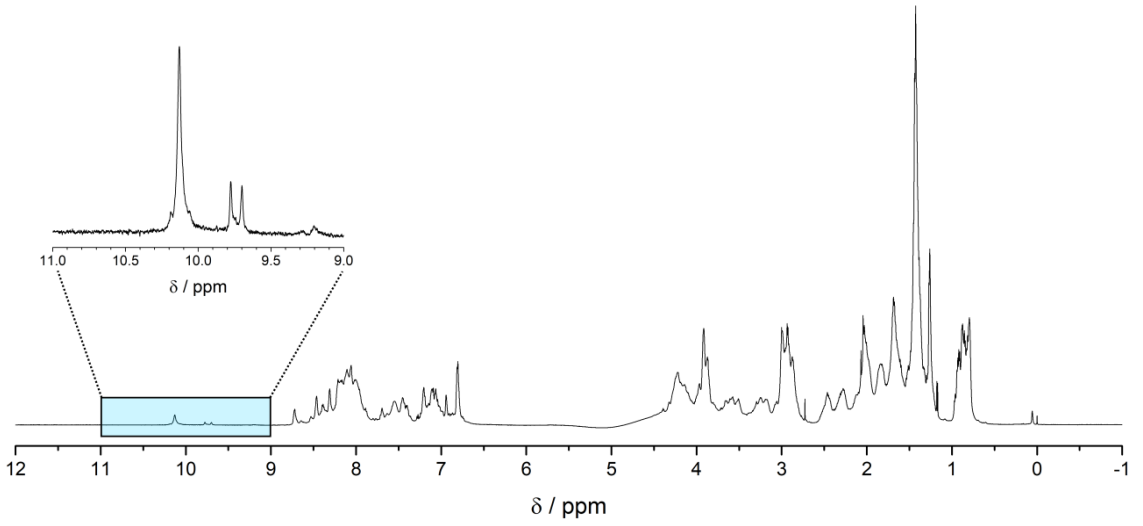

Fig. 90: ^{1}H NMR spectrum of (jg)IBTC-4 in H_2O/D_2O, pH 3, at 298 K with enlargement of the indole proton region around 10 ppm.

Tab. 40: ^{1}H-chemical shifts of the folded conformation of (jg)IBTC-4 in H_2O/D_2O, pH 3, at 274 K.

Residue		Chemical shift δ (ppm)				
		NH	α	β	γ	
1‘	Asp	exch.	4.398	2.959		
2‘	Thr	8.900	4.271	4.277	1.272	
3‘	Ala	8.671	4.249	1.445		
4‘	Ala	n.d.	4.204	1.417		
5‘	Asn	8.577	4.646	2.878		
6‘	Ala					
7‘	Lys	8.248	4.186	1.887	1.447	δ 1.688 ε 2.984 ζ 7.655
8‘	Ala	n.d.				
9‘	Ala	n.d.				
10‘	Ala	n.d.				
11‘	Glu	8.214	4.228	2.130, 2.021	2.487, 2.407	
12‘	Leu	8.028	4.260	1.774, 1.669		
13‘	Thr	8.256	4.118	4.190	1.251	
1	Asp	8.296	4.598	2.902		
2	Lys	8.351	4.194	1.848, 1.747	1.454	δ 1.687 ε 2.981 ζ 7.728
3	Tyr	n.d.	4.116	3.032		δ 7.098 ε 6.812
4	Ala					
5	Gln	8.142	4.213	2.130	2.588, 2.482	
6	Trp	8.022	4.191	3.539, 3.174		δ 7.206 ε 9.721, 7.219 ζ 7.119, 6.989 η 7.212
7	Leu	8.593	3.382	1.838		
8	Ala	n.d.	4.102	1.487		
9	Asp	7.762	4.695	3.007, 2.885		
10	Gly	7.648	4.153, 3.519			
11	Gly	8.181	2.972, 1.197			
12	Pro		4.572	2.485	2.119	δ 4.345, 4.257
13	Ser	7.855	4.466	3.930		
14	Ser	8.179	4.181	3.892		
15	Gly	8.055	4.261, 3.849			
16	Arg	8.143	4.939	1.663	1.474,	δ 3.177

					1.371	ε 7.237
17	Pro		4.712	2.340, 1.989	2.042	δ 3.727
18	Pro		n.d.	1.531, 0.908	1.678, 1.588	δ 3.707, 3.511
19	Pro		4.417	2.291, 2.021	1.971	δ 3.809, 3.604
20	Lys	8.160	4.136	1.865		δ 1.686 ε 2.926 ζ 7.586

Tab. 41: ^{15}N and ^{13}C-chemical shifts of the folded conformation of (jg)IBTC-4 in H_2O/D_2O, pH 3, at 274 K. Shifts marked with an asterix are averaged.

Residue		Chemical shift δ (ppm)				
		N		Cα	Cβ	
1‘	Asp	n.d.		52.79	39.50	
2‘	Thr	115.92		63.11	69.62	γ 21.79
3‘	Ala	126.49		53.98	18.43	
4‘	Ala	n.d.		54.04	18.89	
5‘	Asn	125.90		53.46	38.10	
6‘	Ala	n.d.		53.91 *	18.45 *	
7‘	Lys	120.69	62.43	57.97	32.58	γ 24.88 δ 29.18 ε 42.01
8‘	Ala	n.d.		53.91 *	18.45 *	
9‘	Ala	n.d.		53.91 *	18.45 *	
10‘	Ala	n.d.		53.91 *	18.45 *	
11‘	Glu	118.85		56.65	28.85	γ 33.82
12‘	Leu	121.50		56.54	42.19	
13‘	Thr	115.81		63.96	n.d.	γ 21.67
1	Asp	118.26		54.07	39.50	
2	Lys	n.d.	62.06	56.75	33.11	γ 24.87 δ 29.18 ε 42.01
3	Tyr	n.d.		64.03	38.54	δ 133.08 ε 118.20
4	Ala	n.d.		53.91 *	18.45 *	
5	Gln	118.26		56.75	28.59	γ 33.29
6	Trp	121.30	131.43	58.07	41.24	δ 127.22 ε 120.79 ζ122.18, 114.15 η 124.38
7	Leu	119.77		57.78	42.07	
8	Ala	n.d.		54.04	18.31	
9	Asp	116.55		53.09	38.10	
10	Gly	106.52		49.90		
11	Gly	112.51		42.01		
12	Pro	n.d.		n.d.	33.33	γ 27.30

						δ 52.91
13	Ser	113.34		58.43	63.83	
14	Ser	121.34		57.97	63.78	
15	Gly	109.98		44.95		
16	Arg	120.12	114.44	n.d.	29.18	γ 24.87 δ 43.27
17	Pro	n.d.		n.d.	30.64	γ 27.30 δ 50.27
18	Pro	n.d.		n.d.	27.72	γ26.78 δ 50.27
19	Pro	n.d.		63.05	32.09	γ 27.30 δ 50.40
20	Lys	120.35	62.11	56.82	32.69	δ 29.18 ε 42.01

Tab. 42: ^{1}H-chemical shifts of the folded conformation of (jg)IBTC-4 in H_2O/D_2O, pH 3, at 298 K.

Residue		Chemical shift *δ* (ppm)				
		NH	α	β	γ	
1‘	Asp	exch.	4.394	2.919		
2‘	Thr	8.723	4.328	4.163	1.268	
3‘	Ala	8.463	4.285	1.431		
4‘	Ala					
5‘	Asn	8.378	4.623	2.810		
6‘	Ala					
7‘	Lys	8.104	4.219	1.833	1.432	δ 1.704 ε2.989 ζ 7.552
8‘	Ala	n.d.				
9‘	Ala	n.d.				
10‘	Ala	n.d.				
11‘	Glu	8.127	4.143	2.013	6.181	
12‘	Leu	7.952	4.166	1.791, 1.682		
13‘	Thr	8.085	4.078	4.242	1.265	
1	Asp	8.214	4.639	2.867		
2	Lys	8.063	4.219	1.833	1.432	δ 1.682 ε 2.936 ζ 7.507
3	Tyr	8.525	4.192	3.166, 3.050		δ 7.058, 6.810
4	Ala					
5	Gln	8.101	4.106	2.058	2.457, 2.332	
6	Trp	7.991	4.270	3.345, 3.236		δ 7.204 ε 10.132 ζ 7.460, 6.943 η 7.109
7	Leu	8.395	3.492	1.774		

8	Ala		4.109	1.467		
9	Asp	7.760	4.714	3.022, 2.862		
10	Gly	7.687	4.116, 3.598			
11	Gly	8.110	3.076, 1.841			
12	Pro		4.423	2.258	1.978	δ 3.769, 3.588
13	Ser	7.994	4.486	3.888		
14	Ser	8.094	4.236	4.007, 3.864		
15	Gly	8.010	4.217, 3.806			
16	Arg	8.064	4.895	1.909, 1.817	1.724, 1.695	δ 3.259 ε 7.361
17	Pro		4.677	2.302	2.018	δ 3.800
18	Pro		3.492	1.569	1.643, 1.408	δ 3.669
19	Pro		4.207	1.831, 1.689	1.676	δ 3.182, 2.993
20	Lys	8.166	4.219	1.834	1.432	δ 1.684 ε2.991 ζ 7.598

Tab. 43: ^{15}N and ^{13}C-chemical shifts of the folded conformation of (jg)IBTC-4 in H_2O/D_2O, pH 3, at 298 K. Shifts marked with an asterix are averaged.

Residue		Chemical shift *δ* (ppm)				
		N		Cα	Cβ	
1‘	Asp	n.d.		53.15	39.26	
2‘	Thr	115.60		62.57	69.58	γ 21.71
3‘	Ala	126.65		53.29	18.82	
4‘	Ala	n.d.		53.28 *	18.80 *	
5‘	Asn	122.06		n.d.	38.67	
6‘	Ala	n.d.		53.28 *	18.80 *	
7‘	Lys	121.98	62.45	56.96	32.81	γ 24.82 δ 29.12 ε 39.10
8‘	Ala	n.d.		53.28 *	18.80 *	
9‘	Ala	n.d.		53.28 *	18.80 *	
10‘	Ala	n.d.		53.28 *	18.80 *	
11‘	Glu	122.08		58.28	28.62	γ 33.84
12‘	Leu	121.16		57.39	42.32	
13‘	Thr	118.13		n.d.	69.74	γ 21.71
1	Asp	117.39		n.d.	38.67	
2	Lys	121.96	61.99	56.96	32.81	γ 24.82 δ 29.12 ε 38.60
3	Tyr	123.61		62.55	38.50	δ 133.04

						ε 118.26
4	Ala	n.d.		53.28 *	18.80 *	
5	Gln	118.67		57.72	28.86	γ 33.39
6	Trp	121.36	129.51	56.44	28.96	δ 127.10 ζ 114.64, 122.29 η 124.42
7	Leu	120.17		57.57	42.35	
8	Ala	n.d.		53.96	18.36	
9	Asp	116.27		n.d.	42.09	
10	Gly	106.85		45.35		
11	Gly	111.59		43.59		
12	Pro	n.d.		63.38	31.68	γ 27.23 δ 50.28
13	Ser	113.36		58.48	63.80	
14	Ser	116.73		57.04	63.87	
15	Gly	108.61		45.41		
16	Arg	120.30	114.9	n.d.	30.93	γ 26.76 δ 43.43
17	Pro	n.d.		n.d.	31.14	γ 27.19 δ 50.62
18	Pro	n.d.		57.57	28.90	γ 26.76 δ 50.55
19	Pro	n.d.		62.72	30.80	γ 26.76 δ 50.55
20	Lys	120.00	61.88	56.96	32.81	γ 24.82 δ 29.12 ε 38.46

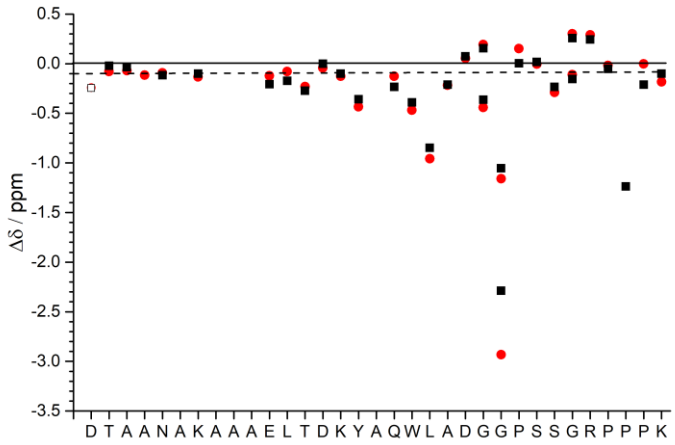

Fig. 91: Hα CSD plots of the folded conformation of (jg)IBTC-4 at pH 3 and 274 K (red circles) and 298 K (black squares). The dashed line at y=-0.1 ppm represents the helical limit.

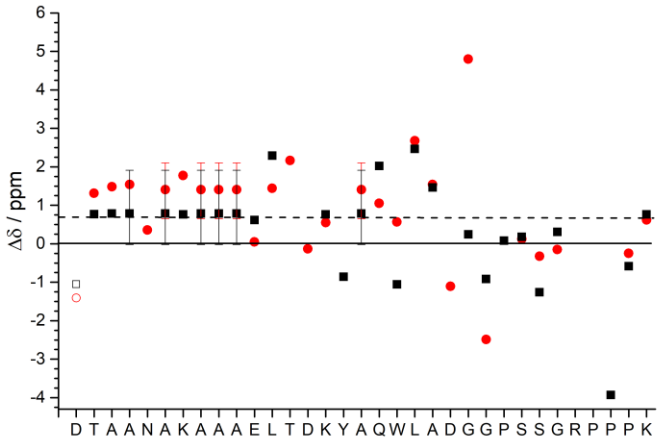

Fig. 92: Cα CSD plots of the folded conformation of (jg)IBTC-4 at pH 3 and 274 K (red circles) and 298 K (black squares). The dashed line at y=0.7 ppm represents the helical limit.

Tab. 44: CSDs for selected protons of the cage structure representing the cage fold of (jg)IBTC-4 at pH 3 and 274 K and 298 K, given the fraction folded according to Lin. [75]

$\chi_{Trp\text{-}cage}$	Δδ (ppm)						Σ
	L7α	G11α’	P18α	Pro18β’	P19δ	P19δ’	
pH 3, 274 K	-0.968	-2.823	-1.360	-1.382	0.219	-0.136	-6.449
pH 3, 298 K	-0.858	-2.179	-1.238		-0.408	0.747	

Tab. 45: CSDs for selected protons in the helical region representing the helix fold of (jg)IBTC-4 at pH 3 and 274 K and 298 K.

χ_{Helix}	Δδ (ppm)							Σ
	K2α	Y3α	A4α	Q5α	W6α	L7α	A8α	
pH 3, 274 K	-0.126	-0.434		-0.127	-0.470	-0.958	-0.218	
pH 3, 298 K	-0.101	-0.358		-0.234	-0.390	-0.849	-0.211	

Antifreeze activity (80 mg/mL, 0.1 M NH_4HCO_3, pH 7.9):

- Ice growth retardation: 0.040 °C
- ice shaping

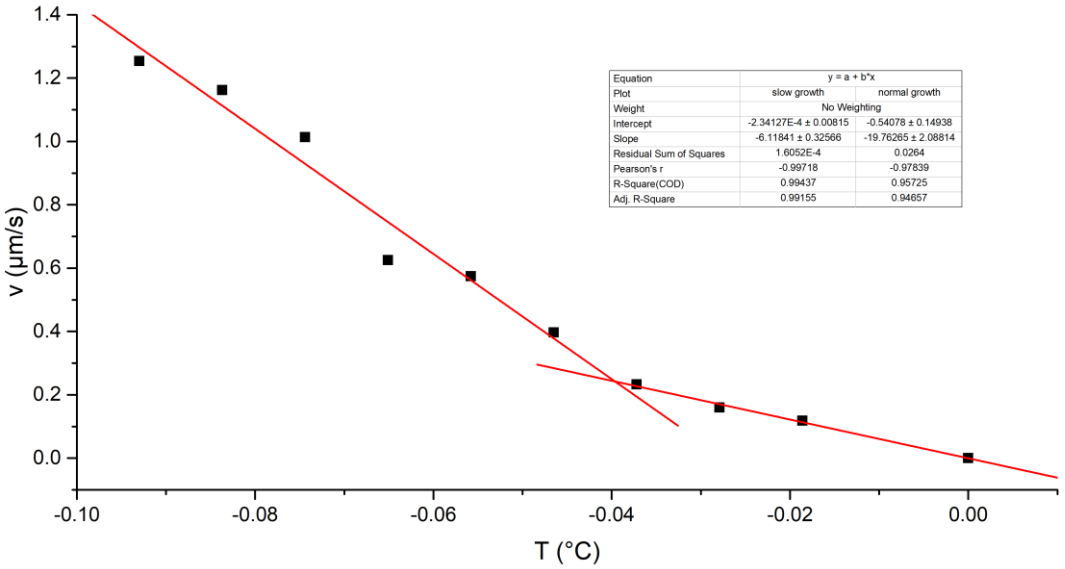

Fig. 93: Ice growth retardation plot of 80 mg/mL (jg)IBTC-4 in 0.1 M NH_4HCO_3, pH 7.9. The growth retardation is 0.040 °C.

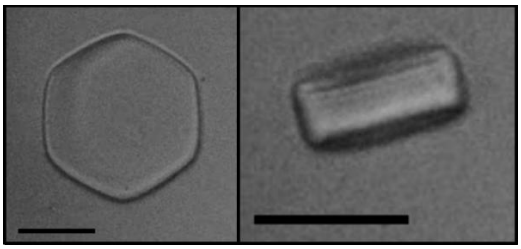

Fig. 94: Ice crystals during the growth in the presence of 80 mg/mL (jg)IBTC-4 in 0.1 M NH_4HCO_3, pH 7.9. Left the top view shows the view perpendicular to the basal plane, while on the right the side view of the crystal is shown. The black scale in each picture is 10 µm long.

5.5 SUMO Protease

Sequence	METGSSHHHH HHSSGLVPRG SHMETDLLEL TEDMETEKEI SNALGHGPQD EILSSAFKLR ITRGDIQTLK NYHWLNDEVI NFYMETNLLV ERNKKQGYPA LHVFSTFFYP KLKSGGYQAV KRWTKGVNLF EQEIILVPIH RKVHWSLVVI DLRKKCLKYL DSMETGQKGH RICEILLQYL QDESKTKRNS DLNLLEWTHH SMETKPHEIP QQLNGSDCGM ETFTCKYADY ISRDKPITFT QHQMETPLFR KKMETVWEIL HQQLL
Molecular weight	31111.52 Da
Absorption coefficient	ε_{280}= 41160 $M^{-1}cm^{-1}$
Yield	2 mg/ L LB medium (500 µL aliquots of 0.89 mg/mL (28.6 µM) stored at -80 °C)

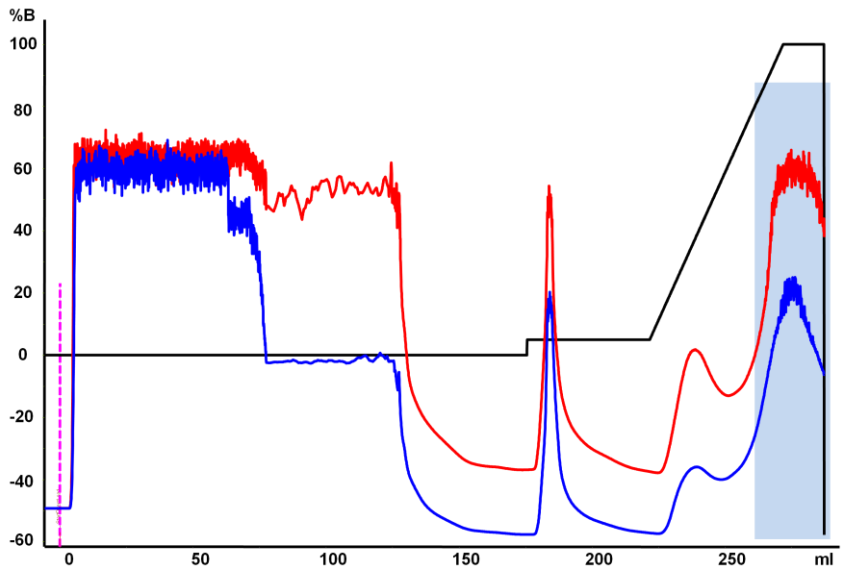

Fig. 95: Profile of the affinity purification of SUMO protease. The signal was detected at 280 nm (blue) and 254 nm (red). The gradient of the elution buffer is shown in black. With the injection at 0 mL the chromatogram starts. Fractions that were combined and collected are marked in blue.

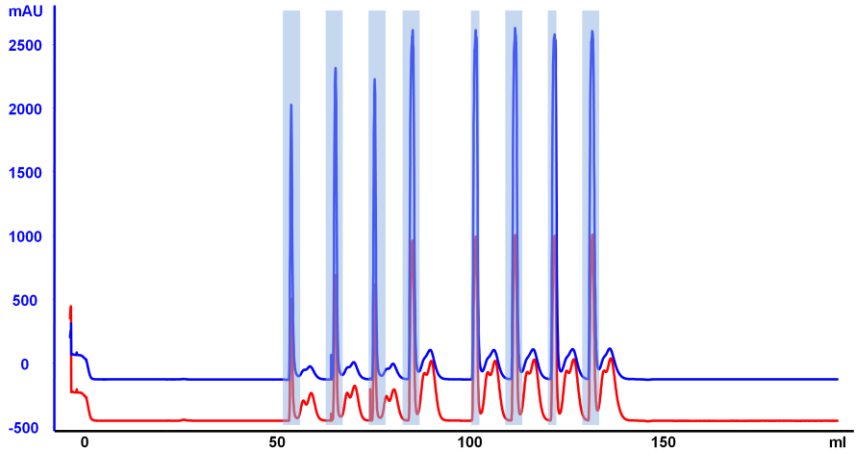

Fig. 96: : Profile of the desalting of SUMO protease. The signal was detected at 280 nm (blue) and 254 nm (red). Fractions that were combined and collected are marked in blue.

5.6 (jg)IBTC-1

Sequence	DTASDAAAYAAWTADGGPSSGRPPPSGS
Molecular weight	2620.68 Da
Absorption coefficient	ε_{280}= 6990 $M^{-1}cm^{-1}$
Yield	1.6 mg/ L LB medium

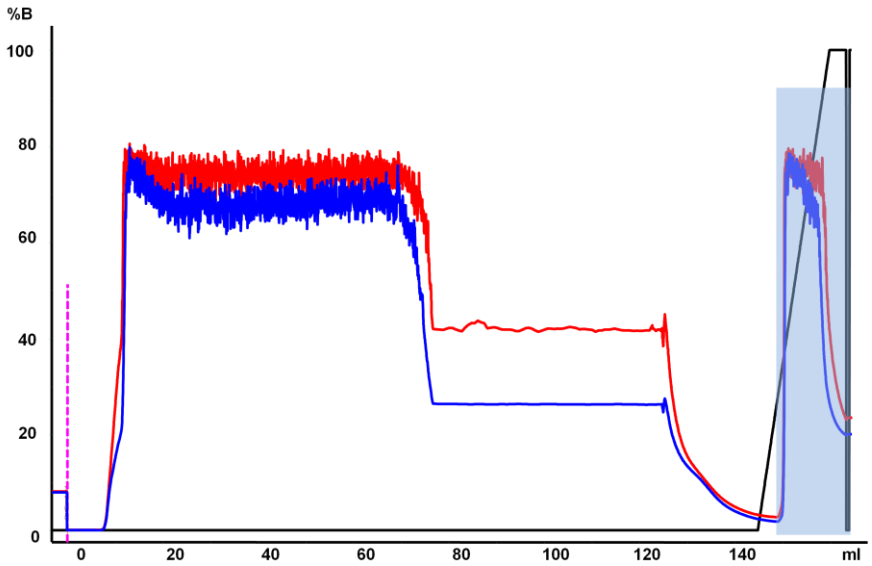

Fig. 97: Profile of the affinity purification of (jg)SUMO-IBTC-1. The signal was detected at 280 nm (blue) and 254 nm (red). The gradient of the elution buffer is shown in black. With the injection at 0 mL the chromatogram starts. Fractions that were combined and collected are marked in blue.

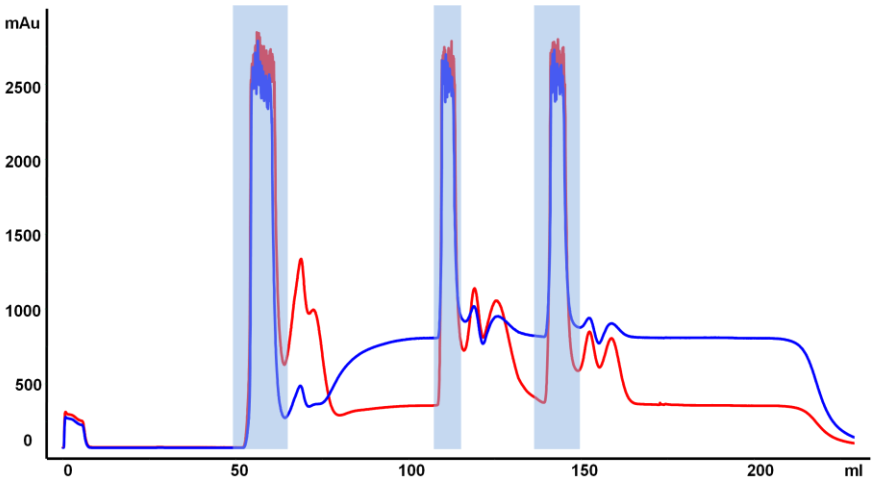

Fig. 98: Profile of the rebuffering of (jg)SUMO-IBTC-1. The signal was detected at 280 nm (blue) and 254 nm (red). Fractions that were combined and collected are marked in blue.

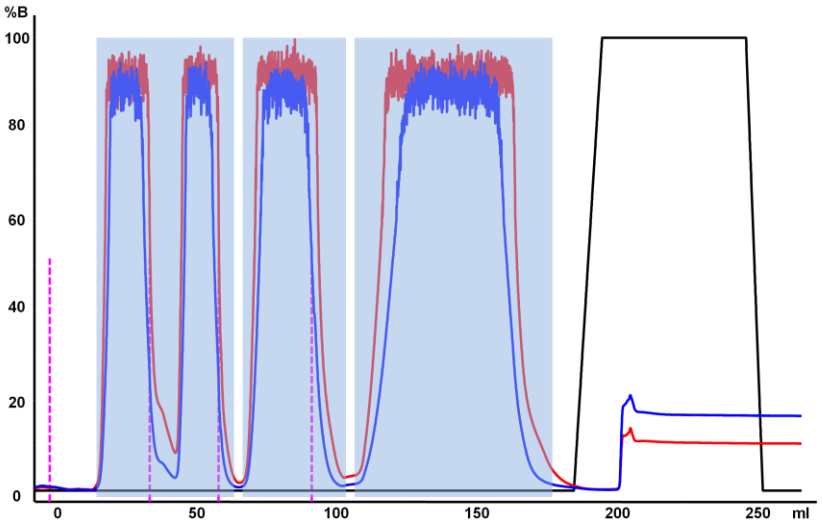

Fig. 99: Profile of the affinity purification of (jg)IBTC-1. The signal was detected at 280 nm (blue) and 254 nm (red). The gradient of the elution buffer is shown in black. The injections are dashed pink lines. Fractions which were collected and combined are marked in blue.

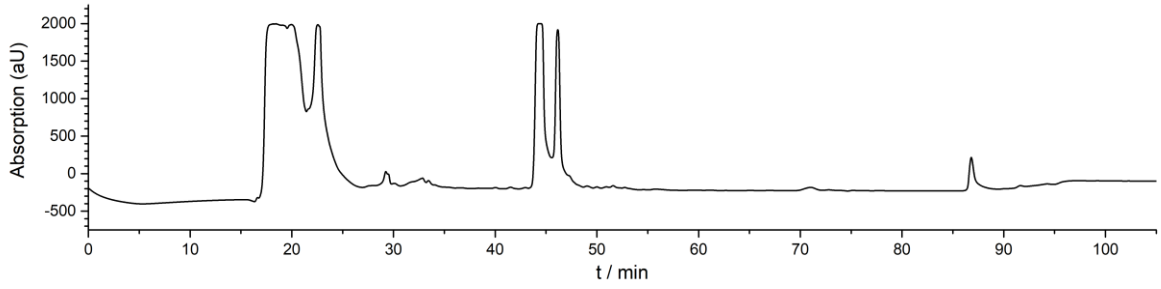

Fig. 100: HPLC profile of the semi-preparative run of (jg)IBTC-1. t_R is 46 min.

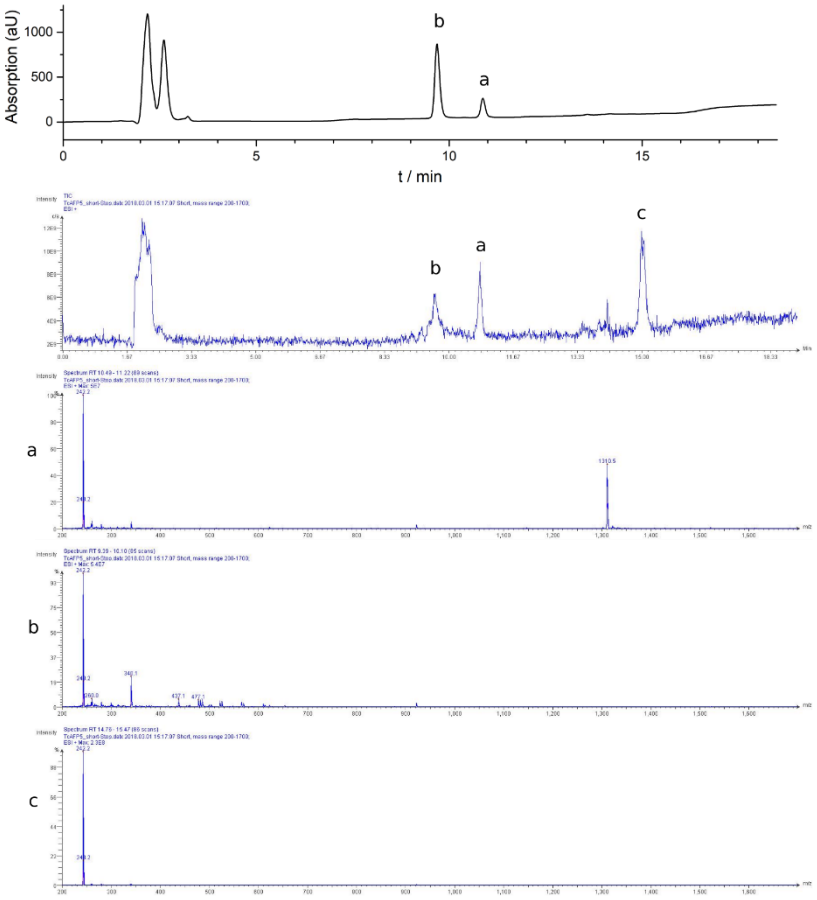

Fig. 101: HPLC profile of the analytical run (top), ion chromatogram (2nd panel from top) and MS spectra of all signals of purified (jg)IBTC-1. *m/z*: $[M+2H]^{2+}$ calcd 1311, found 1310.5. t_R is 10.9 min.

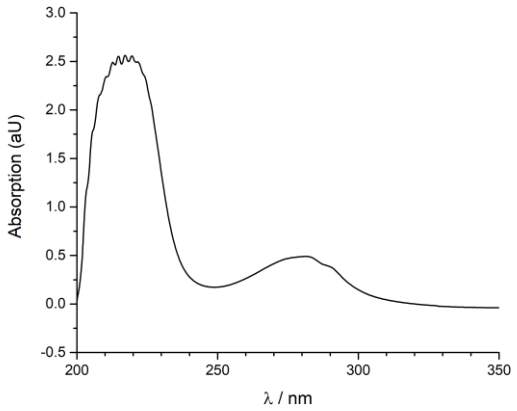

Fig. 102: UV/vis spectrum of (jg)IBTC-1 at 298 K in 0.1 M NH_4HCO_3 buffer, pH 7.9. The spectrum was measured to 600 nm, displayed only to 350 nm.

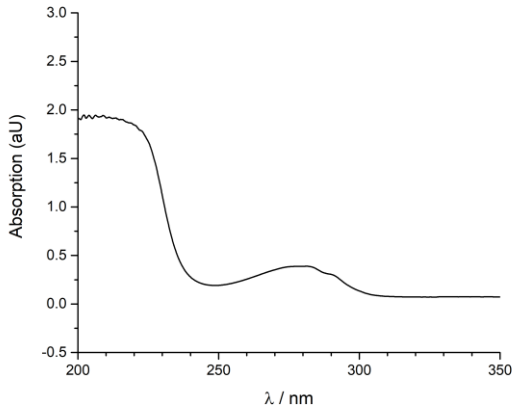

Fig. 103: UV/vis spectrum of (jg)IBTC-1 at 298 K in water at pH 3. The spectrum was measured to 600 nm, displayed only to 350 nm.

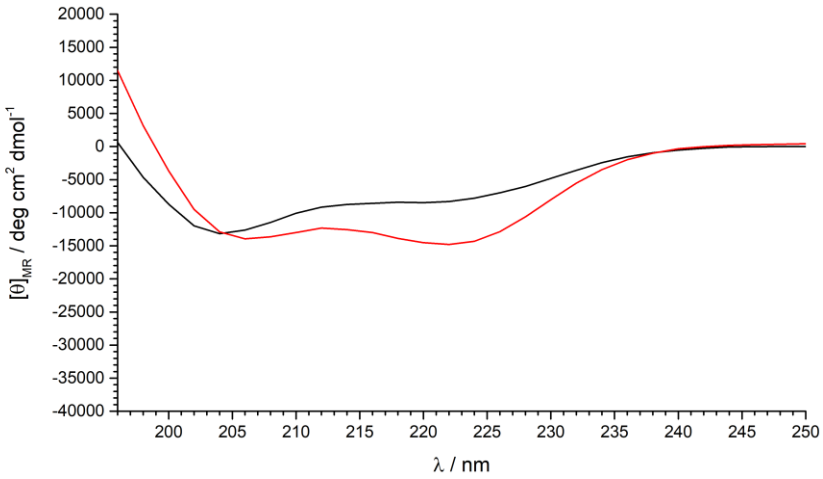

Fig. 104: CD spectra of (jg)IBTC-1 in 0.1 M NH_4HCO_3 buffer, pH 7.9, at 298 K (black) and 274 K (red).

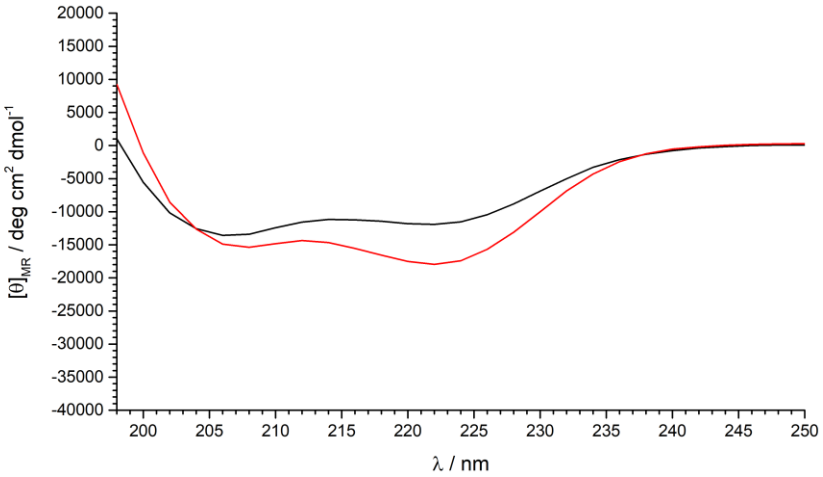

Fig. 105: CD spectra of (jg)IBTC-1 in water, pH 3, at 298 K (black) and 274 K (red).

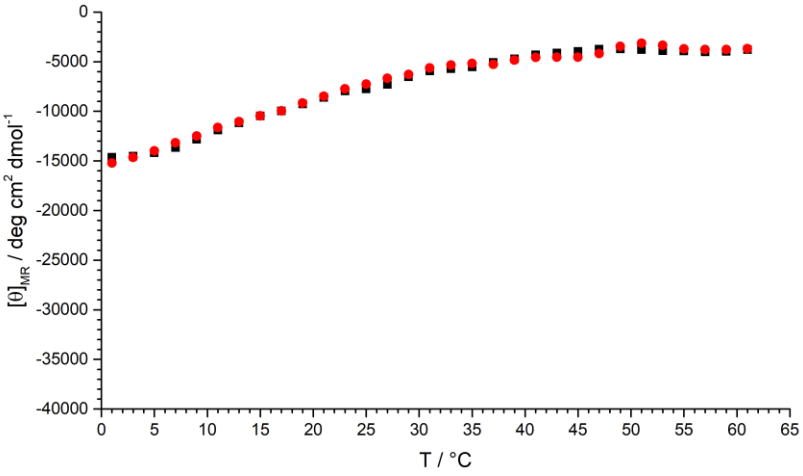

Fig. 106: CD thermal denaturation scan of (jg)IBTC-1 in 0.1 M NH_4HCO_3 buffer, pH 7.9. The black squares show the heating curve, the red circles the cooling curve. The estimated T_m is 12 °C, while the sample shows a complete unfolding above 40 °C.

Tab. 46: Helical content of (jg)IBTC-1 at 1 °C and 0.1 M NH_4HCO_3 buffer, pH 7.9, or water, pH 3.

	0.1 M NH_4HCO_3, pH 7.9	pH 3
$[\Theta]_{obs}$ (deg cm^2 dmol^{-1})	-14.871	-18.051
$[\Theta]_{ref}$ (deg cm^2 dmol^{-1})	-42.188	-42.188
Helical content (%)	35	43

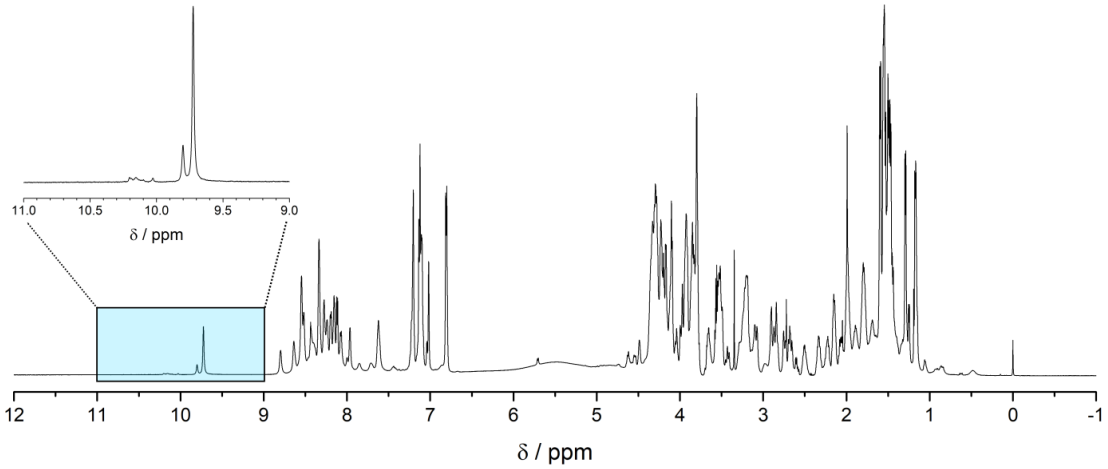

Fig. 107: ^{1}H NMR spectrum of (jg)IBTC-1 in 0.1 M NH_4HCO_3 buffer, pH 7.9, at 274 K with enlargement of the indole proton region around 10 ppm.

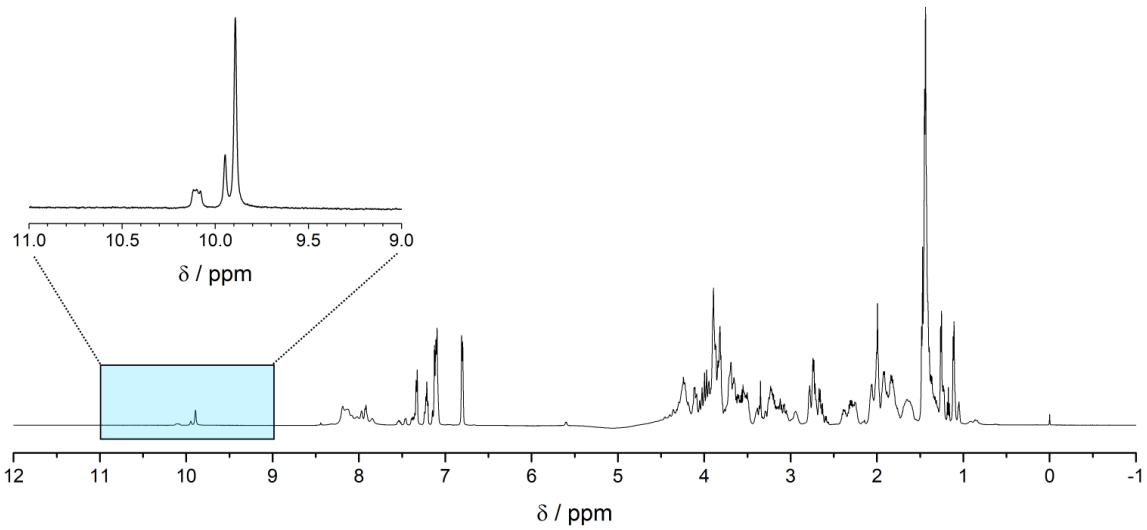

Fig. 108: ^{1}H NMR spectrum of (jg)IBTC-1 in 0.1 M NH_4HCO_3 buffer, pH 7.9, at 298 K with enlargement of the indole proton region around 10 ppm.

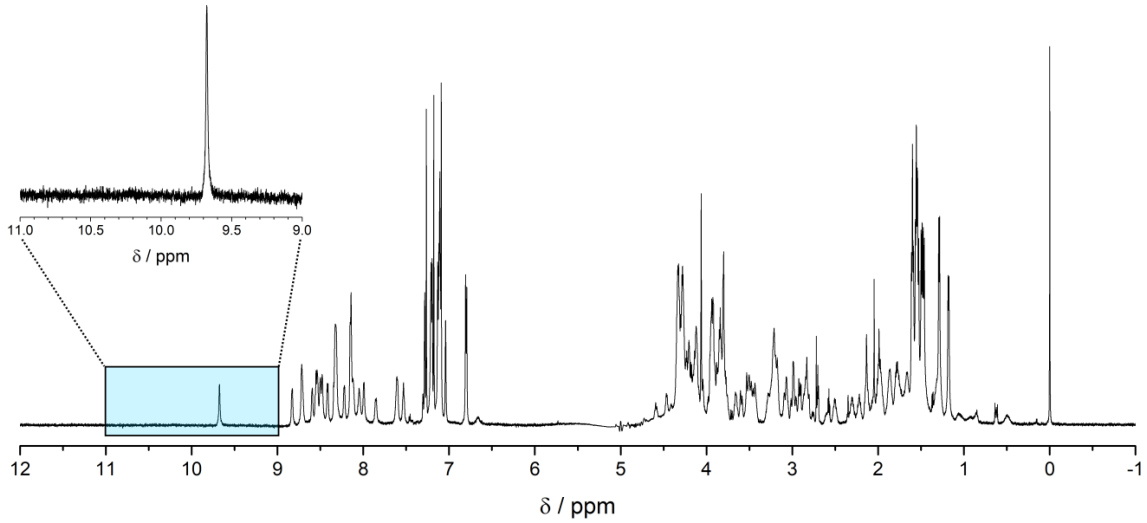

Fig. 109: ^{1}H NMR spectrum of (jg)IBTC-1 in H_2O/D_2O, pH 3, at 274 K with enlargement of the indole proton region around 10 ppm.

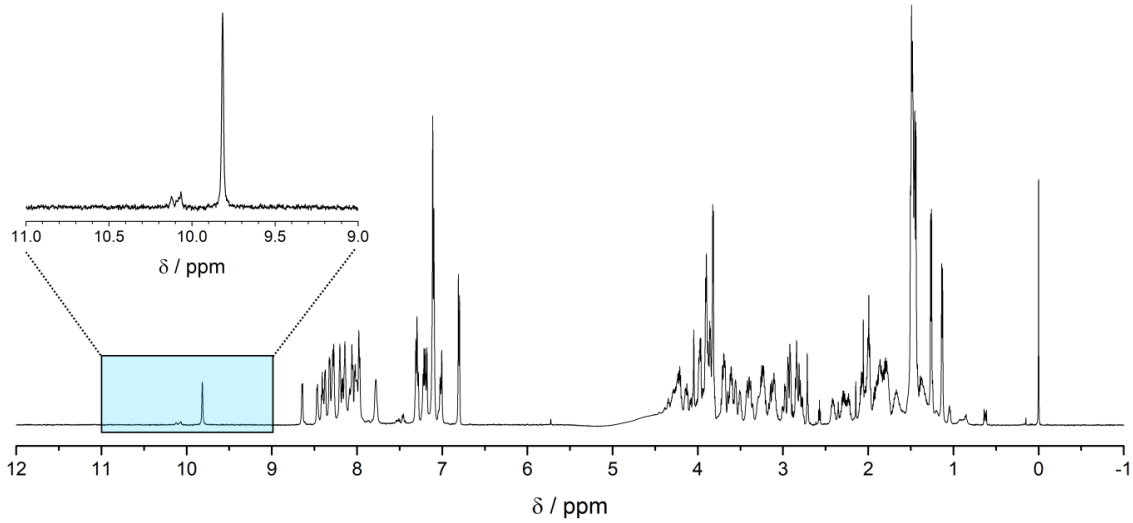

Fig. 110: ^{1}H NMR spectrum of (jg)IBTC-1 in H_2O/D_2O, pH 3, at 298 K with enlargement of the indole proton region around 10 ppm.

Tab. 47: ^{1}H-chemical shifts of (jg)IBTC-1 in 0.1 M NH_4HCO_3 buffer, pH 7.9, at 274 K. Residues marked in italic belong to the second folded conformation.

Residue		Chemical shift *δ* (ppm)				
		NH	α	β	γ	
1‘	Asp	n.d.				
2‘	Thr	8.624	4.228	n.d.	1.444	
3‘	Ala	8.431	4.286	1.474		
4‘	Ser	8.796	4.336	4.048, 3.938		
5‘	Asp	8.546	4.546	2.849, 2.749		
6‘	Ala	8.334	4.338	1.580		
1	Ala	8.317	4.338	1.485		
2	Ala	8.277	4.323	1.554		
3	Tyr	8.544	4.119	3.193		δ7.119 ε6.799
	Tyr	8.510	4.145	3.156		
4	Ala	8.518	4.309	1.599		
5	Ala	8.152	4.230	1.535		
6	Trp	7.964	4.289	3.431, 3.207		δ7.022 ε9.727, 7.091 ζ 7.198, 7.096 η 7.200
	Trp	7.999	4.320	3.409, 3.218		
7	Thr	8.639	3.250	4.266	1.172	
8	Ala	8.341	4.101	1.502		
9	Asp	7.626	4.632	2.853, 2.680		
	Asp	7.120	4.616	2.835, 2.671		
10	Gly	7.609	4.140, 3.507			
	Gly	7.699	4.099, 3.553			
11	Gly	8.237	3.213, 0.972			
12	Pro		4.617	2.501, 2.064	2.153	δ 3.803, 3.528
13	Ser	7.848	4.490	3.926		
14	Ser	8.269	4.173	3.865		
15	Gly	8.073	4.228, 3.804			
16	Arg	8.196	4.998	1.8042, 1.787	1.645	
17	Pro		4.740	2.333, 1.787	1.992	δ 3.856, 3.659
18	Pro		2.623	1.332,	1.693	δ3.520

				0.476		
19	Pro		4.295	2.221, 1.975	1.903, 1.801	δ3.113, 2.909
20	Ser	8.397	4.356	3.823		
21	Gly	8.540	3.962			
22	Ser	8.117	4.228	3.800		

Tab. 48: ^{15}N and ^{13}C-chemical shifts of (jg)IBTC-1 in 0.1 M NH_4HCO_3 buffer, pH 7.9, at 274 K.

Residue		Chemical shift *δ* (ppm)				
		N		Cα	Cβ	
1‘	Asp	n.d.		n.d.		
2‘	Thr	116.41		n.d.		
3‘	Ala	124.78		54.80	17.91	
4‘	Ser	117.79		61.16	62.20	
5‘	Asp	125.71		56.69	40.47	
6‘	Ala	124.43		54.80	17.76	
1	Ala	122.89		54.80	17.77	
2	Ala	122.74		54.80	17.77	
3	Tyr	122.46		62.44	38.27	δ 132.95 ε 118.42
4	Ala	123.19		54.80	17.76	
5	Ala	122.40		54.52	17.77	
6	Trp	120.75	131.59	62.45	28.18	δ 127.47 ε 120.78 ζ 122.53, 114.16 η 123.84
7	Thr	116.41		66.28	68.83	γ 21.53
8	Ala	126.41		54.78	17.77	
9	Asp	117.55		54.35	41.28	
10	Gly	106.10		49.70		
11	Gly	113.77		43.42		
12	Pro	n.d.		64.69	31.87	γ 27.37 δ 51.10
13	Ser	113.39		59.18	63.00	
14	Ser	117.62		60.13	63.98	
15	Gly	110.02		45.05		
16	Arg	120.00		n.d.	27.05	γ 26.83
17	Pro	n.d.		n.d.	30.58	γ 27.11 δ 50.63
18	Pro	n.d.		n.d.	29.15	γ 26.69 δ 49.70
19	Pro	n.d.		62.50	31.71	γ 27.22 δ 49.52
20	Ser	115.62		58.40	63.98	
21	Gly	111.43		45.96		
22	Ser	121.71		59.96	64.71	

Tab. 49: ^{1}H-chemical shifts of (jg)IBTC-1 in H_2O/D_2O, pH 3, at 274 K.

Residue		Chemical shift δ (ppm)				
		NH	α	β	γ	
1‘	Asp	exch.	4.322	2.973		
2‘	Thr	8.719	4.115	4.180	1.288	
3‘	Ala	8.478	4.277	1.470		
4‘	Ser	8.829	4.334	4.051, 3.934		
5‘	Asp	8.501	4.588	2.925, 2.824		
6‘	Ala	8.330	4.333	1.577		
1	Ala	8.313	4.333	1.554		
2	Ala	8.319	4.333	1.559		
3	Tyr	8.594	4.103	3.188, 3.185		δ7.128 ε6.801
4	Ala	8.534	4.311	1.607		
5	Ala	8.146	4.221	1.535		
6	Trp	7.994	4.265	3.458, 3.207		δ7.041 ε9.678, 7.208 ζ 7.107
7	Thr	8.708	3.219	4.274	1.180	
8	Ala	8.316	4.138	1.496		
9	Asp	7.600	4.729	3.002, 2.826		
10	Gly	7.612	4.146, 3.520			
11	Gly	8.118	3.084, 1.035			
12	Pro		4.591	2.507, 2.057	2.140, 2.134	δ 3.765, 3.431
13	Ser	7.852	4.465	3.925		
14	Ser	8.222	4.206	3.891, 3.595		
15	Gly	8.049	4.250, 3.830			
16	Arg	8.147	4.933	1.862, 1.751	1.669	δ3.264 ε7.532
17	Pro		4.714	2.303, 1.785	1.996	δ 3.860, 3.657
18	Pro		2.600	1.542, 0.497	1.709, 1.687	δ3.494, 3.032
19	Pro		4.291	2.219, 1.960	1.866, 1.789	δ3.069, 2.862
20	Ser	8.415	4.342	3.837, 3.803		
21	Gly	8.551	3.947			
22	Ser	8.150	4.281	3.805, 3.805		

Tab. 50: ^{15}N and ^{13}C-chemical shifts of (jg)IBTC-1 in H_2O/D_2O, pH 3, at 274 K.

Residue		Chemical shift δ (ppm)				
		N		Cα	Cβ	
1‘	Asp	n.d.		55.42	38.93	
2‘	Thr	115.64		65.23	69.31	γ21.90
3‘	Ala	124.77		54.78	17.93	
4‘	Ser	117.57		60.83	62.93	
5‘	Asp	125.36		57.44	38.81	
6‘	Ala	122.78		54.79	17.67	
1	Ala	122.69		54.79	17.77	
2	Ala	124.41		54.79	17.69	
3	Tyr	122.62		n.d.	38.13	δ 132.96 ε 118.56
4	Ala	122.98		54.87	17.67	
5	Ala	122.32		54.53	17.85	
6	Trp	120.80	131.57	61.60	n.d.	δ 127.55 ε 123.99 ζ 122.69, 113.95
7	Thr	116.68		66.58	68.91	γ 21.58
8	Ala	125.90		54.52	17.73	
9	Asp	116.33		n.d.	39.48	
10	Gly	106.17		49.63		
11	Gly	112.93		43.41		
12	Pro	n.d.		n.d.	31.77	γ 27.63 δ 51.33
13	Ser	113.50		n.d.	62.78	
14	Ser	117.37		58.70	62.02	
15	Gly	109.98		45.62		
16	Arg	120.19	114.78	n.d.	27.14	γ 26.82 δ 43.18
17	Pro	n.d.		n.d.	30.38	γ 27.16 δ 50.70
18	Pro	n.d.		n.d.	n.d.	γ 26.95 δ 49.94
19	Pro	n.d.		62.00	31.72	γ 27.16
20	Ser	115.73		58.16	64.48	
21	Gly	111.57		45.20		
22	Ser	120.16		59.26	64.48	

Tab. 51: ^{1}H-chemical shifts of (jg)IBTC-1 in H_2O/D_2O, pH 3, at 298 K.

Residue		Chemical shift δ (ppm)				
		NH	α	β	γ	
1‘	Asp	exch.	4.345	2.981		
2‘	Thr	8.645	4.237	4.169	1.262	
3‘	Ala	8.375	4.297	1.446		
4‘	Ser	8.467	4.354	3.981, 3.889		
5‘	Asp	8.323	4.619	2.841, 2.833		
6‘	Ala	8.201	4.267	1.493		
1	Ala	8.149	4.271	1.468		
2	Ala	8.023	4.211	1.468		
3	Tyr	8.291	4.229	3.147, 3.134		δ7.105 ε6.805
4	Ala	8.271	4.244	1.492		
5	Ala	8.201	4.267	1.493		
6	Trp	7.979	4.391	3.397, 3.245		δ7.109 ε9.817, 7.292 ζ 7.350, 7.117 η 7.214
7	Thr	8.320	3.557	4.200	1.429	
8	Ala	8.138	4.139	1.450		
9	Asp	7.785	4.699	2.929, 2.792		
10	Gly	7.771	4.068, 3.665			
11	Gly	8.062	3.360, 2.1339			
12	Pro		4.513	2.411, 2.015	2.073	δ 3.684, 3.419
13	Ser	8.008	4.450	3.902, 3.896		
14	Ser	8.168	4.288	3.903, 3.702		
15	Gly	8.087	4.129, 3.874			
16	Arg	8.053	4.572	1.863, 1.773	1.677	δ3.226 ε7.309
17	Pro		4.682	2.285, 1.815	1.990	δ 3.822, 3.612
18	Pro		3.384	1.526, 1.213	1.801, 1.202	δ3.604, 3.504
19	Pro		4.331	2.234, 1.919	1.867	δ3.286, 3.112
20	Ser	8.278	4.385	3.839, 3.817		
21	Gly	8.409	3.976,			

			3.970			
22	Ser	7.972	4.308	3.823, 3.817		

Tab. 52: ^{15}N and ^{13}C-chemical shifts of (jg)IBTC-1 in H_2O/D_2O, pH 3, at 298 K.

Residue		Chemical shift *δ* (ppm)				
		N		Cα	Cβ	
1‘	Asp	n.d.		52.67	37.95	
2‘	Thr	115.27		63.52	69.53	γ21.78
3‘	Ala	125.67		54.19	18.18	
4‘	Ser	115.86		59.78	62.82	
5‘	Asp	123.27		n.d.	39.32	
6‘	Ala	122.34		54.19	17.88	
1	Ala	122.42		53.97	18.43	
2	Ala	122.08		53.94	18.51	
3	Tyr	120.75		60.76	38.20	δ 132.95 ε 118.44
4	Ala	123.78		54.02	18.16	
5	Ala	124.09		54.19	17.91	
6	Trp	122.26	130.72	58.19	28.51	δ 127.34 ε 120.94 ζ 122.33, 114.41 η 124.20
7	Thr	115.59		64.91	69.34	γ18.43
8	Ala	125.70		53.97	18.46	
9	Asp	116.60		n.d.	39.20	
10	Gly	107.15		44.83		
11	Gly	111.24		n.d.		
12	Pro	n.d.		73.00	32.24	γ 27.36 δ 50.70
13	Ser	114.22		n.d.	63.23	
14	Ser	117.19		59.55	64.51	
15	Gly	109.92		45.53		
16	Arg	120.55	114.85	n.d.	30.56	γ 27.03 δ 43.45
17	Pro	n.d.		n.d.	30.36	γ 27.19 δ 50.94
18	Pro	n.d.		60.65	29.72	γ 27.06 δ 50.15
19	Pro	n.d.		59.91	31.70	γ 27.32 δ 49.90
20	Ser	115.66		60.14	64.42	
21	Gly	111.31		45.31		
22	Ser	120.19		59.48	64.42	

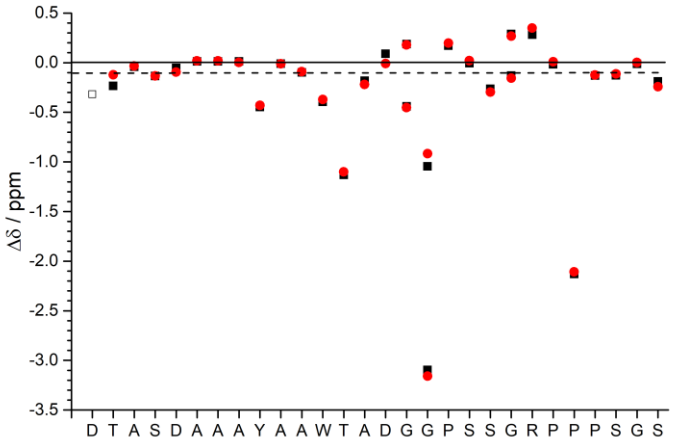

Fig. 111: Hα CSD plots of (jg)IBTC-1 at 274 K and 0.1 M NH_4HCO_3, pH 7.9, (red circles) and H_2O/D_2O, pH 3, (black squares). The dashed line at y=-0.1 ppm represents the helical limit.

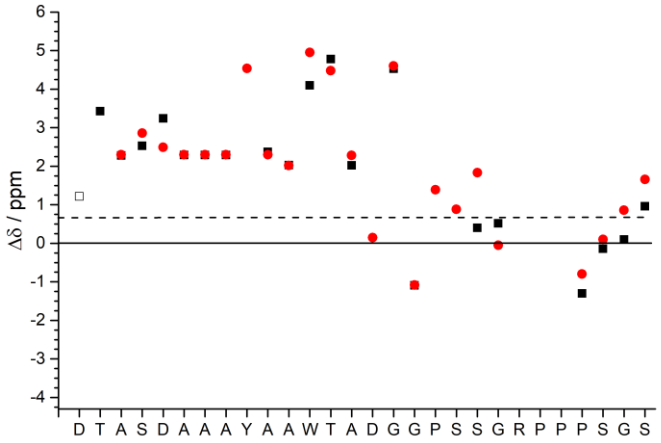

Fig. 112: Cα CSD plots of (jg)IBTC-1 at 274 K and 0.1 M NH_4HCO_3, pH 7.9, (red circles) and H_2O/D_2O, pH 3, (black squares). The dashed line at y=0.7 ppm represents the helical limit.

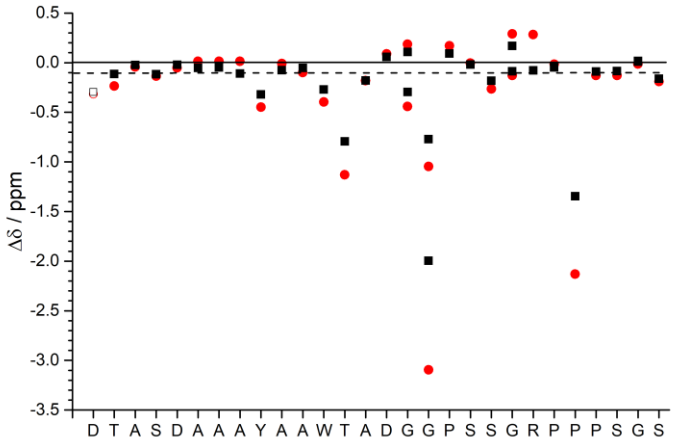

Fig. 113: Hα CSD plots of (jg)IBTC-1 at pH 3 and 274 K (red circles) and 298 K (black squares). The dashed line at y=-0.1 ppm represents the helical limit.

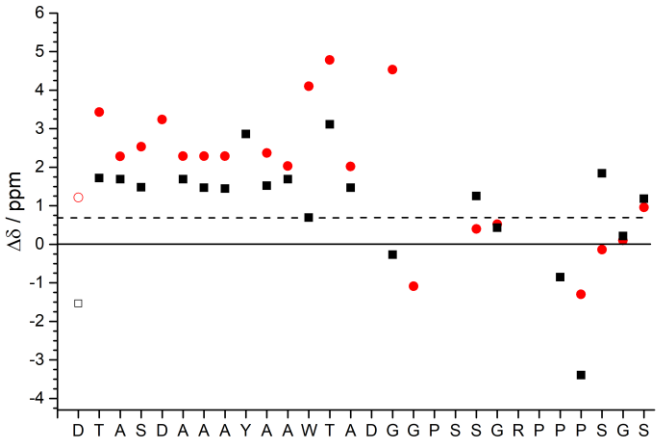

Fig. 114: Cα CSD plots of (jg)IBTC-1 at pH 3 and 274 K (red circles) and 298 K (black squares). The dashed line at y=0.7 ppm represents the helical limit.

Tab. 53: CSDs for selected protons of the cage structure representing the cage fold of (jg)IBTC-1 at pH 3 and pH 7.9 and 274 K and 298 K, given the fraction folded according to Lin *et al*.[75]

$\chi_{Trp\text{-}cage}$	Δδ (ppm)						Σ
	T7α	G11α'	P18α	Pro18β'	P19δ	P19δ'	
pH 7.9, 274 K	-1.100	-3.048	-2.107	-1.814	-0.477	-0.831	-9.377
pH 3, 274 K	-1.131	-2.985	-2.130	-1.793	-0.521	-0.878	-9.439
pH 3, 298 K	-0.793	-1.886	-1.346	-1.077	-0.304	-0.628	-6.034

Tab. 54: CSDs for selected protons in the helical region representing the helix fold of (jg)IBTC-1 at pH 3 and pH 7.9 and 274 K and 298 K.

χ_{Helix}	Δδ (ppm)							Σ
	A2α	Y3α	A4α	A5α	W6α	T7α	A8α	
pH 7.9, 274 K	0.003	-0.431	-0.011	-0.090	-0.371	-1.100	-0.219	-2.219
pH 3, 274 K	0.013	-0.447	-0.009	-0.099	-0.396	-1.131	-0.182	-2.251
pH 3, 298 K	-0.109	-0.321	-0.076	-0.053	-0.270	-0.793	-0.181	-1.803

Antifreeze activity (80 mg/mL, 0.1 M NH_4HCO_3, pH 7.9):

- Ice growth retardation: 0.039 °C
- ice shaping

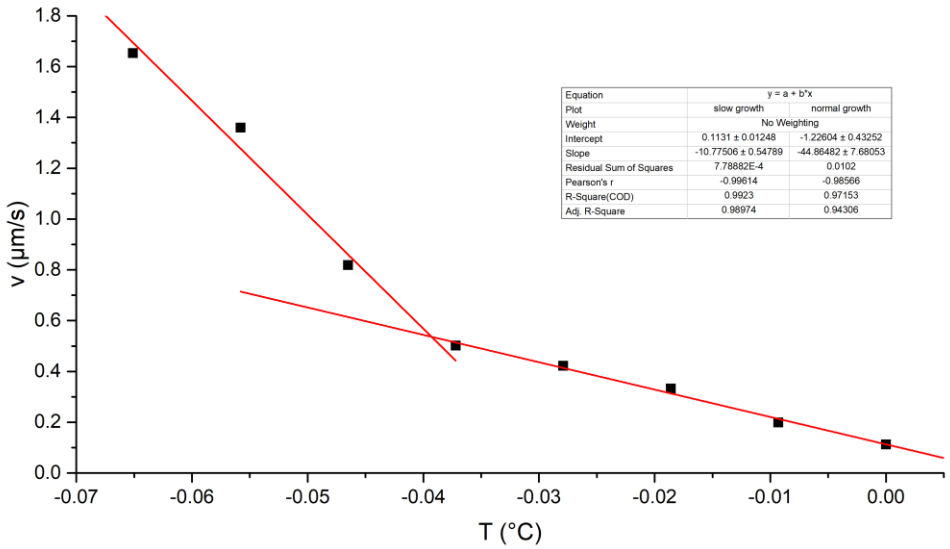

Fig. 115: Ice growth retardation plot of 80 mg/mL (jg)IBTC-1 in 0.1 M NH_4HCO_3, pH 7.9. The growth retardation is 0.039 °C.

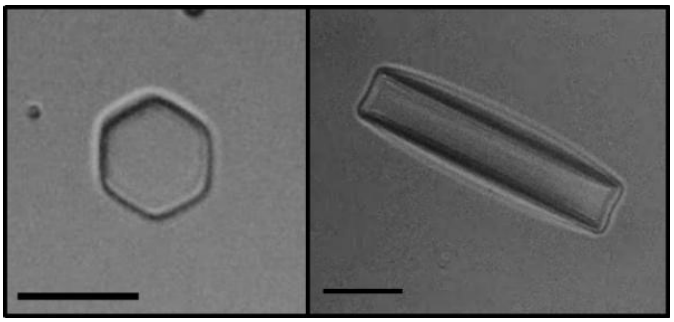

Fig. 116: Ice crystals during the growth in the presence of 80 mg/mL (jg)IBTC-1 in 0.1 M NH_4HCO_3, pH 7.9. Left the top view shows the view perpendicular to the basal plane, while on the right the side view of the crystal is shown. The black scale in each picture is 10 µm long.

5.7 (jg)IBTC-2

Sequence	DTASDAAAAAALTAANAAAYAAWTADGGPSSGRPPPSGS
Molecular weight	3517.68 Da
Absorption coefficient	ε_{280}= 6990 $M^{-1}cm^{-1}$
Yield	1.0 mg/ L LB medium
	0.5 mg/ L minimal medium

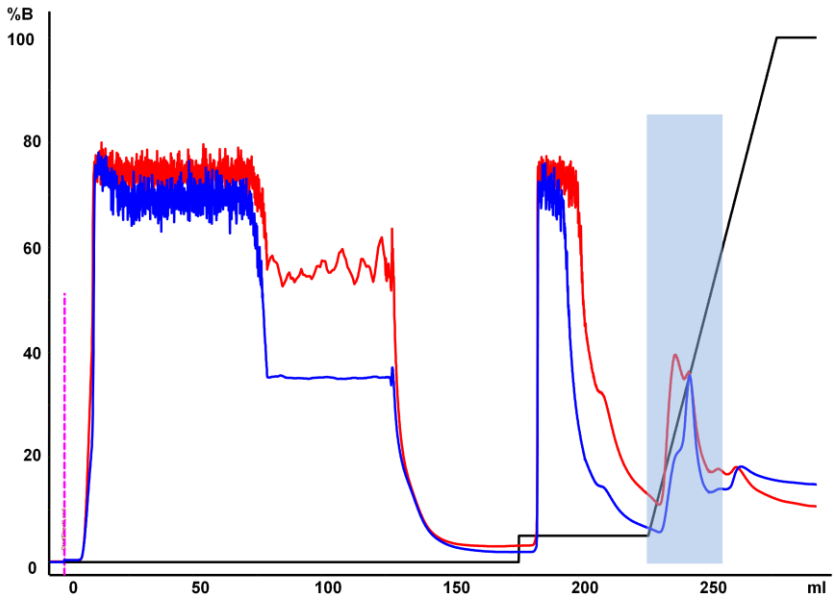

Fig. 117: Profile of the affinity purification of (jg)SUMO-IBTC-2. The signal was detected at 280 nm (blue) and 254 nm (red). The gradient of the elution buffer is shown in black. With the injection at 0 mL the chromatogram starts. Fractions that were combined and collected are marked in blue.

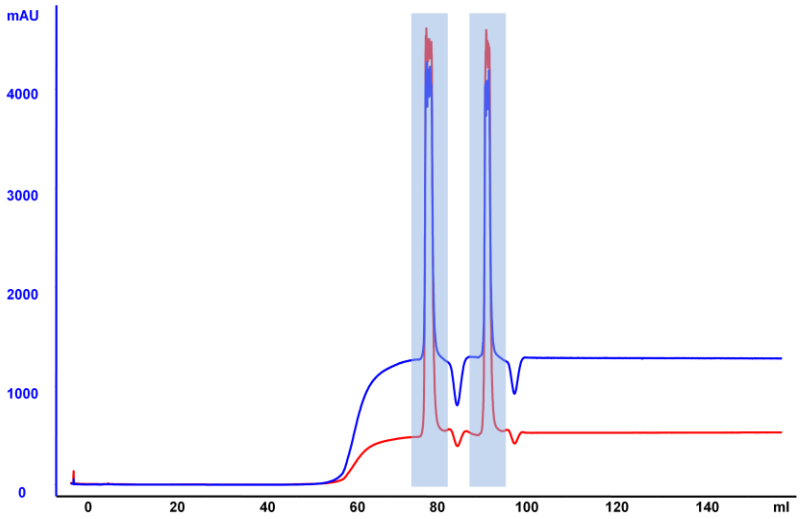

Fig. 118: Profile of the rebuffering of (jg)SUMO-IBTC-2. The signal was detected at 280 nm (blue) and 254 nm (red). Fractions that were combined and collected are marked in blue.

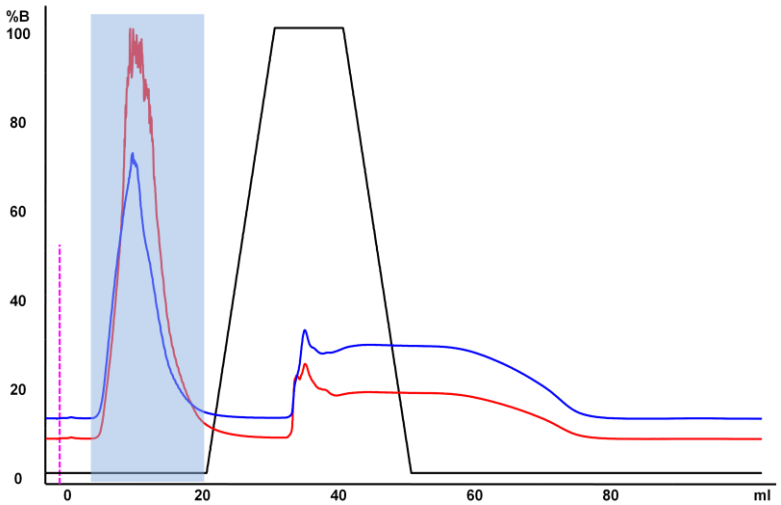

Fig. 119: Profile of the affinity purification of (jg)IBTC-2. The signal was detected at 280 nm (blue) and 254 nm (red). The gradient of the elution buffer is shown in black. The injections are dashed pink lines. Fractions which were collected and combined are marked in blue.

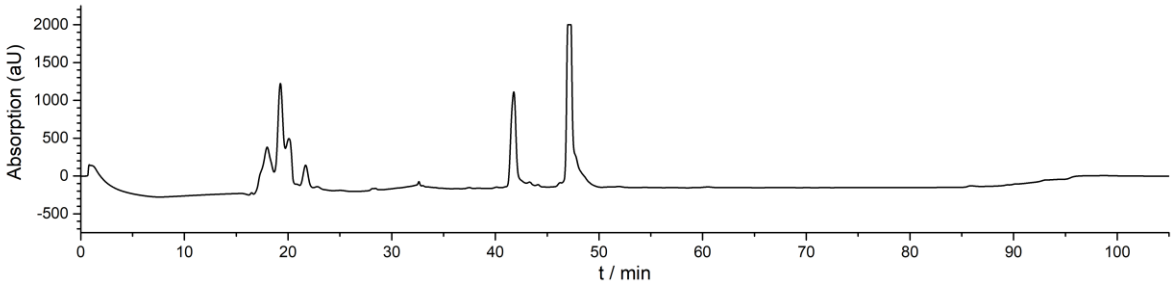

Fig. 120: HPLC profile of the semi-preparative run of (jg)IBTC-2. t_R is 47 min.

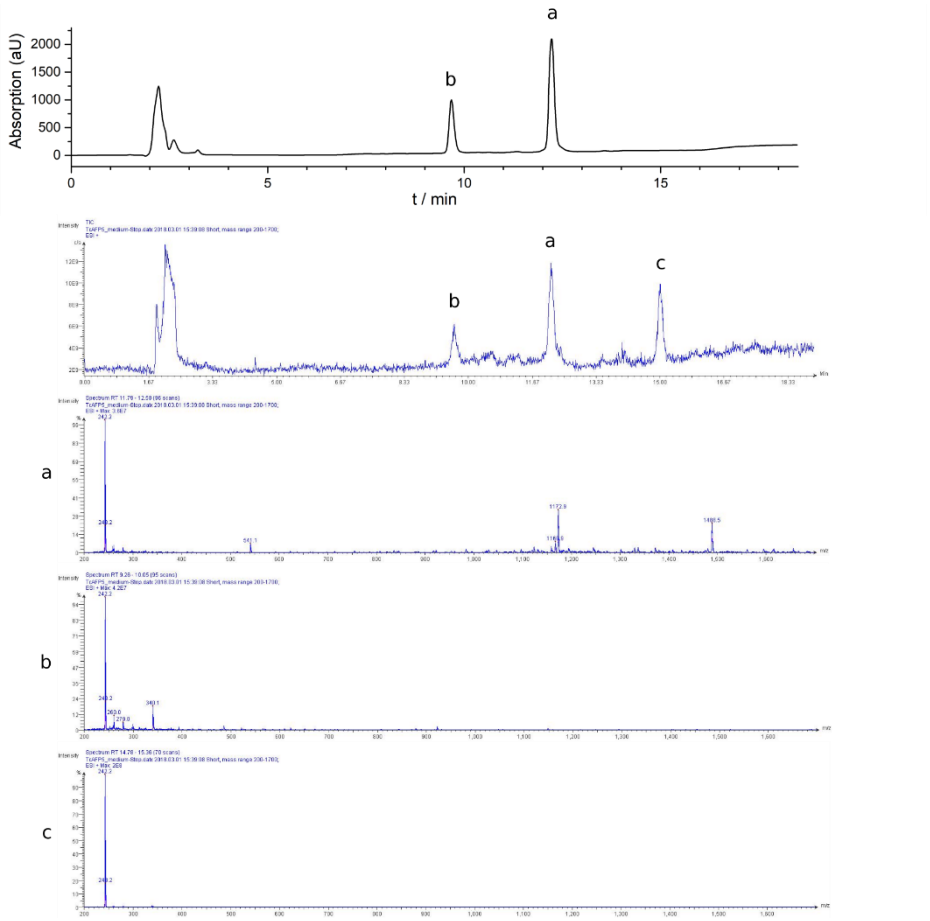

Fig. 121: HPLC profile of the analytical run (top), ion chromatogram (2nd panel from top) and MS spectra of all signals of purified (jg)IBTC-2. *m/z*: $[M+3H]^{3+}$ calcd 1173.6, found 1172.9. t_R is 12.2 min.

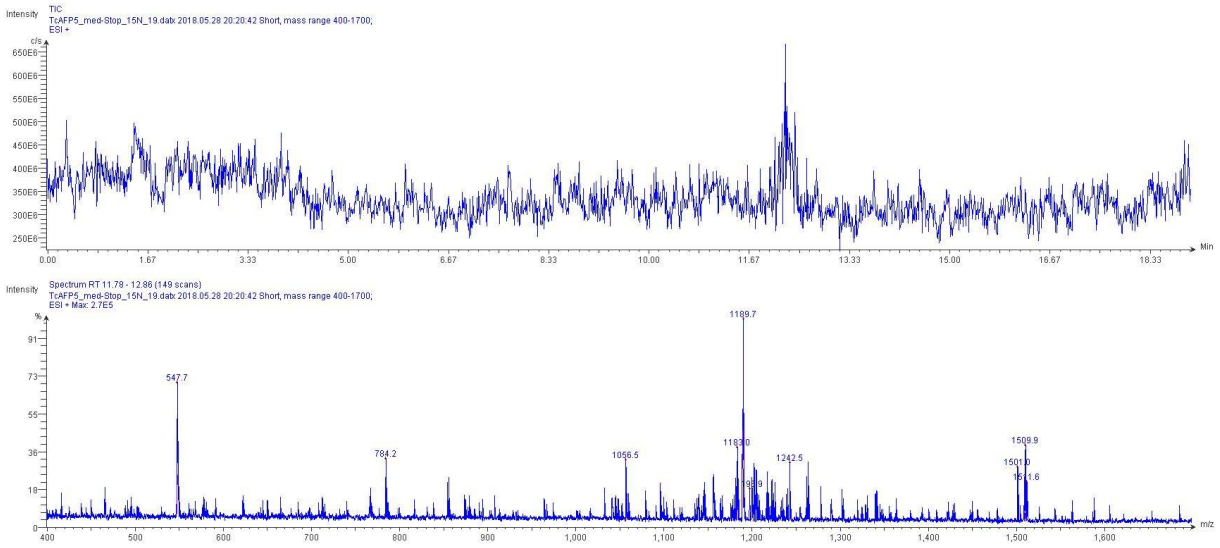

Fig. 122: and ion chromatograms of all signals of purified ^{15}N labeled (jg)IBTC-2. *m/z*: $[M+3H]^{3+}$ calcd 1188.2, found 1189.7. t_R is 12.2 min.

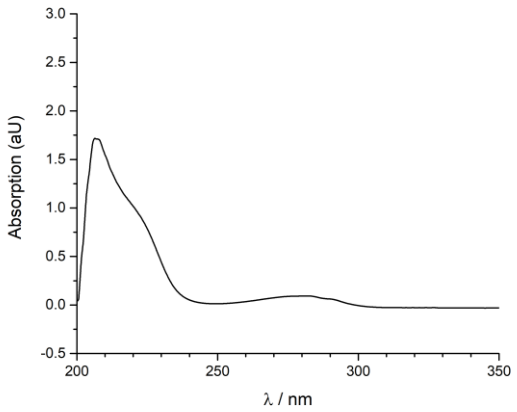

Fig. 123: UV/vis spectrum of (jg)IBTC-2 at 298 K in 0.1 M NH_4HCO_3 buffer, pH 7.9. The spectrum was measured to 600 nm, displayed only to 350 nm.

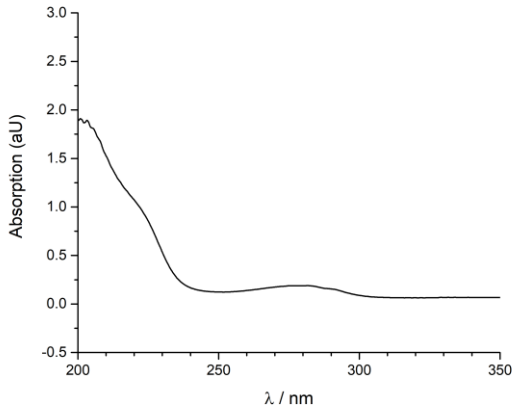

Fig. 124: UV/vis spectrum of (jg)IBTC-2 at 298 K in water at pH 3. The spectrum was measured to 600 nm, displayed only to 350 nm.

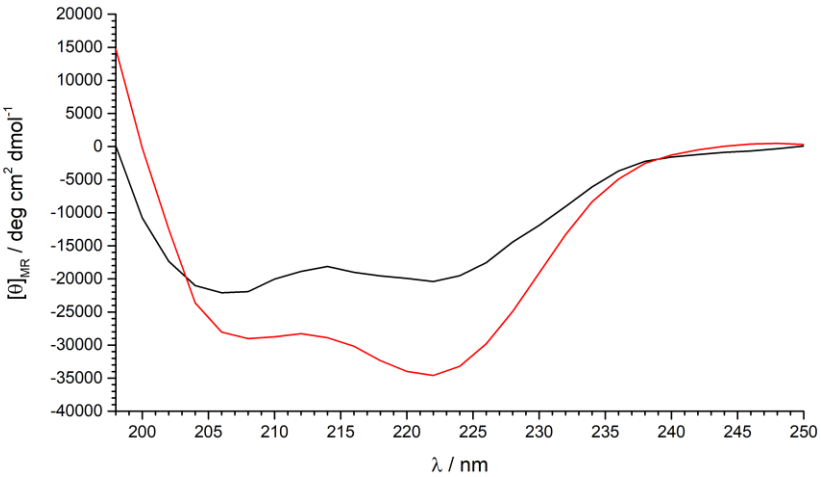

Fig. 125: CD spectra of (jg)IBTC-2 in 0.1 M NH_4HCO_3 buffer, pH 7.9, at 298 K (black) and 274 K (red).

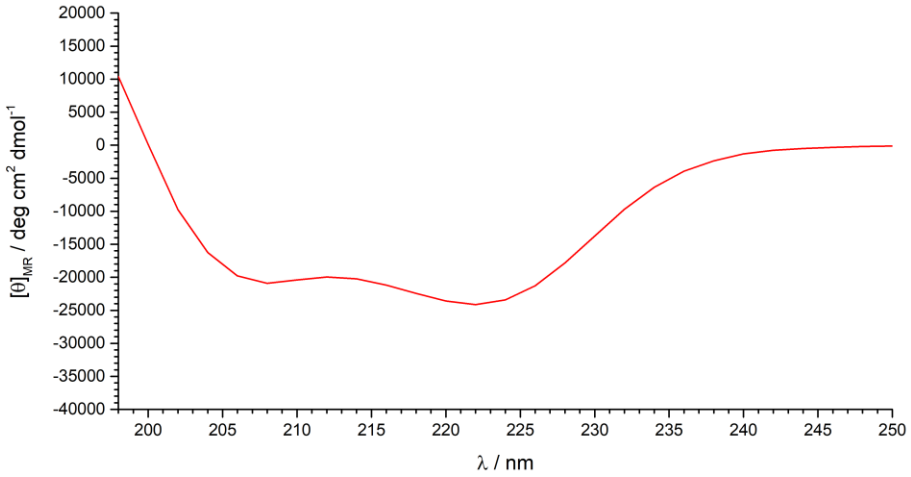

Fig. 126: CD spectra of (jg)IBTC-2 in water, pH 3, at 274 K.

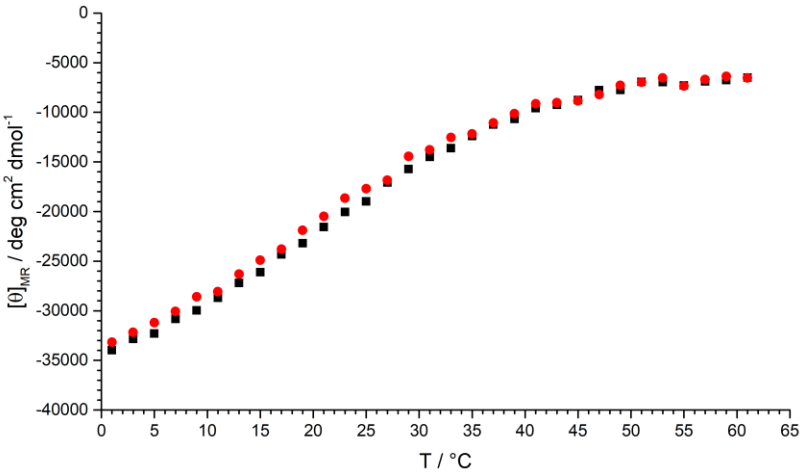

Fig. 127: CD thermal denaturation scan of (jg)IBTC-2 in 0.1 M NH_4HCO_3 buffer, pH 7.9. The black squares show the heating curve, the red circles the cooling curve.

Tabelle 55: Calculated melting points for (jg)IBTC-2 in 0.1 M NH_4HCO_3 buffer, pH 7.9.

	heating	cooling
Boltzmann fit	20.5 ±0.5	19.0 ±0.5

Tab. 56: Helical content of (jg)IBTC-2 at 1 °C and 0.1 M NH_4HCO_3 buffer, pH 7.9, or water, pH 3.

	0.1 M NH_4HCO_3, pH 7.9	pH 3
$[\Theta]_{obs}$ (deg cm^2 dmol^{-1})	-34.195	-24.099
$[\Theta]_{ref}$ (deg cm^2 dmol^{-1})	-42.628	-42.628
Helical content (%)	80	57

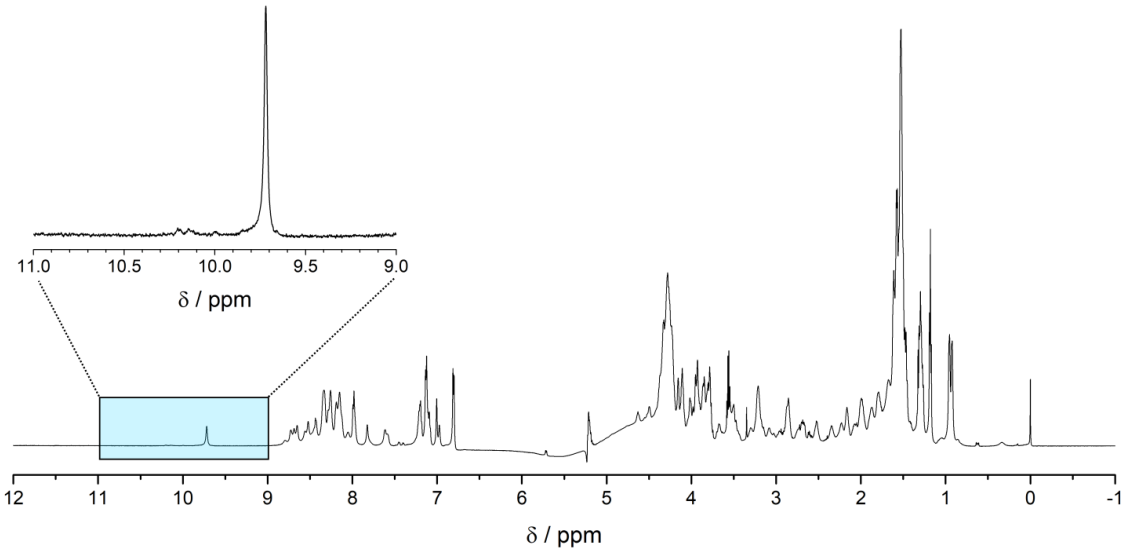

Fig. 128: ^{1}H NMR spectrum of (jg)IBTC-2 in 0.1 M NH_4HCO_3 buffer, pH 7.9, at 274 K with enlargement of the indole proton region around 10 ppm.

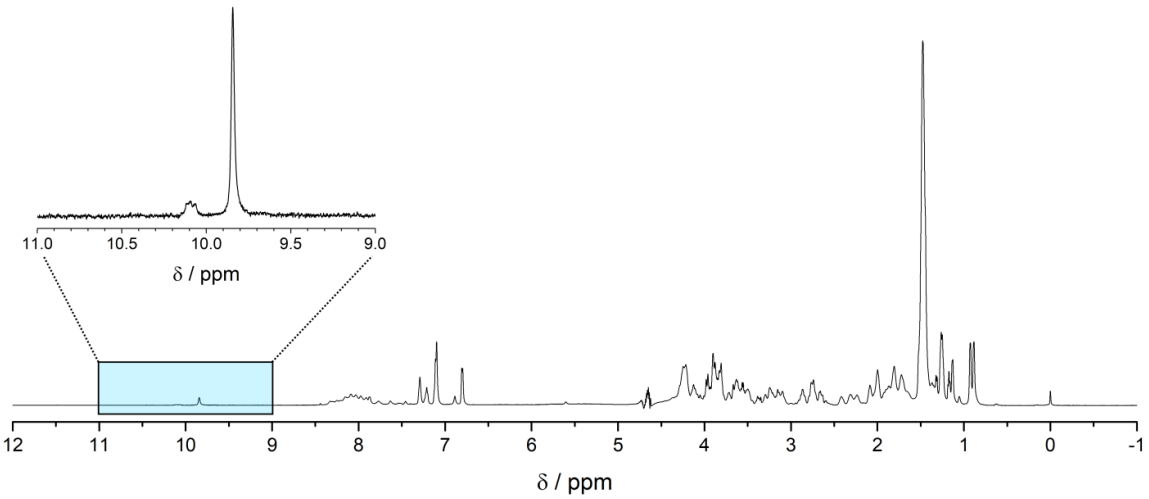

Fig. 129: ^{1}H NMR spectrum of (jg)IBTC-2 in 0.1 M NH_4HCO_3 buffer, pH 7.9, at 298 K with enlargement of the indole proton region around 10 ppm.

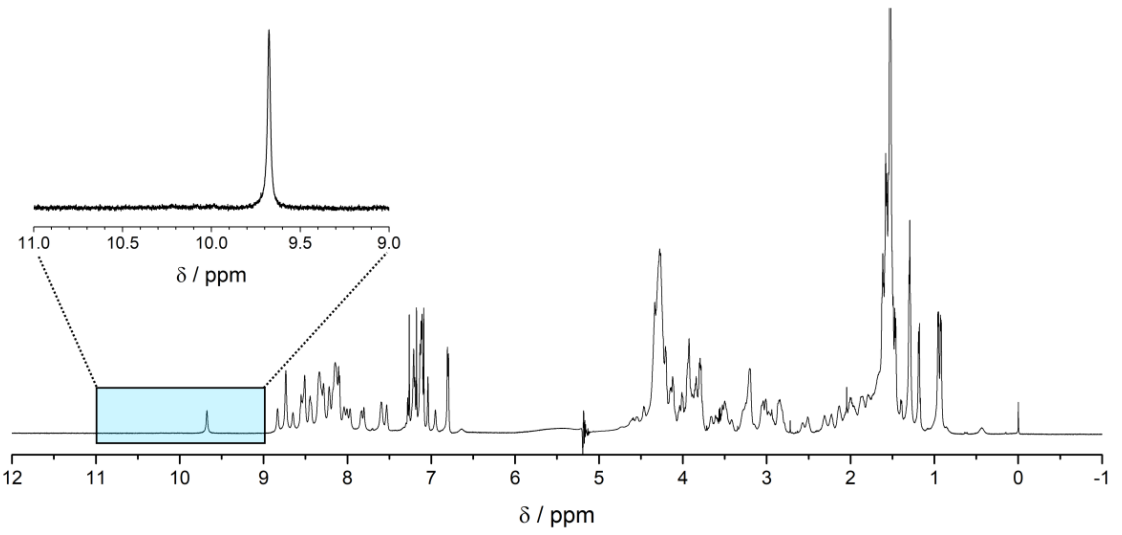

Fig. 130: ^{1}H NMR spectrum of (jg)IBTC-2 in H_2O/D_2O, pH 3, at 274 K with enlargement of the indole proton region around 10 ppm.

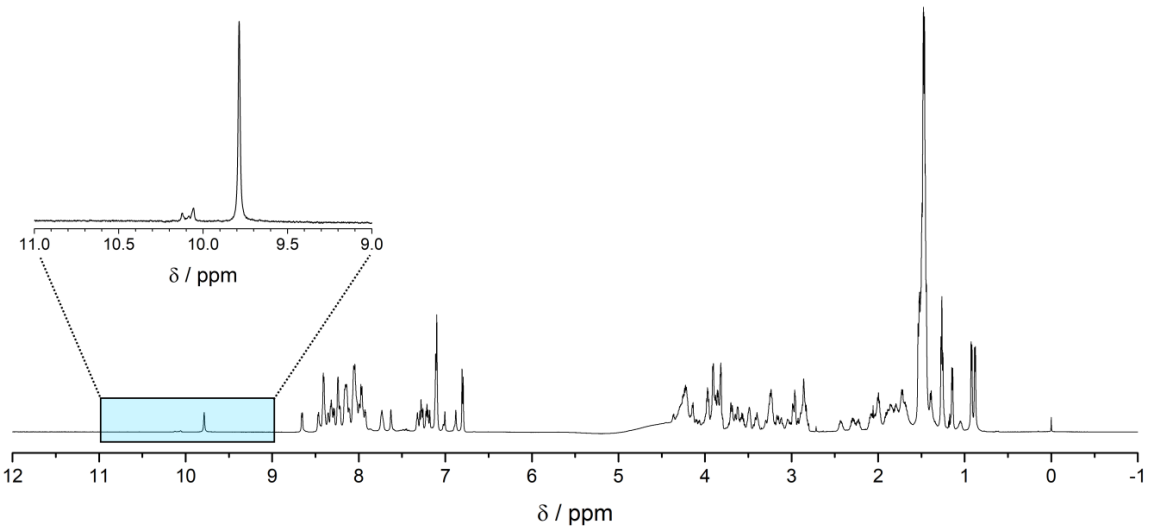

Fig. 131: ^{1}H NMR spectrum of (jg)IBTC-2 in H_2O/D_2O, pH 3, at 298 K with enlargement of the indole proton region around 10 ppm.

Tab. 57: ^{1}H-chemical shifts of (jg)IBTC-2 in 0.1 M NH_4HCO_3 buffer, pH 7.9, at 274 K.

Residue		Chemical shift δ (ppm)				
		NH	α	β	γ	
1‘	Asp	n.d.				
2‘	Thr	n.d.				
3‘	Ala	n.d.				
4‘	Ser	n.d.				
5‘	Asp	n.d.				
6‘	Ala	n.d.				
7‘	Ala	n.d.				
8‘	Ala	n.d.				
9‘	Ala	n.d.				
10‘	Ala	n.d.				
11‘	Ala	n.d.		1.538		
12‘	Leu	7.972	4.304	1.877, 1.739		
13‘	Thr	8.289	4.018	4.264	1.289	
14‘	Ala	8.153	4.243	1.537		
15‘	Ala	n.d.	4.295	1.581		
16‘	Asn	8.724	4.627	2.959, 2.860		
17‘	Ala	8.328	4.358	1.600		
1	Ala					
2	Ala	8.353	4.347	1.590		
3	Tyr	8.652	4.100	3.220		δ7.123 ε6.800
4	Ala	8.523	4.322	1.621		

5	Ala	n.d.				
6	Trp	7.981	4.229	3.454, 3.209		δ7.009 ε 9.723, 7.093 ζ 7.188, 7.116 η7.205
7	Thr	8.688	3.220	4.284	1.193	
8	Ala	8.336	4.252	1.512		
9	Asp	7.617	4.637	2.870, 2.680		
10	Gly	7.583	4.156, 3.491			
11	Gly	8.259	3.190, 0.831			
12	Pro		4.633	2.528, 2.074	2.165	δ3.821, 3.540
13	Ser	n.d.				
14	Ser	8.241	4.257	4.022		
15	Gly	7.989	4.230, 3.781			
16	Arg	8.195	5.041	1.900, 1.815		
17	Pro		4.761	2.345, 1.790	2.000	δ3.870, 3.672
18	Pro		2.534	1.298, 0.349	1.675	δ3.600, 3.546
119	Pro		4.303	2.229, 1.976	1.866, 1.799	δ3.086, 2.849
20	Ser	n.d.				
21	Gly	n.d.				
22	Ser	8.052	4.291	3.822		

Tab. 58: ^{15}N and ^{13}C-chemical shifts of (jg)IBTC-2 in 0.1 M NH_4HCO_3 buffer, pH 7.9, at 274 K. Shifts marked with an asterix are averaged.

Residue		Chemical shift δ (ppm)				
		N		Cα	Cβ	
1‘	Asp	n.d.		n.d.		
2‘	Thr	n.d.		n.d.		
3‘	Ala	n.d.		54.73*	17.67*	
4‘	Ser	n.d.		n.d.		
5‘	Asp	n.d.		n.d.		
6‘	Ala	n.d.		54.73*	17.67*	
7‘	Ala	n.d.		54.73*	17.67*	
8‘	Ala	n.d.		54.73*	17.67*	
9‘	Ala	n.d.		54.73*	17.67*	
10‘	Ala	n.d.		54.73*	17.67*	
11‘	Ala	n.d.		54.73*	17.76	
12‘	Leu	122.38		58.49	41.53	
13‘	Thr	116.89		66.25	68.73	γ 21.78
14‘	Ala	122.32		54.75	17.75	
15‘	Ala	n.d.		54.86	17.70	
16‘	Asn	119.72		55.05	37.29	
17‘	Ala	122.78		54.95	17.72	
1	Ala	n.d.		54.73*	17.67*	
2	Ala	122.78		54.86	17.65	
3	Tyr	n.d.		62.58	38.07	δ 132.86 ε 118.47
4	Ala	123.08		54.93	17.72	
5	Ala	n.d.		54.73*	17.67*	
6	Trp	120.67	131.61	60.01		δ 127.50 ε 121.98 η 123.63 ζ 114.01, 122.79
7	Thr	116.44		66.73	69.06	γ 21.51
8	Ala	124.56		54.82	17.76	
9	Asp	117.58		54.60	41.40	
10	Gly	n.d.		49.49		
11	Gly	n.d.		43.52		
12	Pro	n.d.		n.d.	31.77	γ 27.31 δ 49.82
13	Ser	n.d.		n.d.		
14	Ser	n.d.		60.45	62.05	
15	Gly	n.d.		n.d.		
16	Arg	119.83		n.d.	30.30	
17	Pro	n.d.		n.d.	30.47	γ 27.04 δ 50.70
18	Pro	n.d.		n.d.		γ 26.72 δ 50.07
119	Pro	n.d.		62.41	31.73	γ 26.96 δ 49.37
20	Ser	n.d.		n.d.		

21	Gly	n.d.		n.d.		
22	Ser	n.d.		58.23	64.00	

Tab. 59: ^{1}H-chemical shifts of (jg)IBTC-2 in H_2O/D_2O, pH 3, at 274 K.

Residue		Chemical shift δ (ppm)				
		NH	α	β	γ	
1‘	Asp	exch.	4.319	n.d.		
2‘	Thr	8.736	4.117	4.192	1.298	
3‘	Ala	8.510	4.275	1.468		
4‘	Ser	8.833	4.333	4.045, 3.937		
5‘	Asp	8.510	4.549	2.934, 2.807		
6‘	Ala	8.343	4.276	1.535		
7‘	Ala	n.d.				
8‘	Ala	n.d.				
9‘	Ala	n.d.				
10‘	Ala	n.d.				
11‘	Ala	8.139	4.248	1.535		
12‘	Leu	7.969	4.304	1.880, 1.726		
13‘	Thr	8.289	4.009	4.265	1.292	
14‘	Ala	8.152	4.374	1.535		
15‘	Ala	8.431	4.300	1.577		
16‘	Asn	8.734	4.620	2.959, 2.863		δ 7.707, 7.572
17‘	Ala	8.330	4.351	1.601		
1	Ala	n.d.				
2	Ala	8.349	4.352	1.609		
3	Tyr	8.649	4.100	3.214		δ 7.130 ε 6.803
4	Ala	8.530	4.309	1.623		
5	Ala	8.176	4.215	1.534		
6	Trp	8.007	4.254	3.475, 3.214		δ7.041 ε 9.615 ζ 7.213, 6.953 η 7.111
7	Thr	8.734	3.204	4.278	1.187	
8	Ala	8.310	4.147	1.500		
9	Asp	7.593	4.749	3.029, 2.852		
10	Gly	7.602	4.150, 3.518			
11	Gly	8.101	3.054, 0.991			
12	Pro		4.593	2.507	2.141, 2.062	δ 3.765, 3.415

13	Ser	7.833	4.464	3.925, 3.926		
14	Ser	8.213	4.209	3.896		
15	Gly	8.042	4.256, 3.831			
16	Arg	8.138	4.939	1.875, 1.746	1.668	δ 3.270 ε7.534
17	Pro		4.727	2.308, 1.787	1.994	δ 3.873, 3.663
18	Pro		2.573	1.300, 0.437	1.668	δ3.501
119	Pro		4.292	2.226, 1.952	1.851, 1.799	δ3.058, 2.837
20	Ser	8.449	4.316	3.820		
21	Gly	8.554	3.942			
22	Ser	8.100	4.304	3.793		

Tab. 60: ^{15}N and ^{13}C-chemical shifts of the folded conformation of (jg)IBTC-2 in H_2O/D_2O, pH 3, at 274 K. Shifts marked with an asterix are averaged.

Residue		Chemical shift δ (ppm)				
		N		Cα	Cβ	
1‘	Asp	n.d.		55.06	n.d.	
2‘	Thr	115.72		65.30	69.17	γ 22.20
3‘	Ala	124.76		54.87	18.16	
4‘	Ser	117.64		60.94	62.18	
5‘	Asp	125.14		n.d.	39.02	
6‘	Ala	122.81		55.01	17.72	
7‘	Ala	n.d.		54.87*	17.73*	
8‘	Ala	n.d.		54.87*	17.73*	
9‘	Ala	n.d.		54.87*	17.73*	
10‘	Ala	n.d.		54.87*	17.73*	
11‘	Ala	122.33		54.82	17.66	
12‘	Leu	122.43		58.92	41.69	
13‘	Thr	116.86		66.36	68.85	γ 21.83
14‘	Ala	123.99		54.99	17.60	
15‘	Ala	123.86		54.84	17.71	
16‘	Asn	119.83	114.36	n.d.	39.14	
17‘	Ala	124.58		55.02	17.84	
1	Ala	n.d.		54.87*	17.73*	
2	Ala	122.78		54.96	17.72	
3	Tyr	122.92		62.46	38.22	δ 132.90 ε 118.47
4	Ala	122.98		55.03	17.73	
5	Ala	121.56		54.78	17.83	
6	Trp	120.89	131.62	n.d.	28.09	δ 127.36 ε 124.04 η 122.60 ζ 121.08, 114.16

7	Thr	116.70		66.74	68.64	21.62
8	Ala	125.75		54.65	17.83	
9	Asp	116.08		n.d.	38.51	
10	Gly	110.53		49.59		
11	Gly	112.88		43.42		
12	Pro	n.d.		n.d.	31.85	γ 27.31 δ 51.10
13	Ser	113.42		59.50	62.94	
14	Ser	117.43		60.18	63.22	
15	Gly	109.98		n.d.		
16	Arg	120.01	114.72	n.d.	27.15	γ 26.87 δ 43.48
17	Pro	n.d.		n.d.	30.50	γ 27.15 δ 50.69
18	Pro	n.d.		60.21	29.07	γ 26.81 δ 49.62
119	Pro	n.d.		62.54	31.62	γ 27.13 δ 49.56
20	Ser	116.00		58.74	63.86	
21	Gly	111.39		45.13		
22	Ser	119.25		58.92	64.35	

Tab. 61: ^{1}H-chemical shifts of (jg)IBTC-2 in H_2O/D_2O, pH 3, at 278 K.

Residue		Chemical shift δ (ppm)				
		NH	α	β	γ	
1‘	Asp	exch.				
2‘	Thr	8.751	4.244	4.244	1.297	
3‘	Ala	8.636	4.296	1.455		
4‘	Ser	8.661	4.374	3.973		
5‘	Asp	8.452	4.645	2.984		
6‘	Ala	8.380	4.247	1.508		
7‘	Ala	8.183	4.247	1.529		
8‘	Ala	8.341	4.320	1.588		
9‘	Ala	8.137	4.235	1.525		
10‘	Ala	8.170	4.217	1.519		
11‘	Ala	8.138	4.247	1.506		
12‘	Leu	7.966	4.320	1.767		δ0.921
13‘	Thr	8.269	4.037	4.298	1.292	
14‘	Ala	8.183	4.290	1.524		
15‘	Ala	8.406	4.284	1.571		
16‘	Asn	8.652	4.651	2.938		
17‘	Ala	8.316	4.327	1.588		
1	Ala	8.333	4.269	1.540		
2	Ala	8.319	4.338	1.596		
3	Tyr	8.634	4.132	3.209		
4	Ala	8.507	4.312	1.623		
5	Ala	8.103	4.265	1.518		
6	Trp	8.013	4.274	3.483		δ7.053

						ε9.680
7	Thr	8.713	3.233	4.267	1.185	
8	Ala	8.278	4.155	1.497		
9	Asp	7.598	4.798	3.060, 2.883		
10	Gly	7.612	4.155, 3.551			
11	Gly	8.065	3.032, 1.115			
12	Pro	n.d.				
13	Ser	7.845	4.471	3.935		
14	Ser	8.200	4.256	3.826		
15	Gly	8.037	4.257, 3.854			
16	Arg	8.117	4.969	1.846		δ3.285
17	Pro	n.d.				
18	Pro	n.d.				
119	Pro	n.d.				
20	Ser	8.435	4.320	3.828		
21	Gly	8.540	3.967			
22	Ser	8.203	4.392	3.765		

Tab. 62: ^{15}N-chemical shifts of (jg)IBTC-2 in H_2O/D_2O, pH 3, at 278 K.

Residue		Chemical shift δ (ppm)				
		N				
1‘	Asp	n.d.				
2‘	Thr	115.71				
3‘	Ala	125.86				
4‘	Ser	116.47				
5‘	Asp	123.54				
6‘	Ala	124.70				
7‘	Ala	122.85				
8‘	Ala	122.67				
9‘	Ala	122.13				
10‘	Ala	121.71				
11‘	Ala	122.38				
12‘	Leu	122.24				
13‘	Thr	116.68				
14‘	Ala	124.21				
15‘	Ala	123.48				
16‘	Asn	119.50				
17‘	Ala	124.47				
1	Ala	122.67				
2	Ala	122.87				
3	Tyr	122.54				
4	Ala	123.04				
5	Ala	122.05				
6	Trp	120.83	131.46			

7	Thr	116.59				
8	Ala	125.65				
9	Asp	115.80				
10	Gly	106.27				
11	Gly	112.51				
12	Pro	n.d.				
13	Ser	113.48				
14	Ser	117.30				
15	Gly	109.98				
16	Arg	120.16				
17	Pro	n.d.				
18	Pro	n.d.				
119	Pro	n.d.				
20	Ser	116.09				
21	Gly	111.22				
22	Ser	117.05				

Tab. 63: ^{1}H-chemical shifts of (jg)IBTC-2 in H_2O/D_2O, pH 3, at 298 K.

Residue		Chemical shift *δ* (ppm)				
		NH	α	β	γ	
1‘	Asp	exch.	4.360	2.982		
2‘	Thr	8.653	4.254	4.254	1.269	
3‘	Ala	8.406	4.431	1.461		
4‘	Ser	8.465	4.364	3.983, 3.899		
5‘	Asp	8.323	4.616	2.859		
6‘	Ala	8.238	4.245	1.488		
7‘	Ala	n.d.				
8‘	Ala	n.d.				
9‘	Ala	n.d.				
10‘	Ala	n.d.				
11‘	Ala	n.d.	4.222	1.473		
12‘	Leu	7.925	4.302	1.723		
13‘	Thr	8.107	4.139	4.285	1.253	
14‘	Ala	8.140	4.187	1.475		
15‘	Ala	n.d.				
16‘	Asn	8.344	4.639	2.873		δ 7.629
17‘	Ala	8.212	4.260	1.529		
1	Ala	n.d.				
2	Ala	n.d.				
3	Tyr	8.396	4.300	3.151, 3.101		δ7.101 ε6.798
4	Ala	8.306	4.249	1.530		
5	Ala	n.d.				
6	Trp	7.993	4.363	3.417, 3.249		δ7.106 ε9.784, 7.254 ζ 7.264,

						6.876 η 7.224
7	Thr	8.404	3.483	4.200	1.446	
8	Ala	8.137	4.232	1.453		
9	Asp	7.740	4.724	2.973, 2.827		
10	Gly	7.724	4.082, 3.639			
11	Gly	8.044	3.282, 2.126			
12	Pro		4.519	2.435, 2.026	2.075	δ3.694, 3.395
13	Ser	7.955	4.451	3.909		
14	Ser	8.156	4.274	3.909, 3.694		
15	Gly	8.060	4.142, 3.867			
16	Arg	8.055	4.569	1.894, 1.783	1.683	δ3.237 ε7.324
17	Pro		4.690	2.295, 1.818	1.995	δ3.836, 3.623
18	Pro		3.249	1.464 1.059	1.776	δ3.595, 3.498
119	Pro		4.324	2.230, 1.905,	1.854	δ3.232, 3.046
20	Ser	8.289	4.368	3.839		
21	Gly	8.411	3.968, 3.956			
22	Ser	7.972	4.332	3.819, 3.805		

Tab. 64: ^{15}N and ^{13}C-chemical shifts of the folded conformation of (jg)IBTC-2 in H_2O/D_2O, pH 3, at 298 K. Shifts marked with an asterix are averaged.

Residue		Chemical shift δ (ppm)				
		N		Cα	Cβ	
1‘	Asp	n.d.		54.60	39.81	
2‘	Thr	115.31		63.83	69.77	γ22.06
3‘	Ala	125.82		54.61	18.81	
4‘	Ser	115.84		59.92	63.31	
5‘	Asp	122.98		n.d.	39.47	
6‘	Ala	122.36		53.76	18.45	
7‘	Ala	n.d.		54.43*	18.58*	
8‘	Ala	n.d.		54.43*	18.58*	
9‘	Ala	n.d.		54.43*	18.58*	
10‘	Ala	n.d.		54.43*	18.58*	
11‘	Ala	n.d.		54.25	18.59	
12‘	Leu	121.42		57.17	42.29	
13‘	Thr	115.16		64.71	69.73	γ22.05
14‘	Ala	124.65		54.43	18.57	
15‘	Ala	n.d.		54.43*	18.58*	
16‘	Asn	118.23	111.69	n.d.	38.62	
17‘	Ala	124.21		54.52	18.48	
1	Ala	n.d.		54.43*	18.58*	
2	Ala	n.d.		54.43*	18.58*	
3	Tyr	121.04		59.75	38.69	δ 133.31 ε 118.76
4	Ala	123.58		54.10	18.42	
5	Ala	n.d.		54.43*	18.58*	
6	Trp	120.24	130.84	58.76	28.92	δ 127.65 ε 121.19 ζ 122.69, 114.61 η 124.55
7	Thr	115.57		65.60	69.62	γ18.46
8	Ala	122.37		54.42	18.59	
9	Asp	116.25		n.d.	38.90	
10	Gly	106.78		45.03		
11	Gly	111.37		44.02		
12	Pro	n.d.		n.d.	32.23	γ 27.58 δ50.98
13	Ser	113.94		59.55	63.49	
14	Ser	117.12		59.99	64.96	
15	Gly	109.91		45.73		
16	Arg	120.40	114.85	n.d.	30.89	γ27.17 δ 43.81
17	Pro	n.d.		n.d.	30.85	γ 27.47 δ 50.88
18	Pro	n.d.		60.88	29.98	γ 27.21 δ50.23
119	Pro	n.d.		63.17	32.04	γ27.54 δ 50.09

20	Ser	115.79		59.66	64.24	
21	Gly	111.18		45.60		
22	Ser	119.37		59.61	64.86	

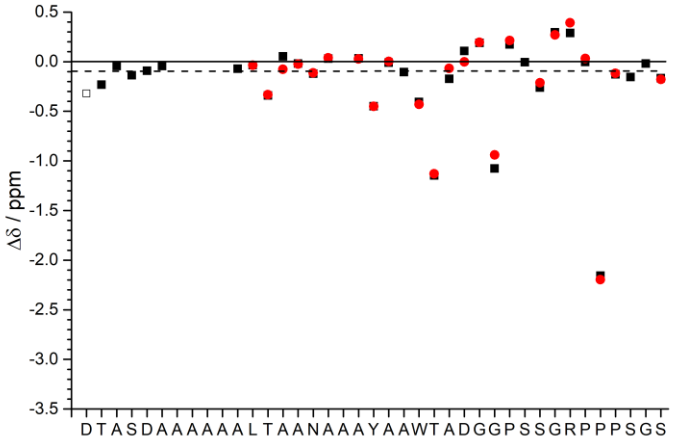

Fig. 132: Hα CSD plots of (jg)IBTC-2 at 274 K and 0.1 M NH_4HCO_3, pH 7.9, (red circles) and H_2O/D_2O, pH 3, (black squares). The dashed line at y=-0.1 ppm represents the helical limit.

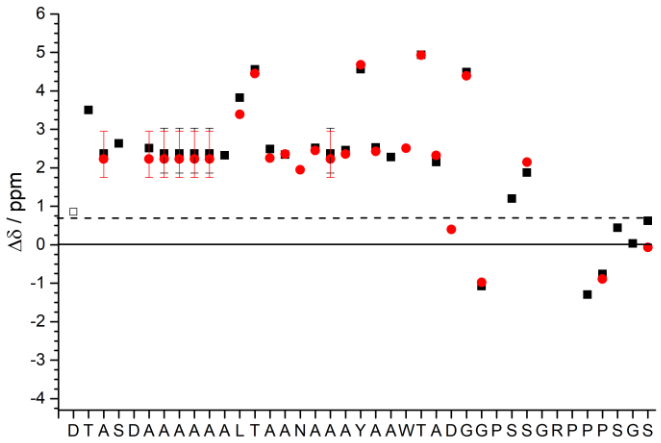

Fig. 133: Cα CSD plots of (jg)IBTC-2 at 274 K and 0.1 M NH_4HCO_3, pH 7.9, (red circles) and H_2O/D_2O, pH 3, (black squares). The dashed line at y=0.7 ppm represents the helical limit.

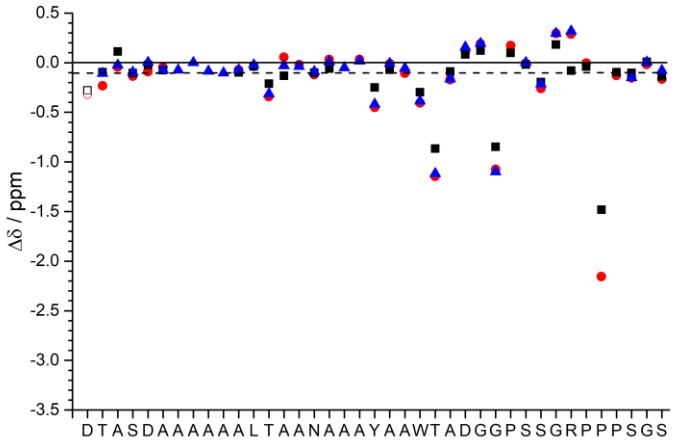

Fig. 134: Hα CSD plots of (jg)IBTC-2 at pH 3 and 274 K (red circles), 278 K (blue triangles) and 298 K (black squares). The dashed line at y=-0.1 ppm represents the helical limit.

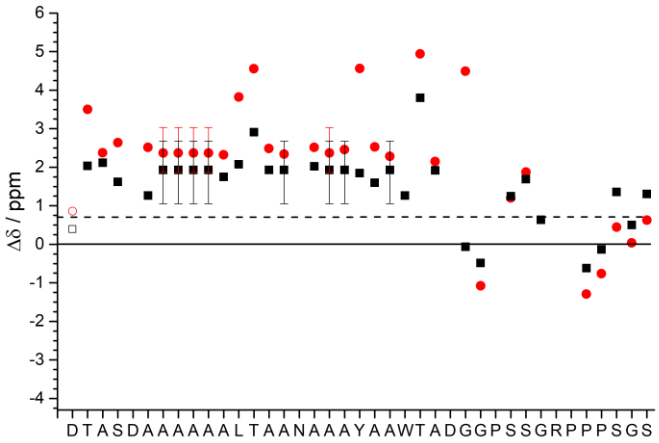

Fig. 135: Cα CSD plots of (jg)IBTC-2 at pH 3 and 274 K (red circles) and 298 K (black squares). The dashed line at y=0.7 ppm represents the helical limit.

Tab. 65: CSDs for selected protons of the cage structure representing the cage fold of (jg)IBTC-2 at pH 3 and pH 7.9 and 274 K and 298 K, given the fraction folded according to Lin [75].

$\chi_{Trp\text{-}cage}$	Δδ (ppm)						Σ
	T7α	G11α'	P18α	Pro18β'	P19δ	P19δ'	
pH 7.9, 274 K	-1.130	-3.189	-2.196	-1.941	-0.504	-0.891	-9.851
pH 3, 274 K	-1.146	-3.029	-2.1566	-1.853	-0.532	-0.903	-9.619
pH 3, 298 K	-0.867	-1.894	-1.481	-1.231	-0.358	-0.694	-6.525

Tab. 66: CSDs for selected protons in the helical region representing the helix fold of (jg)IBTC-2 at pH 3 and pH 7.9 and 274 K, 278 K and 298 K.

χ_{Helix}	Δδ (ppm)							Σ
	A2α	Y3α	A4α	A5α	W6α	T7α	A8α	
pH 7.9, 274 K	0.027	-0.45	0.002		-0.431	-1.130	-0.068	
pH 3, 274 K	0.032	-0.450	-0.011	-0.106	-0.406	-1.146	-0.173	-2.259
pH 3, 278 K	0.018	-0.418	-0.009	-0.055	-0.386	-1.117	-0.165	-2.132
pH 3, 298 K		-0.250	-0.071		-0.297	-0.867	-0.088	

Antifreeze activity (80 mg/mL, 0.1 M NH_4HCO_3, pH 7.9):

- Ice growth retardation: 0.049 °C
- ice shaping

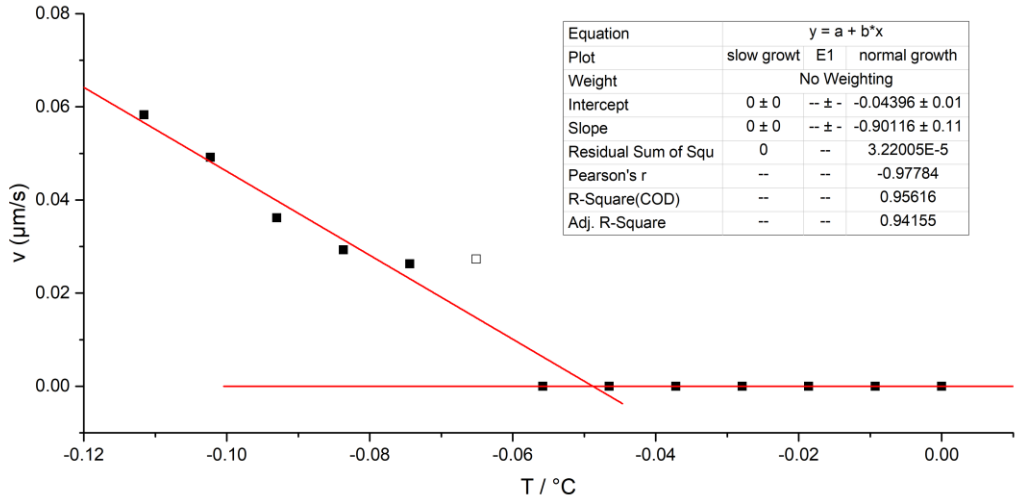

Fig. 136: Ice growth retardation plot of 80 mg/mL (jg)IBTC-2 in 0.1 M NH_4HCO_3, pH 7.9. The growth retardation is 0.049 °C. The hollow square was neglected during the calculations.

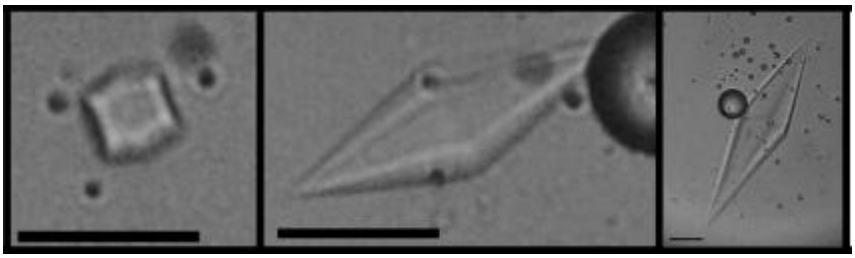

Fig. 137: The shape of metastable ice crystals in the presence of 80 mg/mL (jg)IBTC-2 in 0.1 M NH_4HCO_3, pH 7.9. The hexagonal bipyramidal shape is slightly twisted. The black scale in each picture is 10 µm long. The *c*- to *a*-axis ratio is 3.0:1.

5.8 (jg)IBTC-3

Sequence	DTASDAAAAAALTAANAKAAAELTAANAAAYAAWTAD GGPSSGRPPPSGS
Molecular weight	4529.81 Da
Absorption coefficient	ε_{280}= 6990 $M^{-1}cm^{-1}$
Yield	0.4 mg/ L LB medium

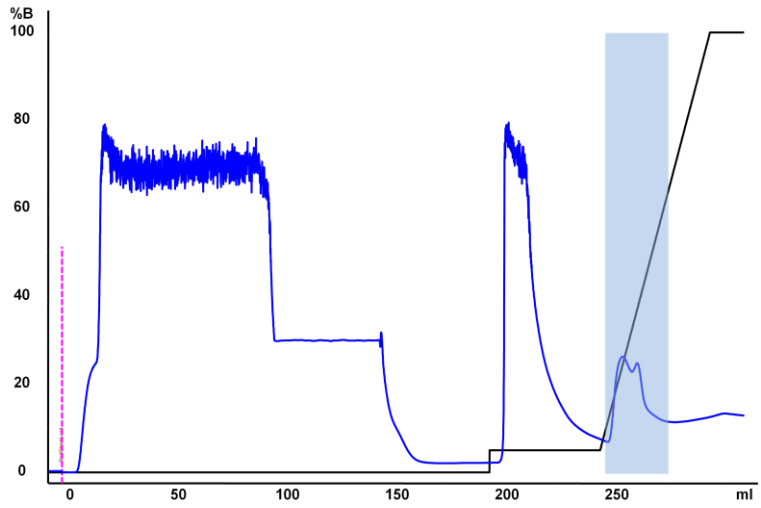

Fig. 138: Profile of the affinity purification of (jg)SUMO-IBTC-3. The signal was detected at 280 nm (blue). The gradient of the elution buffer is shown in black. With the injection at 0 mL the chromatogram starts. Fractions that were combined and collected are marked in blue.

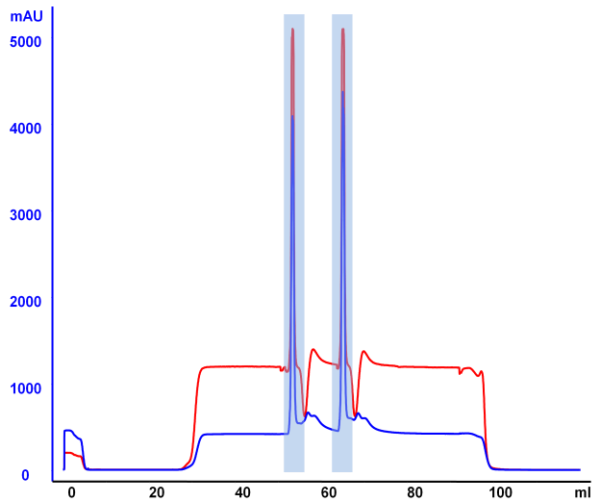

Fig. 139: Profile of the rebuffering of (jg)SUMO-IBTC-3. The signal was detected at 280 nm (blue) and 254 nm (red). Fractions that were combined and collected are marked in blue.

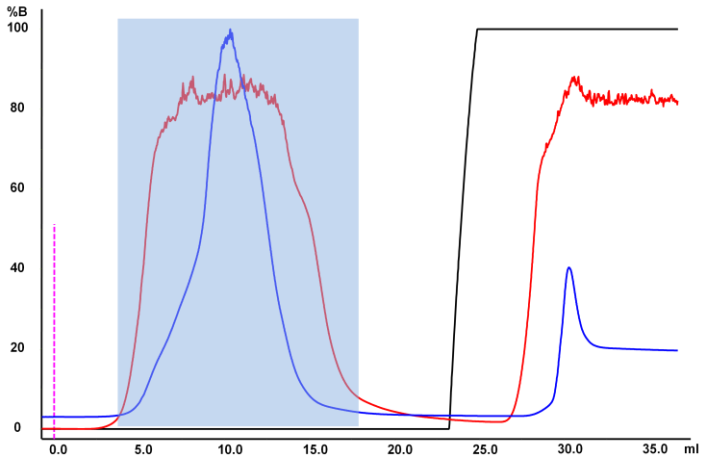

Fig. 140: Profile of the affinity purification of (jg)IBTC-3. The signal was detected at 280 nm (blue) and 254 nm (red). The gradient of the elution buffer is shown in black. The injections are dashed pink lines. Fractions which were collected and combined are marked in blue.

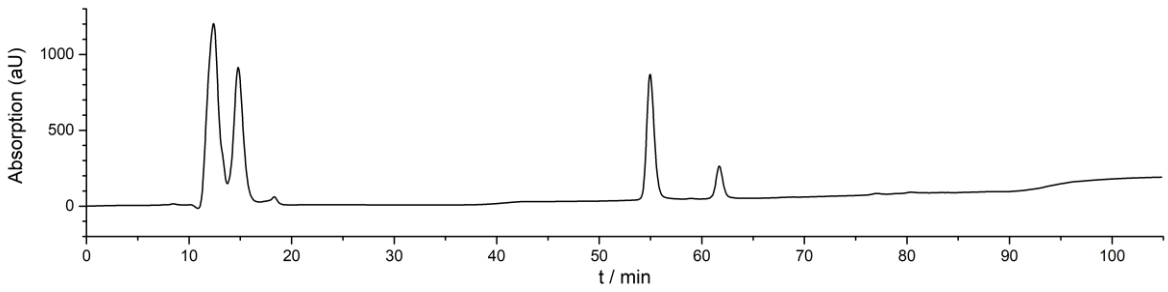

Fig. 141: HPLC profile of the semi-preparative run of (jg)IBTC-3. t_R is 61 min.

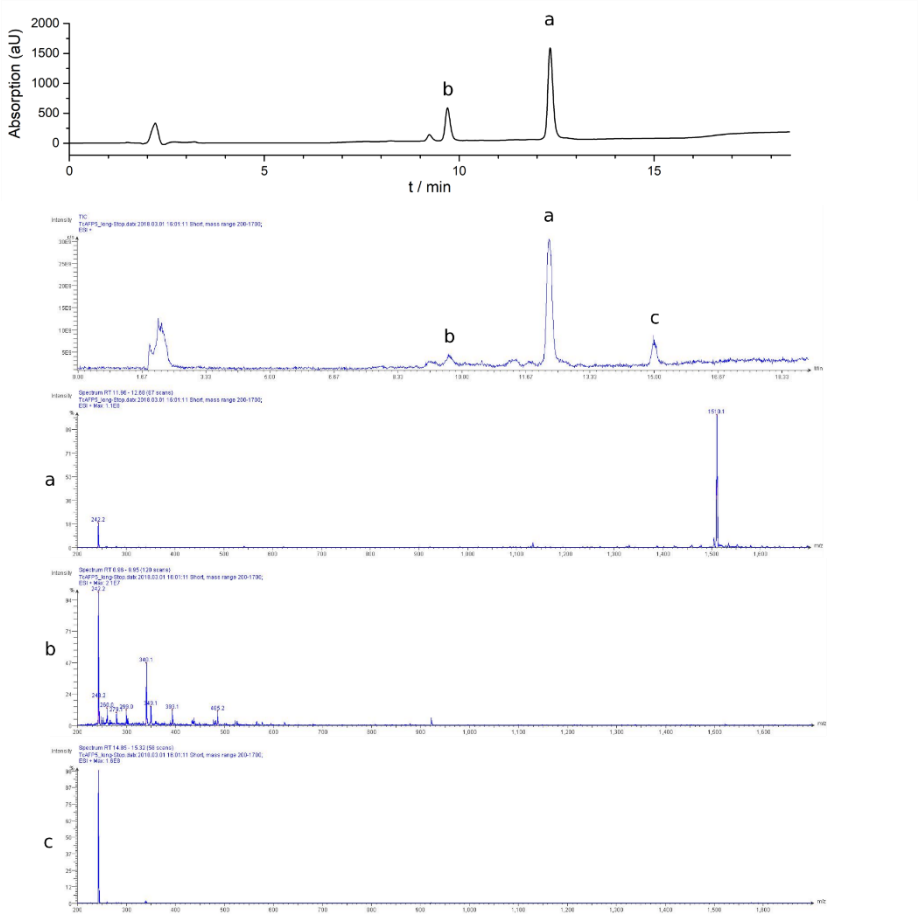

Fig. 142: HPLC profile of the analytical run (top), ion chromatogram (2nd panel from top) and MS spectra of all signals of purified (jg)IBTC-3. *m/z*: $[M+3H]^{3+}$ calcd 1510.9, found 1510.1. t_R is 12.2 min.

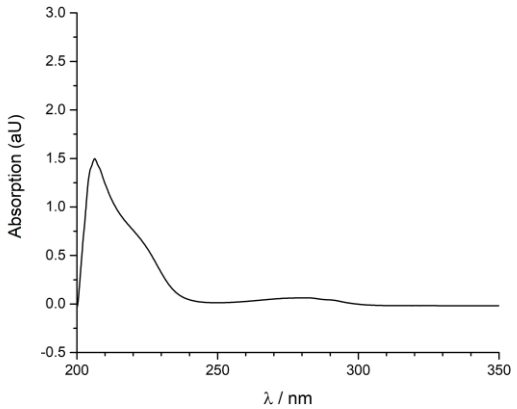

Fig. 143: UV/vis spectrum of (jg)IBTC-3 at 298 K in 0.1 M NH_4HCO_3 buffer, pH 7.9. The spectrum was measured to 600 nm, displayed only to 350 nm.

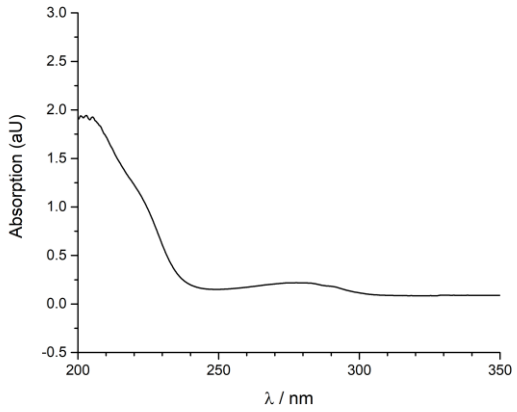

Fig. 144: UV/vis spectrum of (jg)IBTC-3 at 298 K in water at pH 3. The spectrum was measured to 600 nm, displayed only to 350 nm.

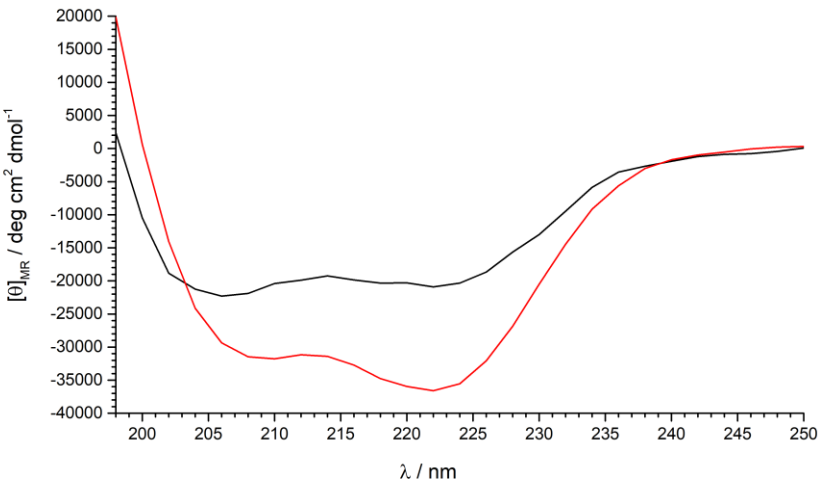

Fig. 145: CD spectra of (jg)IBTC-3 in 0.1 M NH_4HCO_3 buffer, pH 7.9, at 298 K (black) and 274 K (red).

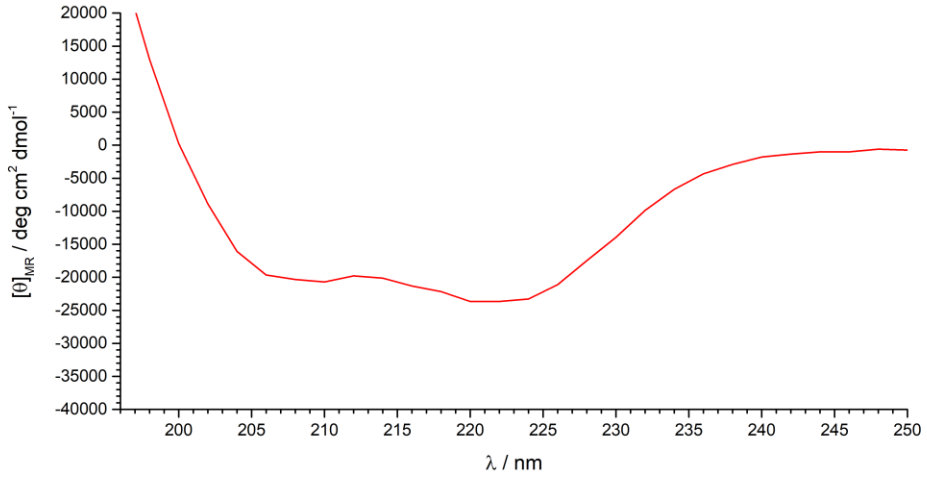

Fig. 146: CD spectra of (jg)IBTC-3 in water, pH 3, at 274 K.

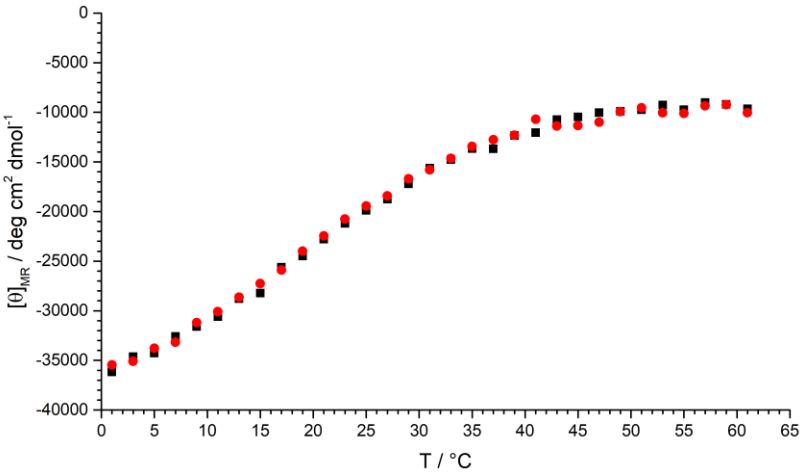

Fig. 147: CD thermal denaturation scan of (jg)IBTC-3 in 0.1 M NH_4HCO_3 buffer, pH 7.9. The black squares show the heating curve, the red circles the cooling curve.

Tabelle 67: Calculated melting points for (jg)IBTC-3 in 0.1 M NH_4HCO_3 buffer, pH 7.9.

	heating	cooling
Boltzmann fit	19.0 ±0.5	18.5 ±0.5

Tab. 68: Helical content of (jg)IBTC-2 at 1 °C and 0.1 M NH_4HCO_3 buffer, pH 7.9, or water, pH 3.

	0.1 M NH_4HCO_3, pH 7.9	pH 3
$[\Theta]_{obs}$ (deg cm^2 dmol^{-1})	-36.070	-23.649
$[\Theta]_{ref}$ (deg cm^2 dmol^{-1})	-42.875	-42.875
Helical content (%)	84	55

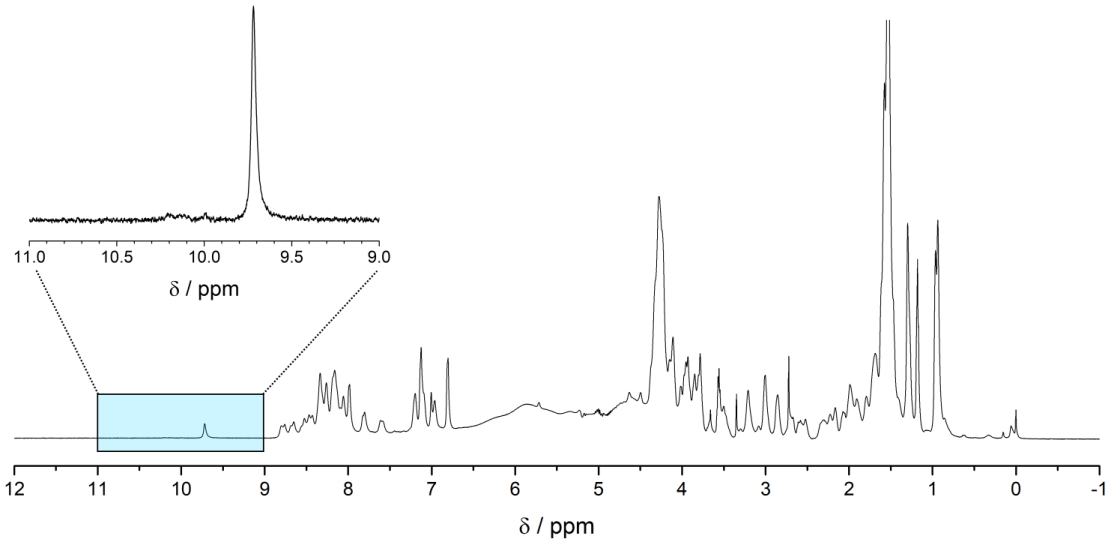

Fig. 148: ^{1}H NMR spectrum of (jg)IBTC-3 in 0.1 M NH_4HCO_3 buffer, pH 7.9, at 274 K with enlargement of the indole proton region around 10 ppm.

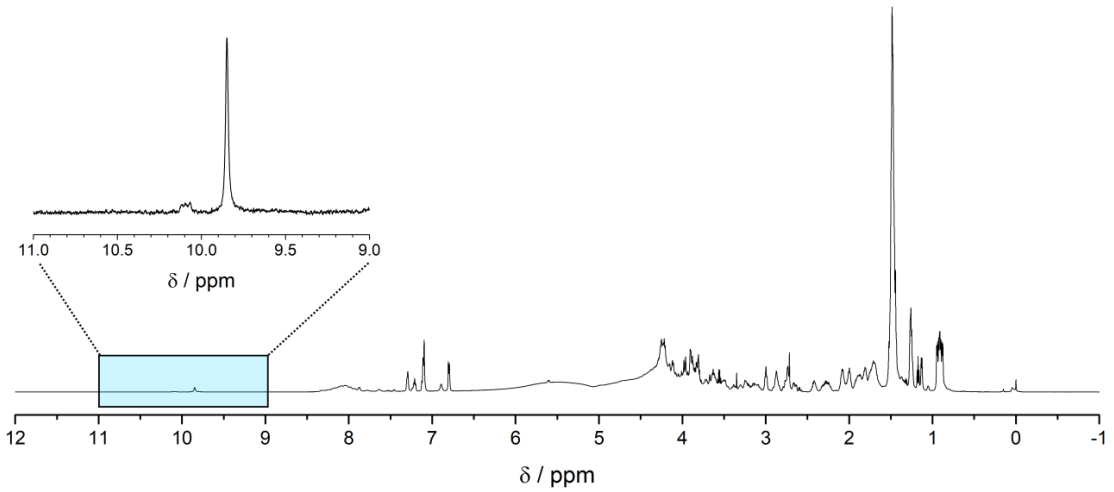

Fig. 149: ^{1}H NMR spectrum of (jg)IBTC-3 in 0.1 M NH_4HCO_3 buffer, pH 7.9, at 298 K with enlargement of the indole proton region around 10 ppm.

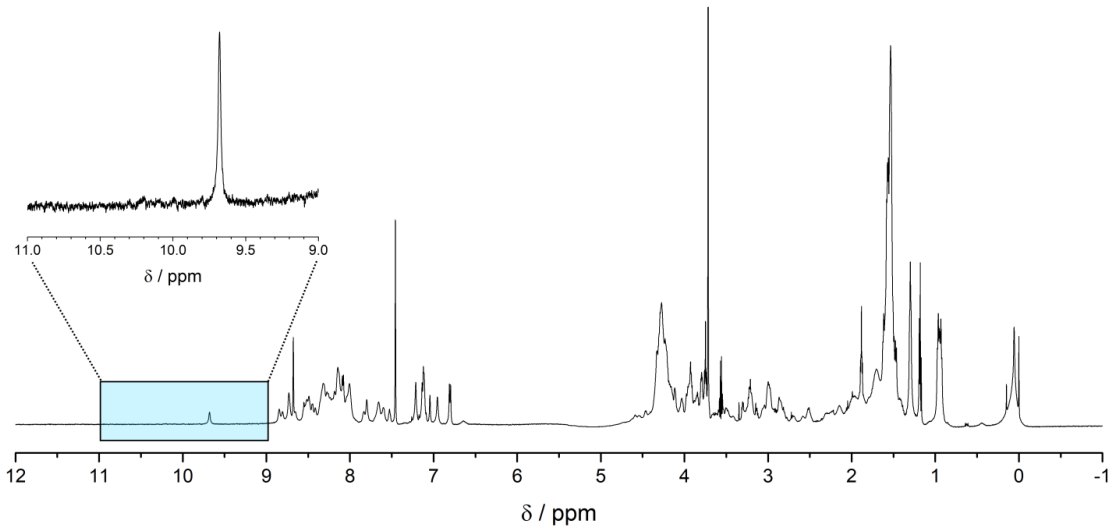

Fig. 150: ^{1}H NMR spectrum of (jg)IBTC-3 in H_2O/D_2O, pH 3, at 274 K with enlargement of the indole proton region around 10 ppm.

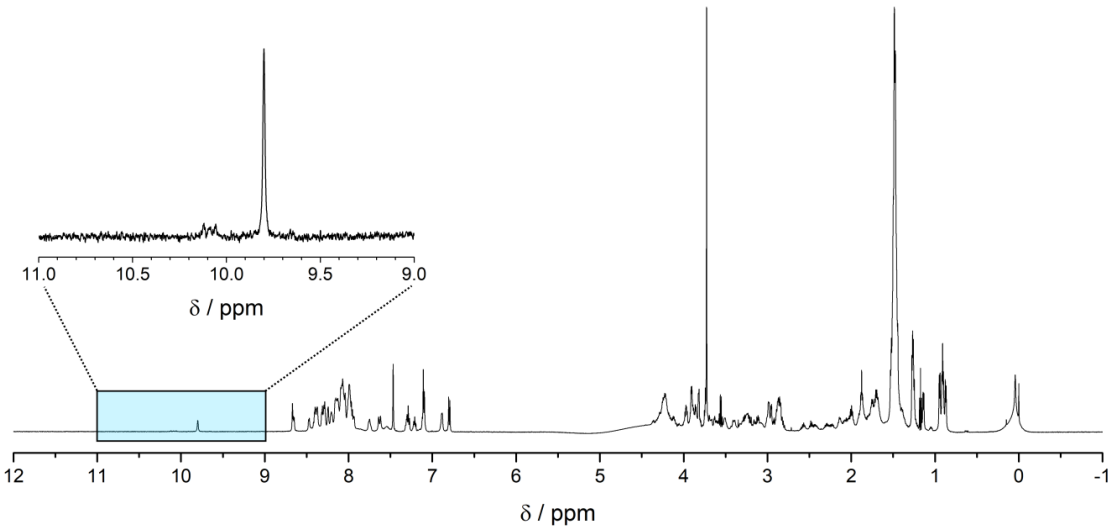

Fig. 151: ^{1}H NMR spectrum of (jg)IBTC-3 in H_2O/D_2O, pH 3, at 298 K with enlargement of the indole proton region around 10 ppm.

Tab. 69: ^{1}H-chemical shifts of (jg)IBTC-3 in H_2O/D_2O, pH 3, at 274 K.

Residue		Chemical shift *δ* (ppm)				
		NH	α	β	γ	
1‘	Asp	n.d.				
2‘	Thr	8.743	4.123	4.193	1.301	
3‘	Ala	8.521	4.278	1.471		
4‘	Ser	8.841	4.333	4.053, 3.939		
5‘	Asp	8.512	4.553	2.950, 2.813		
6‘	Ala	8.352	4.284	1.542		
7‘	Ala	n.d.				
8‘	Ala	n.d.				
9‘	Ala	n.d.				
10‘	Ala	n.d.				
11‘	Ala	n.d.				
12‘	Leu	8.000	4.309	1.909, 1.746	n.d.	δ0.946
13‘	Thr	8.309	3.977	4.273	1.295	
14‘	Ala	n.d.				
15‘	Ala	n.d.		1.584		
16‘	Asn	8.734	4.627	2.992, 2.854		
17‘	Ala	8.320	4.301	1.501		
18‘	Lys	8.209	4.203	1.704	1.403	δ1.547 ε2.989 ζ 7.659

19‘	Ala	n.d.				
20‘	Ala	n.d.				
21‘	Ala	n.d.				
22‘	Glu	8.267	4.165	2.272, 2.174	2.715, 2.514	
23‘	Leu	8.018	4.267	1.887, 1.757	n.d.	δ0.946
24‘	Thr	8.313	3.990	4.294	1.295	
25‘	Ala	n.d.				
26‘	Ala	n.d.		1.568		
27‘	Asn	8.817	4.591	2.994, 2.859		
28‘	Ala	8.259	4.297	1.558		
1	Ala	n.d.				
2	Ala	8.330	4.359	1.607		
3	Tyr	8.655	4.418	3.216		δ7.121 ε6.802
4	Ala	8.532	4.292	1.625		
5	Ala	n.d.				
6	Trp	8.005	4.278	3.475, 3.215		δ7.046 ε9.673 ζ 7.197, 7.099 η 7.203
7	Thr	8.731	3.208	4.345		
8	Ala	8.308	4.203	1.503		
9	Asp	7.595	4.760	3.043, 2.862		
10	Gly	7.601	4.154, 3.521			
11	Gly	8.095	3.055, 1.012			
12	Pro		4.586	2.489, 2.045	2.127	δ3.759, 3.408
13	Ser	7.836	4.461	3.929		
14	Ser	8.204	4.216	3.886		
15	Gly	8.040	4.248, 3.831			
16	Arg	8.135	4.930	1.897	1.771, 1.666	δ3.270 ε7.522
17	Pro		4.721	2.314, 1.794	2.003	δ3.846, 3.642
18	Pro		2.572	0.436	n.d.	δ3.497
19	Pro		4.301	2.231, 1.948	1.891, 1.805	δ3.056, 2.837
20	Ser	8.456	4.314	3.822		
21	Gly	8.561	3.946			
22	Ser	8.123	4.320	3.794		

Tab. 70: ^{15}N and ^{13}C-chemical shifts of the folded conformation of (jg)IBTC-3 in H_2O/D_2O, pH 3, at 274 K. Shifts marked with an asterix are averaged.

Residue		Chemical shift δ (ppm)				
		N		Cα	Cβ	
1‘	Asp	n.d.		n.d.	n.d.	
2‘	Thr	115.63		66.01	69.88	γ22.54
3‘	Ala	n.d.		55.64	18.76	
4‘	Ser	117.55		59.18	62.99	
5‘	Asp	124.98		57.04	42.66	
6‘	Ala	122.81		55.57	18.51	
7‘	Ala	n.d.		55.66*	18.52*	
8‘	Ala	n.d.		55.66*	18.52*	
9‘	Ala	n.d.		55.66*	18.52*	
10‘	Ala	n.d.		55.66*	18.52*	
11‘	Ala	n.d.		55.66*	18.52*	
12‘	Leu	122.75		59.16	42.37	δ24.62
13‘	Thr	117.02		67.04	69.64	γ22.54
14‘	Ala	n.d.		55.66*	18.52*	
15‘	Ala	n.d.		55.66*	18.43	
16‘	Asn	119.76		n.d.	42.71	
17‘	Ala	124.57		55.82	18.55	
18‘	Lys	n.d.		57.18	30.20	γ 25.65 δ 25.62 ε 42.71
19‘	Ala	n.d.		55.66*	18.52*	
20‘	Ala	n.d.		55.66*	18.52*	
21‘	Ala	n.d.		55.66*	18.52*	
22‘	Glu	119.42		59.44	28.32	γ34.43
23‘	Leu	114.02		59.27	42.41	δ24.62
24‘	Thr	116.67		66.94	70.33	γ 22.54
25‘	Ala	n.d.		55.66*	18.52*	
26‘	Ala	n.d.		55.66*	18.43	
27‘	Asn	119.61		n.d.	42.71	
28‘	Ala	124.76		55.71	18.49	
1	Ala	n.d.		55.66*	18.52*	
2	Ala	122.87		55.76	18.43	
3	Tyr	122.81		n.d.	39.20	δ 133.66 ε119.12
4	Ala	122.99		55.66	18.39	
5	Ala	n.d.		55.66*	18.52*	
6	Trp	121.63	131.48	n.d.	n.d.	δ 128.24 ζ 121.81, 114.88 η 124.99
7	Thr	116.65		67.41	n.d.	
8	Ala	125.73		55.33	18.49	
9	Asp	115.91		n.d.	38.04	
10	Gly	n.d.		n.d.		
11	Gly	112.73		42.74		
12	Pro	n.d.		n.d.	32.67	γ28.10

13	Ser	113.42		n.d.	63.82	
14	Ser	117.35		59.29	64.24	
15	Gly	109.78		n.d.		
16	Arg	120.07	114.84	n.d.	27.92	γ 27.59 δ 44.26
17	Pro	n.d.		n.d.	31.29	γ27.93 δ51.34
18	Pro	n.d.		60.73	n.d.	δ50.52
19	Pro	n.d.		61.68	32.45	γ 27.84 δ 50.21
20	Ser	115.92		59.55	64.57	
21	Gly	111.39		45.84		
22	Ser	119.09		59.37	64.97	

Tab. 71: ^{1}H-chemical shifts of (jg)IBTC-3 in H_2O/D_2O, pH 3, at 298 K.

Residue		Chemical shift δ (ppm)				
		NH	α	β	γ	
1‘	Asp	exch.	4.375	2.993		
2‘	Thr	8.657	4.267	4.267	1.272	
3‘	Ala	8.429	4.306	1.444		
4‘	Ser	8.458	4.369	3.982, 3.896		
5‘	Asp	8.385	4.618	2.883		
6‘	Ala	n.d.				
7‘	Ala	n.d.				
8‘	Ala	n.d.				
9‘	Ala	n.d.				
10‘	Ala	n.d.				
11‘	Ala	n.d.	4.221	1.482		
12‘	Leu	7.947	4.303	1.747		
13‘	Thr	8.093	4.118	4.257	1.266	
14‘	Ala	n.d.				
15‘	Ala	n.d.				
16‘	Asn	8.324	4.638	2.885		
17‘	Ala	n.d.				
18‘	Lys	8.076	4.211	1.889		δ1.690 ε2.990 ζ 7.547
19‘	Ala	n.d.				
20‘	Ala	n.d.				
21‘	Ala	n.d.				
22‘	Glu	8.086	4.246	2.144	2.593, 2.493	
23‘	Leu	7.988	4.311	1.712		
24‘	Thr	8.127	4.168	4.279	1.251	
25‘	Ala	n.d.				
26‘	Ala	n.d.				
27‘	Asn	8.324	4.638	2.885		
28‘	Ala	n.d.				

1	Ala	n.d.				
2	Ala	n.d.		1.501		
3	Tyr	8.393	4.413	3.153		δ7.105 ε6.799
4	Ala	8.301	4.244	1.529		
5	Ala	n.d.				
6	Trp	7.995	4.341	3.418, 3.256		δ7.106 ε9.789, 7.260 ζ 7.279, 6.887 η 7.220
7	Thr	8.396	3.486	4.202		
8	Ala	8.129	4.197	1.464		
9	Asp	7.743	4.736	2.990, 2.844		
10	Gly	7.729	4.082, 3.644			
11	Gly	8.031	3.275, 1.953			
12	Pro		4.512	2.427, 2.027	2.058	δ3.685, 3.379
13	Ser	7.955	4.449	3.906		
14	Ser	8.154	4.276	3.911, 3.702		
15	Gly	8.062	4.154, 3.870			
16	Arg	8.049	4.811	1.888, 1.779	1.681	δ3.237 ε7.312
17	Pro		4.685	2.284, 1.818	1.993	δ3.834, 3.620
18	Pro		3.177	1.480	1.759, 1.272	δ3.5845, 3.489
19	Pro		4.324	2.226, 1.898	1.848	δ3.237, 3.049
20	Ser	8.293	4.365	3.840		
21	Gly	8.414	3.970			
22	Ser	8.004	4.359	3.827		

Tab. 72: ^{15}N and ^{13}C-chemical shifts of the folded conformation of (jg)IBTC-3 in H_2O/D_2O, pH 3, at 298 K. Shifts marked with an asterix are averaged.

Residue		Chemical shift *δ* (ppm)				
		N		Cα	Cβ	
1‘	Asp	n.d.		54.61	39.64	
2‘	Thr	115.31		63.69	69.93	γ22.05
3‘	Ala	125.89		54.49	18.72	
4‘	Ser	115.67		59.26	63.38	
5‘	Asp	121.17		n.d.	39.44	
6‘	Ala	n.d.		54.50*	18.61*	

7‘	Ala	n.d.		54.50*	18.61*	
8‘	Ala	n.d.		54.50*	18.61*	
9‘	Ala	n.d.		54.50*	18.61*	
10‘	Ala	n.d.		54.50*	18.61*	
11‘	Ala	n.d.		54.27	18.54	
12‘	Leu	121.18		57.47	42.31	
13‘	Thr	115.15		64.90	69.97	γ 22.05
14‘	Ala	n.d.		54.50*	18.61*	
15‘	Ala	n.d.		54.50*	18.61*	
16‘	Asn	122.69		n.d.	38.66	
17‘	Ala	n.d.		54.50*	18.61*	
18‘	Lys	120.17		57.66	32.78	δ 29.52 ε39.71
19‘	Ala	n.d.		54.50*	18.61*	
20‘	Ala	n.d.		54.50*	18.61*	
21‘	Ala	n.d.		54.50*	18.61*	
22‘	Glu	121.82		57.65	28.62	γ 33.58
23‘	Leu	121.36		57.14	42.31	
24‘	Thr	114.82		64.24	69.97	γ 22.05
25‘	Ala	n.d.		54.50*	18.61*	
26‘	Ala	n.d.		54.50*	18.61*	
27‘	Asn	122.69		n.d.	38.66	
28‘	Ala	n.d.		54.50*	18.61*	
1	Ala	n.d.		54.50*	18.61*	
2	Ala	n.d.		54.50*	18.60	
3	Tyr	118.02		59.34	38.64	δ 133.29 ε 118.77
4	Ala	122.46		54.49	18.41	
5	Ala	n.d.		54.50*	18.61*	
6	Trp	121.83	130.84	59.31	29.18	δ 127.65 ε 121.32 ζ122.67, 114.54 η 124.52
7	Thr	115.58		65.49	69.85	
8	Ala	125.60		54.49	18.64	
9	Asp	116.04		n.d.	38.66	
10	Gly	106.91		n.d.		
11	Gly	111.20		43.78		
12	Pro	n.d.		59.43	32.20	γ 27.50 δ 51.08
13	Ser	114.01		59.43	63.54	
14	Ser	117.06		59.45	63.54	
15	Gly	109.81		45.83		
16	Arg	120.63	114.91	n.d.	30.94	γ 27.18 δ 43.78
17	Pro	n.d.		n.d.	30.81	γ 27.50 δ 50.64
18	Pro	n.d.		n.d.	30.19	γ 27.16 δ 50.25

19	Pro	n.d.		59.38	32.06	γ 27.58 δ 50.21
20	Ser	115.77		59.26	64.67	
21	Gly	111.16		45.63		
22	Ser	120.24		59.35	64.67	

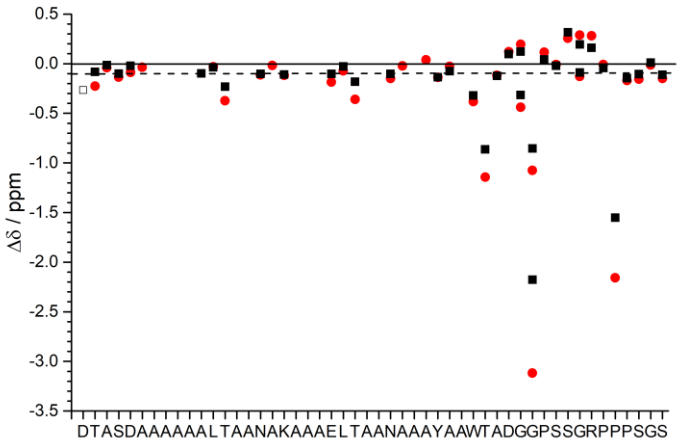

Fig. 152: Hα CSD plots of (jg)IBTC-3 at pH 3 and 274 K (red circles) and 298 K (black squares). The dashed line at y=-0.1 ppm represents the helical limit.

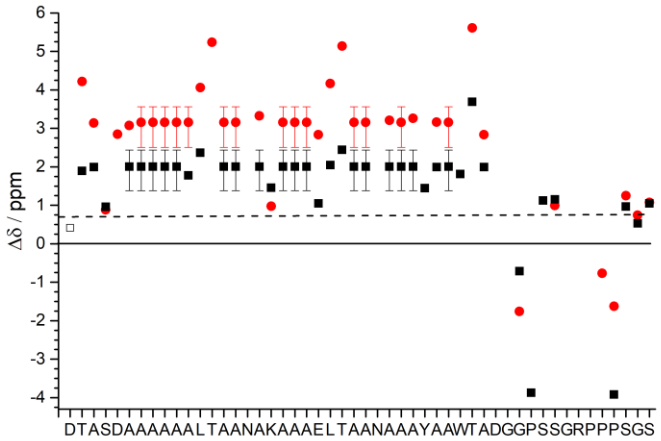

Fig. 153: Cα CSD plots of (jg)IBTC-3 at pH 3 and 274 K (red circles) and 298 K (black squares). The dashed line at y=0.7 ppm represents the helical limit.

Tab. 73: CSDs for selected protons of the cage structure representing the cage fold of (jg)IBTC-3 at pH 3 and 274 K and 298 K, given the fraction folded according to Lin. [75]

$\chi_{Trp\text{-}cage}$	Δδ (ppm)						Σ
	T7α	G11α'	P18α	Pro18β'	P19δ	P19δ'	
pH 3, 274 K	-1.142	-3.008	-2.158	-1.854	-0.534	-0.903	-9.601
pH 3, 298 K	-0.864	-2.067	-1.553	-0.810	-0.354	-0.691	-6.339

Tab. 74: CSDs for selected protons in the helical region representing the helix fold of (jg)IBTC-3 at pH 3 and 274 K and 298 K.

χ_{Helix}	Δδ (ppm)							Σ
	A2α	Y3α	A4α	A5α	W6α	T7α	A8α	
pH 3, 274 K	0.039	-0.132	-0.028		-0.382	-1.143	-0.117	
pH 3, 298 K		-0.137	-0.076		-0.320	-0.864	-0.123	

Antifreeze activity (1 mg/mL, 0.1 M NH_4HCO_3, pH 7.9):

- Thermal hysteresis: 0.3±0.1 °C
- Ice shaping

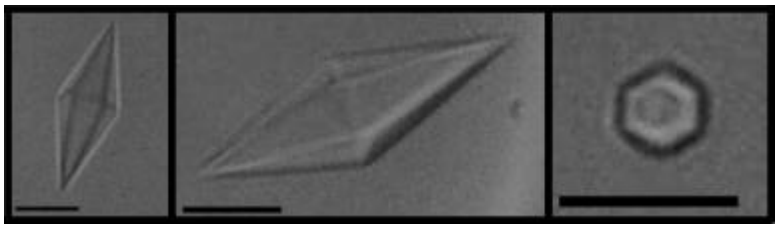

Fig. 154: The shape of metastable ice crystals in the presence of 1 mg/mL (jg)IBTC-3 in 0.1 M NH_4HCO_3, pH 7.9, during the thermal hysteresis gap. The thermal hysteris is 0.3 °C. The pictures on the left show the slightly twisted hexagonal bipyramidal shape in the side view, on the right is the view perpendicular to the basal plane. The black scale in each picture is 10 µm. The *c*- to *a*-axis ratio is 2.8:1.

Antifreeze activity (10 mg/mL, 0.1 M NH_4HCO_3, pH 7.9):

- Thermal hysteresis: 0.6±0.1 °C
- Ice shaping

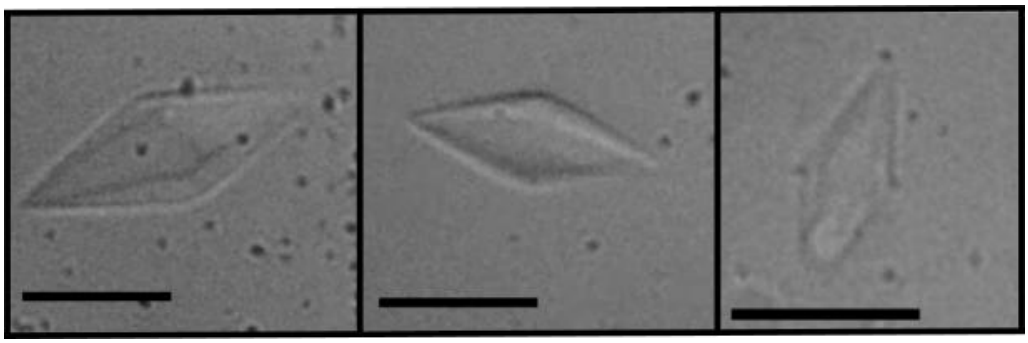

Fig. 155: The shape of metastable ice crystals in the presence of 10 mg/mL (jg)IBTC-3 in 0.1 M NH_4HCO_3, pH 7.9, during the thermal hysteresis gap. The thermal hysteris is 0.6 °C. The hexagonal bipyramidal shape is slightly twisted. The black scale in each picture is 10 µm long. The *c*- to *a*-axis ratio is 2.8:1.

Antifreeze activity (80 mg/mL, 0.1 M NH_4HCO_3, pH 7.9):

- Thermal hysteresis: 0.8±0.1 °C
- Ice shaping

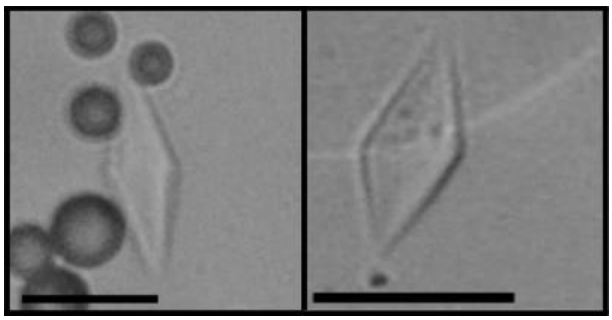

Fig. 156: The shape of metastable ice crystals in the presence of 80 mg/mL (jg)IBTC-3 in 0.1 M NH_4HCO_3, pH 7.9, during the thermal hysteresis gap. The thermal hysteris is 0.8 °C. The hexagonal bipyramidal shape is slightly twisted. The black scale in each picture is 10 µm long. The *c*- to *a*-axis ratio is 3.1:1. The dark gray spheres are air bubbles.

5.9 (jg)IBTC-1-GFP

Sequence	DTASDAAAYAAWTADGGPSSGRPPPSGSVSKGEELFT GVVPILVELD GDVNGHKFSV SGEGEGDATY GKLTLKFICT TGKLPVPWPT LVTTLTYGVQ CFSRYPDHMK QHDFFKSAMP EGYVQERTIF FKDDGNYKTR AEVKFEGDTL VNRIELKGID FKEDGNILGH KLEYNYNSHN VYIMADKQKN GIKVNFKIRH NIEDGSVQLA DHYQQNTPIG DGPVLLPDNH YLSTQSALSK DPNEKRDHMV LLEFVTAAGI TLGMDELYK
Molecular weight	29730.26 Da
Absorption coefficient	ε_{280}= 28880 $M^{-1}cm^{-1}$
Yield	3.2 mg/ L LB medium

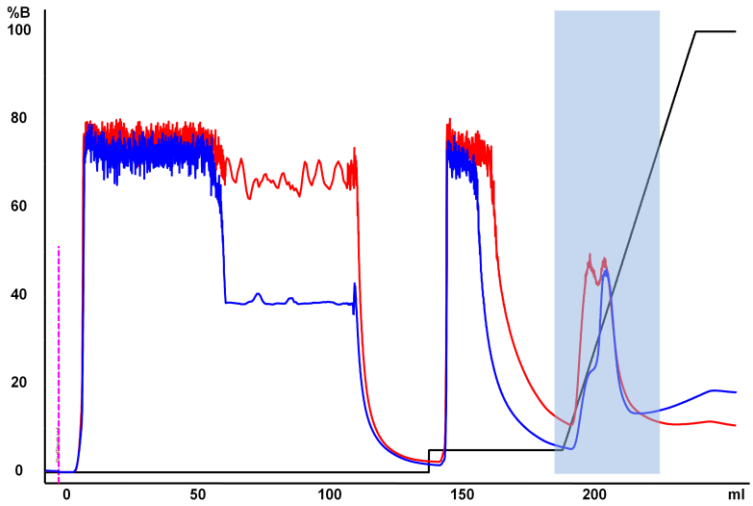

Fig. 157: Profile of the affinity purification of (jg)SUMO-IBTC-1-GFP. The signal was detected at 280 nm (blue) and 254 nm (red). The gradient of the elution buffer is shown in black. With the injection at 0 mL the chromatogram starts. Fractions that were combined and collected are marked in blue.

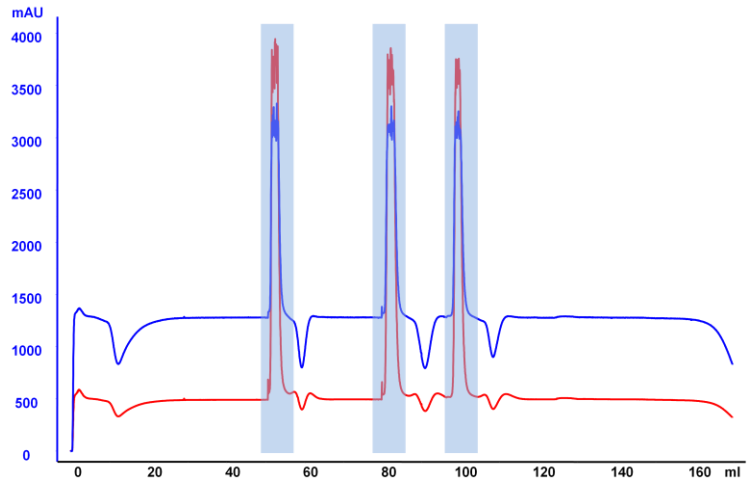

Fig. 158: Profile of the rebuffering of (jg)SUMO-IBTC-1-GFP. The signal was detected at 280 nm (blue) and 254 nm (red). Fractions that were combined and collected are marked in blue.

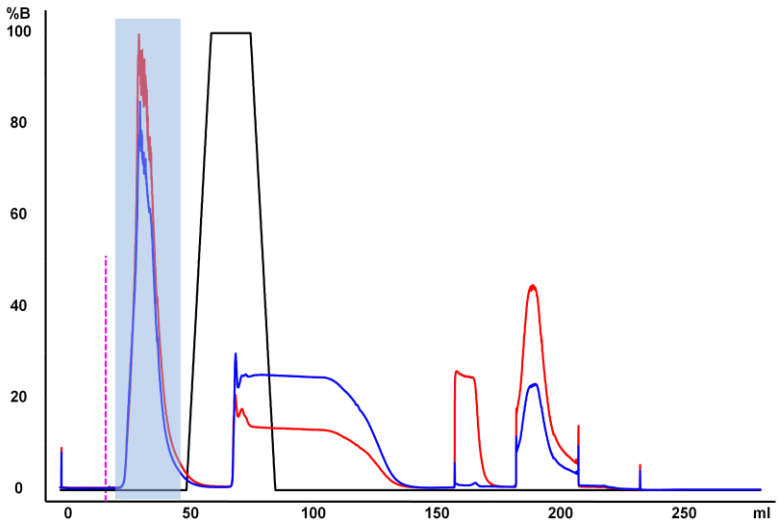

Fig. 159: Profile of the affinity purification of (jg)IBTC-1-GFP. The signal was detected at 280 nm (blue) and 254 nm (red). The gradient of the elution buffer is shown in black. The injections are dashed pink lines. Fractions which were collected and combined are marked in blue.

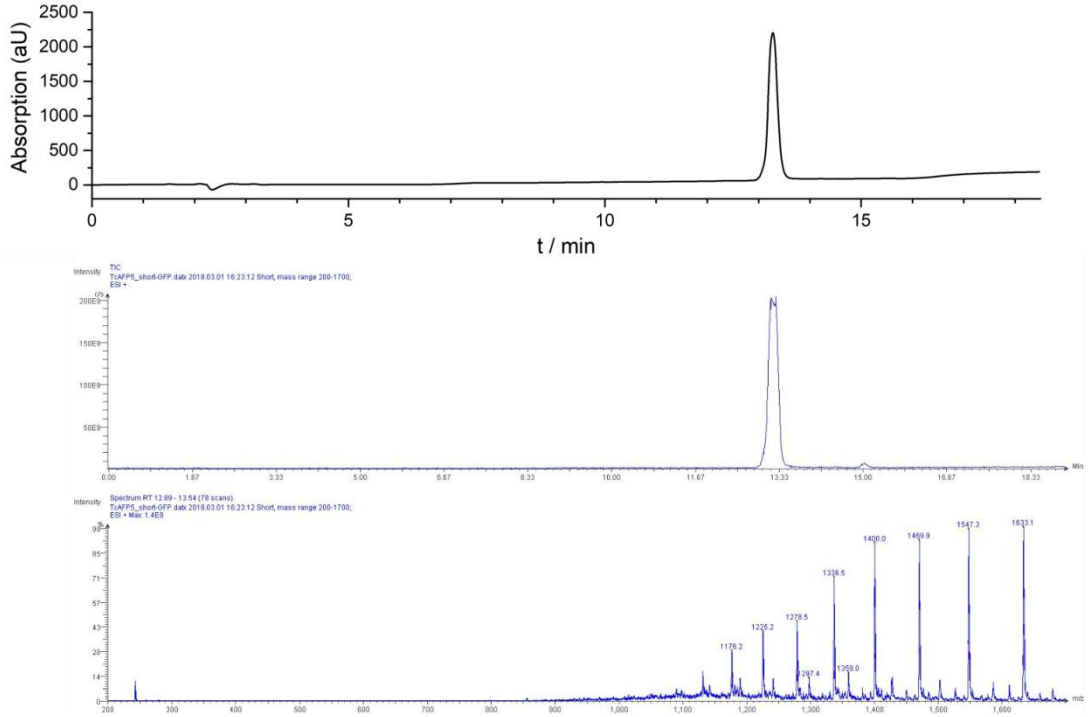

Fig. 160: HPLC profile of the analytical run (top), ion chromatogram (2nd panel from top) and MS spectra of all signals of purified (jg)IBTC-1-GFP. *m/z*: $[M+18H]^{18+}$ calcd 1635.05, found 1633.1. t_R is 13.2 min.

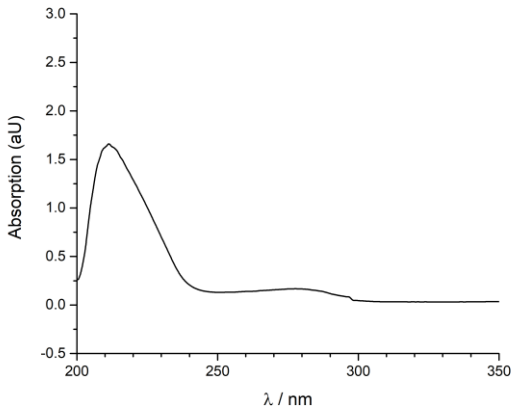

Fig. 161: UV/vis spectrum of (jg)IBTC-1-GFP at 298 K in 0.1 M NH_4HCO_3 buffer, pH 7.9. The spectrum was measured to 600 nm, displayed only to 350 nm.

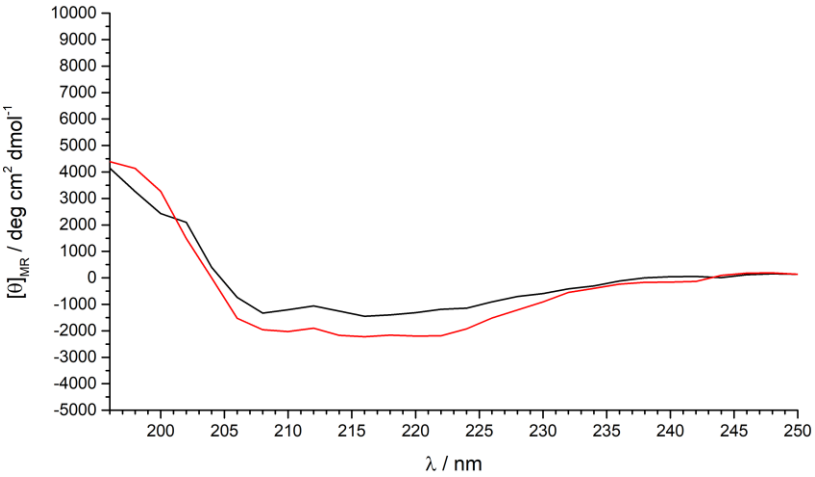

Fig. 162: CD spectra of (jg)IBTC-1-GFP in 0.1 M NH_4HCO_3 buffer, pH 7.9, at 298 K (black) and 274 K (red).

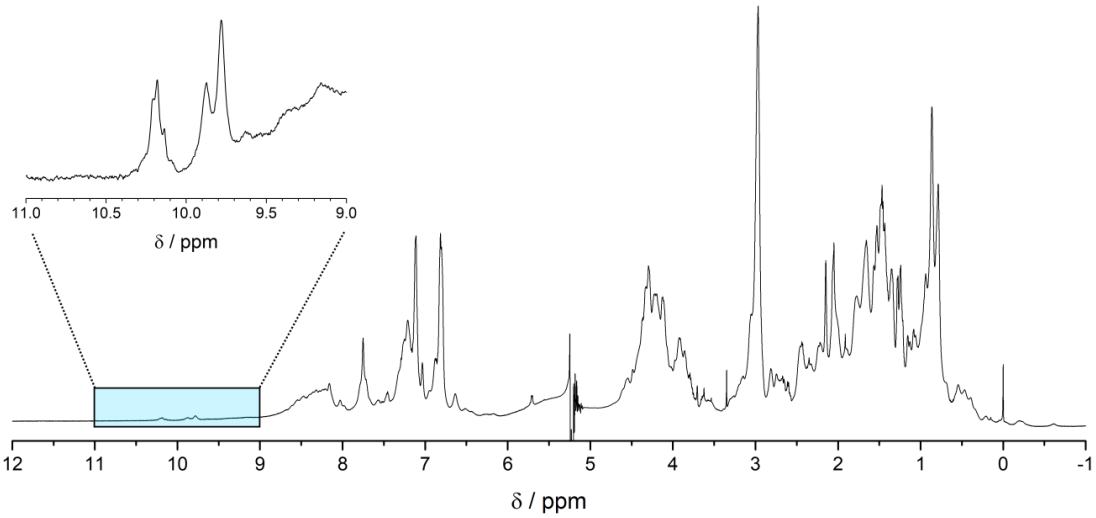

Fig. 163: ^1H NMR spectrum of (jg)IBTC-1-GFP in 0.1 M NH_4HCO_3 buffer, pH 7.9, at 274 K with enlargement of the indole proton region around 10 ppm.

Antifreeze activity (1.09 mg/mL, 0.1 M NH_4HCO_3, pH 7.9):

- No thermal hysteresis
- No ice shaping

Antifreeze activity (10 mg/mL, 0.1 M NH_4HCO_3, pH 7.9):

- Ice growth retardation: 0.046 °C
- Ice shaping

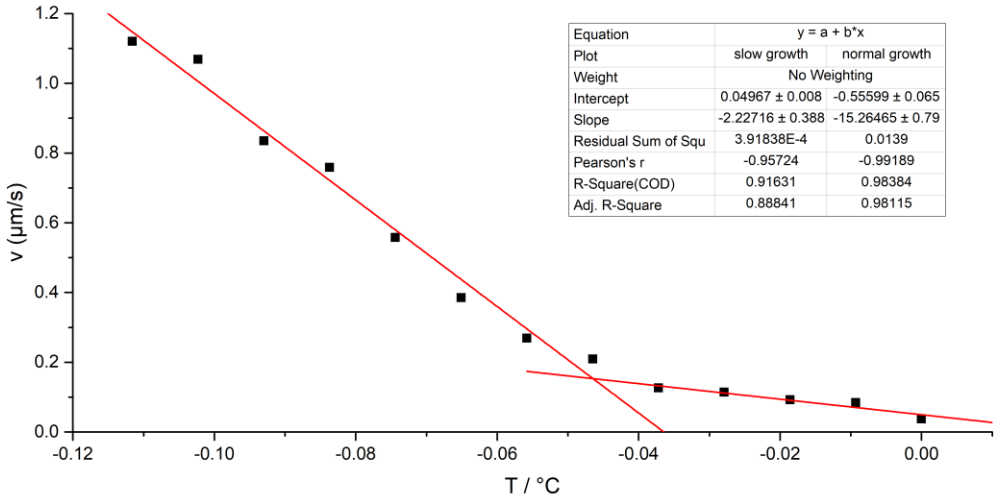

Equation	y = a + b*x	
Plot	slow growth	normal growth
Weight	No Weighting	
Intercept	0.04967 ± 0.008	-0.55599 ± 0.065
Slope	-2.22716 ± 0.388	-15.26465 ± 0.79
Residual Sum of Squ	3.91838E-4	0.0139
Pearson's r	-0.95724	-0.99189
R-Square(COD)	0.91631	0.98384
Adj. R-Square	0.88841	0.98115

Fig. 164: Ice growth retardation plot of 10 mg/mL (jg)IBTC-1-GFP in 0.1 M NH_4HCO_3, pH 7.9. The growth retardation is 0.046 °C.

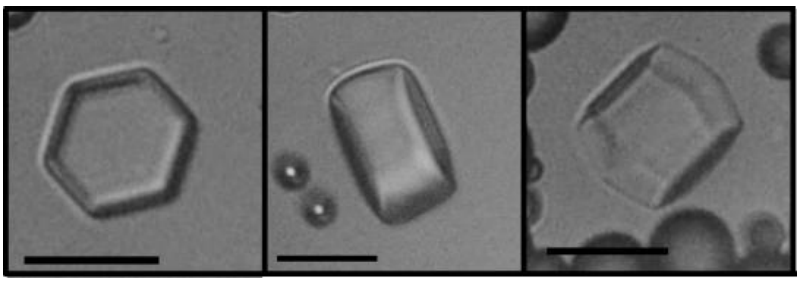

Fig. 165: Ice crystals during the growth in the presence of 10 mg/mL (jg)IBTC-1-GFP in 0.1 M NH_4HCO_3, pH 7.9. Left the top view shows the view perpendicular to the basal plane, while the middle and the right show the side view of the crystal. The black scale in each picture is 10 µm.

5.10 (jg)IBTC-2-GFP

Sequence	DTASDAAAAAALTAANAAAYAAWTADGGPSSGRPPPSGSVSKGEELFT GVVPILVELD GDVNGHKFSV SGEGEGDATY GKLTLKFICT TGKLPVPWPT LVTTLTYGVQ CFSRYPDHMK QHDFFKSAMP EGYVQERTIF FKDDGNYKTR AEVKFEGDTL VNRIELKGID FKEDGNILGH KLEYNYNSHN VYIMADKQKN GIKVNFKIRH NIEDGSVQLA DHYQQNTPIG DGPVLLPDNH YLSTQSALSK DPNEKRDHMV LLEFVTAAGI TLGMDELYK
Molecular weight	30627.26 Da
Absorption coefficient	ε_{280}= 28880 $M^{-1}cm^{-1}$
Yield	9.0 mg/ L LB medium

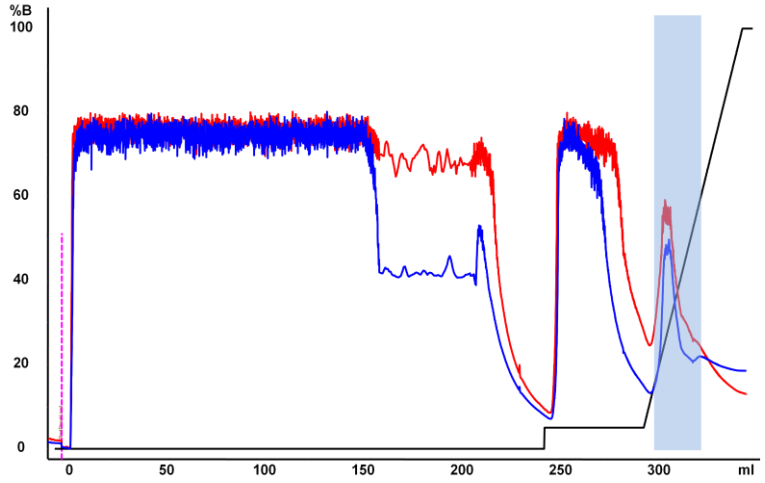

Fig. 166: Profile of the affinity purification of (jg)SUMO-IBTC-2-GFP. The signal was detected at 280 nm (blue) and 254 nm (red). The gradient of the elution buffer is shown in black. With the injection at 0 mL the chromatogram starts. Fractions that were combined and collected are marked in blue.

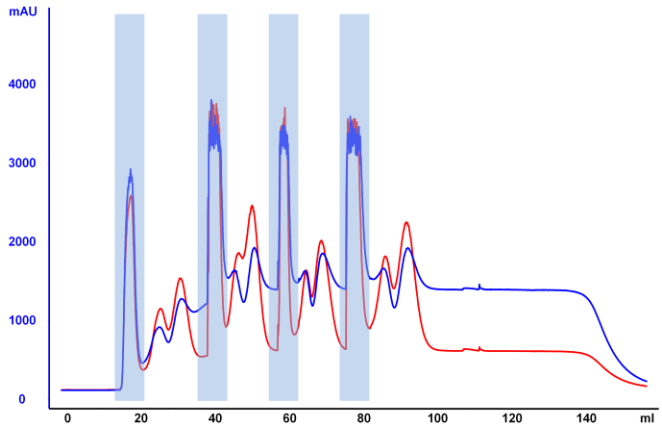

Fig. 167: Profile of the rebuffering of (jg)SUMO-IBTC-2-GFP. The signal was detected at 280 nm (blue) and 254 nm (red). Fractions that were combined and collected are marked in blue.

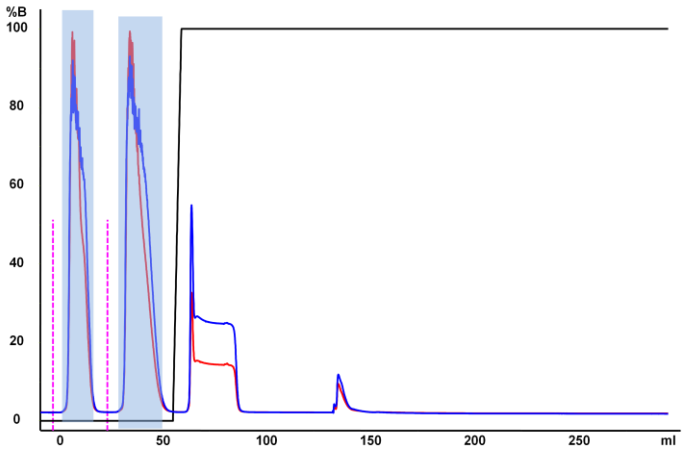

Fig. 168: Profile of the affinity purification of (jg)IBTC-2-GFP. The signal was detected at 280 nm (blue) and 254 nm (red). The gradient of the elution buffer is shown in black. The injections are dashed pink lines. Fractions which were collected and combined are marked in blue.

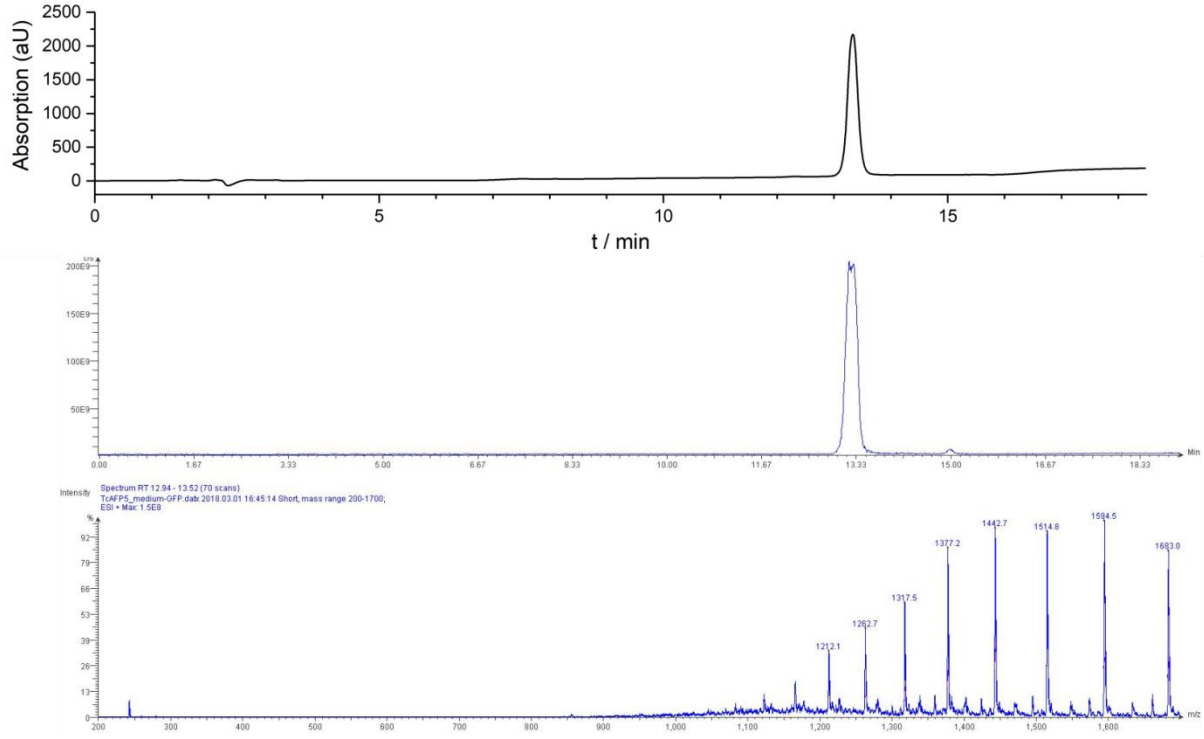

Fig. 169: HPLC profile of the analytical run (top), ion chromatogram (2nd panel from top) and MS spectra of all signals of purified (jg)IBTC-2-GFP. *m/z*: $[M+18H]^{18+}$ calcd 1684.9, found 1683.0. t_R is 13.2 min.

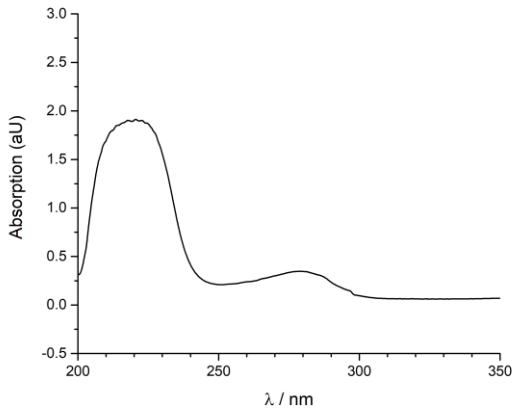

Fig. 170: UV/vis spectrum of (jg)IBTC-2-GFP at 298 K in 0.1 M NH_4HCO_3 buffer, pH 7.9. The spectrum was measured to 600 nm, displayed only to 350 nm.

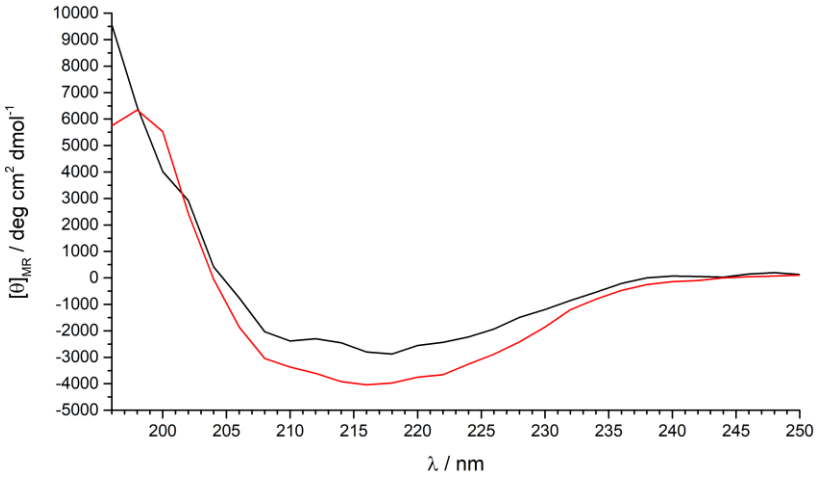

Fig. 171: CD spectra of (jg)IBTC-2-GFP in 0.1 M NH_4HCO_3 buffer, pH 7.9, at 298 K (black) and 274 K (red).

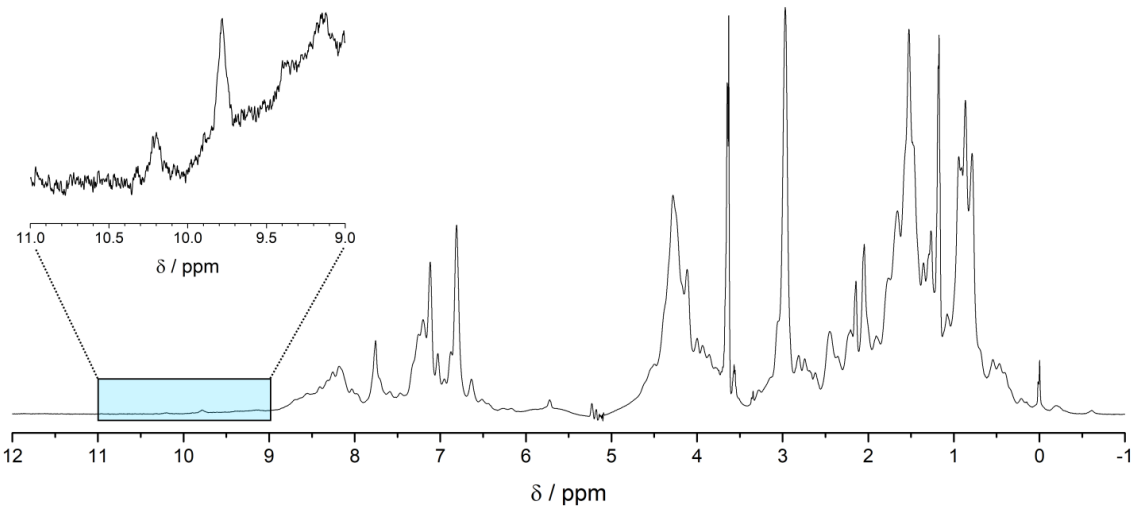

Fig. 172: ^{1}H NMR spectrum of (jg)IBTC-2-GFP in 0.1 M NH_4HCO_3 buffer, pH 7.9, at 274 K with enlargement of the indole proton region around 10 ppm.

Antifreeze activity (1.06 mg/mL, 0.1 M NH_4HCO_3, pH 7.9):

- No thermal hysteresis
- No ice shaping

Antifreeze activity (4.23 mg/mL, 0.1 M NH_4HCO_3, pH 7.9):

- No thermal hysteresis
- ice shaping

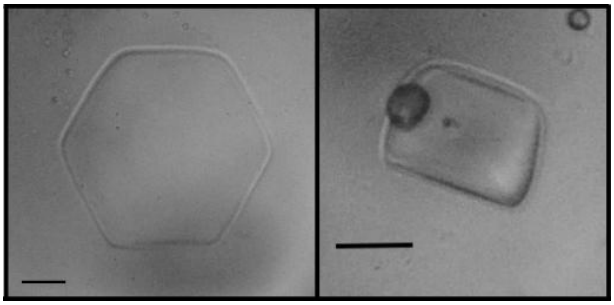

Fig. 173: Ice crystals during the growth in the presence of 4.23 mg/mL (jg)IBTC-2-GFP in 0.1 M NH_4HCO_3, pH 7.9. Left the top view shows the view perpendicular to the basal plane, while on the right the side view of the crystal is shown. The black scale in each picture is 10 µm long.

Antifreeze activity (80 mg/mL, 0.1 M NH_4HCO_3, pH 7.9):

- No thermal hysteresis
- Ice shaping

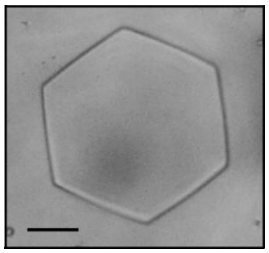

Fig. 174: Ice crystals during the growth in the presence of 80 mg/mL (jg)IBTC-2-GFP in 0.1 M NH_4HCO_3, pH 7.9. The top view shows the view perpendicular to the basal plane. The black scale in each picture is 10 µm long.

5.11 (jg)IBTC-3-GFP

Sequence

DTASDAAAAAALTAANAKAAAELTAANAAAYAAWTADGGPSSGRPPPS
GS
VSKGEELFT GVVPILVELD GDVNGHKFSV SGEGEGDATY GKLTLKFICT
TGKLPVPWPT LVTTLTYGVQ CFSRYPDHMK QHDFFKSAMP
EGYVQERTIF FKDDGNYKTR AEVKFEGDTL VNRIELKGID
FKEDGNILGH KLEYNYNSHN VYIMADKQKN GIKVNFKIRH
NIEDGSVQLA DHYQQNTPIG DGPVLLPDNH YLSTQSALSK
DPNEKRDHMV LLEFVTAAGI TLGMDELYK

Molecular weight 31639.39 Da

Absorption coefficient ε_{280}= 28880 $M^{-1}cm^{-1}$

Yield 3.0 mg/ L LB medium

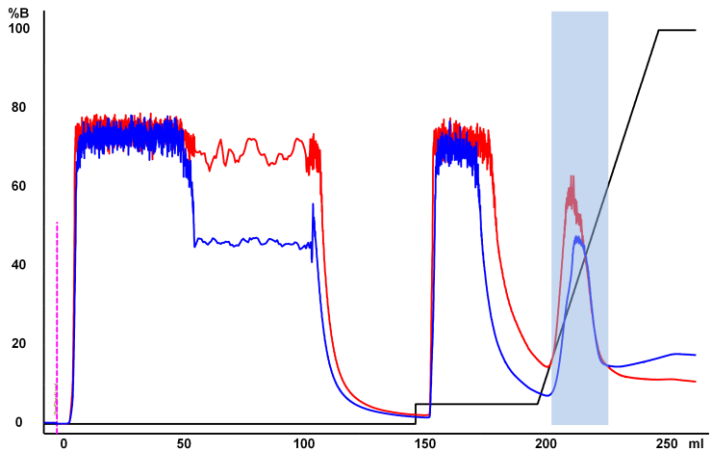

Fig. 175: Profile of the affinity purification of (jg)SUMO-IBTC-3-GFP. The signal was detected at 280 nm (blue) and 254 nm (red). The gradient of the elution buffer is shown in black. With the injection at 0 mL the chromatogram starts. Fractions that were combined and collected are marked in blue.

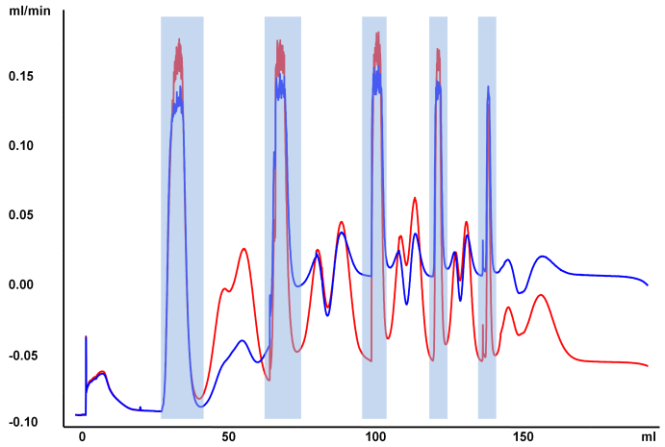

Fig. 176: Profile of the rebuffering of (jg)SUMO-IBTC-3-GFP. The signal was detected at 280 nm (blue) and 254 nm (red). Fractions that were combined and collected are marked in blue.

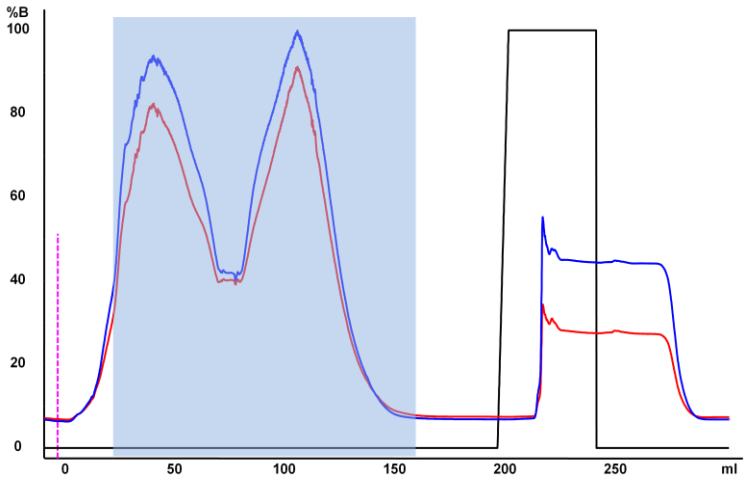

Fig. 177: Profile of the affinity purification of (jg)IBTC-3-GFP. The signal was detected at 280 nm (blue) and 254 nm (red). The gradient of the elution buffer is shown in black. The injections are dashed pink lines. Fractions which were collected and combined are marked in blue.

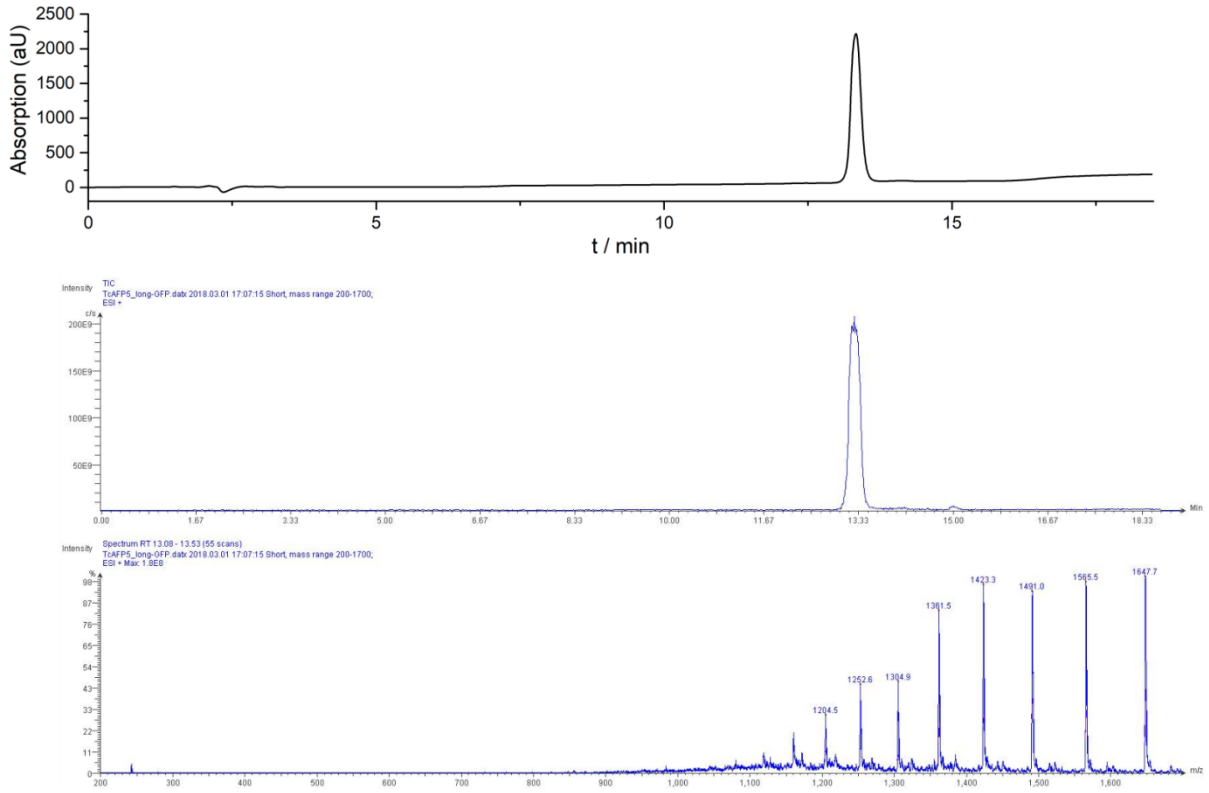

Fig. 178: HPLC profile of the analytical run (top), ion chromatogram (2nd panel from top) and MS spectra of all signals of purified (jg)IBTC-3-GFP. *m/z*: $[M+19H]^{19+}$ calcd 1649.5, found 1647.7. t_R is 13.3 min.

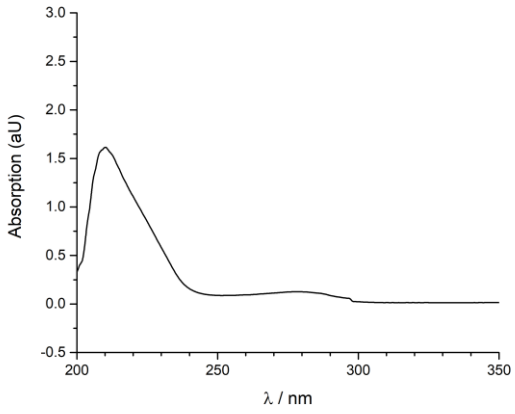

Fig. 179: UV/vis spectrum of (jg)IBTC-3-GFP at 298 K in 0.1 M NH_4HCO_3 buffer, pH 7.9. The spectrum was measured to 600 nm, displayed only to 350 nm.

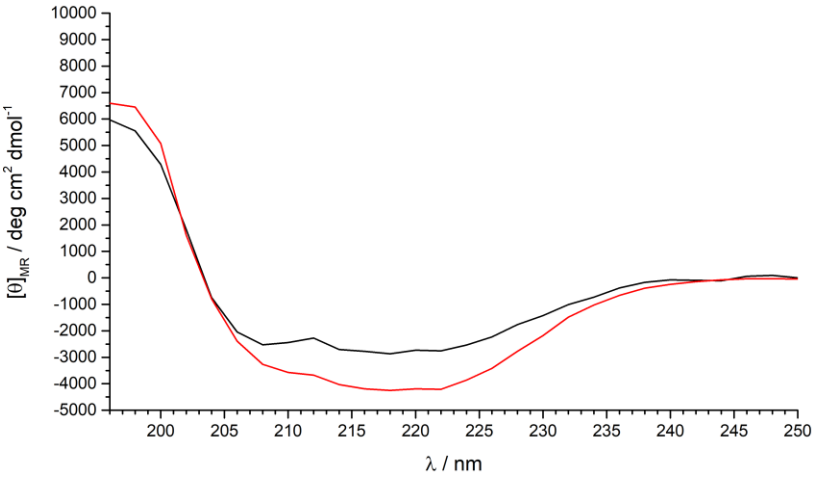

Fig. 180: CD spectra of (jg)IBTC-3-GFP in 0.1 M NH_4HCO_3 buffer, pH 7.9, at 298 K (black) and 274 K (red).

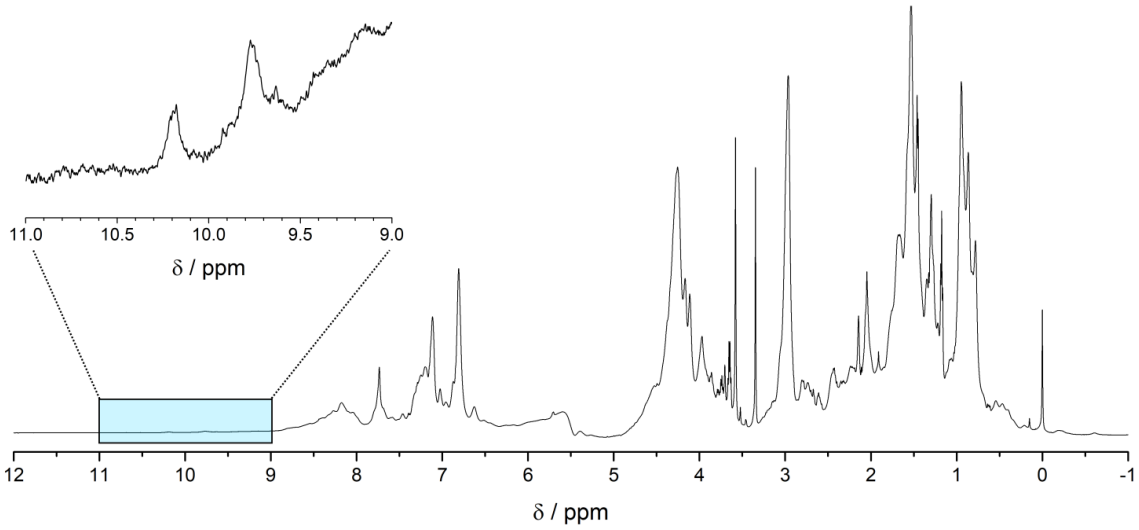

Fig. 181: ^{1}H NMR spectrum of (jg)IBTC-3-GFP in 0.1 M NH_4HCO_3 buffer, pH 7.9, at 274 K with enlargement of the indole proton region around 10 ppm.

Antifreeze activity (0.81 mg/mL, 0.1 M NH_4HCO_3, pH 7.9):

- Ice growth retardation: 0.029 °C
- ice shaping

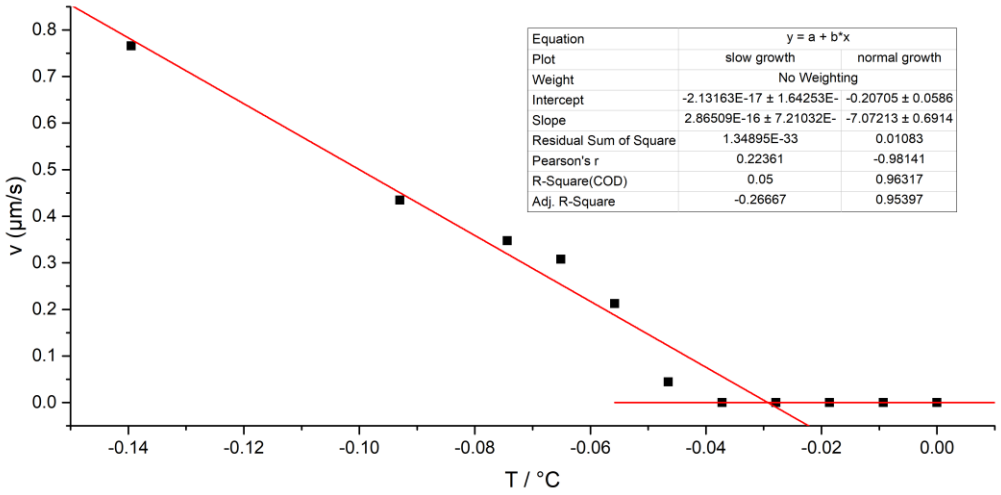

Fig. 182: Ice growth retardation plot of 0.81 mg/mL (jg)IBTC-3-GFP in 0.1 M NH_4HCO_3, pH 7.9. The growth retardation is 0.029 °C.

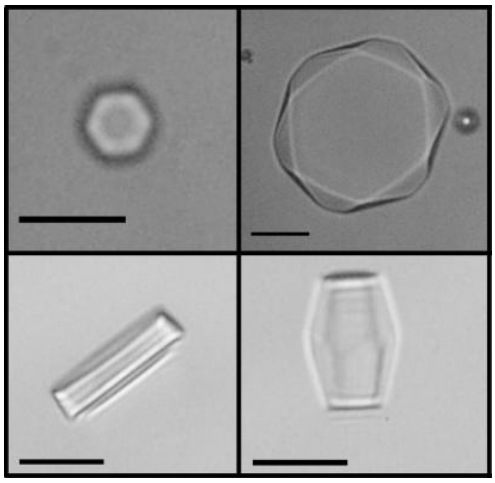

Fig. 183: Ice crystals during the growth in the presence of 0.81 mg/mL (jg)IBTC-3-GFP in 0.1 M NH_4HCO_3, pH 7.9. The top row shows the view perpendicular to the basal plane, while in the bottom row the side view of the crystal is shown. The black scale in each picture is 10 µm long.

Antifreeze activity (15.0 mg/mL, 0.1 M NH_4HCO_3, pH 7.9):

- Thermal hysteresis: 0.4±0.1 °C
- ice shaping

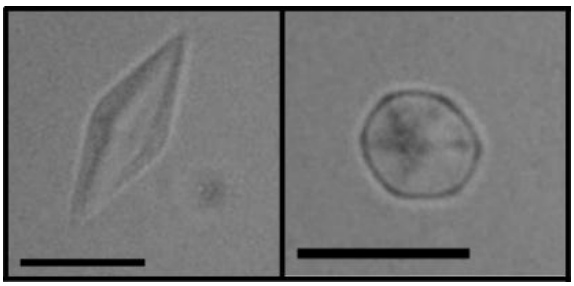

Fig. 184: The shape of metastable ice crystals in the presence of 15 mg/mL (jg)IBTC-3-GFP in 0.1 M NH_4HCO_3, pH 7.9, during the thermal hysteresis gap. The thermal hysteris is 0.4 °C. The left shows the slightly twisted hexagonal bipyramidal shape in the side view, on the right is the view perpendicular to the basal plane. The black scale in each picture is 10 µm. The *c*- to *a*-axis ratio is 2.8:1.

Antifreeze activity (80 mg/mL, 0.1 M NH_4HCO_3, pH 7.9):

- Thermal hysteresis: 0.9±0.1 °C
- ice shaping

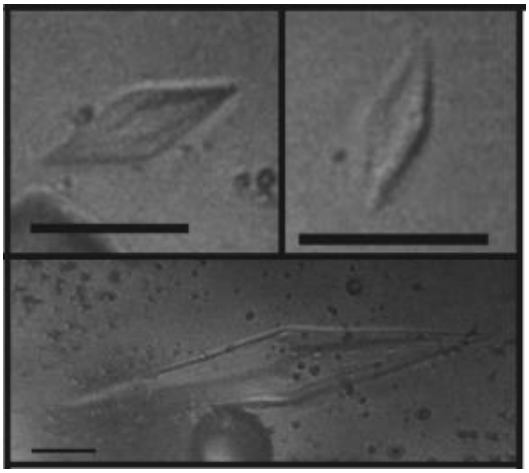

Fig. 185: The shape of metastable ice crystals in the presence of 80 mg/mL (jg)IBTC-3-GFP in 0.1 M NH_4HCO_3, pH 7.9. The thermal hysteresis is 0.9 °C. The top shows the slightly twisted hexagonal bipyramidal shape in the side view during the thermal hysteresis gap, the bottom shortly before the burst. The black scale in each picture is 10 µm long. The *c*- to *a*-axis ratio is 3.0:1. The dark gray spheres are air bubbles.

List of Figures

List of Tables

Abbreviations

Δδ	Sum of the chemical shift deviation
δ	Chemical shift
λ	Wavelength
χ_F	Fraction folded
AFP	Antifreeze protein
APS	Ammoniumperoxodisulfat
CD	Circular dichroism
cosy	Correlation spectroscopy
CSD	Chemical shift deviation
CV	Column volume
Da	Dalton (kDa = Kilodalton)
ddH_2O	Double-distilled water
DIPEA	*N,N'*-diisopropylethylamine
Dmb	3,4-Dimethoxybenyl
DMF	Dimethylformamide
DMSO	Dimethyl sulfoxide
DTT	Dithiothreitol
E. coli	*Escherichia coli*
EDTA	Ethylenediaminetetraacetic acid
ESI	Electron spray ionization
FIPA	Fluorescence-based ice plane affinity
Fmoc	Fluorenylmethoxycarbonyl
g	Gramm (mg = Milligramm)
GFP	Green fluorescent protein

HATU	1-[Bis(dimethylamino)methylene]-1H-1,2,3-triazolo[4,5-b]pyridinium 3-oxide hexafluorophosphate
His	Histidine
HOBt	Benzotriazol-1-ol
HPLC	High-performance liquid chromatography
HSQC	Hetero single quantum coherence
IBP	Ice binding protein
IBS	Ice binding site
IBTC	Ice binding Trp-cage
IPTG	Isopropyl-β-D-galactopyranosid
IUPAC	International Union of Pure and Applied Chemistry
L	Liter (mL = Milliliter, µL = Microliter)
M	Molar (mol/L)
MALDI	Matrix assisted laser desorption ionization
min	Minute
MS	Mass spectrometry
MWCO	Molecular weight cut-off
Ni-NTA	Nickel-nitrilotriacetic acid
nm	Nanometer
NMR	Nuclear magnetic resonance
NOE	Nuclear Overhauser effect
noesy	Nuclear Overhauser effect spectroscopy
OD_{600}	Optical density at 600 nm
PAGE	Polyacrylamide gel electrophoresis
PBS	Phosphate buffered saline
pH	*potential hydrogenii* (negative of the base 10 logarithm of the molar concentration of hydrogen ions)
PLRP-S	Poly(styrene-divinylbenzene)

PMSF	Phenylmethylsulfonyl fluoride
RP	Reverse-phase
rpm	rounds per minute
SDS	Sodium dodecyl sulfate
sec	Second
SENP2	Sentrin-specific protease 2
SPPS	Solid phase peptide synthesis
SUMO	Small ubiquitin-related modifier
T_M	Meltig point
t_R	Retention time
TFA	Trifluoracetic acid
TH	Thermal hysteresis
TIS	triisopropylsilane
tocsy	Total correlation spectroscopy
ToF	Time of flight
Tris	2-Amino-2-(hydroxymethyl)propane-1,3-diol
Trp	Tryptophane
UV	Ultra violet
UV/vis	Ultra violet and visible light
WflAFP	Antifreeze protein of the winder flounder

References

(1) Scholander, P. F.; van Dam, L.; Kanwisher, J. W.; Hammel, H. T.; Gordon, M. S. Supercooling and osmoregulation in arctic fish. *Journal of Cellular and Comparative Physiology* **1957**, *49*, 5–24.

(2) DeVries, A. L.; Wohlschlag, D. E. Freezing Resistance in Some Antarctic Fishes. *Science* **1969**, *163*, 1073–1075.

(3) Sicheri, F.; Yang, D. S. C. Ice-binding structure and mechanism of an antifreeze protein from winter flounder. *Nature* **1995**, *375*, 427–431.

(4) Kwan, A. H.-Y.; Fairley, K.; Anderberg, P. I.; Liew, C. W.; Harding, M. M.; Mackay, J. P. Solution Structure of a Recombinant Type I Sculpin Antifreeze Protein. *Biochemistry* **2005**, *44*, 1980–1988.

(5) Gronwald, W.; Loewen, M. C.; Lix, B.; Daugulis, A. J.; Sönnichsen, F. D.; Davies, P. L.; Sykes, B. D. The Solution Structure of Type II Antifreeze Protein Reveals a New Member of the Lectin Family. *Biochemistry* **1998**, *37*, 4712–4721.

(6) Liu, Y.; Li, Z.; Lin, Q.; Kosinski, J.; Seetharaman, J.; Bujnicki, J. M.; Sivaraman, J.; Hew, C.-L. Structure and Evolutionary Origin of Ca2+-Dependent Herring Type II Antifreeze Protein. *PLOS ONE* **2007**, *2*, 1–11.

(7) Nishimiya, Y.; Kondo, H.; Takamichi, M.; Sugimoto, H.; Suzuki, M.; Miura, A.; Tsuda, S. Crystal Structure and Mutational Analysis of Ca2+-Independent Type II Antifreeze Protein from Longsnout Poacher, Brachyopsis rostratus. *Journal of Molecular Biology* **2008**, *382*, 734–746.

(8) Yang, D. S. C.; Hon, W.-C.; Bubanko, S.; Xue, Y.; Seetharaman, J.; Hew, C. L.; Sicheri, F. Identification of the Ice-Binding Surface on a Type III Antifreeze Protein with a “Flatness Function” Algorithm. *Biophysical Journal* **1998**, *74*, 2142–2151.

(9) Ko, T.-P.; Robinson, H.; Gao, Y.-G.; Cheng, C.-H. C.; DeVries, A. L.; Wang, A. H.-J. The Refined Crystal Structure of an Eel Pout Type III Antifreeze Protein RD1 at 0.62-Å Resolution Reveals Structural Microheterogeneity of Protein and Solvation. *Biophysical Journal* **2003**, *84*, 1228–1237.

(10) Ye, Q.; Leinala, E.; Jia, Z. Structure of type III antifreeze protein at 277 K. *Acta crystallographica. Section D, Biological crystallography* **1998**, *54*, 700–702.

(11) Miura, K.; Ohgiya, S.; Hoshino, T.; Nemoto, N.; Suetake, T.; Miura, A.; Spyracopoulos, L.; Kondo, H.; Tsuda, S. NMR analysis of type III antifreeze protein intramolecular dimer. Structural basis for enhanced activity. *The Journal of Biological Chemistry* **2001**, *276*, 1304–1310.

(12) Sun, T.; Lin, F.-H.; Campbell, R. L.; Allingham, J. S.; Davies, P. L. An Antifreeze Protein Folds with an Interior Network of More Than 400 Semi-Clathrate Waters. *Science* **2014**, *343*, 795–798.

(13) Carter, A.; Riley, T. R.; Hillenbrand, C.-D.; Rittner, M. Widespread Antarctic glaciation during the Late Eocene. *Earth and Planetary Science Letters* **2017**, *458*, 49–57.

(14) Shackleton, N. J.; Backman, J.; Zimmerman, H.; Kent, D. V.; Hall, M. A.; Roberts, D. G.; Schnitker, D.; Baldauf, J. G.; Desprairies, A.; Homrighausen, R. *et al.* Oxygen isotope calibration of the onset of ice-rafting and history of glaciation in the North Atlantic region. *Nature* **1984**, *307*, 620–623.

(15) Scott, G. K.; Fletcher, G. L.; Davies, P. L. Fish Antifreeze Proteins: Recent Gene Evolution. *Canadian Journal of Fisheries and Aquatic Sciences* **1986**, *43*, 1028–1034.

(16) Graham, L. A.; Hobbs, R. S.; Fletcher, G. L.; Davies, P. L. Helical Antifreeze Proteins Have Independently Evolved in Fishes on Four Occasions. *PLOS ONE* **2013**, *8*, 1–12.

(17) Chen, L.; DeVries, A. L.; Cheng, C.-H. C. Convergent evolution of antifreeze glycoproteins in Antarctic notothenioid fish and Arctic cod. *Proceedings of the National Academy of Sciences* **1997**, *94*, 3817–3822.

(18) Graham, L. A.; Li, J.; Davidson, W. S.; Davies, P. L. Smelt was the likely beneficiary of an antifreeze gene laterally transferred between fishes. *BMC Evolutionary Biology* **2012**, *12*, 190.
(19) Ewart, K. V.; Rubinsky, B.; Fletcher, G. L. Structural and Functional Similarity between Fish Antifreeze Proteins and Calcium-Dependent Lectins. *Biochemical and Biophysical Research Communications* **1992**, *185*, 335–340.
(20) Yamashita, Y.; Miura, R.; Takemoto, Y.; Tsuda, S.; Kawahara, H.; Obata, H. Type II Antifreeze Protein from a Mid-latitude Freshwater Fish, Japanese Smelt (*Hypomesus nipponensis*). *Bioscience, Biotechnology, and Biochemistry* **2003**, *67*, 461–466.
(21) Graham, L. A.; Lougheed, S. C.; Ewart, K. V.; Davies, P. L. Lateral Transfer of a Lectin-Like Antifreeze Protein Gene in Fishes. *PLOS ONE* **2008**, *3*, 1–11.
(22) Fletcher, G. L.; Hew, C. L.; Davies, P. L. Antifreeze Proteins of Teleost Fishes. *Annual Review of Physiology* **2001**, *63*, 359–390.
(23) Hobbs, R. S.; Shears, M. A.; Graham, L. A.; Davies, P. L.; Fletcher, G. L. Isolation and characterization of type I antifreeze proteins from cunner, Tautogolabrus adspersus, order Perciformes. *The FEBS Journal* **2011**, *278*, 3699–3710.
(24) Wilkens, C.; Poulsen, J.-C. N.; Ramløv, H.; Lo Leggio, L. Purification, crystal structure determination and functional characterization of type III antifreeze proteins from the European eelpout Zoarces viviparus. *Cryobiology* **2014**, *69*, 163–168.
(25) Mahatabuddin, S.; Fukami, D.; Arai, T.; Nishimiya, Y.; Shimizu, R.; Shibazaki, C.; Kondo, H.; Adachi, M.; Tsuda, S. Polypentagonal ice-like water networks emerge solely in an activity-improved variant of ice-binding protein. *Proceedings of the National Academy of Sciences* **2018**, *115*, 5456–5461.
(26) Chakrabartty, A.; Hew, C. L.; Shears, M.; Fletcher, G. Primary structures of the alanine-rich antifreeze polypeptides from grubby sculpin, Myoxocephalus aenaeus. *Canadian Journal of Zoology* **1988**, *66*, 403–408.
(27) Low, W. K.; Lin, Q.; Stathakis, C.; Miao, M.; Fletcher, G. L.; Hew, C. L. Isolation and characterization of skin-type, type I antifreeze polypeptides from the longhorn sculpin, Myoxocephalus octodecemspinosus. *The Journal of Biological Chemistry* **2001**, *276*, 11582–11589.
(28) Yang, D. S. C.; Sax, M.; Chakrabartty, A.; Hew, C. L. Crystal structure of an antifreeze polypeptide and its mechanistic implications. *Nature* **1988**, *333*, 232–237.
(29) Evans, R. P.; Fletcher, G. L. Isolation and characterization of type I antifreeze proteins from Atlantic snailfish (Liparis atlanticus) and dusky snailfish (Liparis gibbus). *Biochimica et Biophysica Acta (BBA) - Protein Structure and Molecular Enzymology* **2001**, *1547*, 235–244.
(30) Scott, G. K.; Davies, P. L.; Shears, M. A.; Fletcher, G. L. Structural variations in the alanine-rich antifreeze proteins of the pleuronectinae. *European Journal of Biochemistry* **1987**, *168*, 629–633.
(31) Garnham, C. P.; Campbell, R. L.; Davies, P. L. Anchored clathrate waters bind antifreeze proteins to ice. *Proceedings of the National Academy of Sciences* **2011**, *108*, 7363–7367.
(32) Middleton, A. J.; Marshall, C. B.; Faucher, F.; Bar-Dolev, M.; Braslavsky, I.; Campbell, R. L.; Walker, V. K.; Davies, P. L. Antifreeze Protein from Freeze-Tolerant Grass Has a Beta-Roll Fold with an Irregularly Structured Ice-Binding Site. *Journal of Molecular Biology* **2012**, *416*, 713–724.
(33) Kondo, H.; Hanada, Y.; Sugimoto, H.; Hoshino, T.; Garnham, C. P.; Davies, P. L.; Tsuda, S. Ice-binding site of snow mold fungus antifreeze protein deviates from structural regularity and high conservation. *Proceedings of the National Academy of Sciences* **2012**, *109*, 9360–9365.

(34) Liou, Y.-C.; Tocilj, A.; Davies, P. L.; Jia, Z. Mimicry of ice structure by surface hydroxyls and water of a β-helix antifreeze protein. *Nature* **2000**, *406*, 322–324.
(35) Raymond, J. A. Algal ice-binding proteins change the structure of sea ice. *Proceedings of the National Academy of Sciences* **2011**, *108*, E198-E198.
(36) Davies, P. L. Ice-binding proteins: A remarkable diversity of structures for stopping and starting ice growth. *Trends in Biochemical Sciences* **2014**, *39*, 548–555.
(37) Pentelute, B. L.; Gates, Z. P.; Tereshko, V.; Dashnau, J. L.; Vanderkooi, J. M.; Kossiakoff, A. A.; Kent, S. B. H. X-ray Structure of Snow Flea Antifreeze Protein Determined by Racemic Crystallization of Synthetic Protein Enantiomers. *Journal of the American Chemical Society* **2008**, *130*, 9695–9701.
(38) Leinala, E. K.; Davies, P. L.; Doucet, D.; Tyshenko, M. G.; Walker, V. K.; Jia, Z. A beta-helical antifreeze protein isoform with increased activity. Structural and functional insights. *The Journal of Biological Chemistry* **2002**, *277*, 33349–33352.
(39) Hakim, A.; Nguyen, J. B.; Basu, K.; Zhu, D. F.; Thakral, D.; Davies, P. L.; Isaacs, F. J.; Modis, Y.; Meng, W. Crystal structure of an insect antifreeze protein and its implications for ice binding. *The Journal of Biological Chemistry* **2013**, *288*, 12295–12304.
(40) Raymond, J. A.; DeVries, A. L. Adsorption inhibition as a mechanism of freezing resistance in polar fishes. *Proceedings of the National Academy of Sciences* **1977**, *74*, 2589–2593.
(41) Knight, C. A.; DeVries, A. L. Melting Inhibition and Superheating of Ice by an Antifreeze Glycopeptide. *Science* **1989**, *245*, 505–507.
(42) Pertaya, N.; Marshall, C. B.; DiPrinzio, C. L.; Wilen, L.; Thomson, E. S.; Wettlaufer, J. S.; Davies, P. L.; Braslavsky, I. Fluorescence Microscopy Evidence for Quasi-Permanent Attachment of Antifreeze Proteins to Ice Surfaces. *Biophysical Journal* **2007**, *92*, 3663–3673.
(43) Celik, Y.; Drori, R.; Pertaya-Braun, N.; Altan, A.; Barton, T.; Bar-Dolev, M.; Groisman, A.; Davies, P. L.; Braslavsky, I. Microfluidic experiments reveal that antifreeze proteins bound to ice crystals suffice to prevent their growth. *Proceedings of the National Academy of Sciences* **2013**, *110*, 1309–1314.
(44) Lonsdale, K. Y.; Bernal, J. D. The structure of ice. *Proceedings of the Royal Society of London. Series A. Mathematical and Physical Sciences* **1958**, *247*, 424–434.
(45) Madura, J. D.; Baran, K.; Wierzbicki, A. Molecular recognition and binding of thermal hysteresis proteins to ice. *Journal of Molecular Recognition* **2000**, *13*, 101–113.
(46) Chakrabartty, A.; Yang, D. S. C.; Hew, C. L. Structure-function relationship in a winter flounder antifreeze polypeptide. II. Alteration of the component growth rates of ice by synthetic antifreeze polypeptides. *The Journal of Biological Chemistry* **1989**, *264*, 11313–11316.
(47) Bar-Dolev, M.; Celik, Y.; Wettlaufer, J. S.; Davies, P. L.; Braslavsky, I. New insights into ice growth and melting modifications by antifreeze proteins. *Journal of the Royal Society, Interface* **2012**, *9*, 3249–3259.
(48) Knight, C. A.; Cheng, C. C.; DeVries, A. L. Adsorption of alpha-helical antifreeze peptides on specific ice crystal surface planes. *Biophysical Journal* **1991**, *59*, 409–418.
(49) Garnham, C. P.; Natarajan, A.; Middleton, A. J.; Kuiper, M. J.; Braslavsky, I.; Davies, P. L. Compound Ice-Binding Site of an Antifreeze Protein Revealed by Mutagenesis and Fluorescent Tagging. *Biochemistry* **2010**, *49*, 9063–9071.
(50) Basu, K.; Garnham, C. P.; Nishimiya, Y.; Tsuda, S.; Braslavsky, I.; Davies, P. Determining the ice-binding planes of antifreeze proteins by fluorescence-based ice plane affinity. *Journal of Visualized Experiments* **2014**, e51185.

(51) Marshall, C. B.; Daley, M. E.; Graham, L. A.; Sykes, B. D.; Davies, P. L. Identification of the ice-binding face of antifreeze protein from Tenebrio molitor. *FEBS Letters* **2002**, *529*, 261–267.
(52) DeLuca, C. I.; Davies, P. L.; Ye, Q.; Jia, Z. The effects of steric mutations on the structure of type III antifreeze protein and its interaction with ice11Edited by I. A. Wilson. *Journal of Molecular Biology* **1998**, *275*, 515–525.
(53) Sönnichsen, F. D.; DeLuca, C. I.; Davies, P. L.; Sykes, B. D. Refined solution structure of type III antifreeze protein: Hydrophobic groups may be involved in the energetics of the protein–ice interaction. *Structure* **1996**, *4*, 1325–1337.
(54) Modig, K.; Qvist, J.; Marshall, C. B.; Davies, P. L.; Halle, B. High water mobility on the ice-binding surface of a hyperactive antifreeze protein. *Physical Chemistry Chemical Physics* **2010**, *12*, 10189–10197.
(55) Hudait, A.; Moberg, D. R.; Qiu, Y.; Odendahl, N.; Paesani, F.; Molinero, V. Preordering of water is not needed for ice recognition by hyperactive antifreeze proteins. *Proceedings of the National Academy of Sciences* **2018**, *115*, 8266–8271.
(56) Chakrabartty, A.; Ananthanarayanan, V. S.; Hew, C. L. Structure-function relationships in a winter flounder antifreeze polypeptide. I. Stabilization of an alpha-helical antifreeze polypeptide by charged-group and hydrophobic interactions. *The Journal of Biological Chemistry* **1989**, *264*, 11307–11312.
(57) Andrew J. Doig. Chapter 1 - Stability and Design of α-Helical Peptides. In *Molecular Biology of Protein Folding, Part A*; P. Michael Conn, Ed.; Progress in Molecular Biology and Translational Science; Academic Press, 2008; pp 1–52.
(58) Nomenclature and symbolism for amino acids and peptides (Recommendations 1983). *Pure and Applied Chemistry* **1984**, *56*, 595–624.
(59) Houston, M. E.; Chao, H.; Hodges, R. S.; Sykes, B. D.; Kay, C. M.; Sönnichsen, F. D.; Loewen, M. C.; Davies, P. L. Binding of an oligopeptide to a specific plane of ice. *The Journal of Biological Chemistry* **1998**, *273*, 11714–11718.
(60) Baardsnes, J.; Kondejewski, L. H.; Hodges, R. S.; Chao, H.; Kay, C.; Davies, P. L. New ice-binding face for type I antifreeze protein. *FEBS Letters* **1999**, *463*, 87–91.
(61) Wen, D.; Laursen, R. A. A model for binding of an antifreeze polypeptide to ice. *Biophysical Journal* **1992**, *63*, 1659–1662.
(62) Chao, H.; Houston, M. E.; Hodges, R. S.; Kay, C. M.; Sykes, B. D.; Loewen, M. C.; Davies, P. L.; Sönnichsen, F. D. A Diminished Role for Hydrogen Bonds in Antifreeze Protein Binding to Ice. *Biochemistry* **1997**, *36*, 14652–14660.
(63) Haymet, A. D. J.; Ward, L. G.; Harding, M. M.; Knight, C. A. Valine substituted winter flounder 'antifreeze': Preservation of ice growth hysteresis. *FEBS Letters* **1998**, *430*, 301–306.
(64) Haymet, A. D. J.; Ward, L. G.; Harding, M. M. Winter Flounder "Antifreeze" Proteins: Synthesis and Ice Growth Inhibition of Analogues that Probe the Relative Importance of Hydrophobic and Hydrogen-Bonding Interactions. *Journal of the American Chemical Society* **1999**, *121*, 941–948.
(65) Patel, S. N.; Graether, S. P. Increased flexibility decreases antifreeze protein activity. *Protein Science* **2010**, *19*, 2356–2365.
(66) Park, K.-S.; Jung, W.-S.; Kim, H.-J.; Shin, S.-Y. Determination of the Minimal Sequence Required for Antifreeze Activity of Type I Antifreeze Protein (AFP 37). *Bulletin of the Korean Chemical Society* **2010**, *31*, 3791–3793.

(67) Neidigh, J. W.; Fesinmeyer, R. M.; Andersen, N. H. Designing a 20-residue protein. *Nature Structural Biology* **2002**, *9*, 425 - 430.
(68) Eng, J.; Kleinman, W. A.; Singh, L.; Singh, G.; Raufman, J. P. Isolation and characterization of exendin-4, an exendin-3 analogue, from Heloderma suspectum venom. Further evidence for an exendin receptor on dispersed acini from guinea pig pancreas. *The Journal of Biological Chemistry* **1992**, *267*, 7402–7405.
(69) Barua, B.; Lin, J. C.; Williams, V. D.; Kummler, P.; Neidigh, J. W.; Andersen, N. H. The Trp-cage: Optimizing the stability of a globular miniprotein. *Protein Engineering, Design and Selection* **2008**, *21*, 171–185.
(70) Rovó, P.; Farkas, V.; Hegyi, O.; Szolomájer-Csikós, O.; Tóth, G. K.; Perczel, A. Cooperativity network of Trp-cage miniproteins: Probing salt-bridges. *Journal of Peptide Science : an official publication of the European Peptide Society* **2011**, *17*, 610–619.
(71) Byrne, A.; Williams, D. V.; Barua, B.; Hagen, S. J.; Kier, B. L.; Andersen, N. H. Folding Dynamics and Pathways of the Trp-Cage Miniproteins. *Biochemistry* **2014**, *53*, 6011–6021.
(72) Pitera, J. W.; Swope, W. Understanding folding and design: Replica-exchange simulations of "Trp-cage" miniproteins. *Proceedings of the National Academy of Sciences* **2003**, *100*, 7587–7592.
(73) Markiewicz, B. N.; Jo, H.; Culik, R. M.; DeGrado, W. F.; Gai, F. Assessment of Local Friction in Protein Folding Dynamics Using a Helix Cross-Linker. *The Journal of Physical Chemistry B* **2013**, *117*, 14688–14696.
(74) Williams, D. V.; Byrne, A.; Stewart, J.; Andersen, N. H. Optimal Salt Bridge for Trp-Cage Stabilization. *Biochemistry* **2011**, *50*, 1143–1152.
(75) Lin, J. C.; Barua, B.; Andersen, N. H. The Helical Alanine Controversy: An (Ala)6 Insertion Dramatically Increases Helicity. *Journal of the American Chemical Society* **2004**, *126*, 13679–13684.
(76) Hałabis, A.; Żmudzińska, W.; Liwo, A.; Ołdziej, S. Conformational Dynamics of the Trp-Cage Miniprotein at Its Folding Temperature. *The Journal of Physical Chemistry B* **2012**, *116*, 6898–6907.
(77) Barua, B.; Andersen, N. H. Determinants of miniprotein stability: can anything replace a buried H-bonded Trp sidechain? *Letters in Peptide Science* **2001**, *8*, 221–226.
(78) Lipfert, M. Design of a Stabilizing and Switching Module for alpha-Helical Peptides. Dissertation, Christian-Albrechts-Universität zu Kiel, Kiel, 2017.
(79) Malakhov, M. P.; Mattern, M. R.; Malakhova, O. A.; Drinker, M.; Weeks, S. D.; Butt, T. R. SUMO fusions and SUMO-specific protease for efficient expression and purification of proteins. *Journal of Structural and Functional Genomics* **2004**, *5*, 75–86.
(80) Zimm, B. H.; Bragg, J. K. Theory of the Phase Transition between Helix and Random Coil in Polypeptide Chains. *The Journal of Chemical Physics* **1959**, *31*, 526–535.
(81) Liu, Y.; Liu, Z.; Androphy, E.; Chen, J.; Baleja, J. D. Design and Characterization of Helical Peptides that Inhibit the E6 Protein of Papillomavirus. *Biochemistry* **2004**, *43*, 7421–7431.
(82) Boujard, D.; Anselme, B.; Cullin, C.; Raguénès-Nicol, C.; Lechowski, S. *Zell- und Molekularbiologie im Überblick*; Springer Spektrum: Berlin, 2014.
(83) Cai, M.; Huang, Y.; Sakaguchi, K.; Clore, G. M.; Gronenborn, A. M.; Craigie, R. An efficient and cost-effective isotope labeling protocol for proteins expressed in shape Escherichia coli. *Journal of Biomolecular NMR* **1998**, *11*, 97–102.
(84) Chan, W. C.; White, P. D. *Fmoc solid phase peptide synthesis: A practical approach*; The practical approach series 222; Oxford University Press: New York, 2000.

(85) Krchnák, V.; Flegelová, Z.; Vágner, J. Aggregation of resin-bound peptides during solid-phase peptide synthesis. *International Journal of Peptide and Protein Research* **1993**, *42*, 450–454.
(86) Dawson, P. E.; Muir, T. W.; Clark-Lewis, I.; Kent, S. B. Synthesis of proteins by native chemical ligation. *Science* **1994**, *266*, 776–779.
(87) Saxon, E.; Armstrong, J. I.; Bertozzi, C. R. A "Traceless" Staudinger Ligation for the Chemoselective Synthesis of Amide Bonds. *Organic Letters* **2000**, *2*, 2141–2143.
(88) Nilsson, B. L.; Kiessling, L. L.; Raines, R. T. Staudinger Ligation: A Peptide from a Thioester and Azide. *Organic Letters* **2000**, *2*, 1939–1941.
(89) Patgiri, A.; Jochim, A. L.; Arora, P. S. A Hydrogen Bond Surrogate Approach for Stabilization of Short Peptide Sequences in α-Helical Conformation. *Accounts of Chemical Research* **2008**, *41*, 1289–1300.
(90) Ali, A. M.; Woolley, G. A. The effect of azobenzene cross-linker position on the degree of helical peptide photo-control. *Organic & Biomolecular Chemistry* **2013**, *11*, 5325–5331.
(91) Bundi, A.; Wüthrich, K. 1H-nmr parameters of the common amino acid residues measured in aqueous solutions of the linear tetrapeptides H-Gly-Gly-X-L-Ala-OH. *Biopolymers* **1979**, *18*, 285–297.
(92) Kardos, J.; Kiss, B.; Micsonai, A.; Rovó, P.; Menyhárd, D. K.; Kovács, J.; Váradi, G.; Tóth, G. K.; Perczel, A. Phosphorylation as Conformational Switch from the Native to Amyloid State: Trp-Cage as a Protein Aggregation Model. *The Journal of Physical Chemistry B* **2015**, *119*, 2946–2955.
(93) Mikolajczyk, J.; Drag, M.; Békés, M.; Cao, J. T.; Ronai, Z.'e.; Salvesen, G. S. Small ubiquitin-related modifier (SUMO)-specific proteases: Profiling the specificities and activities of human SENPs. *The Journal of Biological Chemistry* **2007**, *282*, 26217–26224.
(94) Li, H.; Robertson, A. D.; Jensen, J. H. Very fast empirical prediction and rationalization of protein pKa values. *Proteins: Structure, Function, and Bioinformatics* **2005**, *61*, 704–721.
(95) Cochran, D. A.E.; Penel, S.; Doig, A. J. Effect of the N1 residue on the stability of the α-helix for all 20 amino acids. *Protein Science* **2001**, *10*, 463–470.
(96) Royant, A.; Noirclerc-Savoye, M. Stabilizing role of glutamic acid 222 in the structure of Enhanced Green Fluorescent Protein. *Journal of Structural Biology* **2011**, *174*, 385–390.
(97) Khan, F.; Stott, K.; Jackson, S. Letter to the Editor: 1H, 15N and 13C backbone assignment of the Green Fluorescent Protein (GFP). *Journal of Biomolecular NMR* **2003**, *26*, 281–282.
(98) Wishart, D. S.; Bigam, C. G.; Holm, A.; Hodges, R. S.; Sykes, B. D. 1H, 13C and 15N random coil NMR chemical shifts of the common amino acids. I. Investigations of nearest-neighbor effects. *Journal of Biomolecular NMR* **1995**, *5*, 67–81.
(99) Wishart, D. S.; Sykes, B. D.; Richards, F. M. The chemical shift index: A fast and simple method for the assignment of protein secondary structure through NMR spectroscopy. *Biochemistry* **1992**, *31*, 1647–1651.
(100) Gronwald, W.; Chao, H.; Reddy, D. V.; Davies, P. L.; Sykes, B. D.; Sönnichsen, F. D. NMR Characterization of Side Chain Flexibility and Backbone Structure in the Type I Antifreeze Protein at Near Freezing Temperatures. *Biochemistry* **1996**, *35*, 16698–16704.
(101) Wishart, D. S.; Sykes, B. D. The 13C Chemical-Shift Index: A simple method for the identification of protein secondary structure using 13C chemical-shift data. *Journal of Biomolecular NMR* **1994**, *4*, 171–180.
(102) Brahms, S.; Brahms, J. Determination of protein secondary structure in solution by vacuum ultraviolet circular dichroism. *Journal of Molecular Biology* **1980**, *138*, 149–178.

(103) Miles, A. J.; Wallace, B. A. Circular dichroism spectroscopy of membrane proteins. *Chem. Soc. Rev.* **2016**, *45*, 4859–4872.
(104) Luo, P.; Baldwin, R. L. Mechanism of Helix Induction by Trifluoroethanol: A Framework for Extrapolating the Helix-Forming Properties of Peptides from Trifluoroethanol/Water Mixtures Back to Water. *Biochemistry* **1997**, *36*, 8413–8421.
(105) Chakrabartty, A.; Kortemme, T.; Padmanabhan, S.; Baldwin, R. L. Aromatic side-chain contribution to far-ultraviolet circular dichroism of helical peptides and its effect on measurement of helix propensities. *Biochemistry* **1993**, *32*, 5560–5565.
(106) Haymet, A.D.J.; Ward, L. G.; Harding, M. M. Hydrophobic analogues of the winter flounder 'antifreeze' protein. *FEBS Letters* **2001**, *491*, 285–288.
(107) Takamichi, M.; Nishimiya, Y.; Miura, A.; Tsuda, S. Fully active QAE isoform confers thermal hysteresis activity on a defective SP isoform of type III antifreeze protein. *The FEBS Journal* **2009**, *276*, 1471–1479.
(108) Mahatabuddin, S.; Hanada, Y.; Nishimiya, Y.; Miura, A.; Kondo, H.; Davies, P. L.; Tsuda, S. Concentration-dependent oligomerization of an alpha-helical antifreeze polypeptide makes it hyperactive. *Scientific Reports* **2017**, *7*, 42501 EP -.
(109) Kuiper, M. J.; Fecondo, J. V.; Wong, M. G. Rational design of α-helical antifreeze peptides. *The Journal of Peptide Research* **2002**, *59*, 1–8.
(110) Kun, H.; Mastai, Y. Activity of short segments of Type I antifreeze protein. *Peptide Science* **2007**, *88*, 807–814.
(111) Zhang, Y.; Liu, K.; Li, K.; Gutowski, V.; Yin, Y.; Wang, J. Fabrication of Anti-Icing Surfaces by Short α-Helical Peptides. *ACS Applied Materials & Interfaces* **2018**, *10*, 1957–1962.
(112) Wen, D.; Laursen, R. A. Structure-function relationships in an antifreeze polypeptide. The role of neutral, polar amino acids. *The Journal of Biological Chemistry* **1992**, *267*, 14102–14108.
(113) DeLuca, C. I.; Comley, R.; Davies, P. L. Antifreeze Proteins Bind Independently to Ice. *Biophysical Journal* **1998**, *74*, 1502–1508.
(114) Drori, R.; Celik, Y.; Davies, P. L.; Braslavsky, I. Ice-binding proteins that accumulate on different ice crystal planes produce distinct thermal hysteresis dynamics. *Journal of The Royal Society Interface* **2014**, *11*, 20140526.
(115) Harding, M. M.; Ward, L. G.; Haymet, A. D. J. Type I 'antifreeze' proteins. *European Journal of Biochemistry* **1999**, *264*, 653–665.
(116) Warren, G. J.; Hague, C. M.; Corotto, L. V.; Mueller, G. M. Properties of engineered antifreeze peptides. *FEBS Letters* **1993**, *321*, 116–120.
(117) McMillan, A. W.; Kier, B. L.; Shu, I.; Byrne, A.; Andersen, N. H.; Parson, W. W. Fluorescence of Tryptophan in Designed Hairpin and Trp-Cage Miniproteins: Measurements of Fluorescence Yields and Calculations by Quantum Mechanical Molecular Dynamics Simulations. *The Journal of Physical Chemistry B* **2013**, *117*, 1790–1809.
(118) *Molecular Machines and Motors;* Sauvage, J.-P.; Amendola, V.; Ballardini, R.; Balzani, V.; Credi, A.; Fabbrizzi, L.; Gandolfi, M. T.; Gimzewski, J. K.; Gómez-Kaifer, M.; Joachim, C. *et al., Eds.*; Structure and Bonding 99; Springer Berlin Heidelberg: Berlin, Heidelberg, 2001.
(119) Bandara, H. M. D.; Burdette, S. C. Photoisomerization in different classes of azobenzene. *Chem. Soc. Rev.* **2012**, *41*, 1809–1825.
(120) Siewertsen, R.; Neumann, H.; Buchheim-Stehn, B.; Herges, R.; Näther, C.; Renth, F.; Temps, F. Highly Efficient Reversible Z–E Photoisomerization of a Bridged Azobenzene with Visible Light

through Resolved S1(nπ*) Absorption Bands. *Journal of the American Chemical Society* **2009**, *131*, 15594–15595.
(121) Klajn, R. Spiropyran-based dynamic materials. *Chem. Soc. Rev.* **2014**, *43*, 148–184.
(122) Kolb, H. C.; Finn, M. G.; Sharpless, K. B. Click Chemistry: Diverse Chemical Function from a Few Good Reactions. *Angewandte Chemie International Edition* **2001**, *40*, 2004–2021.
(123) Chong, S. Overview of Cell-Free Protein Synthesis: Historic Landmarks, Commercial Systems, and Expanding Applications. *Current Protocols in Molecular Biology* **2014**, *108*, 16.30.1-16.30.11.
(124) Brinkley, M. A brief survey of methods for preparing protein conjugates with dyes, haptens and crosslinking reagents. *Bioconjugate Chemistry* **1992**, *3*, 2–13.
(125) Lee, M. S.; Gippert, G. P.; Soman, K. V.; Case, D. A.; Wright, P. E. Three-dimensional solution structure of a single zinc finger DNA-binding domain. *Science* **1989**, *245*, 635–637.
(126) Blundell, T. L.; Pitts, J. E.; Tickle, I. J.; Wood, S. P.; Wu, C.-W. X-ray analysis (1. 4-\r A resolution) of avian pancreatic polypeptide: Small globular protein hormone. *Proceedings of the National Academy of Sciences* **1981**, *78*, 4175–4179.
(127) Glover, I.; Haneef, I.; Pitts, J.; Wood, S.; Moss, D.; Tickle, I.; Blundell, T. Conformational flexibility in a small globular hormone: X-ray analysis of avian pancreatic polypeptide at 0.98-Å resolution. *Biopolymers* **1983**, *22*, 293–304.
(128) Montclare, J. K.; Schepartz, A. Miniature Homeodomains: High Specificity without an N-Terminal Arm. *Journal of the American Chemical Society* **2003**, *125*, 3416–3417.
(129) Högbom, M.; Eklund, M.; Nygren, P.-\r. A.; Nordlund, P. Structural basis for recognition by an in vitro evolved affibody. *Proceedings of the National Academy of Sciences* **2003**, *100*, 3191–3196.
(130) McKnight, C. J.; Matsudaira, P. T.; Kim, P. S. NMR structure of the 35-residue villin headpiece subdomain. *Nature Structural Biology* **1997**, *4*, 180–184.
(131) Merrifield, R. B. Solid Phase Peptide Synthesis. I. The Synthesis of a Tetrapeptide. *Journal of the American Chemical Society* **1963**, *85*, 2149–2154.
(132) Carpino, L. A.; Han, G. Y. 9-Fluorenylmethoxycarbonyl amino-protecting group. *The Journal of Organic Chemistry* **1972**, *37*, 3404–3409.
(133) Nicolás, E.; Pedroso, E.; Girald, E. Formation of aspartimide peptides in Asp-Gly sequences. *Tetrahedron Letters* **1989**, *30*, 497–500.
(134) Dölling, R.; Beyermann, M.; Haenel, J.; Kernchen, F.; Krause, E.; Franke, P.; Brudel, M.; Bienert, M. Piperidine-mediated side product formation for Asp(OBut)-containing peptides. *J. Chem. Soc., Chem. Commun.* **1994**, 853–854.
(135) Mergler, M.; Dick, F.; Sax, B.; Stähelin, C.; Vorherr, T. The aspartimide problem in Fmoc-based SPPS. Part II. *Journal of Peptide Science* **2003**, *9*, 518–526.
(136) Mergler, M.; Dick, F.; Sax, B.; Weiler, P.; Vorherr, T. The aspartimide problem in Fmoc-based SPPS. Part I. *Journal of Peptide Science* **2003**, *9*, 36–46.
(137) Cardona, V.; Eberle, I.; Barthélémy, S.; Beythien, J.; Doerner, B.; Schneeberger, P.; Keyte, J.; White, P. D. Application of Dmb-Dipeptides in the Fmoc SPPS of Difficult and Aspartimide-Prone Sequences. *International Journal of Peptide Research and Therapeutics* **2008**, *14*, 285–292.
(138) Chen, Y.; Mant, C. T.; Hodges, R. S. Preparative reversed-phase high-performance liquid chromatography collection efficiency for an antimicrobial peptide on columns of varying diameters (1mm to 9.4mm I.D.). *Journal of Chromatography A* **2007**, *1140*, 112–120.

(139) Rovó, P.; Farkas, V.; Stráner, P.; Szabó, M.; Jermendy, Á.; Hegyi, O.; Tóth, G. K.; Perczel, A. Rational Design of α-Helix-Stabilized Exendin-4 Analogues. *Biochemistry* **2014**, *53*, 3540–3552.
(140) Harris, R. K.; Becker, E. D.; Cabral de Menezes, S. M.; Granger, P.; Hoffman, R. E.; Zilm, K. W. Further conventions for NMR shielding and chemical shifts (IUPAC Recommendations 2008). *Pure and Applied Chemistry* **2008**, *80*, 59–84.
(141) Aeschbacher, T.; Schubert, M.; Allain, F. H.-T. A procedure to validate and correct the 13C chemical shift calibration of RNA datasets. *Journal of Biomolecular NMR* **2012**, *52*, 179–190.
(142) Hwang, T. L.; Shaka, A. J. Water Suppression That Works. Excitation Sculpting Using Arbitrary Wave-Forms and Pulsed-Field Gradients. *Journal of Magnetic Resonance, Series A* **1995**, *112*, 275–279.
(143) Wüthrich, K. Sequential individual resonance assignments in the 1H-NMR spectra of polypeptides and proteins. *Biopolymers* **1983**, *22*, 131–138.
(144) Fesinmeyer, R. M.; Hudson, F. M.; Andersen, N. H. Enhanced Hairpin Stability through Loop Design: The Case of the Protein G B1 Domain Hairpin. *Journal of the American Chemical Society* **2004**, *126*, 7238–7243.
(145) *Maestro*; Schrödinger, LLC: New York, NY, 2019.
(146) *MacroModel*; Schrödinger, LLC: New York, NY, 2019.
(147) Harder, E.; Damm, W.; Maple, J.; Wu, C.; Reboul, M.; Xiang, J. Y.; Wang, L.; Lupyan, D.; Dahlgren, M. K.; Knight, J. L. *et al.* OPLS3: A Force Field Providing Broad Coverage of Drug-like Small Molecules and Proteins. *Journal of Chemical Theory and Computation* **2016**, *12*, 281–296.
(148) Shivakumar, D.; Williams, J.; Wu, Y.; Damm, W.; Shelley, J.; Sherman, W. Prediction of Absolute Solvation Free Energies using Molecular Dynamics Free Energy Perturbation and the OPLS Force Field. *Journal of Chemical Theory and Computation* **2010**, *6*, 1509–1519.
(149) Jorgensen, W. L.; Maxwell, D. S.; Tirado-Rives, J. Development and Testing of the OPLS All-Atom Force Field on Conformational Energetics and Properties of Organic Liquids. *Journal of the American Chemical Society* **1996**, *118*, 11225–11236.
(150) Jorgensen, W. L.; Tirado-Rives, J. The OPLS [optimized potentials for liquid simulations] potential functions for proteins, energy minimizations for crystals of cyclic peptides and crambin. *Journal of the American Chemical Society* **1988**, *110*, 1657–1666.
(151) Polak, E.; Ribiere, G. Note sur la convergence de méthodes de directions conjuguées. *R.I.R.O.* **1969**, *3*, 35–43.
(152) *The PyMOL Molecular Graphics System*; Schrödinger, LLC: New York, NY, 2019.
(153) Walker, J. M. *The Proteomics Protocols Handbook*; Humana Press: Totowa, NJ, 2005.
(154) Anthis, N. J.; Clore, G. M. Sequence-specific determination of protein and peptide concentrations by absorbance at 205 nm. *Protein Science* **2013**, *22*, 851–858.
(155) Kuipers, B. J. H.; Gruppen, H. Prediction of Molar Extinction Coefficients of Proteins and Peptides Using UV Absorption of the Constituent Amino Acids at 214 nm To Enable Quantitative Reverse Phase High-Performance Liquid Chromatography−Mass Spectrometry Analysis. *Journal of Agricultural and Food Chemistry* **2007**, *55*, 5445–5451.